Tesis Doctoral
Ingeniería Industrial

Optimization and Multivariable Control of Refrigeration Systems

Autor: Guillermo Bejarano Pellicer
Directores: Manuel G. Ortega Linares
Francisco Rodríguez Rubio

Ingeniería de Sistemas y Automática
Escuela Técnica Superior de Ingeniería
Universidad de Sevilla

Sevilla, 2017

Tesis Doctoral
Ingeniería Industrial

Optimization and Multivariable Control of Refrigeration Systems

Autor:

Guillermo Bejarano Pellicer

Directores:

Manuel G. Ortega Linares

Profesor Titular

Francisco Rodríguez Rubio

Catedrático de Universidad

Ingeniería de Sistemas y Automática
Escuela Técnica Superior de Ingeniería
Universidad de Sevilla

2017

Tesis Doctoral: Optimization and Multivariable Control of Refrigeration Systems

Autor: Guillermo Bejarano Pellicer
Directores: Manuel G. Ortega Linares
Francisco Rodríguez Rubio

El tribunal nombrado para juzgar la Tesis arriba indicada, compuesto por los siguientes doctores:

Presidente:

Vocales:

Secretario:

acuerdan otorgarle la calificación de:

El Secretario del Tribunal

Fecha:

To my family and Patri, the real support of my life

Acknowledgements

The successful completion of this Thesis is due to the effort, cooperation, support, help, understanding, and dedication of many people. May the reader forgive me for writing the acknowledgements in my mother tongue.

En primer lugar, quisiera mostrar mi agradecimiento a mis directores de Tesis, Manolo Gil y Paco Rodríguez Rubio. Desde mis comienzos en tareas de investigación creyeron en mí mucho más que yo mismo, dándome múltiples oportunidades para desarrollar mis capacidades y mis ideas. Sin su ayuda y apoyo constante ninguno de mis logros habría sido posible, y esta Tesis no es más que el resultado de varios años de formación, seguimiento y guía acertada por su parte. En especial quisiera agradecer a Manolo Gil su predisposición a ayudar en cualquiera tarea, relacionada o no con la Tesis, y la confianza que me dio desde que finalicé mi Carrera, contando conmigo en múltiples proyectos de muy diferente índole, en los cuales nos embarcamos juntos sin saber muy bien cómo llegaríamos al final, pero que han resultado sin duda exitosos. Gracias por todo.

También debo agradecer su intenso trabajo a todos aquellos que han participado conmigo en el desarrollo de los proyectos sobre refrigeración en los que se enmarca la Tesis. Profesores como Fernando Castaño, Manolo Vargas, y Carlos Vivas, que ya fue tutor de mi Proyecto Fin de Carrera, con diversas ocupaciones docentes e investigadoras y poco tiempo disponible, han hecho lo posible por ayudar en el desarrollo del proyecto, permitiendo con sus consejos y paciencia que hoy presente este trabajo. Asimismo, debo agradecer a Julio Normey-Rico y Alexandre Trofino-Neto su magnífica atención durante mi estancia de investigación en Brasil, así como su valiosa ayuda en todos los aspectos de una estancia que ha resultado a nivel personal extremadamente enriquecedora, además de productiva y provechosa a nivel profesional.

Cómo no, tengo mucho que agradecer también a mis compañeros de trabajo. A David por su gusto artístico para las gráficas y su intensa dedicación a la planta experimental, a José Joaquín por sus conceptos de transferencia de calor que van a resultar extremadamente útiles en el proyecto sobre almacenamiento de frío, y sobre todo a José Enrique, mi

compañero inseparable desde el comienzo del programa de doctorado, a quien nunca pensé que echaría tanto de menos como durante los meses que estuve en Brasil y los meses que él estuvo en EEUU. Gracias por escucharme, por tu trabajo incansable, tus consejos sobre LaTeX y tu optimismo perenne. Y no puedo olvidarme de Ramón, que a pesar de no participar directamente en la investigación sobre refrigeración, ha sido durante años la alegría del despacho, y sin cuyos consejos sobre redacción y normativa aún me quedarían años para presentar este trabajo. También quiero acordarme de César y Álvaro, mis compañeros durante la estancia en Brasil, que me ayudaron a encontrar mi lugar a tantos kilómetros de casa.

Mi agradecimiento asimismo a la Universidad de Sevilla y el Ministerio de Economía, Industria y Competitividad del Gobierno de España por la financiación de los proyectos de investigación en los que se enmarca esta Tesis: *OCROSIRE* (DPI2013-44135-R) y *OPF-SAE* (DPI2015-70973-R).

Sin embargo, las personas a las que más tengo que agradecer no han participado en el proyecto sobre refrigeración. De hecho, ni siquiera saben mucho sobre él, al margen de sufrir los inconvenientes provocados por mis disgustos, tensión, estrés, frustración, falta de tiempo o la lejanía por mi estancia en Brasil. Todos estos inconvenientes se han visto reflejados para ellos en menos horas de sueño diario, cansancio físico y emocional, incluso enfermedades. No encuentro palabras para agradecerles por tanto a cambio de tan poco. Mi familia y Patri, vosotros sí que sois los verdaderos artífices y héroes de este trabajo.

El talento gana partidos, pero el trabajo en equipo y la inteligencia ganan campeonatos.

Michael Jordan

Guillermo Bejarano Pellicer
Sevilla, 2017

Resumen

Los ciclos de refrigeración por compresión de vapor constituyen el método más extendido a nivel mundial para la generación de frío. Estos sistemas se utilizan en áreas tan diversas como regulación de la temperatura en estancias habitadas, almacenamiento y transporte de alimentos y múltiples procesos industriales. Dado el considerable impacto causado por el consumo energético de estos sistemas en los balances económicos y medioambientales de los países desarrollados y en vías de desarrollo, y teniendo en cuenta la escasez creciente de fuentes de energía fósiles y el desarrollo todavía lento de las diferentes tecnologías de energía renovable, la operación óptima en términos de eficiencia energética de los sistemas de refrigeración por compresión de vapor existentes se presenta como un problema clave que abordar.

Esta Tesis aborda la operación óptima de los ciclos de refrigeración desde el punto de vista de la eficiencia energética. Aunque el trabajo se centra principalmente en sistemas de una etapa de compresión y un recinto a refrigerar, se analizan también otras configuraciones con varias etapas y varios recintos. Existen varios factores clave para alcanzar la operación óptima de un sistema de refrigeración en el campo del Control Automático: el modelado, la optimización y el control propiamente dicho.

En primer lugar, se estudia ampliamente el modelado estático y dinámico de los sistemas de refrigeración. En cuanto al segundo, se desarrolla un modelo dinámico simplificado y orientado al control de un ciclo de una etapa de compresión y un recinto a refrigerar. El objetivo es que pueda ser incorporado en estrategias de control basado en modelo, donde se requieren tanto una baja carga computacional como una descripción suficientemente precisa de la dinámica dominante del sistema, de acuerdo con los objetivos de control.

En segundo lugar, se analiza la operación óptima en régimen permanente de un ciclo de una etapa de compresión y un recinto a refrigerar. Dada una cierta demanda de frío, el objetivo de la fase de optimización es calcular el ciclo en régimen permanente que alcanza la máxima eficiencia energética posible asegurando la satisfacción de la demanda de frío y a la vez respetando las restricciones de operación. Una vez calculado, se pretende que este ciclo óptimo constituya la referencia a seguir por parte del controlador.

Finalmente, se estudia asimismo el problema de control. En la literatura sobre sistemas de refrigeración se encuentran principalmente dos esquemas: el control convencional

y el control centrado en la eficiencia energética. En el primer esquema, además de la referencia impuesta por la demanda de frío, se impone un valor bajo pero constante como referencia para el grado de sobrecalentamiento del refrigerante a la salida del evaporador, y el controlador se diseña simplemente para conseguir que las variables controladas alcancen sus valores de referencia. Sin embargo, en el caso del segundo esquema, las referencias para el control de bajo nivel se calculan teniendo en cuenta explícitamente la eficiencia energética global del ciclo. En cuanto al control de seguimiento, se propone un controlador multivariable centralizado H_∞ basado en el Problema de Sensibilidad Mixta *S/KS/T*. Respecto al control centrado en la eficiencia energética, en primer lugar se analiza por qué muchas de las técnicas de la literatura no son capaces de alcanzar el ciclo definido en la fase de optimización manipulando las acciones de control disponibles. Se estudia la controlabilidad de un ciclo de una etapa de compresión y un recinto a refrigerar mediante la teoría de sistemas lineales, así como mediante un análisis no lineal punto a punto basado en el método del retrato de fases. Dadas las conclusiones del análisis de controlabilidad, se propone una estrategia subóptima de control jerárquico, cuyo objetivo es alcanzar la máxima eficiencia energética posible asegurando la satisfacción de la demanda de frío.

La mayoría de las contribuciones de la Tesis son teóricas. No obstante, se pretende aplicar la estrategia de control propuesta a una planta experimental configurable que permite simular ciclos con múltiples etapas de compresión y múltiples recintos a refrigerar. Como primer paso, se lleva a cabo la identificación en régimen permanente de la planta a partir de datos experimentales, así como la validación de los modelos obtenidos para diferentes configuraciones de la planta.

Abstract

The vapour-compression refrigeration cycle is the most extensive method worldwide for cooling generation. Such systems are involved in as widely diverse areas as human comfort, food storage and transportation, and industrial processes. Given the huge impact of these systems on economic and environmental balances in both developed and developing countries, and taking into account the increasing shortage of fossil energy sources and the still slow development of renewable technologies, optimal operation of existing vapour-compression refrigeration systems in terms of energy efficiency while satisfying the cooling demand appears as a key problem to cope with.

This Thesis addresses optimal operation of refrigeration cycles from the point of view of energy efficiency. Although the work is mainly focused on one-compression-stage, one-load-demand systems, other multi-stage and multi-load-demand configurations are also analysed. Several key factors are required to achieve optimal operation of a refrigeration system within automatic control: modelling, optimization, and control *per se*.

First of all, steady-state and dynamic modelling of refrigeration systems are widely studied. Concerning the latter, a simplified control-oriented dynamic model of a one-stage, one-load-demand cycle is developed, in order to be included in model-based control strategies, where low computational load and accurate enough description of dominant dynamics according to control objectives are required.

Secondly, optimal steady-state operation of a one-stage, one-load-demand cycle is also analysed. Given a certain cooling demand, the objective of the optimization stage is to calculate the steady-state cycle achieving the highest energy efficiency which satisfies the cooling demand while observing some operating constraints. Once calculated, this optimal cycle is intended to be set as the reference for the controller.

Eventually, control issues are examined. There are two main schemes in the literature about control of refrigeration systems: the conventional scheme and the *energy-efficiency-aware* one. In the first one, in addition to the reference imposed by the cooling demand, a low but constant set point on the degree of superheating of the refrigerant at the evaporator outlet is applied, and the controller is merely designed to get the controlled variables to track their references. However, energy efficiency is explicitly considered when calculating the references for the low-level controller in the second scheme. Regarding the tracking

control, a multivariable centralised H_∞ controller, based on the *S/KS/T* Mixed Sensitivity Problem, is proposed. Concerning the *energy-efficiency-aware* control, it is analysed why many approaches in the literature have shown not to be able to achieve the cycle defined by the optimization stage by manipulating the available control actions. Therefore, the controllability of the one-stage, one-load-demand cycle is analysed using linear theory and a nonlinear pointwise analysis based on the phase portrait method. Given the conclusions of the controllability analysis, a suboptimal hierarchical control strategy is proposed to achieve the highest possible efficiency while satisfying the cooling load.

Most contributions of this Thesis are of theoretical nature. Notwithstanding, the application of the proposed control strategy to a multi-compression-stage, multi-load-demand experimental plant is intended. Then, steady-state identification of the plant is performed from experimental data, whereas validation of the models considering different plant configurations is also carried out.

Contents

Acronyms

CV	configuration valve
DMC	Dynamical Matrix Control
EEV	electronic expansion valve
ESC	extremum-seeking control
FB+FF	feedback-plus-feedforward
FV	*finite-volume*
GPC	Generalised Predictive Control
IP	initial point
ISE	Integral of Square Error
ITAE	Integral of Time multiplied by Absolute Error
LQG	linear-quadratic-Gaussian
LQR	linear-quadratic regulator
MB	*moving boundary*
MIMO	multiple-input-multiple-output
MPC	Model Predictive Control
OLE	Object Linking and Embedding
OP	operating point
OPC	OLE for Process Control
P-h	pressure-specific enthalpy
PCM	Phase change material
PFC	Predictive Functional Control
PI	proportional-integral
PID	proportional-integral-derivative
PLC	Programmable Logic Controller
PNMPC	Practical Nonlinear Model Predictive Control
PO	Percentage Overshoot
PWM	pulse-width-modulation
QP	quadratic programming

RECS	Residential Energy Consumption Survey
RHP	right-half plane
RMS	Root Mean Square
RNGA	Relative Normalized Gain Array
SCADA	Supervisory Control And Data Acquisition
SHC	suboptimal hierarchical control
SISO	single-input-single-output
SMB	*switched moving boundary*
SVC	superheat valve controller
TES	Thermal Energy Storage
TV-ESC	*time-varying* ESC
VFD	variable frequency drive
VSC	variable speed compressor

Notation

Latin symbols

$\boldsymbol{A}$	Linear model state matrix
A	Heat transfer perimeter [m]
A_v	Expansion valve opening [%]
$\boldsymbol{B}$	Linear model input matrix
b	Compressor parameter
b_{ij}	Element {i,j} in matrix $\boldsymbol{B}$
$\mathbb{C}$	Controllability matrix
C	Thermal capacity ratio
CH	Control horizon
COP	Coefficient of performance
c	Compressor parameter [m^3]
c_{eev}	Electronic expansion valve coefficient [m^2]
c_p	Specific heat at constant pressure [J kg^{-1} K^{-1}]
c_{puv}	Pressure upholding valve coefficient [m^2]
c_v	Specific heat at constant volume [J kg^{-1} K^{-1}]
$\boldsymbol{D}$	Linear reduced model input vector
$D_F(z)$	Low-pass-filter denominator (discrete)
d_i	Element {i} in vector $\boldsymbol{D}$
$\hat{\boldsymbol{E}}_{OP_i}(s)$	Multiplicative output uncertainty transfer matrix at the operating point OP_i (continuous)
E	Mechanical energy [W h]
$\boldsymbol{e}$	Error vector
$F(z)$	Discrete low-pass filter
$\boldsymbol{f}$	Force function in the heat exchanger model
f_i	Element {i} in force function $\boldsymbol{f}$
$\boldsymbol{G}$	Jacobian matrix
$\boldsymbol{G}(s)$	Continuous transfer matrix

$\hat{\boldsymbol{G}}(s)$	Scaled continuous transfer matrix
$\hat{\boldsymbol{G}}_{OP_i}(s)$	Scaled continuous transfer matrix at the operating point OP_i
$\boldsymbol{GP}(s)$	Generalised plant for the *S/KS/T* Problem (continuous)
g	Heat exchanger characteristic function
h	Specific enthalpy [J kg^{-1}]
J	Cost function
$\boldsymbol{K}(s)$	Controller continuous transfer matrix
$\hat{\boldsymbol{K}}(s)$	Scaled controller continuous transfer matrix
K	Static gain
k	Discrete time step
k_{drop}	Pressure drop factor [kg^{-1} m^{-1}]
L	Heat exchanger length [m]
MI	Number of manipulated inputs
$\dot{m}$	Mass flow [kg s^{-1}]
$\boldsymbol{NLF}$	Generic nonlinear function
N	Compressor speed [Hz]
NTU	Number of Transfer Units
n_i	Parameters of c_{eev} correlation ($\forall i = 0,1,...,4$)
P	Pressure [Pa]
PH	Prediction horizon
$\boldsymbol{Q}$	Tracking error weighting matrix
$\dot{Q}$	Cooling power [W]
q	Vapour quality
$\boldsymbol{R}$	Control effort weighting matrix
R	Thermal resistance [m^2 K W^{-1}]
RE	Relative error [%]
$\mathbb{S}$	Controllable subspace
$\boldsymbol{S}_0(s)$	Output sensitivity continuous transfer matrix
$\boldsymbol{SM}$	Scaling matrix
S_t	Compressor parameter [m^3]
s	Specific entropy [J kg^{-1} K^{-1}]
$\boldsymbol{T}_0(s)$	Output complementary sensitivity continuous transfer matrix
$\boldsymbol{T}_{\boldsymbol{z\omega}}(s)$	Generalised plant closed-loop continuous transfer matrix
T	Temperature [K]
T_{SC}	Degree of subcooling [K]
T_{SH}	Degree of superheating [K]
t	Time
t_r	Rise time [s]
t_s	Settling time [s]
UA	Global heat transfer coefficient [W K^{-1}]
$\boldsymbol{u}$	Manipulable input vector
V_R	Heat exchanger volume [m^3]

$\boldsymbol{v}$	Generalised plant measured vector
v	Specific volume [m^3 kg^{-1}]
$\boldsymbol{W_{KS}}(s)$	Control sensitivity weighting matrix (continuous)
$\boldsymbol{W_S}(s)$	Output sensitivity weighting matrix (continuous)
$\boldsymbol{W_T}(s)$	Output complementary sensitivity weighting matrix (continuous)
$\dot{W}$	Mechanical power [W]
$\boldsymbol{w}$	Input vector of the heat exchanger model
$\boldsymbol{x}$	State vector
$\boldsymbol{y}$	Output vector
$\boldsymbol{Z}$	Coefficient matrix
Z	Total number of experimental data
$\boldsymbol{z}$	Generalised plant error vector
z	Transfer function *zero*
z_{ij}	Element {i,j} in coefficient matrix $\boldsymbol{Z}$

Greek symbols

α	Overall heat transfer coefficient between the refrigerant and the secondary flux [W m^{-2} K^{-1}]
β	Output sensitivity weighting matrix parameter within the H_∞ controller design
$\boldsymbol{\Gamma}$	Experimental output vector in the identification process
γ	Ratio between the energy of $\boldsymbol{z}$ and $\boldsymbol{\omega}$
$\bar{\gamma}$	Mean void fraction at the heat exchanger
δ	Distance to the controllable subspace
ε	Heat exchange effectiveness
ζ	Normalised heat exchanger zone length
η	Correction to predicted output
$\boldsymbol{\theta}$	Parameter vector in the identification process
κ	Bandwidth parameter within the H_∞ controller design
$\boldsymbol{\Lambda}$	Projection matrix
λ	Convective heat transfer coefficient [W m^{-2} K^{-1}]
μ	Output sensitivity weighting matrix parameter within the H_∞ controller design
ν	Prediction error
$\boldsymbol{\xi}$	Residue vector in the identification process
ρ	Density [kg m^{-3}]
σ	*Singular value*
τ	Time constant [s]
υ	Differential increment
ϕ	Measurable variable set
φ	Experimental input matrix in the identification process
$\boldsymbol{\chi}$	Deviation with respect to the desired state

χ_i	Element {i} in vector χ
ψ	Optimization variable set
ω	Exogenous signal vector
ω	Frequency [rad s^{-1}]
ω_B	Crossover frequency with -3 dB of output sensitivity function [rad s^{-1}]
ω_{CN}	Frequency where the *condition number* reaches its minimum [rad s^{-1}]
ω_{cr}	Achievable control bandwidth [rad s^{-1}]
$\omega_{min,SV}$	Crossover frequency of minimum *singular value* [rad s^{-1}]
ω_T	Crossover frequency of output complementary sensitivity weight [rad s^{-1}]

Subscripts and superscripts

boost	booster compressor
c	condenser
cntrl	control
comp	compressor
cond	conduction
cycle	vapour-compression cycle
diag	diagonal
dis	discharge
e	evaporator
*e*5	evaporator at 5°C
*e*20	evaporator at -20°C
eev	electronic expansion valve
err	tracking error
FB	feedback
FF	feedforward
f	saturated liquid
fast	fast
forced	forced response
free	free response
g	saturated vapour
he	heat exchanger
in	inlet
int	integral effect
inv	inverse
is	isentropic
it	iterative
*m*1	condenser *mode* 1
*m*2	condenser *mode* 2
main	main compressor

max	maximum
meas	measured
mid	middle
min	minimum
nom	nominal operating point
out	outlet
PNMPC	Practical Nonlinear MPC
past	past and current
predict	predicted
RHP	right-half plane
ref	reference
sat	saturation
sc	subcooled liquid zone
sec	secondary flux
settle	settling
sh	superheated vapour zone
slow	slow
start	control start
suc	suction
surr	compressor surroundings
tot	complete phase change
tp	two-phase zone
track	tracking
trnsf	heat transfer
u	input
valve	expansion valve
w	wall
wc	without correction
z	*zero*

1 Introduction

The secret of getting ahead is getting started.

MARK TWAIN

Contents

The first Chapter is devoted to presenting the refrigeration systems and their relevance, as well as including a review of the literature about modelling, experimentation, optimization, and control. The objectives and the organisation of the Thesis are also explained. Furthermore, the publications related to the Thesis are included at the end of the Chapter.

1.1 Context

Refrigeration based on vapour compression is the leading technology worldwide in cooling generation, including air conditioning, refrigeration, and freezing. Controlling room temperature is involved in as widely diverse areas as human comfort, food storage and transportation, and industrial processes. Therefore, the applications of vapour-compression

refrigeration systems are extensive: domestic, commercial, and industrial refrigeration, whose power range varies from less than 1 kW to above 1 MW [1]. Although in some cases air conditioning and refrigeration are separately considered, these systems all work the same way: they utilise the inverse Rankine cycle to remove heat from a cold reservoir (i.e. a cold storage room) and transfer it to a hot reservoir, normally the surroundings. A great deal of energy is required in such tasks, in both developing and developed countries, which impacts negatively on energy and economic balances [2]. It is reported that approximately 30% of total energy all over the world is consumed by Heating, Ventilating, and Air Conditioning (HVAC) processes, as well as refrigerators and water heaters [3], while the most recent Residential Energy Consumption Survey (RECS) shows that air conditioners and refrigerators represent 28% of home energy consumption in the United States [4]. Furthermore, supermarkets and department stores are known to be one of the largest consumers in energy field, since official reports estimate that the average energy intensity for grocery stores is around 500 kWh/m^2 a year in USA, which means more than twice the energy consumed by a hotel or an office of the same size [5]. It is stated that a medium-sized supermarket consumes up to 3 millions kWh a year [6], and around 60% of this great energy consumption is related to refrigeration systems [7]. Considering commercial and residential buildings, around 45% of total electricity consumption is devoted to HVAC systems [8, 9].

Moreover, environmental issues related to refrigerant and energy waste merit consideration. Since not only more and more studies suggest that actual fossil fuel reserves and non-renewable energy sources are much smaller than we perceive to be today, but the cost of energy is also quickly and significantly increasing, greater efforts to increment energy efficiency while reducing environmental impact of current vapour-compression systems have been carried out. Furthermore, the still moderate progress of sustainable energy technologies turns this problem into a priority.

Some improvement has already been achieved; for instance, space heating and cooling (space conditioning) accounted for more than half of all residential energy consumption in USA for decades. Estimates from the most recent RECS show that 48% of energy consumption in USA homes in 2009 was for heating and cooling, down from 58% in 1993 [4]. However, there is still more room for improvement. This intended improvement involves, among others:

- *Energy-efficiency-aware* redesign of heat exchangers, pursuing a significant improvement in performance.
- Integration of electronics and control systems, in order to operate with floating pressures.
- Automatic fault detection and recovery capabilities.
- Use of optimization techniques which allow to continuously seek high efficiency, regardless of external or uncontrollable conditions, both in steady state and in transient.
- Use of environmentally-friendly and harmless -in terms of their impact on the ozone layer- refrigerants.

A canonical one-compression-stage, one-load-demand refrigeration cycle is shown in Figure 1.1, where the main components (the expansion valve, the compressor, the evaporator, and the condenser) are represented. Due to the growth of the electronics field, variable speed compressors (VSC) and electronic expansion valves (EEV) have gradually replaced older single speed compressors and thermostatic expansion valves, respectively. Such new components allow the development of smarter control strategies, not only to save energy but also to reduce fluctuations in the controlled variables and therefore achieve a more accurate control. The objective of the cycle is to remove heat from the secondary flux at the evaporator and reject heat at the condenser by transferring it to the secondary flux. The inverse Rankine cycle is applied, where the refrigerant enters the evaporator at low temperature and pressure and it evaporates while removing heat from the evaporator secondary flux. Then, the compressor increases the refrigerant pressure and temperature and it enters the condenser, where first its temperature decreases, secondly it condenses and finally it may become subcooled liquid while transferring heat to the condenser secondary flux. The expansion valve closes the cycle by upholding the pressure difference between the condenser and the evaporator.

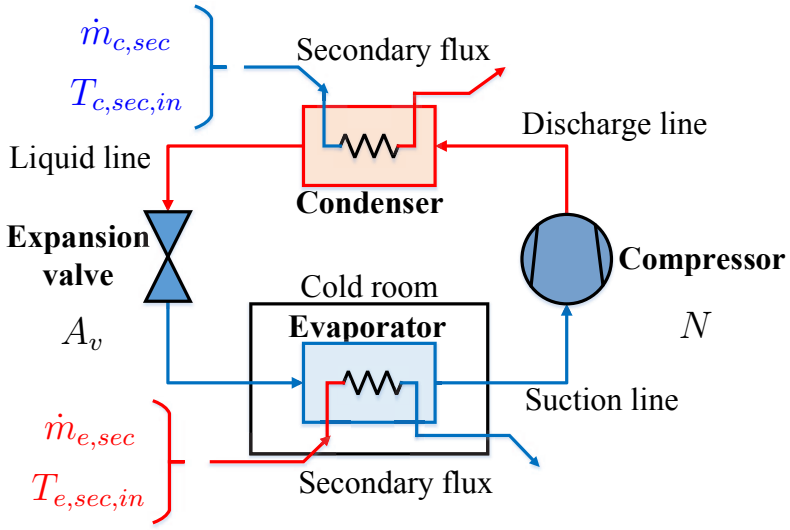

Figure 1.1 One-compression-stage, one-load-demand vapour-compression refrigeration cycle.

The main control objective is to provide the desired cooling power $\dot{Q}_e$. Furthermore, the generation of this cooling power is intended to be as efficient as possible. As widely known, energy efficiency is usually described in refrigeration field using the Coefficient of Performance (*COP*), which is defined as the ratio between the cooling power generated at the evaporator $\dot{Q}_e$ and the mechanical power provided by the compressor $\dot{W}_{comp}$, as indicated in Equation (1.1). Considering a one-compression-stage, one-load-demand cycle, the refrigerant mass flow $\dot{m}$ is the same at both components, thus the *COP* turns

out to depend only on intensive variables, specifically the characteristic enthalpies of the cycle, which are represented in the generic pressure-specific enthalpy chart (P-h diagram) shown in Figure 1.2. Note that the blue dashed line related to the cooling level simply represents the refrigerant saturation pressure at the inlet temperature of the evaporator secondary flux $T_{e,sec,in}$. Similarly, the red dashed line related to the ambient refers to the refrigerant saturation pressure at the inlet temperature of the condenser secondary flux $T_{c,sec,in}$. They have been included in the P-h diagram only to represent qualitatively the sign of the temperature difference between the refrigerant and the secondary flux at both heat exchangers.

$$COP = \frac{\dot{Q}_e}{\dot{W}_{comp}} = \frac{\dot{m}(h_{e,out} - h_{e,in})}{\dot{m}(h_{c,in} - h_{e,out})} = \frac{h_{e,out} - h_{e,in}}{h_{c,in} - h_{e,out}} \tag{1.1}$$

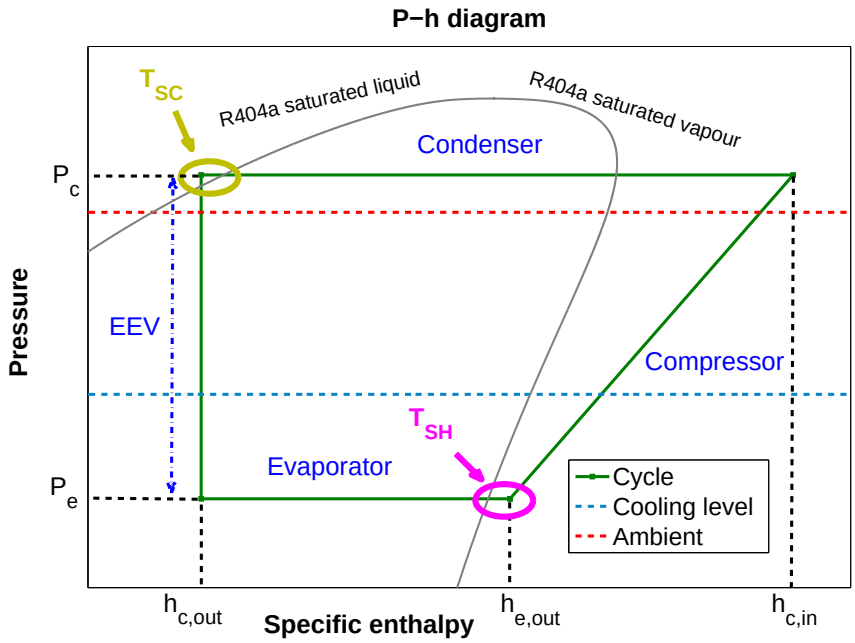

Figure 1.2 P-h diagram of a one-compression-stage, one-load-demand vapour-compression cycle.

This is the simplest vapour-compression cycle used in industry and domestic applications. Nevertheless, for instance at a supermarket, or simply at an ordinary domestic refrigerator, different service specifications usually coexist at the same system, for instance air conditioning, refrigeration, and freezing. Their temperature levels and cooling demands may vary, thus multi-compression-stage and multi-load-demand refrigeration cycles have been used in recent years to satisfy the refrigeration needs of such applications.

Consider the example of a supermarket, where some food products require refrigeration

to retain their nutritional properties. They are generally exposed in display cases where people take the products under a self-service system. The refrigeration system can be divided into a low temperature section for storage of frozen food and a medium/high temperature section for refrigerated non-frozen food.

If only one section is considered, for instance the medium/high temperature one, a supermarket refrigeration system basically works the same way as a one-stage, one-load-demand refrigeration system, represented above in Figure 1.1. A simplified supermarket refrigeration layout is shown in Figure 1.3, in accordance with Larsen [10]. The compressors are generally gathered in a rack where several units are arranged in parallel. The compressor rack increases the refrigerant pressure from the suction manifold. After compression the refrigerant reaches the condenser unit, where it transfers heat to ambient and condenses. The liquid refrigerant is gathered at the liquid manifold and then through some expansion valves the evaporators which lie in the display cases are fed. The refrigerant at the evaporator outlet flows on to the suction manifold and the cycle is closed.

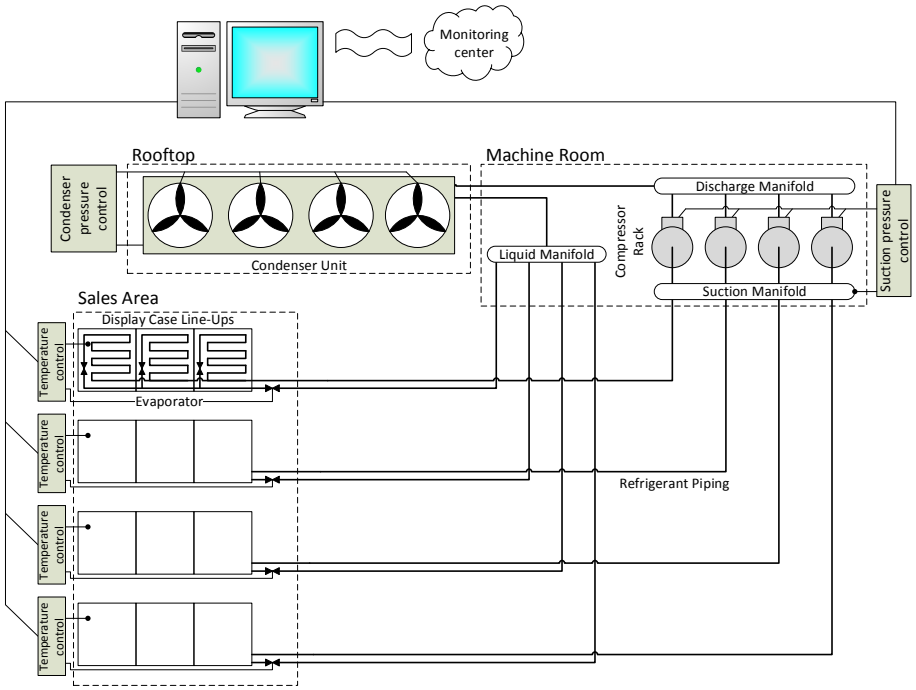

Figure 1.3 A typical layout of a supermarket refrigeration system, according to Larsen [10].

If various temperature sections are simultaneously considered, with different load demands, the system turns into a multi-load-demand cycle. Figure 1.4 represents a one-compression-stage, two-load-demand refrigeration cycle. It consists of two expansion valves, one variable speed compressor, and three heat exchangers (two evaporators and one condenser), in addition to a pressure upholding valve. Heat is removed at both evaporators

(specifically from their secondary fluxes) by evaporating the refrigerant at low pressure and temperature. The temperature and pressure of the refrigerant are increased at the compression stage. Then, heat is transferred to the secondary flux at the condenser by condensing and subsequently subcooling the initially superheated refrigerant. Pressures are usually quite different at the cooling and freezing chamber, which involves different evaporation temperatures. Thus, the pressure upholding valve just maintains the pressure difference between Evaporator 1 and Evaporator 2. The less restrictive it is, the less the pressure difference is between both evaporators, which implies that the temperature difference between the refrigerant and the secondary flux at Evaporator 1 is greater. At the output of the pressure upholding valve, two refrigerant flows are mixed together: that circulating through the Evaporator 2 at low temperature, and that expanded through the pressure upholding valve which comes from the Evaporator 1. The expansion valves allow the cycle to be closed by holding up the pressure difference between the condenser and each evaporator.

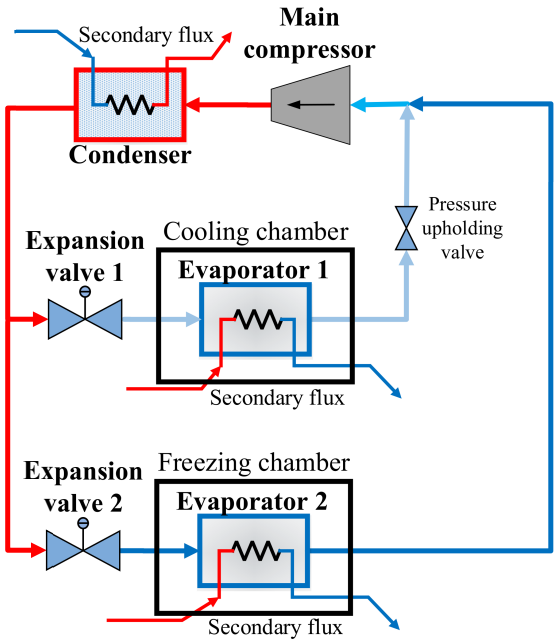

Figure 1.4 One-compression-stage, two-load-demand refrigeration cycle.

In these applications the availability of multi-compression-stage refrigeration cycles is useful to achieve greater energy efficiency. For instance, a two-compression-stage, two-load-demand refrigeration system is represented in Figure 1.5. In this case the refrigerant flow is compressed in two stages, using the main compressor and the booster one. Since there are different temperature requirements at the freezing and cooling chambers, the

mentioned extra valve is required in order to hold up the pressure difference between the Evaporator 1 output and the discharge of the booster compressor.

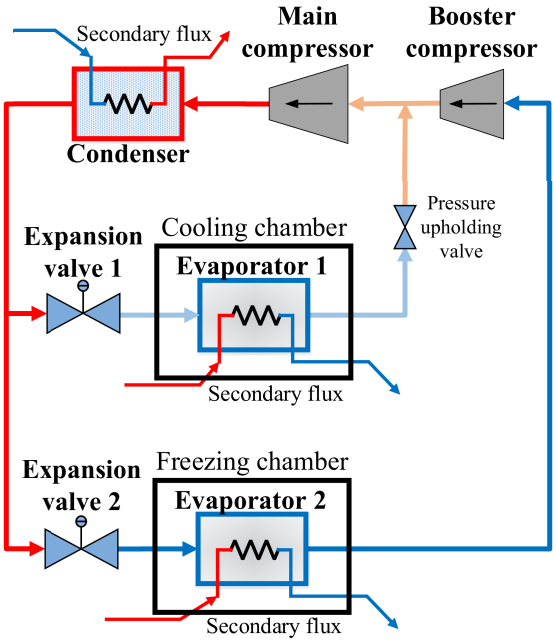

Figure 1.5 Two-compression-stage, two-load-demand refrigeration cycle.

In addition to multi-stage configurations, automatic control and optimization have potential to improve the performance of current refrigeration systems and they are expected to contribute to energy efficiency enhancement. However, it requires a deep knowledge of the process and modelling of such systems with required accuracy plays a central role, since many of the developed optimization techniques for vapour-compression refrigeration cycles involve components and system modelling, at least static models. Moreover, availability of a purpose-built breadboard refrigeration plant which allows to test such optimization techniques, along with novel control strategies, is of the utmost importance to obtain real enhancements regarding energy efficiency and control performance. Some examples of experimental plants found in the literature are those described by Rasmussen *et al.* [1], Larsen [10], and Schurt *et al.* [11], but they are usually one-compression-stage refrigeration cycles, with one or more cooling demands. That is why an experimental refrigeration plant, which can be configured to work with up to two compression stages and up to two load demands, has been set up at the Department of System Engineering and Automatic Control of University of Seville. Optimization and control issues which arise when regulating actual multi-stage, multi-load-demand refrigeration systems are intended to be simulated using this experimental facility.

1.2 State of Art

1.2.1 Problem statement

In this Thesis a particular application of refrigeration systems is considered. The cycle is expected to provide a certain cooling power $\dot{Q}_e$ to a continuous flow entering the evaporator as secondary flux. Neither the mass flow $\dot{m}_{e,sec}$ nor the inlet temperature $T_{e,sec,in}$ of such secondary flux are to be controlled, since they may be managed by another high-level controller. Therefore, the cooling demand can be expressed as a reference on the outlet temperature of the evaporator secondary flux $T_{e,sec,out}$, where the mass flow and inlet temperature behave as measurable disturbances to the refrigeration system. The difference with respect to the conventional case analysed in the literature lies in not considering the secondary mass flow as manipulable, since conventionally the cooling demand is merely a certain thermal power to be provided to the secondary flux for any mass flow, which is used as an additional manipulated input. Regarding the condenser, the inlet temperature $T_{c,sec,in}$ and mass flow $\dot{m}_{c,sec}$ of the secondary flux are also considered as disturbances.

It is shown in the literature that adding controllable inputs to the problem does not remove its underactuated features. Some works study the degrees of freedom of a vapour-compression cycle [12, 13, 14]. Particularly, Jensen and Skogestad consider more manipulated variables (four, including variable heat transfer coefficients at the evaporator and condenser, or equivalently considering adjustable secondary fluxes) than those considered in this Thesis [13]. Jensen and Skogestad state that five design specifications must be proposed to define a cycle given equipment, while only four controllable inputs are available. The fifth variable to be manipulated in operation is the so-called *active charge*, related to the refrigerant mass flow. One of the main conclusions of the work by Jensen and Skogestad is that this additional degree of freedom related to the *active charge* cannot be manipulated without introducing a variable-level liquid tank in the cycle, which implies modifying the topology of the system.

Therefore, adding the secondary mass flows as manipulated inputs only increases the complexity of the control system and it does not help reduce the *degree of underactuation*, neither solves it the controllability issues, as described later in this Thesis. Then, only the compressor speed N and the valve opening A_v are considered as manipulated variables, whereas both secondary flux mass flows and inlet temperatures act as measurable disturbances, as depicted in the schematic drawing shown in Figure 1.6.

1.2.2 Modelling

Refrigeration systems are, as generally known, closed cycles, whose components are connected through various pipes and valves, which causes strong nonlinearities and high coupling between variables. This is why dynamic modelling of vapour-compression refrigeration systems is not definitely trivial matter. The most important elements regarding the dynamic modelling are the heat exchangers, since the expansion valve, the compressor, and the thermal behaviour of the secondary fluxes are statically modelled, because their dynamics are usually at least one order of magnitude faster than those of the evaporator and condenser.

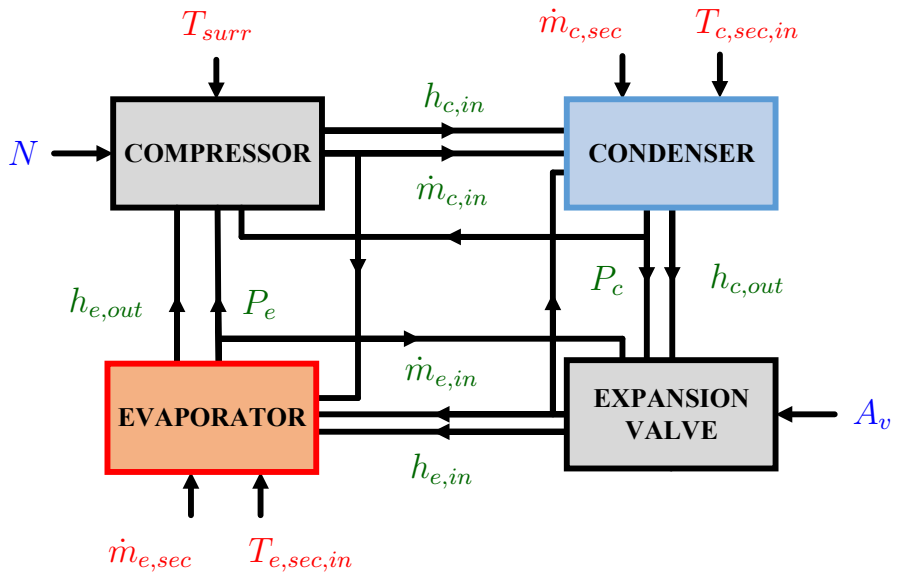

Figure 1.6 Diagram of variables involved in the cycle (blue colour refers to manipulated variables, red to disturbances and green to internal variables).

A very detailed model of a heat exchanger is based on mass, energy, and momentum balances of the refrigerant, the secondary flux, and the material separating them which comprises the heat exchanger itself. This approach, dating to MacArthur [15], involves spatially discretizing the heat exchanger into an arbitrary number of control volumes [16, 17], and thus leading to a numerical solution of a set of differential equations discretized into a finite difference form [18, 19]. The *finite-volume* (FV) approach provides very detailed knowledge about the system statics and dynamics, but due to its computational cost and complexity it is inappropriate for identification purposes and model-based control strategies.

A simpler model with better balance between accuracy and computational cost may be obtained using the *moving boundary* (MB) approach. This methodology divides the heat exchanger into a number of zones corresponding to different refrigerant states: superheated vapour, two-phase fluid, and/or subcooled liquid [1, 20]. Mass and energy balances are applied to each zone and, taking into account theses balances as well as other system constraints, the refrigerant variables at the heat exchanger outlet are obtained. The zone lengths are state variables, since they can vary with time depending on inputs and disturbances. A step further is developed by McKinley and Alleyne: some control volumes are allowed to completely disappear and reappear without simulation issues, giving rise to the *switched moving boundary* (SMB) model [21]. Different representations of the heat exchanger model, also known as *modes*, are defined depending on the existence or absence of each zone. For example, in the case of the evaporator, two *modes* are defined depending on the amount of superheated vapour, as seen in Figure 1.7. In the case of the condenser,

up to five different *modes* are considered, as shown in Figure 1.8. This model is validated and extended to startup and shutdown processes by Li and Alleyne [22, 23].

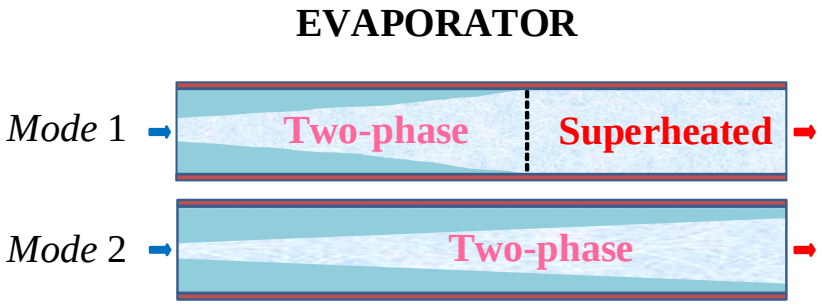

Figure 1.7 Evaporator *modes* according to the SMB approach [23].

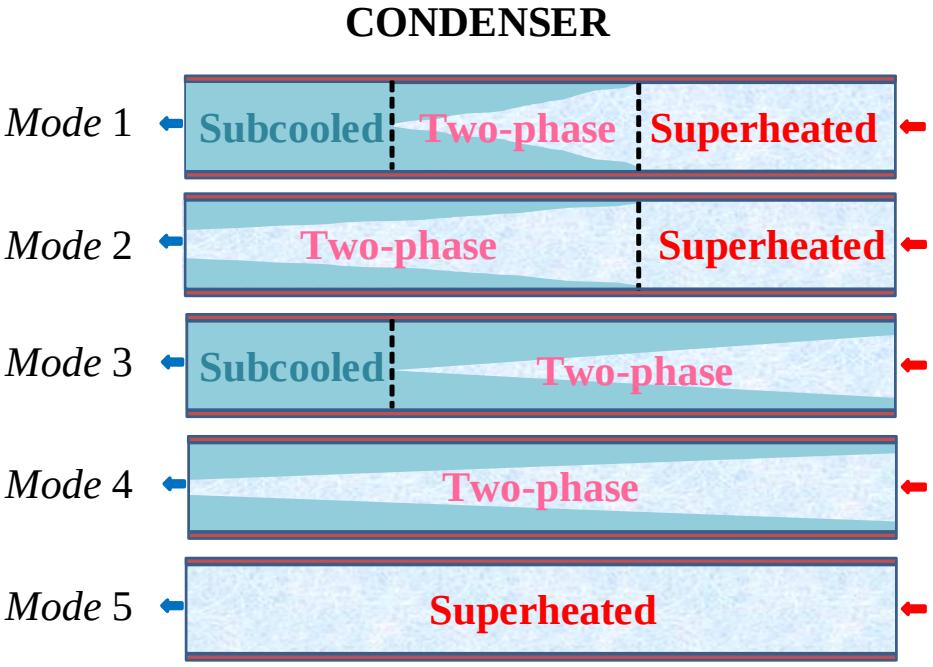

Figure 1.8 Condenser *modes* according to the SMB approach [23].

The complexity, computational load, and accuracy of the SMB model have been recently compared to those of the FV formulation [24]. It has been concluded that while the SMB approach can execute much more quickly in simulation than the FV approach, there is little difference in the achievable accuracy with respect to experimental data.

In addition to the FV and MB approaches, black-box models can be found in the literature, where any variable defining the cooling power is to be predicted from the manipulated variables. For instance, Bittanti and Piroddi propose a neural network approach to identification of a heat exchanger [25], while Romero *et al.* propose a simplified black-box model to predict accurately the chilled water temperature dynamic response of a vapour-compression chiller, where the Box-Jenkins structure gets the best fit to experimental results [26]. This modelling approach is suitable for control purposes, but only the identified output variables can be controlled.

1.2.3 Optimization and Control

To achieve high energy efficiency while satisfying the cooling demand, it must be taken into account that heat transfer at the evaporator is determining for the overall efficiency. Heat transfer is widely recognised to be much higher when the refrigerant flow is two-phase. Thus, the highest evaporator efficiency would be achieved if the refrigerant at the evaporator outlet was saturated vapour. This ideal behaviour is not advisable nor applicable in practice, since the risk of liquid droplets appearing at the evaporator outlet is very high in transient, which must be definitely avoided because the evaporator outlet matches the compressor intake. Therefore, the approach conventionally applied in industry consists in operating the cycle with a certain degree of superheating of the refrigerant at the evaporator outlet (T_{SH}), which is held low to approximate to the ideal behaviour previously described.

Therefore, the conventional control scheme is very simple: in addition to the reference on $T_{e,sec,out}$ imposed by the cooling demand, a low but constant set point on T_{SH} is applied and the controller is designed to get these two variables to track their references as efficiently as possible in presence of disturbances by manipulating N and A_v.

To design the tracking controller used within the conventional control scheme, it is important to take into account that the difficulty in controlling this process lies in high thermal inertia, dead times, high coupling between variables, and strong nonlinearities. The most used linear techniques which can be found in the literature regarding tracking control are decentralised control [27, 28, 29, 30]; decoupling multivariable control [31], LQG control [11, 32, 33]; model predictive control (MPC) [34, 35, 36, 37], and robust H_∞ control [38].

Regarding decentralised control, Marcinichen *et al.* have proposed a SISO dual strategy for N and A_v simultaneous control using PI controllers and the most used matching in industry: regulating the cooling capacity (namely $T_{e,sec,out}$) through N and the degree of superheating with A_v. Wang *et al.* implement an hybrid PID-Neural Network controller, which consists in a neural network which tunes the PID parameters online [28]. Underwood proposes a control strategy where two PID controllers (one for each manipulated variable) are jointly tuned through optimisation techniques [29]. Meanwhile, Salazar and Méndez apply a decentralised PID control over a single-stage transcritical CO_2 refrigeration cycle, where a lumped energy balance model to derive a set of non-linear first order differential equations for the gas cooler and the evaporator is proposed [30]. Two insights are considered: linear PID control (by means of linearisation of the obtained models) and PID feedforward compensation techniques.

Furthermore, Shen *et al.* propose a decoupling control system design based on the Relative Normalized Gain Array (RNGA) [31]. Using the gain and phase information provided by the RNGA, an equivalent transfer function matrix for a closed-loop control system is obtained, and its relationship with the inverse of the process transfer matrix is established. Moreover, the criterion to determine a stable, proper, and causal ideal-diagonal decoupler is established. The main advantage of this method is its simplicity, since it does not require extensive calculation effort.

As fas as LQG control is concerned, similar approaches have been proposed by He and Schurt *et al.* [11, 32, 33]. The three works design a MIMO controller based on the LQG method using a Kalman filter for the estimator design. An integrator is incorporated to the design to reject disturbances and also to keep the time response of the closed-loop system approximately the same as that of the open-loop system. Schurt *et al.* use only a linearised model to derive the controller [11, 33], while He linearises the system in a few operating points and a gain-scheduling scheme is proposed [32].

Concerning MPC, Razi *et al.* propose a neuro-predictive control algorithm, where a neural network is used to estimate the state and the MPC calculates the control actions, compensating the delays of the model [34]. The performance of the neuro-predictive control algorithm is compared with that of a fuzzy PID controller, showing better performance although more computational load. Furthermore, Sarabia *et al.* study a hybrid MPC controller applied to a supermarket refrigeration system, where the compressor speed and valve opening are only on-off variables [35]. This study is extended by Ricker and the approach suggested turns out to be scalable to large systems, since the computational effort is modest [36]. It increases linearly with the number of display cases, but it is independent of the number of compressors, since online optimization is avoided. Fallahsohi *et al.*, in turn, propose a Predictive Functional Control (PFC) to regulate the degree of superheating using the expansion valve opening as manipulated variable [37]. This method is shown to be more accurate than the conventional PID control. As the PFC improves disturbance rejection compared to a PID control, it is possible to reduce the reference on T_{SH} and to prevent any unevaporated refrigerant liquid from reaching the compressor. As a consequence, the use of PFC leads to an increase of *COP* which depends on operating conditions.

Regarding the robust control strategy, Larsen and Holm have designed a MIMO H_∞ controller which solves the *S/KS* problem [38]. For the considered system the coupling between $T_{e,sec,out}$ and A_v is weak, which is taken into account when designing the reduced-order controller. A comparison between the designed controller and a SISO one (calculated by easing the closed-loop system bandwidth but following the same procedure) is also addressed. In this work several operating points are not taken into account when solving the *S/KS* problem, but only uncertainties along the frequency are considered.

However, optimal steady-state operation is not explored through the references in the conventional control scheme, but the low degree of superheating set as reference is believed to lead the cycle to high energy efficiency. Nevertheless, some studies have shown that there are plenty more scope for efficiency improvement if optimal references are imposed on the evaporator and condenser pressures [39, 40]. Alternatively to conventional set point selection, it is possible to perform a global optimization in order to obtain the optimal operating point, given a certain cooling demand, a specific facility and some

constraints regarding the secondary fluxes. A steady-state model of the cycle is required, being the solution of the global optimization a cycle which generates the desired cooling power with as high as possible energy efficiency. This efficiency is measured by any metrics. The solution should also observe all physical and technological constraints of the components, in addition to some operating constraints, for example that of minimum degree of superheating for safe operation of the compressor.

Within this line of research Jain and Alleyne implement a exergy-based global optimization [41]. The destroyed exergy used as metrics presents some advantages over other first-law metrics, such as energy consumption, since it is a measure of how effectively the exergy supplied to a system, in this case work done on the system by the compressor, is used. It also enables the objective function to be scalable with respect to subsystem configuration and subsystem capacity. The optimal cycle and simultaneously the optimal values of the manipulated variables are calculated.

Regarding the optimization procedure, Zhao *et al.* develop a modified genetic algorithm combined with a solution strategy for a group of nonlinear equations to minimize energy consumption [42]. Some experimental results show that the calculated set points may reduce energy consumption compared to traditional on-off control. Zhao *et al.* also present a steady-state decentralised optimization, where total energy consumption is minimized [43]. The novelty consists in the decentralised algorithm, which divides the global problem into three optimization subproblems. They are constrained by some shared variables which are updated online. The decentralised procedure achieves good accuracy compared to a global optimization while dramatically reducing the computation time.

Regarding the *energy-efficiency-aware* control strategies, Jain presents a multivariable feedback-plus-feedforward (FB+FF) control strategy to achieve the set points generated by the offline global optimizer previously commented [12]. The latter also generates the values of the steady-state control actions, which are used as feedforward contribution to the control law. The feedback controller is a linear-quadratic regulator (LQR) based on a linear model identified around the desired point. The optimal cycle generated by the optimizer is defined by three variables, but only two control actions are available, thus the optimal solution is projected from the three-degree-of-freedom optimization space onto the two-degree-of-freedom control space, in such a way that the achieved steady-state cycle is no longer optimal, but suboptimal.

Given this limitation, Jain and Alleyne propose a MPC which uses a dynamic exergy-based cost function to determine the optimal control actions. The objective is to maximize the exergetic efficiency while achieving the desired cooling load [44]. That is, online optimization and control are achieved at once. Simulation results comparing the exergy-based MPC and a first-law MPC are presented, showing that optimal cycles for a given facility and a desired cooling demand are slightly different when optimizing the *COP* and the exergetic efficiency.

Jensen and Skogestad deal with the selection of controlled variables which allow to achieve in practice close-to-optimal operation with a constant set point policy, considering some modifications on the basic cycle such as a liquid receiver on the low pressure side which ensures that the vapour entering the compressor is saturated [45].

Larsen *et al.* propose an online optimization where no dynamic model is needed [46]. The authors consider four control actions and two major control objectives: to

satisfy the cooling demand and to hold the degree of superheating low and constant. The two remaining control actions are devoted to controlling the condenser and evaporator pressures independently, in such a way that the total power consumption is minimized. The optimization is based on the power gradient estimation, which must be convex, and the derivation of a simple static model.

Other line of research concerning *energy-efficiency-aware* control is extremum-seeking control (ESC). Burns and Laughman propose an online optimization of energy consumption using ESC, that means, without relying on a dynamic model of the system [47]. It requires that the relationship between a system input and the output to be optimized is convex. In the context of this application, convexity is required in the input-output map between one of the vapour compression system inputs and the electric power consumption. The evaporator fan speed is selected as the variable to be disturbed, whereas the remaining inputs are devoted to regulating the cooling demand and the system states by means of a feedback controller. The ESC is designed so that the adaptation is slow compared to dominant dynamics of the cycle and the regulating controller. Guay has recently proposed a novel technique called *time-varying* ESC (TV-ESC) with greater convergence rate than traditional *perturbation-based* ESC [48], which has been successfully applied to refrigeration systems [49]. The control architecture is also modified, since the ESC deals with the adjustment of the set point of the compressor discharge temperature, whose relationship with power consumption is shown to be convex, while the compressor speed regulates the cooling power. The temperature at the compressor discharge is chosen instead of the degree of superheating, since the first one can be easily measured because the refrigerant at this location in the cycle is always superheated vapour, whereas the last one is often difficult to measure, it is not defined for values less than zero and produces no change in sensible temperature when two-phase refrigerant exits the evaporator.

1.3 Objectives

In recent years energy efficient control of existing vapour-compression systems has attracted great attention. Several elements are required to achieve optimal operation of a refrigeration system from the point of view of energy efficiency. If a classical hierarchical control structure is proposed, as shown in Figure 1.9, where a reference generator calculates the set points for the controlled variables and the controller merely gets the outputs to track their references, three key factors are involved:

- **Modelling**: the static and dynamic behaviour of the whole cycle must be modelled for optimization purposes and controller design, thus modelling plays a key role.
- **Optimization**: a model-based optimization stage is intended to generate optimal references to the control system, considering energy efficiency and power consumption, and using a steady-state model of the cycle.
- **Control**: the control stage must be designed based on the dynamic model in such a way that the calculated references are achieved despite uncertainties and disturbances.

The main objective of the Thesis is to analyse in depth these three factors.

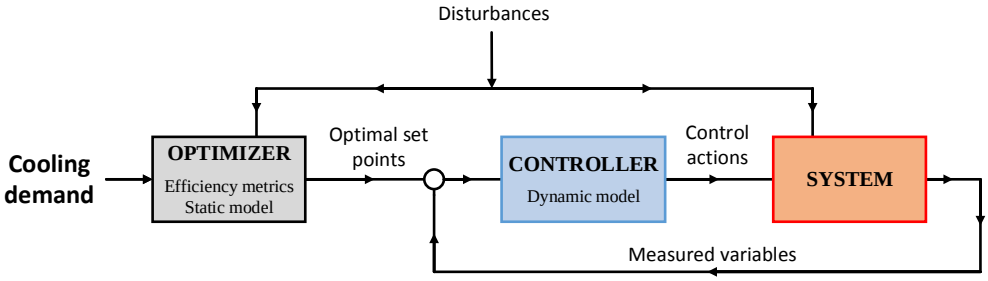

Figure 1.9 Hierarchical optimization and control structure.

Regarding modelling, different approaches have been developed in the literature, focusing on the heat exchangers, because their dynamics are usually at least one order of magnitude slower than those of the remaining elements of the cycle. The modelling technique achieving best balance between accuracy and computational cost is the MB approach. However, although it has been verified that the complexity and computational load of the MB model is minor compared to the FV formulation while achieving comparable accuracy, the model order remains high enough to limit its use to simulation and hinders its integration in model-based control strategies, since the simplest refrigeration cycle is made up of two heat exchangers and each one generates a high-order state vector. The first objective of the Thesis is to develop a simplified control-oriented dynamic model of a one-stage, one-load-demand cycle, which might be more suitable to model-based control strategies regarding computational load, but without excessive inaccuracy concerning the dominant dynamics.

Moreover, the optimization of a one-stage, one-load-demand cycle is to be analysed. Given a certain cooling demand, the objective of the optimization stage is to calculate the steady-state cycle achieving the highest energy efficiency which satisfies the cooling demand while satisfying some operating constraints. This optimal cycle implies an upper bound on the achievable energy efficiency, whereas some of the variables defining the cycle are to be set as optimal references to the tracking controller. Nevertheless, similar approaches in the literature have been shown to fail in achieving the optimal cycle in the control stage. That is why the controllability of the one-stage, one-load-demand cycle is to be analysed using linear theory and a nonlinear pointwise analysis based on the phase portrait method.

Concerning control, the objective is to make a contribution in the two main schemes in the literature about control of refrigeration systems: the conventional scheme and the *energy-efficiency-aware* one. In the first one, in addition to the reference on the outlet temperature of the evaporator secondary flux imposed by the cooling demand, a low but constant set point on the degree of superheating is applied, and the controller is merely designed to get these two variables to track their references. However, energy efficiency is explicitly considered when calculating the references for the low-level controller in the second scheme.

Regarding the tracking control, a multivariable centralised H_∞ controller, based on the

S/KS/T Mixed Sensitivity Problem, is to be proposed. This controller is intended to be robust at the different operating points which could be reached while satisfying the cooling demand and holding the low degree of superheating set as reference. The results provided by the H_∞ controller are to be compared to other conventional controllers in this field, such as MPC and decentralised PID, including reference tracking, coupling between variables, and disturbance rejection.

Concerning the *energy-efficiency-aware* control, and given the conclusions of the controllability analysis previously performed, a suboptimal hierarchical control (SHC) strategy is proposed to achieve the highest possible efficiency while satisfying the cooling load. The performance of the SHC architecture is to be compared to other similar techniques in the literature, regarding the *COP* achieved in steady state and the dynamic behaviour of the controlled variables.

Finally, the optimization and control algorithms are intended to be tested at the configurable experimental plant located at the Department of System Engineering and Automatic Control of University of Seville. To do this, the first step is to obtain an accurate enough model of the system, thus identification is to be performed from experimental data, and validation of the models considering different plant configurations is planned.

1.4 Thesis overview

The Thesis is organised as follows:

- **Chapter 2** presents the modelling of the one-compression-stage, one-load-demand refrigeration system. Different modelling techniques are considered and the SMB approach is selected to model the refrigerant behaviour at the heat exchangers, namely the evaporator and condenser. Steady-state models are developed and detailed for all elements, paying special attention to the heat exchangers. Furthermore, dynamic modelling is also addressed. The SMB approach is used as starting point, and some considerations are taken into account in order to reduce the model order and therefore the complexity of the SMB formulation. A simplified control-oriented dynamic model is proposed describing the complete cycle, and inaccuracy of the latter with respect to the original SMB model is analysed as well as the difference concerning computational load.
- **Chapter 3** describes the design, implementation, and automation of the two-stage, two-load-demand experimental refrigeration plant mentioned in Section 1.1. Parameter identification of the plant is also addressed, and a new methodology to identify the heat transfer coefficients according to experimental data is presented. The proposed procedure is based on inaccessible refrigerant phase-change zones, assuming that a constant overall heat transfer coefficient can be identified for each zone. Consistent values of all parameters are obtained considering only steady-state experimental data and some orders of magnitude found in the literature. Global validation considering the one-stage, two-load-demand configuration and the two-stage, two-load-demand one is also performed, in order to check how precise the parameters obtained are in order to describe the steady-state behaviour of the whole cycle.

- **Chapter 4** addresses energy efficiency and optimal operation of vapour-compression refrigeration systems. Global optimization of a one-stage, one-load-demand cycle is carried out, where the calculation of the cycle which generates a certain cooling load while maximizing energy efficiency is intended. Given a specific facility, the different optimal cycles for a certain achievable cooling load range are compared. Moreover, the control problem of achieving the optimal cycle from an arbitrary point is in depth analysed. The simplified control-oriented model presented in Chapter 2 is reformulated in such a way that a controllability analysis based on linear control theory is carried out, whereas a pointwise nonlinear analysis based on the phase portrait method is also performed.
- **Chapter 5** aims to make a contribution in the two main schemes in the literature about control of refrigeration systems: the conventional scheme and the *energy-efficiency-aware* one.

  Regarding the tracking control, a multivariable centralised H_∞ controller, based on the *S/KS/T* Mixed Sensitivity Problem, is proposed. Simulation results provided by the H_∞ controller, a decentralised PID controller, and a MPC strategy are compared, including reference tracking, coupling measurement, and disturbance rejection. Moreover, the robustness of the H_∞ controller is studied at non-nominal operating points.

  Concerning the *energy-efficiency-aware* control, and given the conclusions of the controllability analysis performed in Chapter 4, a suboptimal hierarchical control strategy is proposed to achieve the highest possible efficiency while satisfying the cooling load. The performance of the SHC architecture is compared to the FB+FF strategy proposed by Jain [12] and the TV-ESC developed by Guay [48], regarding the *COP* achieved in steady state and the dynamic behaviour of the controlled variables.
- **Chapter 6** summarises the contributions and results presented in the Thesis and suggests possible future lines of research.

1.5 List of Publications

The following articles have been issued or submitted for publication during the elaboration of this Thesis:

Journal papers:

1) [50] G. Bejarano, C. Vivas, M. G. Ortega, and M. Vargas, "Suboptimal hierarchical control strategy to improve energy efficiency of vapour-compression refrigeration systems," *Appl. Therm. Eng.*, 2017. Submitted for publication with preliminary review status: potentially publishable.

2) [51] G. Bejarano, M. G. Ortega, J. E. Normey-Rico, and F. R. Rubio, "Optimal control analysis of vapour-compression refrigeration systems. Application of Practical Nonlinear Model Predictive Control," *J. of Process Control*, 2017. Submitted for publication with preliminary review status: potentially publishable.

3) [52] D. Rodríguez, G. Bejarano, J. A. Alfaya, M. G. Ortega, and F. Castaño, "Parameter identification of a multi-stage, multi-load-demand experimental refrigeration plant," *Control Eng. Pract.*, vol. 60, pp. 133–147, 2017.

4) [53] G. Bejarano, J. A. Alfaya, M. G. Ortega, and M. Vargas, "On the difficulty of globally optimally controlling refrigeration systems," *Appl. Therm. Eng.*, vol. 111, pp. 1143–1157, 2017.

5) [54] G. Bejarano, D. Rodríguez, J. A. Alfaya, M. G. Ortega, and F. Castaño, "On identifying steady-state parameters of an experimental mechanical-compression refrigeration plant," *Appl. Therm. Eng.*, vol. 109, pp. 318–333, 2016.

6) [55] G. Bejarano, J. A. Alfaya, M. G. Ortega, and F. R. Rubio, "Multivariable analysis and H_∞ control of a one-stage refrigeration cycle," *Appl. Therm. Eng.*, vol. 91, pp. 1156–1167, 2015.

7) [56] J. A. Alfaya, G. Bejarano, M. G. Ortega, and F. R. Rubio, "Controllability analysis and robust control of a one-stage refrigeration system," *Eur. J. of Control*, vol. 26, pp. 53–62, 2015.

Conference papers:

1) [57] G. Bejarano, M. G. Ortega, and F. R. Rubio, "Optimización global estática de sistemas de refrigeración," in *XXXVII Jorn. de Autom., Madrid (Spain)*, 2016, pp. 19–26.

2) [58] D. Rodríguez, J. A. Alfaya, G. Bejarano, M. G. Ortega, and F. Castaño, "Identificación paramétrica del condensador de una planta experimental de refrigeración," in *XXXVII Jorn. de Autom., Madrid (Spain)*, 2016, pp. 27–34.

3) [59] D. Rodríguez, J. A. Alfaya, G. Bejarano, M. G. Ortega, and F. Castaño, "Steady-state parameter estimation of an experimental vapour compression refrigeration plant," in *Eur. Control Conf. (ECC), Aalborg (Denmark)*. IEEE, 2016, pp. 43–48.

4) [60] G. Bejarano, M. G. Ortega, and F. R. Rubio, "Optimization and multivariable robust control of refrigeration systems," in *XIV Simp. CEA de Ing. de Control, Logroño (Spain)*, 2016.

5) [61] D. Rodríguez, J. A. Alfaya, G. Bejarano, M. G. Ortega, and F. Castaño, "Estimación de parámetros de una planta experimental de refrigeración," in *XXXVI Jorn. de Autom., Bilbao (Spain)*, 2015, pp. 951–958.

6) [62] J. A. Alfaya, G. Bejarano, M. G. Ortega, and F. R. Rubio, "Multi-operating-point robust control of a one-stage refrigeration cycle," in *Eur. Control Conf. (ECC), Linz (Austria)*. IEEE, 2015, pp. 3490–3495.

7) [63] G. Bejarano, J. A. Alfaya, M. G. Ortega, and F. R. Rubio, "Design, automation and control of a two-stage, two-load-demand experimental refrigeration plant," in *23rd Mediterranean Conf. on Control and Autom., Torremolinos (Spain)*, 2015, pp. 537–544.

8) [64] J. A. Alfaya, G. Bejarano, M. G. Ortega, and F. R. Rubio, "Control robusto multivariable de un ciclo de refrigeración," in *XXXV Jorn. de Autom., Valencia (Spain)*, 2014.

9) [65] G. Bejarano, M. G. Ortega, F. R. Rubio, and F. Morilla, "Modelado simplificado y orientado al control de sistemas de refrigeración," in *XXXIV Jorn. de Autom., Terrassa (Spain)*, 2013, pp. 506–513.

Furthermore, additional publications by the author concerning other research topics are the following:

- [66] P. Millán, L. Orihuela, G. Bejarano, C. Vivas, T. Alamo, and F. R. Rubio, "Design and application of suboptimal mixed H_2/H_∞ controllers for networked control systems," *IEEE Trans. on Control Syst. Technol.*, vol. 20, no. 4, pp. 1057–1065, 2012.
- [67] L. Orihuela, P. Millán, G. Bejarano, C. Vivas, and F. R. Rubio, "Optimal networked control of a 2 degree-of-freedom direct drive robot manipulator," in *Emerg. Technol. and Fact. Autom. (ETFA), 2010 IEEE Conf. on*. IEEE, 2010.
- [68] G. Bejarano, C. Vivas, and F. R. Rubio, "Experiencias de identificación de un robot de accionamiento directo," in *XXX Jorn. de Autom., Valladolid (Spain)*, 2009.

2 Modelling

Do not quench your inspiration and your imagination; do not become the slave of your model.

VINCENT VAN GOGH

Contents

This chapter is devoted to modelling of vapour-compression refrigeration systems. For the sake of simplicity only one-compression-stage, one-load-demand cycles are considered, since more complex configurations only include the elements of which the simplest cycle is made up: expansion valve, compressor, evaporator, and condenser. Since they are separately modelled, the extension to modelling of multi-stage and/or multi-load-demand cycles only increases the number of elements and their interconnection.

Different modelling techniques are considered and the MB approach is selected to model the refrigerant behaviour at the heat exchangers, namely the evaporator and condenser. Steady-state models are developed and detailed for all elements, paying special attention to the heat exchangers.

Furthermore, dynamic modelling is also addressed. The MB approach is selected due to its trade-off between accuracy and computational cost. However, although the complexity and computational load of the MB model is minor compared to the FV formulation while achieving comparable accuracy [24], up to nine state variables for the condenser and up to six variables for the evaporator are necessary to completely describe the system behaviour. It makes this model still too complex to be used within a model-based strategy.

Some considerations are taken into account in order to reduce the model order and therefore the complexity of the MB formulation. Typical internal volumes of evaporator and condenser are taken into account, as well as their consequences for the system dynamics. Moreover, fast dynamics of some states of the condenser model are disregarded, giving rise to a simplified control-oriented nonlinear model of the whole cycle, characterised by only three state variables. The complete evaporator state is disregarded as well as some fast states of the condenser, which implies a novelty in modelling of refrigeration systems and reduces the model complexity and computational cost. Some simulation results are presented comparing the original MB model with the control-oriented MB when some step changes on manipulated variables are imposed. Inaccuracy of the control-oriented dynamic model with respect to the original MB model is analysed as well as the difference concerning computational load.

The contents of this Chapter have been included in some of the publications presented in Chapter 1, Section 1.5 [51, 53, 60, 65].

2.1 Steady-state modelling

Before addressing the dynamic modelling, the steady-state behaviour of a typical one-stage, one-load-demand cycle is studied. Nonlinear steady-state models are presented below for all elements in the cycle.

2.1.1 Expansion valve

The steady-state model of the expansion valve is based on the methodology presented by Schurt *et al.* [11, 33]. This model receives the pressures P_c, P_e, and the inlet specific enthalpy $h_{c,out}$ as inputs, and the output is the expanded refrigerant mass flow $\dot{m}_e$, as shown in Equation Set (2.1). $\dot{m}_e$ is denoted this way in order to highlight that it matches the inlet mass flow of the evaporator in a one-stage, one-load-demand cycle, whereas A_v is the expansion valve opening.

$$\begin{aligned} \dot{m}_e &= c_{eev}\, A_v \sqrt{2\rho_{c,out}\,(P_c - P_e)} \\ h_{e,in} &= h_{c,out} \end{aligned} \tag{2.1}$$

$\rho_{c,out} = \rho(P_c, h_{c,out})$ is a refrigerant-specific function to compute the corresponding thermodynamic property. The *CoolProp* tool is used to calculate all properties of the

refrigerant and secondary fluxes [69]. The expansion through the valve is considered to be isenthalpic, as indicated in Equation Set (2.1). The coefficient c_{eev} is a characteristic parameter of the valve.

2.1.2 Compressor

Similarly, the steady-state model of the compressor is based on the method described by Schurt *et al.* [11, 33]. The model receives the pressures P_c and P_e and the suction specific enthalpy $h_{e,out}$ as inputs, whereas the outputs are the refrigerant mass flow compressed and discharged to the condenser $\dot{m}_c$, the discharge specific enthalpy $h_{c,in}$, and the power consumption of the compressor $\dot{W}_{comp}$, as indicated in Equation Set (2.2). Note again that the notation is adapted to the one-stage, one-load-demand configuration, since the compressor suction matches the evaporator outlet and the compressor discharge matches the condenser inlet.

$$\begin{aligned}
\dot{m}_c &= \left[S_t - c \left(\left(\frac{P_c}{P_e} \right)^{\frac{c_{v,e,g}}{c_{p,e,g}}} - 1 \right) \right] \frac{N}{v_{e,out}} \\
\dot{W}_{comp} &= b\, \dot{m}_c \, (h_{c,in,is} - h_{e,out}) \\
T_{c,in,is} &= T_c + \frac{h_{c,in,is} - h_{c,g}}{c_{p,c,g}} \\
h_{c,in} &= h_{e,out} + \frac{\dot{W}_{comp} - UA(T_{c,in,is} - T_{surr})}{\dot{m}_c}
\end{aligned} \tag{2.2}$$

The parameters b, c, S_t, and UA are characteristics of the compressor. Some refrigerant-specific functions are used to estimate the thermodynamic properties; their prototypes and arguments are indicated in Table 2.1. Note that q refers to the vapour quality and $q = 1$ involves that the corresponding thermodynamic property is calculated considering saturated vapour. Once again the *CoolProp* tool is used [69].

Table 2.1 Functions used to calculate the thermodynamic properties of the refrigerant involved in the compressor model.

Variable	Function	Argument 1	Argument 2
$v_{e,out}$	$v(P, h)$	P_e	$h_{e,out}$
$c_{v,e,g}$	$c_v(P, q)$	P_e	1
$c_{p,e,g}$	$c_p(P, q)$	P_e	1
$s_{e,out}$	$s(P, h)$	P_e	$h_{e,out}$
$h_{c,in,is}$	$h(P, s)$	P_c	$s_{e,out}$
T_c	$T(P, q)$	P_c	1
$h_{c,g}$	$h(P, q)$	P_c	1
$c_{p,c,g}$	$c_p(P, q)$	P_c	1

2.1.3 Evaporator

The equations which describe the steady-state model of the evaporator depend on its specific configuration. In the case of study, a brazed-plate counter-current heat exchanger is considered and hereafter modelled. A diagram of heat transfer along the evaporator is represented in Figure 2.1(a), whereas Figure 2.1(b) shows a qualitative temperature diagram of both refrigerant and secondary flux as they pass through the evaporator.

According to this configuration, the equations which describe heat transfer at the evaporator are expressed in Equation Set (2.3), regarding the superheated vapour zone, and Equation Set (2.4), for the two-phase zone. The *effectiveness-NTU* method is used when calculating both partial thermal powers $\dot{Q}_{e,sh}$ and $\dot{Q}_{e,tp}$ [70, 71].

$$\begin{aligned}
\dot{Q}_{e,sh} &= \varepsilon_{e,sh}(\dot{m}c_p)_{min}(T_{e,sec,in} - T_e) \\
C_{e,sh} &= \frac{(\dot{m}c_p)_{min}}{(\dot{m}c_p)_{max}} \\
NTU_{e,sh} &= \frac{UA_{e,sh}}{(\dot{m}c_p)_{min}} \\
UA_{e,sh} &= \alpha_{e,sh}\,(1-\zeta_{e,tp})\,A_{e,trnsf}\,L_e \\
\varepsilon_{e,sh} &= g_{he}(NTU_{e,sh}, C_{e,sh}) \\
\dot{Q}_{e,sh} &= \dot{m}_e(h_{e,out} - h_{e,g}) \\
T_{e,sec,mid} &= T_{e,sec,in} - \frac{\dot{Q}_{e,sh}}{\dot{m}_{e,sec}\,c_{p,e,sec}}
\end{aligned} \tag{2.3}$$

$$\begin{aligned}
\dot{Q}_{e,tp} &= \varepsilon_{e,tp}(\dot{m}c_p)_{min}(T_{e,sec,mid} - T_e) \\
C_{e,tp} &= \frac{(\dot{m}c_p)_{min}}{(\dot{m}c_p)_{max}} = \{phase\ change\} = 0 \\
NTU_{e,tp} &= \frac{UA_{e,tp}}{(\dot{m}c_p)_{min}} \\
UA_{e,tp} &= \alpha_{e,tp}\,\zeta_{e,tp}\,A_{e,trnsf}\,L_e \\
\varepsilon_{e,tp} &= g_{he}(NTU_{e,tp}, C_{e,tp}) \\
\dot{Q}_{e,tp} &= \dot{m}_e(h_{e,g} - h_{e,in}) \\
T_{e,sec,out} &= T_{e,sec,mid} - \frac{\dot{Q}_{e,tp}}{\dot{m}_{e,sec}\,c_{p,e,sec}}
\end{aligned} \tag{2.4}$$

The function $\varepsilon = g_{he}(NTU,C)$ in Equation Sets (2.3) and (2.4) refers to the heat-exchanger-specific curve used within the *effectiveness-NTU* method [72], whereas T_e is the saturation temperature at evaporator pressure P_e. The thermodynamic properties of the refrigerant at the evaporator outlet are calculated using Equation Set (2.5).

$$T_{e,out} = T(P_e, h_{e,out}) \qquad T_{SH} = T_{e,out} - T_e \tag{2.5}$$

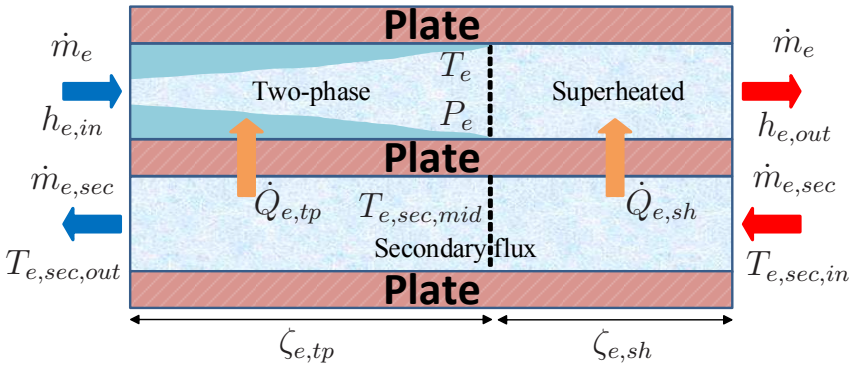

(a) Heat transfer diagram along the evaporator according to the brazed-plate counter-current configuration

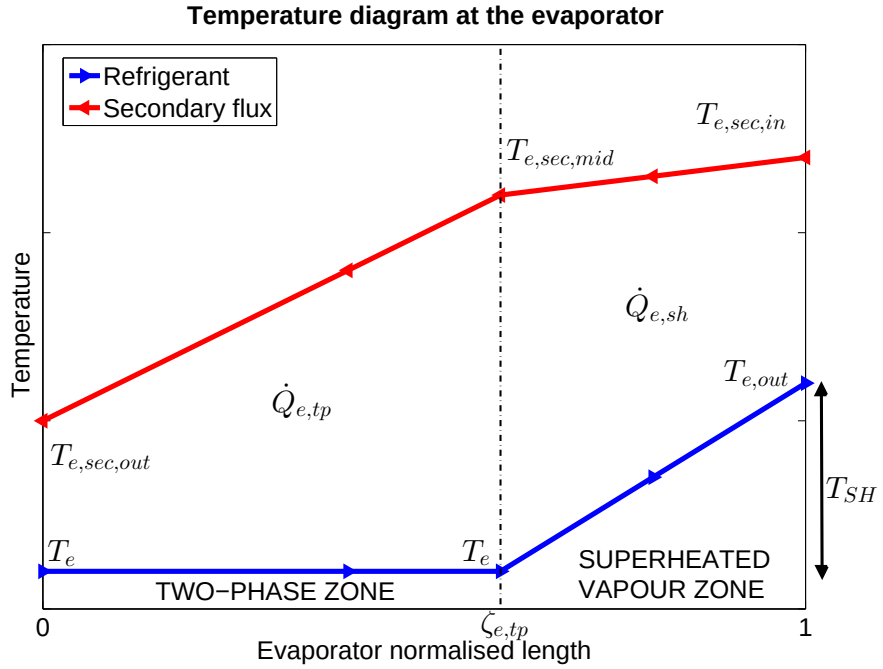

(b) Temperature diagram of both the refrigerant and secondary flux along the evaporator length

Figure 2.1 Heat transfer and temperature diagram of both the refrigerant and secondary flux along the evaporator length according to the brazed-plate counter-current configuration.

Once again $T_{e,out} = T(P_e, h_{e,out})$ is a thermodynamic function included in the *CoolProp* tool. The degree of superheating T_{SH} is calculated as the difference between the refrigerant outlet temperature and the saturation temperature at evaporator pressure. $\alpha_{e,sh}$ and $\alpha_{e,tp}$ are the overall heat transfer coefficients in the superheated vapour zone and the two-phase zone, respectively.

Note that in a one-stage, one-load-demand cycle, a certain degree of superheating is desired for the sake of safe operation of the compressor, then the evaporator *mode* 1 is the most probable in steady state. This is the reason why only the evaporator *mode* 1 has been described and modelled in this Subsection. Anyway, the steady-state model in *mode* 2 can be easily developed from Equation Set (2.4) imposing that $\zeta_{e,tp} = 1$.

2.1.4 Condenser

The equations which describe the steady-state model of the condenser also depend on its particular configuration. In the case of study, an air-cooled cross-flow heat exchanger is modelled. A diagram of the heat transfer along the condenser is represented in Figure 2.2(a), whereas Figure 2.2(b) shows a qualitative temperature diagram of the refrigerant and secondary flux as they pass through the condenser when operating in *mode* 1. The same is represented in Figures 2.3(a) and 2.3(b) when the condenser works in *mode* 2. Note that the most plausible condenser *modes* in steady state are *modes* 1 and 2, being possible the remaining ones shown in Figure 1.8 in startup and shutdown processes, as detailed by Li [22].

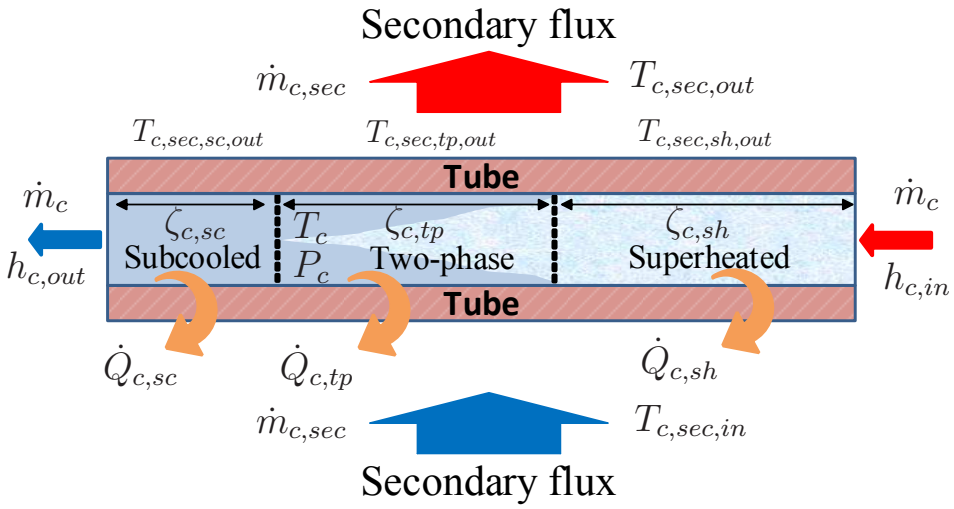

(a) Heat transfer diagram along the condenser according to the cross-flow configuration and considering *mode* 1

Figure 2.2 Heat transfer and temperature diagram of both the refrigerant and secondary flux along the condenser length according to the cross-flow configuration and considering *mode* 1.

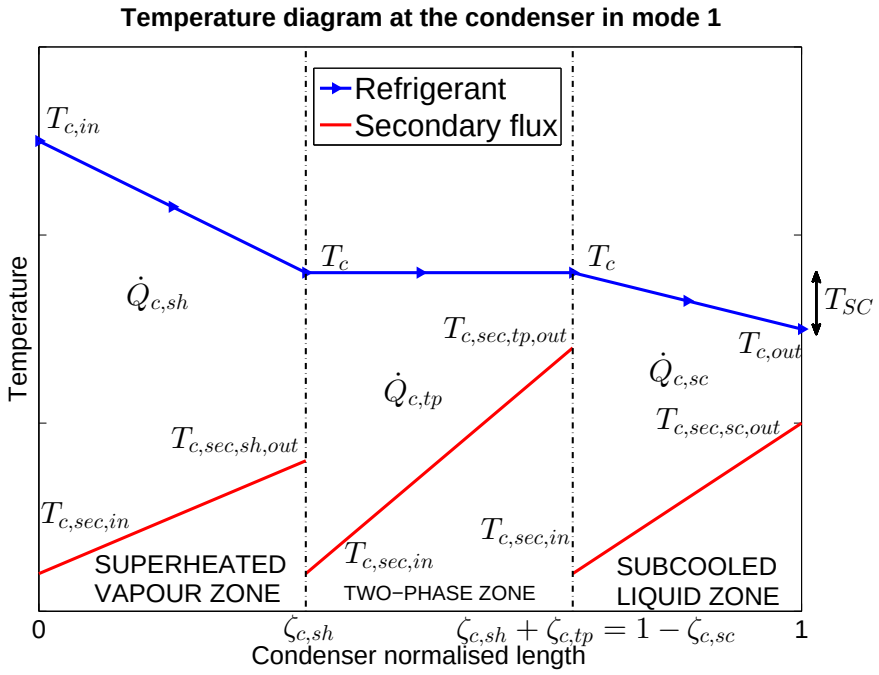

(b) Temperature diagram along the condenser length considering *mode* 1

Figure 2.2 Heat transfer and temperature diagram of both the refrigerant and secondary flux along the condenser length according to the cross-flow configuration and considering *mode* 1.

According to this configuration, the equations which describe heat transfer at the condenser are gathered in Equation Sets (2.6) – (2.8), regarding the superheated vapour zone, the two-phase zone, and the subcooled liquid zone (only in *mode* 1). The *effectiveness-NTU* method is used again when calculating all partial thermal powers [70, 71].

$$\begin{aligned}
\dot{Q}_{c,sh} &= \varepsilon_{c,sh}(\dot{m}c_p)_{min}(T_{c,in}-T_{c,sec,in}) \\
C_{c,sh} &= \frac{(\dot{m}c_p)_{min}}{(\dot{m}c_p)_{max}} \\
NTU_{c,sh} &= \frac{UA_{c,sh}}{(\dot{m}c_p)_{min}} \\
UA_{c,sh} &= \alpha_{c,sh}\,\zeta_{c,sh}\,A_{c,trnsf}\,L_c \\
\varepsilon_{c,sh} &= g_{he}(NTU_{c,sh}, C_{c,sh}) \\
\dot{Q}_{c,sh} &= \dot{m}_c(h_{c,in}-h_{c,g})
\end{aligned} \tag{2.6}$$

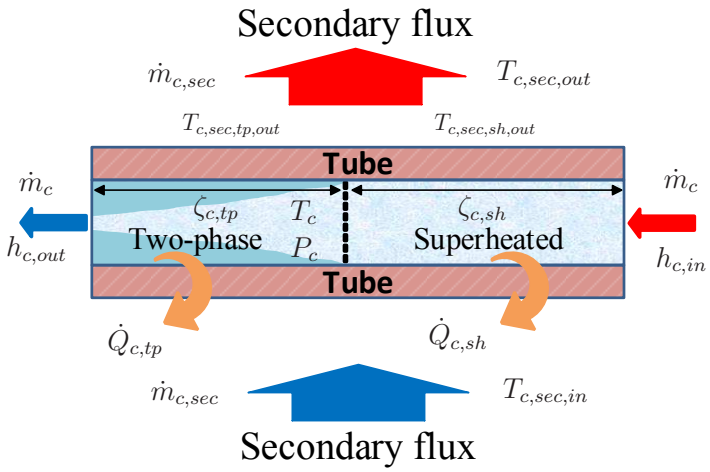

(a) Heat transfer diagram along the condenser according to the cross-flow configuration and considering *mode* 2

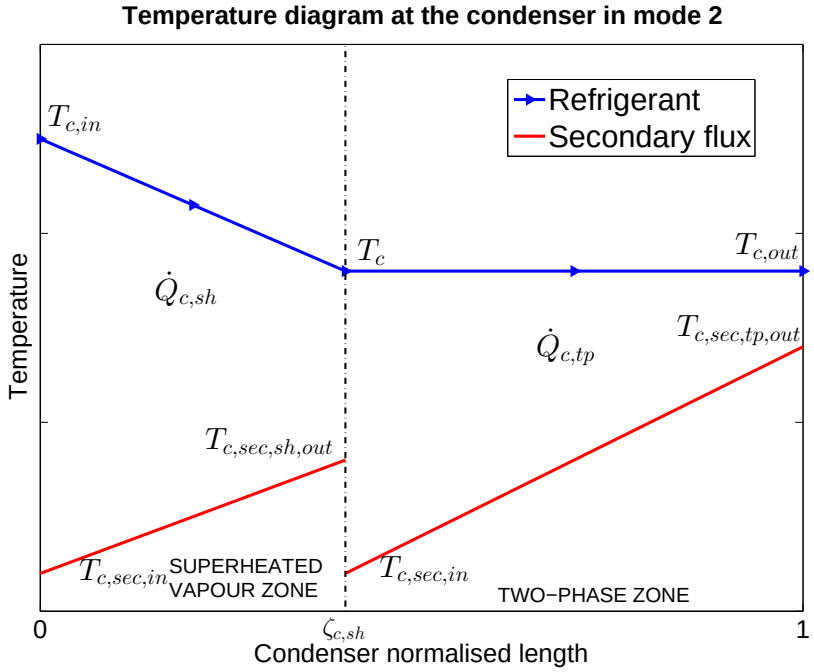

(b) Temperature diagram along the condenser length considering *mode* 2

Figure 2.3 Heat transfer and temperature diagram of both the refrigerant and secondary flux along the condenser length according to the cross-flow configuration and considering *mode* 2.

$$
\begin{aligned}
\dot{Q}_{c,tp} &= \varepsilon_{c,tp}(\dot{m}c_p)_{min}(T_c - T_{c,sec,in}) \\
C_{c,tp} &= \frac{(\dot{m}c_p)_{min}}{(\dot{m}c_p)_{max}} = \{phase\ change\} = 0 \\
NTU_{c,tp} &= \frac{UA_{c,tp}}{(\dot{m}c_p)_{min}} \\
UA_{c,tp} &= \alpha_{c,tp}\ \zeta_{c,tp}\ A_{c,trnsf}\ L_c \\
\varepsilon_{c,tp} &= g_{he}(NTU_{c,tp}, C_{c,tp}) \\
\dot{Q}_{c,tp} &= \dot{m}_c(h_{c,g} - h_{c,f})
\end{aligned}
\tag{2.7}
$$

$$
\begin{aligned}
\dot{Q}_{c,sc} &= \varepsilon_{c,sc}(\dot{m}c_p)_{min}(T_c - T_{c,sec,in}) \\
C_{c,sc} &= \frac{(\dot{m}c_p)_{min}}{(\dot{m}c_p)_{max}} \\
NTU_{c,sc} &= \frac{UA_{c,sc}}{(\dot{m}c_p)_{min}} \\
UA_{c,sc} &= \alpha_{c,sc}\ \zeta_{c,sc}\ A_{c,trnsf}\ L_c \\
\varepsilon_{c,sc} &= g_{he}(NTU_{c,sc}, C_{c,sc}) \\
\dot{Q}_{c,sc} &= \dot{m}_c(h_{c,f} - h_{c,out})
\end{aligned}
\tag{2.8}
$$

When modelling the *mode* 2 the equations which describe the two-phase zone are slightly different, as indicated in Equation Set (2.9).

$$
\begin{aligned}
\dot{Q}_{c,tp} &= \varepsilon_{c,tp}(\dot{m}c_p)_{min}(T_c - T_{c,sec,in}) \\
C_{c,tp} &= \frac{(\dot{m}c_p)_{min}}{(\dot{m}c_p)_{max}} = \{phase\ change\} = 0 \\
NTU_{c,tp} &= \frac{UA_{c,tp}}{(\dot{m}c_p)_{min}} \\
UA_{c,tp} &= \alpha_{c,tp}\ \zeta_{c,tp}\ A_{c,trnsf}\ L_c \\
\varepsilon_{c,tp} &= g_{he}(NTU_{c,tp}, C_{c,tp}) \\
\dot{Q}_{c,tp} &= \dot{m}_c(h_{c,g} - h_{c,out})
\end{aligned}
\tag{2.9}
$$

Once again the function $\varepsilon = g_{he}(NTU,C)$ in Equation Sets (2.6) – (2.9) refers to the heat-exchanger-specific curve used within the *effectiveness-NTU* method [72]. $\alpha_{c,sh}$, $\alpha_{c,tp}$, and $\alpha_{c,sc}$ are the overall heat transfer coefficients in the superheated vapour zone, the two-phase zone and the subcooled liquid zone, respectively. T_c refers to the saturation temperature at condenser pressure P_c. Eventually, Equation Sets (2.10) or (2.11) are used to calculate the refrigerant thermodynamic state at the condenser outlet, in *mode* 1 or *mode*

2, respectively.

$$\begin{aligned} h_{c,out} &= h_{c,sc} \\ T_{c,out} &= T(P_c,\, h_{c,out}) \\ T_{SC} &= T_c - T_{c,out} \end{aligned} \tag{2.10}$$

$$\begin{aligned} \bar{q}_c &= Thom^{-1}(P_c,\, \bar{\gamma}_c) \\ q_{c,out} &= 2\bar{q}_c - 1 \\ h_{c,out} &= (1 - q_{c,out})\, h_{c,f} + q_{c,out}\, h_{c,g} \\ T_{c,out} &= T_c \\ T_{SC} &= 0\ K \end{aligned} \tag{2.11}$$

$T_{c,out} = T(P_c, h_{c,out})$ is calculated using the *CoolProp* tool, and the degree of subcooling T_{SC} in *mode* 1 is defined as the difference between the saturation temperature T_c and the refrigerant temperature at the condenser outlet $T_{c,out}$, whereas in *mode* 2 the function $\bar{q} = Thom^{-1}(P,\bar{\gamma})$ refers to the void fraction correlation [73], in this case inversely applied, which allows to calculate the mean vapour quality at the two-phase zone $\bar{q}_c$ and consequently the outlet vapour quality $q_{c,out}$ and the outlet specific enthalpy $h_{c,out}$. Finally, the secondary flux outlet temperature $T_{c,sec,out}$ is calculated as a weighted average of the partial outlet temperatures $T_{c,sec,sh,out}$, $T_{c,sec,tp,out}$, and $T_{c,sec,sc,out}$, in accordance with the zone lengths $\zeta_{c,sh}$, $\zeta_{c,tp}$, and $\zeta_{c,sc}$, as indicated in Equation Set (2.12).

$$\begin{aligned} T_{c,sec,sh,out} &= T_{c,sec,in} + \frac{\dot{Q}_{c,sh}}{\dot{m}_{c,sec}\ \zeta_{c,sh}\ c_{p,c,sec}} \\ T_{c,sec,tp,out} &= T_{c,sec,in} + \frac{\dot{Q}_{c,tp}}{\dot{m}_{c,sec}\ \zeta_{c,tp}\ c_{p,c,sec}} \\ T_{c,sec,sc,out} &= T_{c,sec,in} + \frac{\dot{Q}_{c,sc}}{\dot{m}_{c,sec}\ \zeta_{c,sc}\ c_{p,c,sec}} \\ T_{c,sec,out} &= \zeta_{c,sh}\ T_{c,sec,sh,out} + \zeta_{c,tp}\ T_{c,sec,tp,out} + \zeta_{c,sc}\ T_{c,sec,sc,out} \end{aligned} \tag{2.12}$$

2.2 Dynamic modelling

2.2.1 Starting point

As commented in Chapter 1, only the heat exchangers are usually dynamically modelled, since their dynamics are dominant over the remaining components of the cycle.

The dynamic model of the heat exchangers is based on the SMB model [21, 23]. As stated in Chapter 1, this methodology divides the heat exchanging volume into variable-length zones, namely superheated vapour, two-phase and/or subcooled liquid zones, giving rise to different *modes*, depending on the refrigerant specific enthalpy at the heat exchanger

inlet and outlet, related to saturated liquid and vapour specific enthalpies. Hence, the evaporator *modes* differentiate according to the existence (*mode* 1) or not (*mode* 2) of superheated vapour at its outlet, whereas the five condenser *modes* are defined by the refrigerant enthalpy at its inlet and outlet, in relation to saturated vapour and liquid specific enthalpies (see Figures 1.7 and 1.8).

For all *modes*, the state vectors in Equation Set (2.13) gather all relevant information concerning the condenser and the evaporator at each instant. The state vectors $\boldsymbol{x}_c$ and $\boldsymbol{x}_e$ include heterogeneous variables such as the condensation and evaporation pressures P_c and P_e, specific enthalpies describing the single-phase zones such as $h_{c,sh}$, $h_{c,sc}$, and $h_{e,sh}$, the zone lengths $\zeta_{c,sh}$, $\zeta_{c,tp}$, and $\zeta_{e,tp}$, and the mean void fractions within both heat exchangers $\bar{\gamma}_c$ and $\bar{\gamma}_e$.

$$\begin{aligned} \boldsymbol{x}_c &= [h_{c,sh} \;\; P_c \;\; h_{c,sc} \;\; \zeta_{c,sh} \;\; \zeta_{c,tp} \;\; \bar{\gamma}_c]^T \\ \boldsymbol{x}_e &= [\zeta_{e,tp} \;\; P_e \;\; h_{e,sh} \;\; \bar{\gamma}_e]^T \\ \boldsymbol{x}_{cycle} &= [\boldsymbol{x}_c \;\; \boldsymbol{x}_e]^T \end{aligned} \tag{2.13}$$

These state vectors have been obtained by removing the wall temperature states from the original modelling developed by Li and Alleyne [23], since the thermal powers are calculated using the *effectiveness-NTU* method [70, 71]. The uniformity of the state vectors, regardless of the *mode*, allows to retain a constant dynamic structure formulated in the nonlinear descriptor form shown in Equation Set (2.14), for the evaporator and condenser, where $\boldsymbol{w}_c$ and $\boldsymbol{w}_e$ refer to the input vector to the corresponding heat exchanger, as explained by Li and Alleyne [23].

$$\begin{aligned} \boldsymbol{Z}_c(\boldsymbol{x}_c, \boldsymbol{w}_c)\, \dot{\boldsymbol{x}}_c &= \boldsymbol{f}_c(\boldsymbol{x}_c, \boldsymbol{w}_c) \\ \boldsymbol{Z}_e(\boldsymbol{x}_e, \boldsymbol{w}_e)\, \dot{\boldsymbol{x}}_e &= \boldsymbol{f}_e(\boldsymbol{x}_e, \boldsymbol{w}_e) \end{aligned} \tag{2.14}$$

Coefficient matrices $\boldsymbol{Z}_i(\boldsymbol{x}_i, \boldsymbol{w}_i)$ and forcing functions $\boldsymbol{f}_i(\boldsymbol{x}_i, \boldsymbol{w}_i) \quad \forall i = c,e$ can be derived from the governing equations detailed in the related literature for each *mode*, which include refrigerant thermodynamic properties and geometric parameters, in addition to mass flow and energy balance terms [21, 22]. It is important to remark that the elements in coefficient matrices $\boldsymbol{Z}_c$ and $\boldsymbol{Z}_e$ depend only on refrigerant thermodynamic properties and geometric parameters, such as the internal volume, which is usually known. However, the elements in forcing functions $\boldsymbol{f}_c$ and $\boldsymbol{f}_e$, which define the system statics, depend strongly on thermal powers transferred at each zone. Tracking references are imposed on the variables related to a specific zone when it is inactive. The dynamic models are simulated by calculating $\dot{\boldsymbol{x}}_i(k) = \boldsymbol{Z}_i^{-1}(k)\boldsymbol{f}_i(k) \quad \forall i = c,e$ at each time step k and numerically integrating to obtain the state vector $\boldsymbol{x}_i(k+1) \quad \forall i = c,e$.

The time-varying model inputs, which are provided by other component models, are gathered in Equation Set (2.15). The outputs of each model depend on the interfaces with the other component models.

$$\begin{aligned} \boldsymbol{w}_c &= [\dot{m}_{c,sec} \;\; T_{c,sec,in} \;\; \dot{m}_{c,in} \;\; \dot{m}_{c,out} \;\; h_{c,in}]^T \\ \boldsymbol{w}_e &= [\dot{m}_{e,sec} \;\; T_{e,sec,in} \;\; \dot{m}_{e,in} \;\; \dot{m}_{e,out} \;\; h_{e,in}]^T \end{aligned} \tag{2.15}$$

2.2.2 Assumptions and considerations

As stated in Subsection 2.2.1, up to ten state variables are required within the SMB model to accurately describe the dynamic behaviour of a one-stage, one-load-demand cycle. The still high order of the SMB model continues to limit its use in practical model-based control strategies. Some considerations are taken into account in order to reduce the model order and therefore the complexity of the SMB model.

Firstly, progressive replacement of environment-unfriendly refrigerants and rising costs of raw material have motivated changes in evaporator design, seeking low internal volume [74]; micro channel and plate heat exchangers are some examples of this trend. As a result, evaporator dynamics become faster and, if compared to typical condenser dominant time constant, they can be disregarded without too much inaccuracy, thus the evaporator may be statically modelled and the condenser dynamics are considered as dominant. Note that the evaporator internal volume must be reduced enough so that their dynamics can be disregarded compared to those of typically-sized condensers. This depends on the specific facility, in such a way that the application of this assumption is not general, but as commented previously, lowering internal volume is a successful trend in evaporator design and it is expected that new refrigeration equipments will include small-sized but high-efficiency evaporators in a few years. Refrigerant selection has also a certain influence in this issue, since according to European directives, CFC refrigerants must be substituted temporarily by HCFCs until 2015, and after that year only HFC refrigerants must be used in new facilities [75].

Furthermore, there is another argument which might help to compare condenser and evaporator dynamics without considering the heat exchanger volumes at the specific facility. As stated in the original formulation of the SMB model which is taken as starting point [23], the expressions of vectors equivalent to $\boldsymbol{f}_c$ and $\boldsymbol{f}_e$ (independent terms in dynamic equations similar to $\boldsymbol{Z}\,\dot{\boldsymbol{x}} = \boldsymbol{f}$) include mass and energy balances at each variable-length zone, which obviously are cancelled out at equilibrium. The denominators of the elements in $\boldsymbol{f}_c$ and $\boldsymbol{f}_e$ include the internal volume of the corresponding zone and the representative refrigerant density. It is easy to check that the density has a significant influence on the dynamics, apart from the total internal volume of the heat exchanger and the particular length of each zone. First of all, superheated vapour density is at least one order of magnitude lower than subcooled liquid density. Thus, it is possible to affirm that intrinsic dynamics of the states related to the superheated vapour zones are much faster than those corresponding to the states related to the remaining zones at both heat exchangers, specially the subcooled liquid zone at the condenser. As the refrigerant enters the evaporator as two-phase fluid (with not insignificant vapour quality), while the condenser may have a subcooled liquid zone, this is a first argument which may justify that the evaporator dynamics are faster than those of the condenser. Moreover, if thermodynamic properties are analysed for a given refrigerant (R404a in this case), one can calculate density of a two-phase mixture with a typical mean vapour quality at the evaporator two-phase zone at typical evaporator pressure. Similarly, density of a two-phase mixture with a typical mean vapour quality at the condenser two-phase zone at typical condenser pressure can be also calculated. When comparing both densities, the first one turns out to be about one order of magnitude lower than the second one. The same occurs when evaluating

density of saturated vapour at typical evaporator and condenser pressures. It enables to affirm that intrinsic dynamics of the evaporator states are faster than those of the condenser ones, specially those corresponding to the subcooled liquid zone. Even if the latter does not exist, the two-phase zone at the condenser has slower dynamics than the two-phase zone at the evaporator, only due to the refrigerant thermodynamic properties and without considering the specific internal volumes of the involved heat exchangers.

Secondly, the refrigerant mass flow equilibrium between the condenser inlet and outlet is very fast compared to the heat transfer dominant dynamics, therefore a unique refrigerant mass flow passing through the condenser might be assumed, disregarding the fast transient due to mass flow imbalance.

Considering the mentioned simplifications, and analysing the intrinsic dynamics of each state, it can be verified that, when the condenser works in *mode* 1, the states whose dynamics are dominant are those shown in Equation (2.16).

$$\boldsymbol{x}_{c,m1} = [P_c \;\; \zeta_{c,sc} \;\; h_{c,sc}]^T \tag{2.16}$$

Intrinsic dynamics of $h_{c,sh}$ and $\bar{\gamma}_c$ (state variables which define the characteristic enthalpy at the superheated vapour and the two-phase zone, respectively) have been disregarded due to density difference previously analysed, which implies faster dynamics of the states related to the superheated vapour zone and the two-phase zone when compared with the dominant dynamics related to the subcooled liquid zone. In particular, $\bar{\gamma}_c$ matches $\bar{\gamma}_{c,tot}$ if there is a subcooled liquid zone, since the refrigerant phase change is complete and $\bar{\gamma}_{c,tot}$ depends only on the condenser pressure P_c. Furthermore, the zone lengths $\zeta_{c,sh}$ and $\zeta_{c,tp}$ have been collapsed in a new state variable $\zeta_{c,sc}$ which refers to the subcooled liquid zone length, whose dynamics show again to be dominant. Pressure P_c is hold as state variable since its original existence as a state arises from the selected pair of intensive variables used to thermodynamically define the refrigerant properties at all zones [21].

Similarly, when the condenser works in *mode* 2, the dominant states are shown in Equation (2.17).

$$\boldsymbol{x}_{c,m2} = [P_c \;\; \zeta_{c,sh} \;\; \bar{\gamma}_c]^T \tag{2.17}$$

In this case, $h_{c,sc}$ and $\zeta_{c,sc}$ are related to the subcooled liquid zone, which is inactive, thus tracking references are imposed on them (the specific enthalpy of saturated liquid at condenser pressure on $h_{c,sc}$ and simply zero on $\zeta_{c,sc}$, as proposed by Li and Alleyne [23]). Intrinsic dynamics of the two-phase zone length $\zeta_{c,tp}$ disappear, since $\dot{\zeta}_{c,tp}$ simply opposes to $\dot{\zeta}_{c,sh}$.

Note that only *modes* 1 and 2 have been so far considered. The reason is that, as studied by Li [22], the most plausible condenser *modes* in steady state are *modes* 1 and 2, being possible the remaining ones in startup and shutdown processes. The control-oriented SMB model is intended to describe the behaviour of the system when modifying the manipulated inputs and the disturbances, but it is not intended to simulate the transient behaviour in startup and shutdown processes, which has been already studied in detail by Li [22, 23].

Considering all these simplifications, the state vector of the whole cycle is reduced to that of the condenser, for both *modes* 1 and 2. Even though the state vector must be

uniform regardless of the condenser *mode* (and therefore include five different states) to avoid numerical issues when simulating the process, only three states are simultaneously *active* in each *mode*. This reduces the model order as desired and retains the dominant dynamics. The remaining elements are statically modelled using their nonlinear equations. All of this makes this simplified model more suitable for model-based control strategies and controllability analysis.

2.2.3 Control-oriented simplified model

The equations which describe the simplified dynamic model of the condenser are detailed in this Subsection, in addition to the static equations which enable the calculation of the remaining condenser variables. Moreover, a solution strategy is designed to close the cycle and calculate all cycle variables related to the statically modelled elements such as the expansion valve, the compressor, and the evaporator.

Condenser model

In Equation Set (2.18) the simplified condenser model is detailed for *mode* 1, whereas specific terms on force function $\boldsymbol{f}_{c,m1}$ and coefficient matrix $\boldsymbol{Z}_{c,m1}$ are collected in Equation Sets (2.19) and (2.20), respectively.

$$
\begin{aligned}
\boldsymbol{Z}_{c,m1}(\boldsymbol{x}_{c,m1},\boldsymbol{w}_c)\,\dot{\boldsymbol{x}}_{c,m1} &= \boldsymbol{f}_{c,m1}(\boldsymbol{x}_{c,m1},\boldsymbol{w}_c)\\
\boldsymbol{x}_{c,m1} &= [P_c \;\; \zeta_{c,sc} \;\; h_{c,sc}]^T\\
\boldsymbol{w}_c &= [\dot{m}_{c,sec} \;\; T_{c,sec,in} \;\; \dot{m} \;\; h_{c,in}]^T\\
\boldsymbol{Z}_{c,m1}(\boldsymbol{x}_{c,m1},\boldsymbol{w}_c) &= \begin{bmatrix} z_{c,m1,11}(\boldsymbol{x}_{c,m1},\boldsymbol{w}_c) & -1 & z_{c,m1,13}(\boldsymbol{x}_{c,m1},\boldsymbol{w}_c)\\ z_{c,m1,21}(\boldsymbol{x}_{c,m1},\boldsymbol{w}_c) & 0 & z_{c,m1,23}(\boldsymbol{x}_{c,m1},\boldsymbol{w}_c)\\ z_{c,m1,31}(\boldsymbol{x}_{c,m1},\boldsymbol{w}_c) & -1 & z_{c,m1,33}(\boldsymbol{x}_{c,m1},\boldsymbol{w}_c) \end{bmatrix}\\
\boldsymbol{f}_{c,m1}(\boldsymbol{x}_{c,m1},\boldsymbol{w}_c) &= [f_{c,m1,1}(\boldsymbol{x}_{c,m1},\boldsymbol{w}_c) \;\; f_{c,m1,2}(\boldsymbol{x}_{c,m1},\boldsymbol{w}_c) \;\; f_{c,m1,3}(\boldsymbol{x}_{c,m1},\boldsymbol{w}_c)]^T
\end{aligned}
\tag{2.18}
$$

$$
\begin{aligned}
f_{c,m1,1}(\boldsymbol{x}_{c,m1},\boldsymbol{w}_c) &= \frac{1}{\rho_{c,tp}\,V_R}\frac{1}{h_{c,f}-h_{c,sc}}\left(\dot{Q}_{c,sc}+\dot{m}\,(h_{c,f}-h_{c,sc})\right)\\
f_{c,m1,2}(\boldsymbol{x}_{c,m1},\boldsymbol{w}_c) &= \frac{1}{\rho_{c,tp}\,\zeta_{c,tp}\,V_R}\left(\dot{Q}_{c,tp}+\dot{m}\,(h_{c,g}-h_{c,tp})+\frac{h_{c,f}-h_{c,tp}}{h_{c,f}-h_{c,sc}}\,\dot{Q}_{c,sc}\right)\\
f_{c,m1,3}(\boldsymbol{x}_{c,m1},\boldsymbol{w}_c) &= \frac{1}{\rho_{c,sc}\,V_R}\frac{1}{h_{c,f}-h_{c,sc}}\left(\dot{Q}_{c,sc}+\dot{m}\,(h_{c,f}-h_{c,sc})\right)
\end{aligned}
\tag{2.19}
$$

$$
\begin{aligned}
z_{11,m1}(\boldsymbol{x}_{c,m1},\boldsymbol{w}_c) &= \frac{1}{2}\frac{\partial h_{c,g}}{\partial P_c}\left(\frac{\zeta_{c,sh}}{\rho_{c,sh}}\frac{\partial \rho_{c,sh}}{\partial h_{c,sh}} - \frac{\zeta_{c,sh}}{h_{c,g}-h_{c,sh}}\right) + \\
&+ \frac{\zeta_{c,sh}}{\rho_{c,sh}}\frac{\partial \rho_{c,sh}}{\partial P_c} + \frac{\zeta_{c,sh}}{\rho_{c,sh}(h_{c,g}-h_{c,sh})} + \frac{\zeta_{c,tp}}{\rho_{c,tp}}\frac{\partial \rho_{c,tp}}{\partial P_c} - \\
&- \frac{\zeta_{c,sh}}{\rho_{c,tp}(h_{c,g}-h_{c,sh})} - \frac{\zeta_{c,sc}}{\rho_{c,tp}(h_{c,f}-h_{c,sc})} + \\
&+ \frac{1}{2}\frac{\partial h_{c,g}}{\partial P_c}\left(\frac{\rho_{c,sh}}{\rho_{c,tp}}\frac{\zeta_{c,sh}}{h_{c,g}-h_{c,sh}} + \frac{\partial \bar{\gamma}_c}{\partial P_c}\frac{\zeta_{c,tp}}{\rho_{c,tp}}\frac{\partial \rho_{c,tp}}{\partial \bar{\gamma}_c}\right) \\
z_{13,m1}(\boldsymbol{x}_{c,m1},\boldsymbol{w}_c) &= \frac{\rho_{c,sc}}{\rho_{c,tp}}\frac{\zeta_{c,sc}}{h_{c,f}-h_{c,sc}} \\
z_{21,m1}(\boldsymbol{x}_{c,m1},\boldsymbol{w}_c) &= \frac{\partial h_{c,tp}}{\partial P_c} - \frac{1}{\rho_{c,tp}} + \frac{\partial \bar{\gamma}_c}{\partial P_c}\frac{\partial h_{c,tp}}{\partial \bar{\gamma}_c} - \frac{\zeta_{c,sh}}{\zeta_{c,tp}}\frac{1}{\rho_{c,tp}}\frac{h_{c,g}-h_{c,tp}}{h_{c,g}-h_{c,sh}} - \\
&- \frac{\zeta_{c,sc}}{\zeta_{c,tp}}\frac{1}{\rho_{c,tp}}\frac{h_{c,f}-h_{c,tp}}{h_{c,f}-h_{c,sc}} + \frac{1}{2}\frac{\partial h_{c,g}}{\partial P_c}\frac{\zeta_{c,sh}}{\zeta_{c,tp}}\frac{\rho_{c,sh}}{\rho_{c,tp}}\frac{h_{c,g}-h_{c,tp}}{h_{c,g}-h_{c,sh}} \\
z_{23,m1}(\boldsymbol{x}_{c,m1},\boldsymbol{w}_c) &= \frac{\zeta_{c,sc}}{\zeta_{c,tp}}\frac{\rho_{c,sc}}{\rho_{c,tp}}\frac{h_{c,f}-h_{c,tp}}{h_{c,f}-h_{c,sc}} \\
z_{31,m1}(\boldsymbol{x}_{c,m1},\boldsymbol{w}_c) &= -\frac{\zeta_{c,sc}}{\rho_{c,sc}}\frac{1}{h_{c,f}-h_{c,sc}} \\
z_{33,m1}(\boldsymbol{x}_{c,m1},\boldsymbol{w}_c) &= -\frac{\zeta_{c,sc}}{\rho_{c,sc}}\frac{\partial \rho_{c,sc}}{\partial h_{c,sc}} + \frac{\zeta_{c,sc}}{h_{c,f}-h_{c,sc}}
\end{aligned}
\tag{2.20}
$$

Note that a unique refrigerant mass flow passing through the condenser $\dot{m}$ is considered in Equation Sets (2.18) and (2.19), since the fast transient due to mass flow imbalance is considered negligible, as discussed in Subsection 2.2.2. Note also that the elements in forcing function $\boldsymbol{f}_{c,m1}$ include energy balances at each variable-length zone, which obviously are cancelled out at equilibrium. These balances define the system statics and they depend strongly on thermal powers $\dot{Q}_{c,tp}$ and $\dot{Q}_{c,sc}$, whose calculation is determined by the specific configuration of the heat exchanger and heat transfer at both zones. However, the elements in coefficient matrix $\boldsymbol{Z}_{c,m1}$, which define the system dynamics along with the heat exchanger internal volume V_R and the representative refrigerant density at each zone included in the denominator of the elements in $\boldsymbol{f}_{c,m1}$, depend only on refrigerant thermodynamic properties. This structure is inherited from the original SMB model described by Li [22].

Similarly, in Equation Set (2.21) the simplified condenser model is shown for *mode* 2, whereas specific terms on matrix $\boldsymbol{Z}_{c,m2}$ and force function $\boldsymbol{f}_{c,m2}$ are presented in Equation

Sets (2.22) and (2.23), respectively.

$$
\begin{aligned}
\boldsymbol{Z}_{c,m2}(\boldsymbol{x}_{c,m2},\boldsymbol{w}_c)\,\dot{\boldsymbol{x}}_{c,m2} &= \boldsymbol{f}_{c,m2}(\boldsymbol{x}_{c,m2},\boldsymbol{w}_c)\\
\boldsymbol{x}_{c,m2} &= [P_c \;\; \zeta_{c,sh} \;\; \bar{\gamma}_c]^T\\
\boldsymbol{w}_c &= [\dot{m}_{c,sec} \;\; T_{c,sec,in} \;\; \dot{m} \;\; h_{c,in}]^T\\
\boldsymbol{Z}_{c,m2}(\boldsymbol{x}_{c,m2},\boldsymbol{w}_c) &= \begin{bmatrix} z_{c,m2,11}(\boldsymbol{x}_{c,m2},\boldsymbol{w}_c) & 0 & z_{c,m2,13}(\boldsymbol{x}_{c,m2},\boldsymbol{w}_c)\\ z_{c,m2,21}(\boldsymbol{x}_{c,m2},\boldsymbol{w}_c) & 1 & 0\\ z_{c,m2,31}(\boldsymbol{x}_{c,m2},\boldsymbol{w}_c) & -1 & z_{c,m2,33}(\boldsymbol{x}_{c,m2},\boldsymbol{w}_c)\end{bmatrix}\\
\boldsymbol{f}_{c,m2}(\boldsymbol{x}_{c,m2},\boldsymbol{w}_c) &= [f_{c,m2,1}(\boldsymbol{x}_{c,m2},\boldsymbol{w}_c) \;\; f_{c,m2,2}(\boldsymbol{x}_{c,m2},\boldsymbol{w}_c) \;\; f_{c,m2,3}(\boldsymbol{x}_{c,m2},\boldsymbol{w}_c)]^T
\end{aligned}
\tag{2.21}
$$

$$
\begin{aligned}
z_{c,m2,11}(\boldsymbol{x}_{c,m2},\boldsymbol{w}_c) &= \frac{\partial h_{c,tp}}{\partial P_c} - \frac{1}{\rho_{c,tp}} - \frac{\zeta_{c,sh}}{\zeta_{c,tp}}\frac{1}{\rho_{c,tp}}\frac{h_{c,g}-h_{c,tp}}{h_{c,g}-h_{c,sh}} +\\
&\quad + \frac{1}{2}\frac{\partial h_{c,g}}{\partial P_c}\frac{\zeta_{c,sh}}{\zeta_{c,tp}}\frac{\rho_{c,sh}}{\rho_{c,tp}}\frac{h_{c,g}-h_{c,tp}}{h_{c,g}-h_{c,sh}}\\
z_{c,m2,13}(\boldsymbol{x}_{c,m2},\boldsymbol{w}_c) &= \frac{\partial h_{c,tp}}{\partial \bar{\gamma}_c}\\
z_{c,m2,21}(\boldsymbol{x}_{c,m2},\boldsymbol{w}_c) &= \frac{\zeta_{c,sh}}{\rho_{c,sh}}\frac{\partial \rho_{c,sh}}{\partial P_c} + \frac{\zeta_{c,sh}}{\rho_{c,sh}(h_{c,g}-h_{c,sh})} +\\
&\quad + \frac{1}{2}\frac{\partial h_{c,g}}{\partial P_c}\left(\frac{\zeta_{c,sh}}{\rho_{c,sh}}\frac{\partial \rho_{c,sh}}{\partial h_{c,sh}} - \frac{\zeta_{c,sh}}{h_{c,g}-h_{c,sh}}\right)\\
z_{c,m2,31}(\boldsymbol{x}_{c,m2},\boldsymbol{w}_c) &= \frac{\zeta_{c,tp}}{\rho_{c,tp}}\frac{\partial \rho_{c,tp}}{\partial P_c} - \frac{\zeta_{c,sh}}{\rho_{c,tp}(h_{c,g}-h_{c,sh})} +\\
&\quad + \frac{1}{2}\frac{\partial h_{c,g}}{\partial P_c}\frac{\rho_{c,sh}}{\rho_{c,tp}}\frac{\zeta_{c,sh}}{h_{c,g}-h_{c,sh}}\\
z_{c,m2,33}(\boldsymbol{x}_{c,m2},\boldsymbol{w}_c) &= \frac{\zeta_{c,tp}}{\rho_{c,tp}}\frac{\partial \rho_{c,tp}}{\partial \bar{\gamma}_c}
\end{aligned}
\tag{2.22}
$$

$$
\begin{aligned}
f_{c,m2,1}(\boldsymbol{x}_{c,m2},\boldsymbol{w}_c) &= \frac{1}{\rho_{c,tp}\,\zeta_{c,tp}\,V_R}\left[\dot{Q}_{c,tp} - \dot{m}\,(h_{c,out}-h_{c,tp}) +\right.\\
&\quad \left. + \frac{h_{c,g}-h_{c,tp}}{h_{c,g}-h_{c,sh}}\left(\dot{Q}_{c,sh} + \dot{m}\,(h_{c,in}-h_{c,sh})\right)\right]\\
f_{c,m2,2}(\boldsymbol{x}_{c,m2},\boldsymbol{w}_c) &= \frac{1}{\rho_{c,sh}\,V_R}\frac{1}{h_{c,g}-h_{c,sh}}\left(-\dot{Q}_{c,sh} + \dot{m}\,(h_{c,g}-h_{c,in})\right)\\
f_{c,m2,3}(\boldsymbol{x}_{c,m2},\boldsymbol{w}_c) &= \frac{1}{\rho_{c,tp}\,V_R}\frac{1}{h_{c,g}-h_{c,sh}}\left(\dot{Q}_{c,sh} - \dot{m}\,(h_{c,g}-h_{c,in})\right)
\end{aligned}
\tag{2.23}
$$

The calculation of the thermal powers $\dot{Q}_{c,sh}$, $\dot{Q}_{c,tp}$, and $\dot{Q}_{c,sc}$ in *mode* 1 is performed using Equation Sets (2.6) – (2.8) shown in Subsection 2.1.4, whereas Equation Sets (2.6) and (2.9) are used in *mode* 2. Eventually, to calculate the refrigerant thermodynamic state at the condenser outlet Equation Sets (2.10) or (2.11) are used, in *mode* 1 or *mode* 2, respectively, while the secondary flux outlet temperature is calculated using Equation Set (2.12).

As stated in Subsection 2.2.2, intrinsic dynamics of some states are disregarded in order to reduce the condenser model order. It involves that the equilibrium value of these states must be statically calculated at each instant, from the model inputs and the remaining states. For example, the characteristic specific enthalpy of the superheated vapour zone $h_{c,sh}$ and the mean void fraction $\bar{\gamma}_c$ are no longer state variables in *mode* 1. $h_{c,sh}$ is simply calculated using Equation (2.24), whereas $\bar{\gamma}_c$ can be calculated as shown in Equation Set (2.25), since the refrigerant phase change is complete.

$$h_{c,sh} = \frac{1}{2}(h_{c,in} + h_{c,g}) \tag{2.24}$$

$$\begin{aligned} \bar{q}_c &= 0.5 \\ \bar{\gamma}_c &= Thom(P_c, \bar{q}_c) \end{aligned} \tag{2.25}$$

Eventually, also in *mode* 1, since only $\zeta_{c,sc}$ among the zone lengths is a state variable and the others are collapsed, one of them must be calculated statically. $\zeta_{c,sh}$ can be produced imposing the condition shown in Equation (2.26), supposing that thermal equilibrium at the superheated vapour zone is fast enough.

$$\dot{Q}_{c,sh} = \dot{m}\,(h_{c,in} - h_{c,g}) \tag{2.26}$$

When considering *mode* 2, tracking references are imposed on the characteristic specific enthalpy $h_{c,sc}$ and the length $\zeta_{c,sc}$ of the subcooled liquid zone. Then, $h_{c,sc}$ tends to $h_{c,f}$, whereas $\zeta_{c,sc} = 0$ while the condenser remains in *mode* 2. Moreover, $\zeta_{c,tp} = 1 - \zeta_{c,sh}$ is no longer a state variable. Equation (2.24) can be also applied to calculate the equilibrium value of $h_{c,sh}$.

Solution strategy

To integrate the condenser dynamic model presented in Equation Set (2.18) for the *mode* 1 and in Equation Set (2.21) for the *mode* 2, the model input vector must be calculated at each instant. In Equation (2.27) the input vector $\boldsymbol{w}_c$ is once again shown, which is valid for all *modes*.

$$\boldsymbol{w}_c = [\dot{m}_{c,sec} \;\; T_{c,sec,in} \;\; \dot{m} \;\; h_{c,in}]^T \tag{2.27}$$

While $\dot{m}_{c,sec}$ and $T_{c,sec,in}$ are measurable disturbances, the refrigerant mass flow $\dot{m}$ and its inlet specific enthalpy $h_{c,in}$ must be calculated based on the steady-state models of the remaining elements of the cycle. The boundary conditions of this calculation are determined by the condenser states, namely the specific enthalpy at the condenser outlet and the condenser pressure. P_c is a *mode*-independent state, whereas $h_{c,out}$ is also a state in *mode* 1, as previously shown in Equation Set (2.10). If considering *mode* 2, $h_{c,out}$ can

be calculated using exclusively the *mode* 2 state information, as presented in Equation Set (2.11).

Once determined the boundary conditions at each instant, the valve expansion model (Equation Set (2.1)), the compressor model (Equation Set (2.2)), and the evaporator steady-state model (Equation Sets (2.3) – (2.5)) constitute a nonlinear equation system with two unknown variables: P_e and $h_{e,out}$. An iterative procedure has been designed to solve the system, which is described in Figure 2.4. As a result, not only the unknown evaporator variables (P_e and $h_{e,out}$) are obtained, but also some other cycle variables are calculated and gathered in the output vector $\boldsymbol{y}$, as shown in Figure 2.4 and Equation (2.28). Specifically, the refrigerant mass flow $\dot{m}$ and the condenser inlet specific enthalpy $h_{c,in}$ are included in $\boldsymbol{y}$, therefore all information of the condenser input vector $\boldsymbol{w}_c$ is now calculated.

$$\boldsymbol{y} = \begin{bmatrix} h_{c,in} \\ h_{e,in} \\ \dot{W}_{comp} \\ \dot{m} \\ T_{SH} \\ T_{e,sec,out} \\ \zeta_{e,tp} \end{bmatrix} \tag{2.28}$$

2.2.4 Comparison simulations

Some simulation results are presented below comparing the original SMB model with the control-oriented one when some step changes on both manipulated variables (N and A_v) are imposed. In Figure 2.5 a step change on N is applied, holding the expansion valve opening, whereas in Figure 2.6 a step change on A_v is implemented. In this case both step changes are applied while the condenser works in *mode* 1.

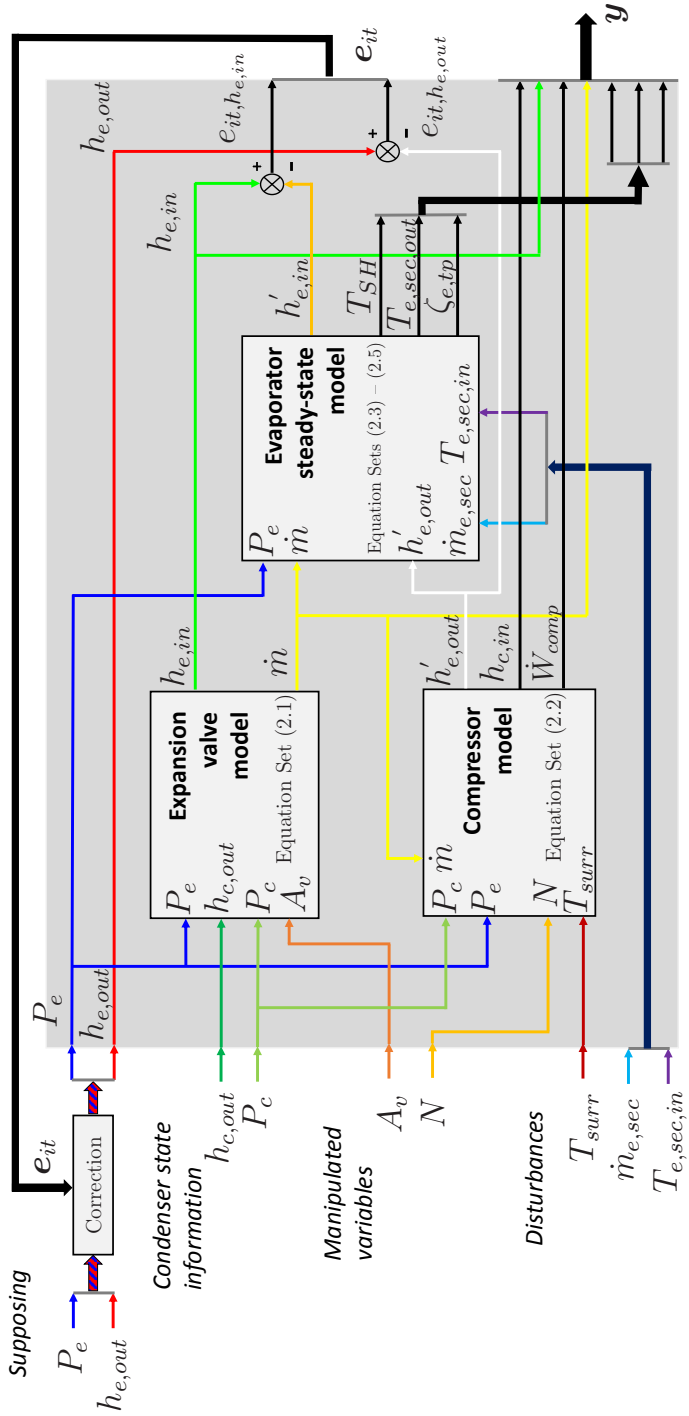

Figure 2.4 Iterative procedure to solve evaporator variables.

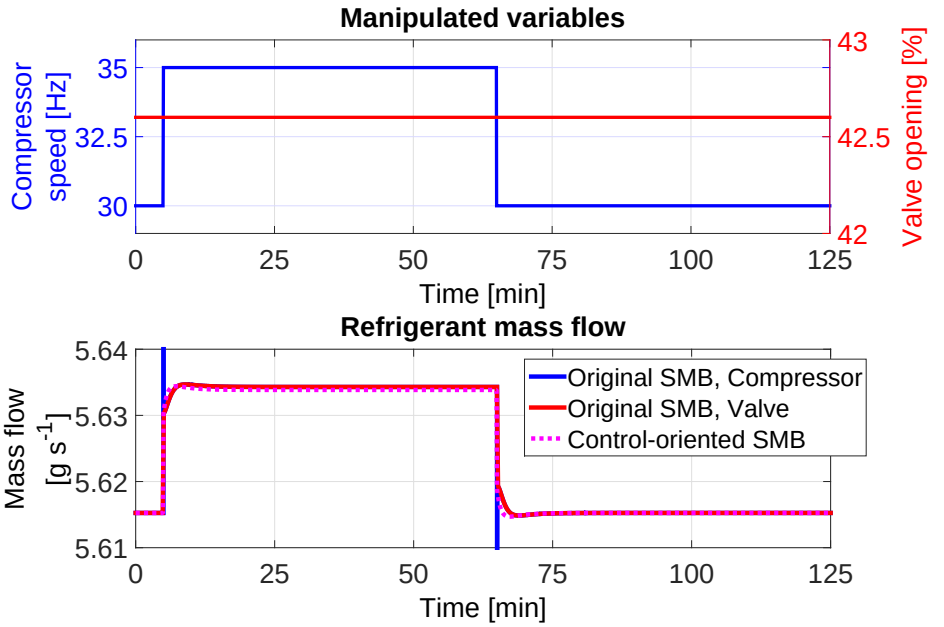

(a) Manipulated variables and refrigerant mass flow

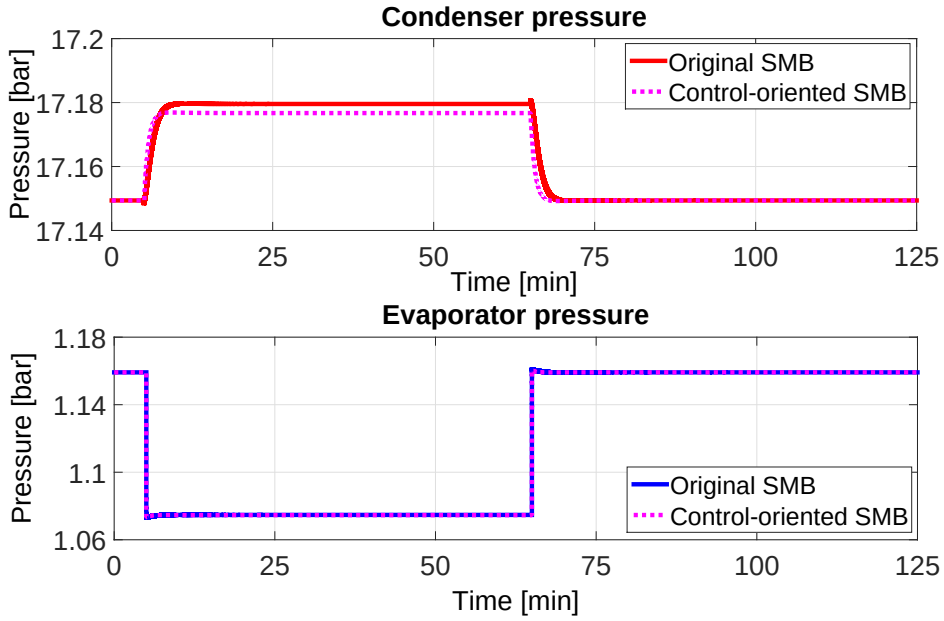

(b) Condenser and evaporator pressures

Figure 2.5 Comparison between the original SMB model and the control-oriented SMB model (*mode* 1) when applying a step change on the compressor speed N.

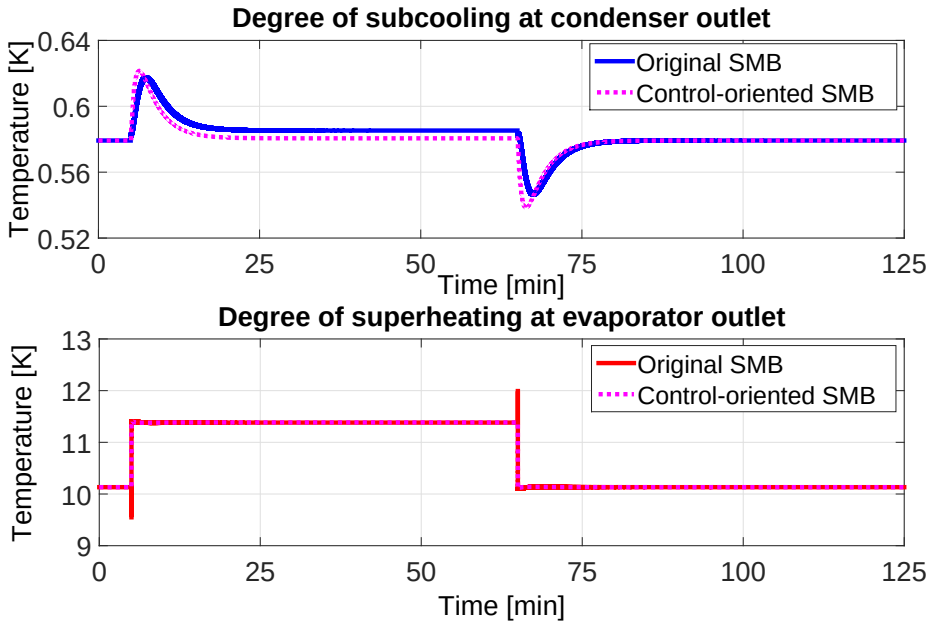

(c) Degree of subcooling and superheating

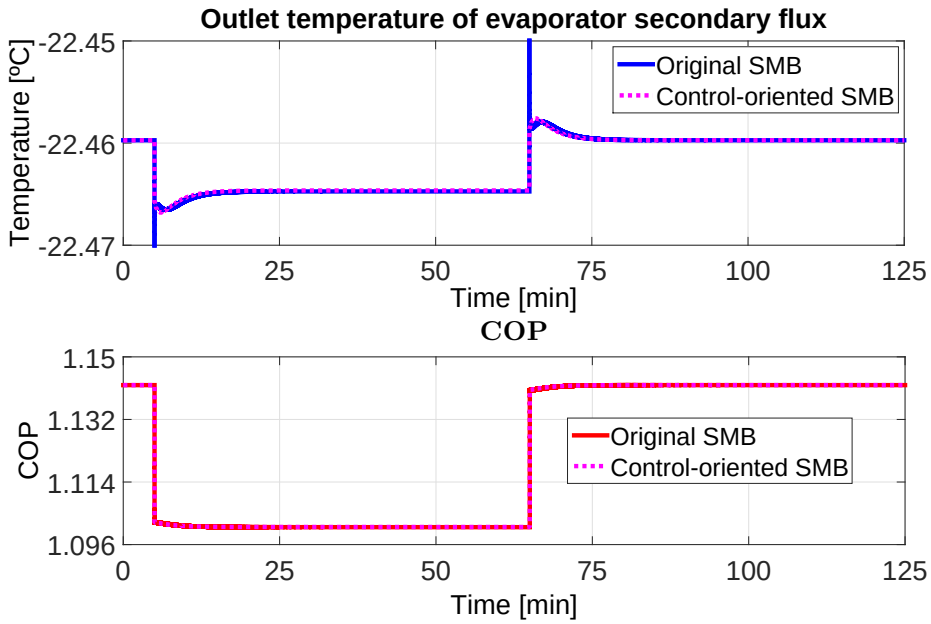

(d) Outlet temperature of evaporator secondary flux and Coefficient of Performance

Figure 2.5 Comparison between the original SMB model and the control-oriented SMB model (*mode* 1) when applying a step change on the compressor speed N.

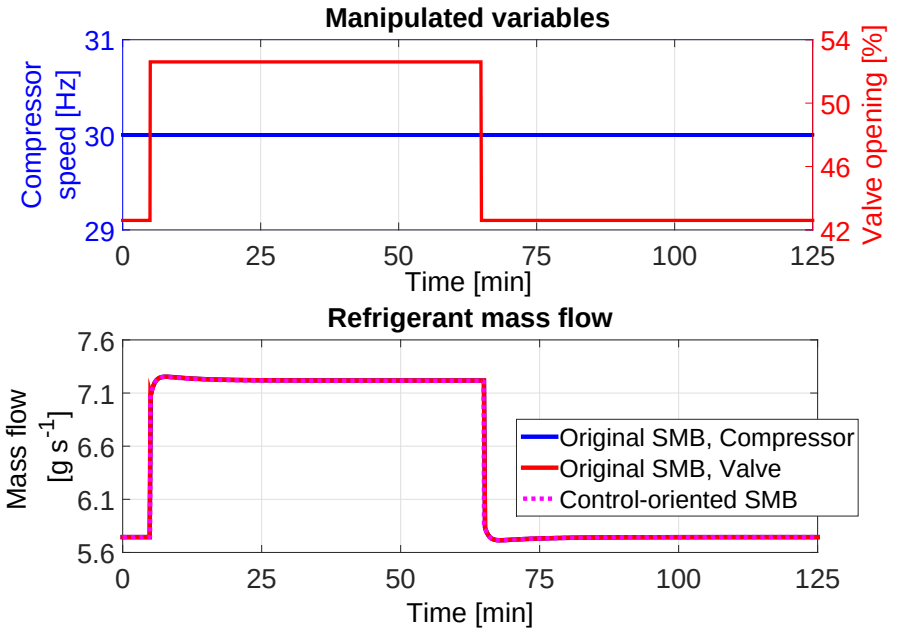

(a) Manipulated variables and refrigerant mass flow

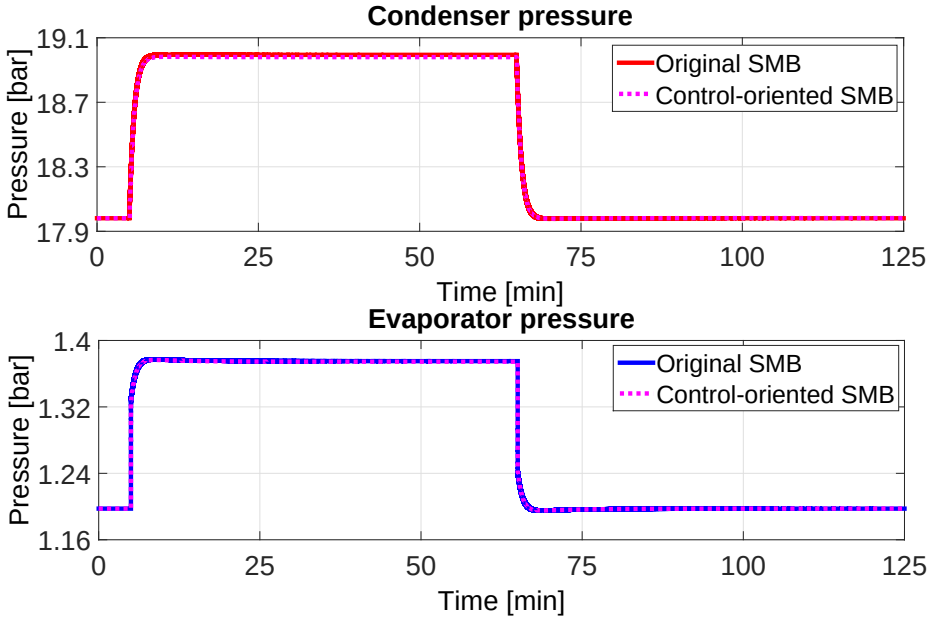

(b) Condenser and evaporator pressures

Figure 2.6 Comparison between the original SMB model and the control-oriented SMB model (*mode* 1) when applying a step change on the valve opening A_v.

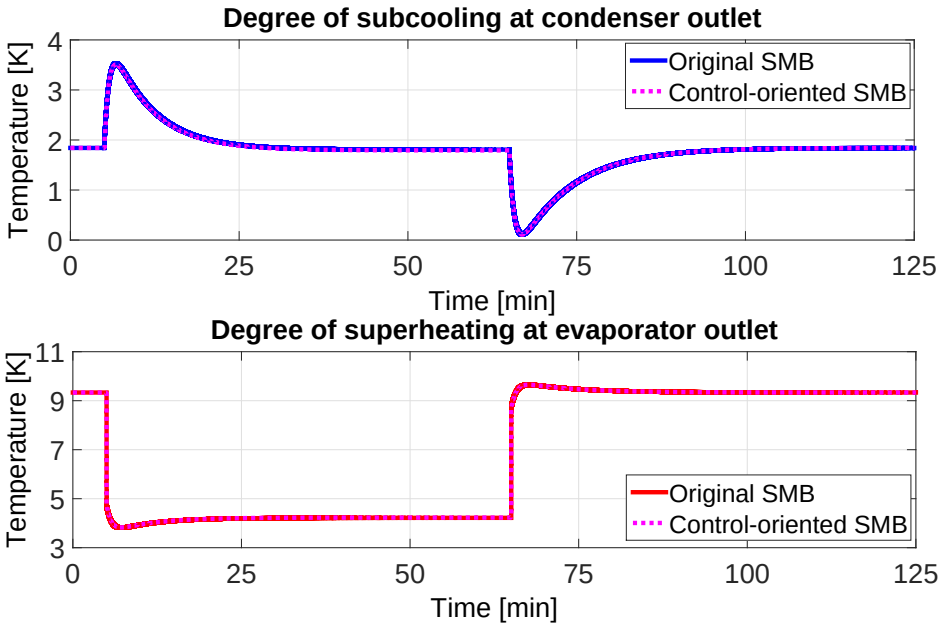

(c) Degree of subcooling and superheating

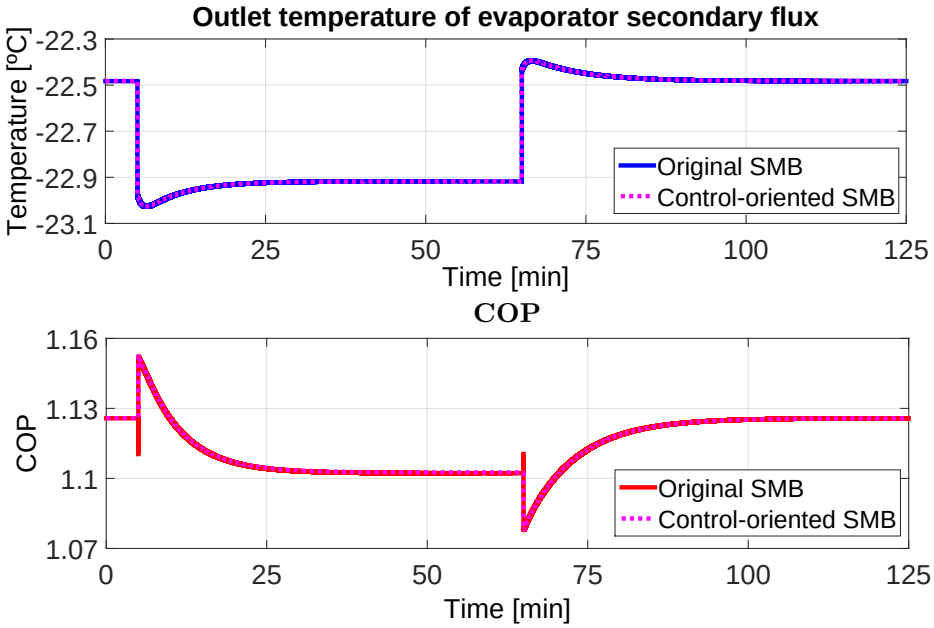

(d) Outlet temperature of evaporator secondary flux and Coefficient of Performance

Figure 2.6 Comparison between the original SMB model and the control-oriented SMB model (*mode* 1) when applying a step change on the valve opening A_v.

As shown in Figures 2.5 and 2.6, minor differences are appreciated between the original SMB model and the control-oriented one. Only immediately after the step change, when there is not refrigerant mass flow equilibrium and the assumption of a unique refrigerant mass flow in the cycle does not exactly apply there are appreciable differences. As shown in Figures 2.5 and 2.6, the step response of all cycle variables, both in the original SMB and the control-oriented one, includes two dynamic components: one very fast, due to the mass flow imbalance and the evaporator intrinsic dynamics, and another one slower, due to the dominant condenser dynamics. As expected, since it does not consider the evaporator dynamics and the fast effects of mass flow imbalance, the control-oriented SMB model does not reproduce properly the fast response of the variables, especially those related to the evaporator, such as the degree of superheating and the output temperature of the evaporator secondary flux. However, the control-oriented SMB model does represent properly the slow dominant dynamics of the cycle. The transient differences cause the small steady-state errors, since it will be explained in Chapter 4 that the system has multiple equilibria given a couple of manipulated variables N and A_v, and the steady-state equilibrium depends on the transient trajectory. Changes on the compressor speed cause greater mass flow imbalance, therefore the errors in Figure 2.5 are greater than in Figure 2.6. Anyway, the differences are small enough to be compensated by the controller robustness, and the computation time of the control-oriented model is about 2% of that of the original SMB model.

Moreover, some simulation results when the condenser operates in *mode* 2 are presented. In Figure 2.7 a step change on N is applied, whereas in Figure 2.8 a step change on A_v is implemented. In this case, since no degree of subcooling exists, the refrigerant vapour quality at the condenser outlet is represented, on account of that it is no longer zero in *mode* 2. The conclusions are similar to those derived when the condenser works in *mode* 1: there are more differences when the compressor speed changes, because the transient mass flow imbalance is greater, and only immediately after the step change there are noticeable differences.

2.3 Final remarks

This Chapter has been devoted to modelling of vapour-compression refrigeration systems, focusing on the one-compression-stage, one-load-demand configuration. Firstly, steady-state modelling has been addressed and each element of the cycle has been separately modelled, paying special attention to the heat exchangers: evaporator and condenser. Regarding heat transfer, the *effectiveness-NTU* method has been used to model the different *modes* considered for each heat exchanger.

Secondly, the dynamic modelling of such systems has been also addressed, also focusing on the heat exchangers, since they concentrate the dominant dynamics. Different approaches from the literature have been assessed and the *switched moving boundary* (SMB) model has been taken as starting point. However, the development of a control-oriented simplified model seems interesting, since the still high order of the SMB model continues to limit its use in practical model-based control strategies. Some considerations have been taken into account to reduce the model order and thus the complexity of the original SMB model. Then, frequency differences between the dynamics of both

the evaporator and the condenser concerning their internal volumes and the refrigerant thermodynamic properties have been detailed and assessed. It has been concluded that the evaporator dynamics are usually much faster than those of the condenser, because of the lower internal volume of the first one, and also given that the refrigerant properties, especially the density, cause the evaporator dynamics to be intrinsically faster than those of the condenser. Moreover, the dynamics due to the refrigerant mass flow imbalance within the cycle considered in the original SMB model have been assessed and it has been concluded that the refrigerant mass flow equilibrium between the condenser inlet and outlet is very fast compared to the heat transfer dominant dynamics, therefore a unique refrigerant mass flow passing through the condenser might be assumed, disregarding the fast transient due to mass flow imbalance. A simplified control-oriented nonlinear model of the whole one-stage, one-load-demand cycle has been proposed, whose state vector is made up of only three variables, all related to the condenser, which turns out to generate the slowest and thus dominant dynamics.

Differences between the control-oriented model and the original SMB model have been assessed in simulation, applying step changes on the manipulated variables. The differences show to be negligible regarding dominant dynamics, whereas the computation load is definitely reduced. All of this causes this simplified model to fit the requirements usually imposed when using model-based control strategies: reasonable accuracy and low computational load. The control-oriented dynamic model, which reduces the complexity of the original SMB model while retaining the dominant dynamics, is one of the main contributions of the Thesis.

The steady-state models developed in Chapter 2 are to be used both in the parameter identification of the plant, performed in Chapter 3, and also when analysing the optimization stage of the model-based control strategy described in Chapter 4. Furthermore, the control-oriented dynamic model proposed in this Chapter is used in Chapter 4 to study the controllability of the one-stage, one-load-demand cycle, along with the control simulations included in Chapter 5.

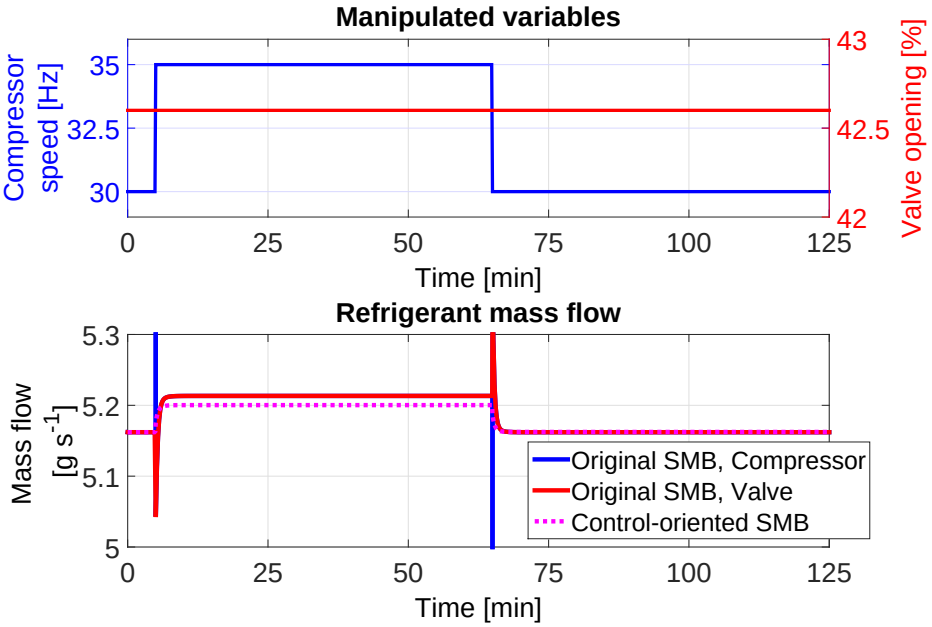

(a) Manipulated variables and refrigerant mass flow

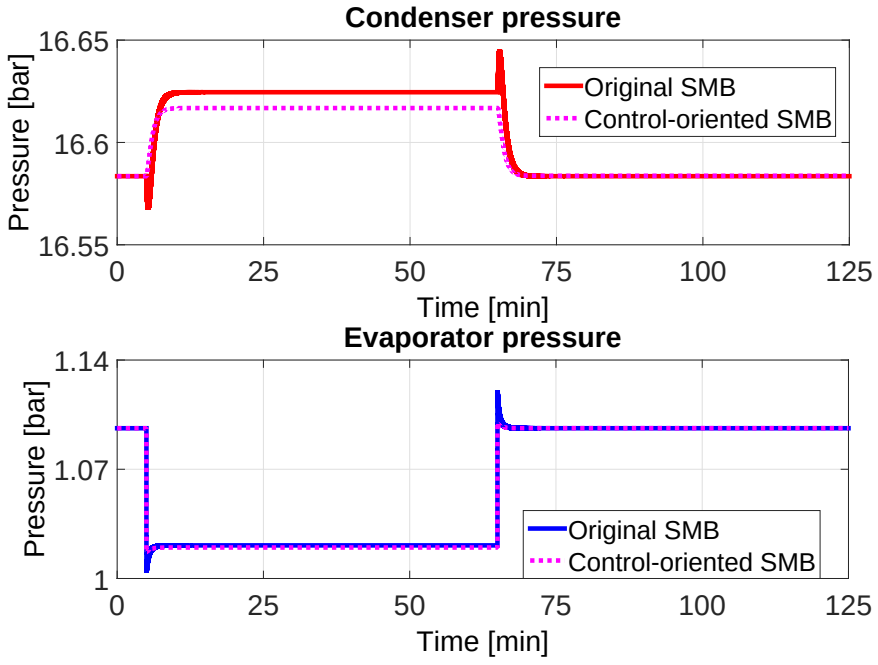

(b) Condenser and evaporator pressures

Figure 2.7 Comparison between the original SMB model and the control-oriented SMB model (*mode* 2) when applying a step change on the compressor speed N.

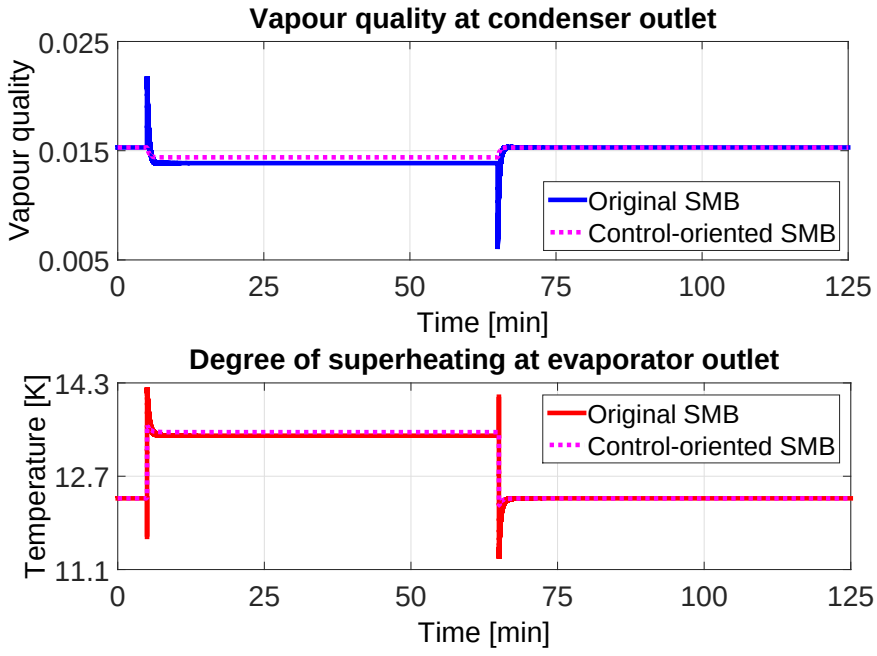

(c) Vapour quality at condenser outlet and degree of superheating

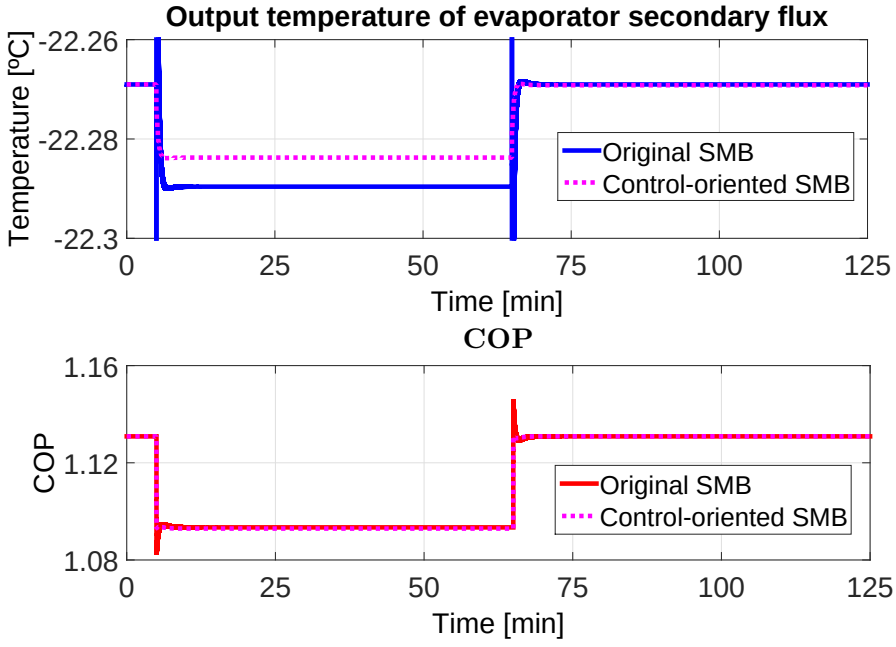

(d) Outlet temperature of evaporator secondary flux and Coefficient of Performance

Figure 2.7 Comparison between the original SMB model and the control-oriented SMB model (*mode* 2) when applying a step change on the compressor speed N.

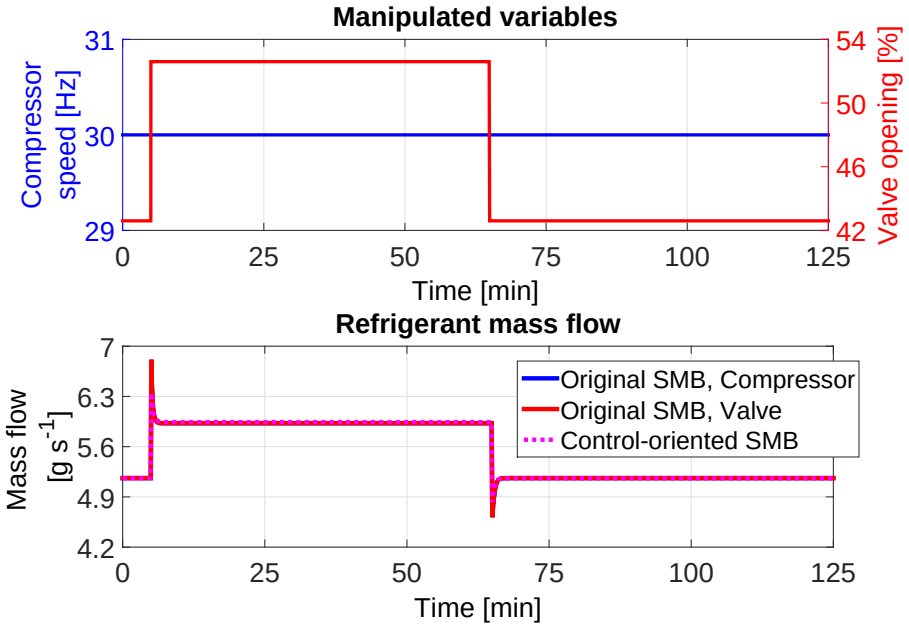

(a) Manipulated variables and refrigerant mass flow

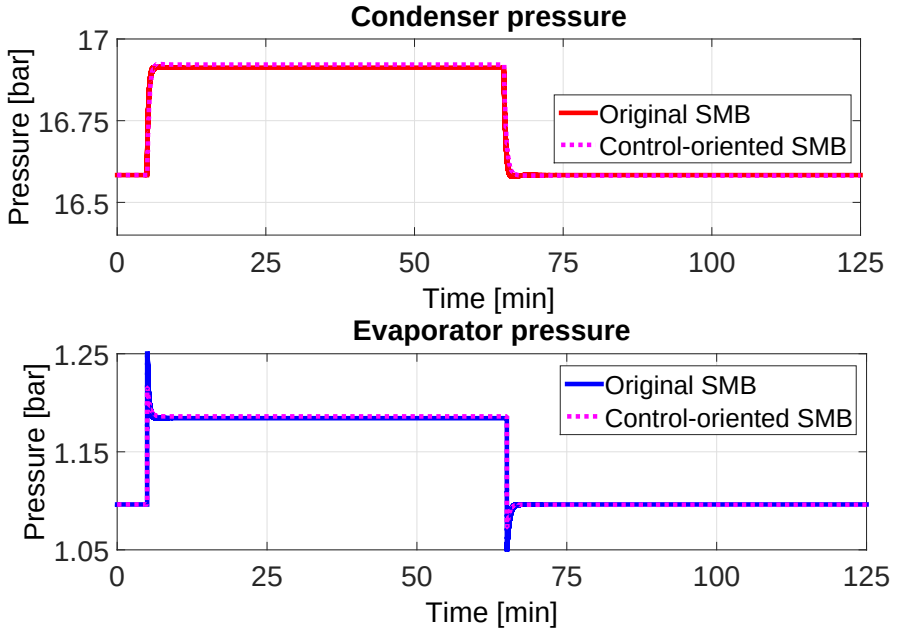

(b) Condenser and evaporator pressures

Figure 2.8 Comparison between the original SMB model and the control-oriented SMB model (*mode* 2) when applying a step change on the valve opening A_v.

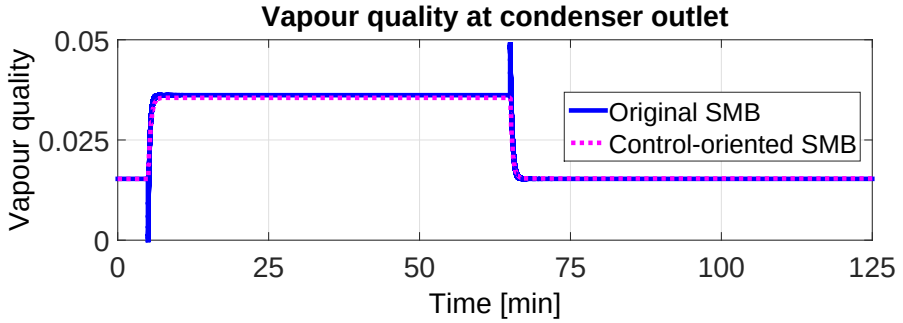

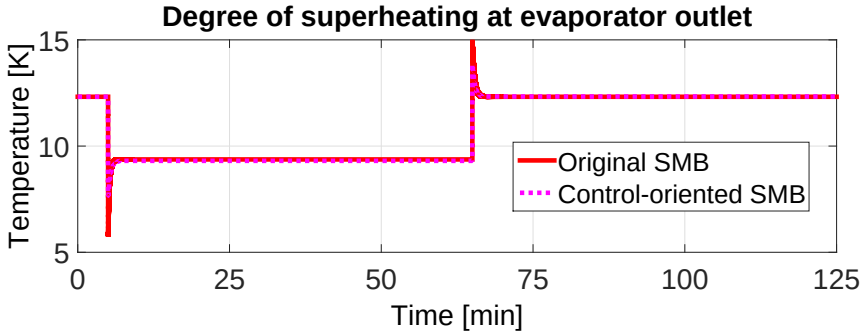

(c) Vapour quality at condenser outlet and degree of superheating

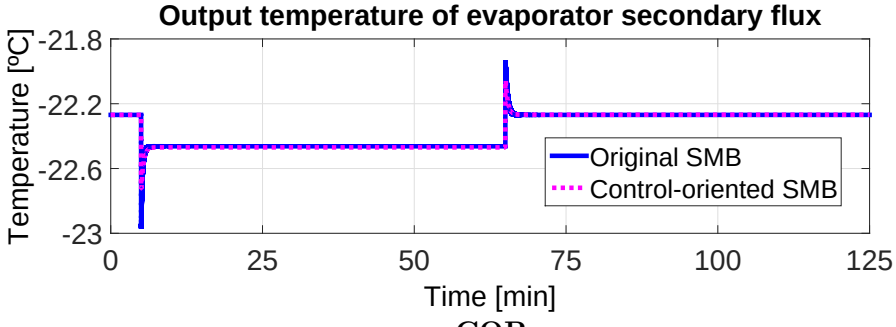

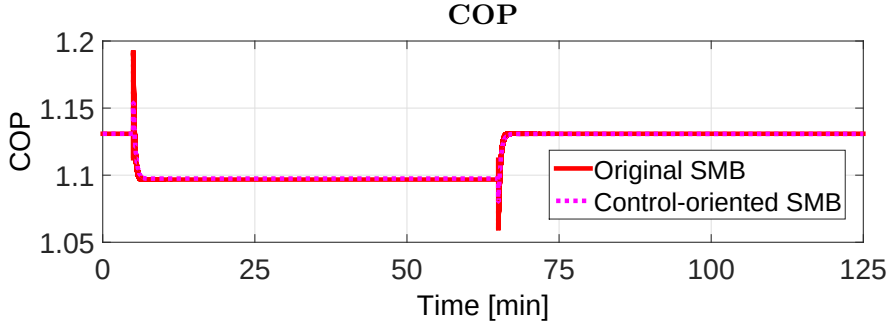

(d) Outlet temperature of evaporator secondary flux and Coefficient of Performance

Figure 2.8 Comparison between the original SMB model and the control-oriented SMB model (*mode* 2) when applying a step change on the valve opening A_v.

3 Experimental plant

No amount of experimentation can ever prove me right; a single experiment can prove me wrong.

ALBERT EINSTEIN

Contents

In this chapter the design, implementation, and automation of the two-stage, two-load-demand experimental refrigeration plant are described. The facility is fully configurable, since cycles with one or two compression stages, and one or two load demands can be set up. Detailed description of the experimental facility concerning the physical components, actuators, and sensors is addressed, as well as low-level control and communication bus issues. The high-level control environment and the communication with the low-level controller are also approached.

Parameter identification of the refrigeration plant is also addressed. It is shown that dominant system dynamics are those of heat exchangers, and their heat-transfer-related parameters affect system statics but barely influence system dynamics. Note that the MB approach selected as modelling technique for the heat exchangers is a first-principle methodology, therefore the parameters of each heat exchanger model are estimated. Many authors who make use of this approach propose to use correlations to calculate the heat-transfer-related parameters [20, 23], using a white-box model approach. These correlations (when available for the refrigerant and the type of heat exchanger at the specific facility) might lead to modelling errors which may be greater than the generated when identifying these coefficients according to real data. Most correlations are used for heat exchanger design and not for real-time simulation, and not all flow conditions (laminar or turbulent regime) are usually considered for all fluids and heat exchanger typologies. Moreover, having an estimation of heat transfer coefficients according to experimental data and therefore closer to real values than those provided by correlations is expected to generate in simulation a more accurate estimation of the length of the different heat exchanger zones. Those non-measurable variables, among others, determine the cycle state and they are key variables to define the optimal cycle corresponding to a certain cooling demand, as analysed in Chapter 4. Thus, an accurate estimator of such variables is required when trying to achieve optimal control.

A novel identification procedure focused on the heat exchangers is presented. Diverse refrigerant phases along each heat exchanger, according to the MB modelling approach, are considered, thus diverse zones are differentiated, whose lengths are inaccessible state variables. An overall heat transfer coefficient is considered for each zone. Therefore, a grey-box modelling approach is proposed, where a structure based on conservation equations is considered and some parameters, namely the overall heat transfer coefficients, are identified according to experimental data. Consistent values of all parameters are obtained considering only steady-state experimental data and some orders of magnitude found in the literature. Experiments have been carried out in order to validate this method, using both the one-stage, two-load-demand and the two-stage, two-load-demand plant configurations. Although all components are separately identified, a global validation method is implemented.

The contents of this Chapter have been included in some of the publications presented in Chapter 1, Section 1.5 [52, 54, 58, 59, 61, 63].

3.1 Description of the experimental plant

3.1.1 Design and components

Figure 3.1 shows a schematic diagram of the designed refrigeration system, which uses R404a as refrigerant. Two compressors and two evaporators with their respective expansion valves have been included in this experimental plant, in order to explore multivariable control strategies for two compression stages and two different load demands, whereas two alternative condensers are also included. Nevertheless, the plant is fully configurable: it is possible to control a two-stage compression cycle with two refrigeration levels and a one-stage cycle with one or two refrigeration levels, by means of some configuration valves (CV). Specifically, CV_1 and CV_2 enable the configuration of the plant regarding the compression stages and load demands; Figures 3.2 – 3.4 show three typical configurations. It is desired that the Evaporator 1 works around 5°C and the Evaporator 2 around -20 °C, since they are reference temperatures for cooling and freezing purposes, respectively.

The variable-speed compressors are of semihermetic reciprocating type, with minimum and maximum speed of 25 and 70 Hz, respectively. The booster compressor has 2 cylinders and 1.8 kW power, while the main one is a four-cylinder device, with 6.4 kW power. Both compressors work with a variable frequency drive (VFD), designed to achieve more accurate speed control. Selection of the compressors regarding power and speed has been carried out in order to ensure compression capacity in all possible plant configurations, and bearing in mind the temperature requirements to be accomplished in both evaporators. Both compressors, along with some other elements, can be observed in Figure 3.5.

Both evaporators are brazed-plate heat exchangers, connected to two different temperature and flow-controlled secondary heat transfer loops, while two alternative condensers are available: an air-cooled cross-flow tube heat exchanger and a water-cooled brazed-plate one, but only one of the two condensers can be used at the same time. This feature increases the configurability of the plant, since not only ambient temperature can be used as hot source of the refrigeration cycle. The use of the air-cooled or the water-cooled condenser is selected through CV_3 and CV_4, as shown in Figure 3.1. The air-cooled condenser is selected in the configurations shown in Figures 3.2 – 3.4, which is achieved by opening CV_3 and closing CV_4, since most experiments have been carried out using this condenser.

Brine of around 28% mono-ethylene glycol aqueous solution is used in Tank 1, as long as brine of 60% propylene glycol aqueous solution is used in Tank 2, due to its lower enough freezing point for the freezing level. The secondary heat transfer loops are controlled by means of a pair of electric resistances with a nominal power of 2 kW each, whereas the brine flows are controlled via two in-line pumps with a power of 0.25 kW each. Moreover, the water flow for the water-cooled condenser is also controlled through an additional in-line pump. Like the compressors, each pump works with a VFD. Meanwhile, a fan with a power of 1.05 kW boosts heat transfer between air and the refrigerant at high pressure and temperature at the air-cooled condenser.

The expansion devices are pulse-width-modulation (PWM) electronic expansion valves. These devices can be controlled either directly through a digital signal from the PLC (using a solid state relay with enough power) or using a superheat valve controller (SVC), a device which calculates the degree of superheating at the evaporator outlet and drives the valve

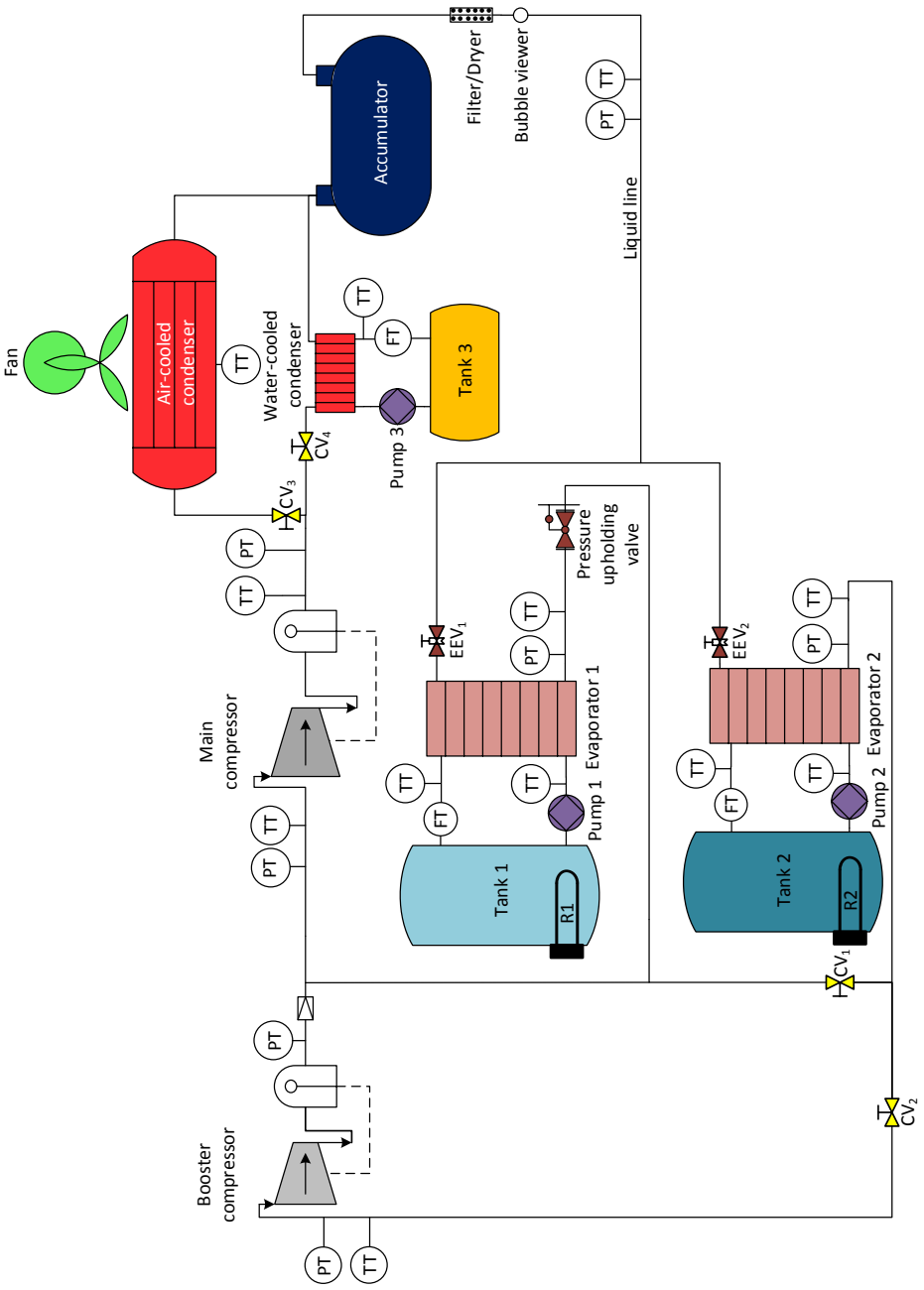

Figure 3.1 Experimental plant layout.

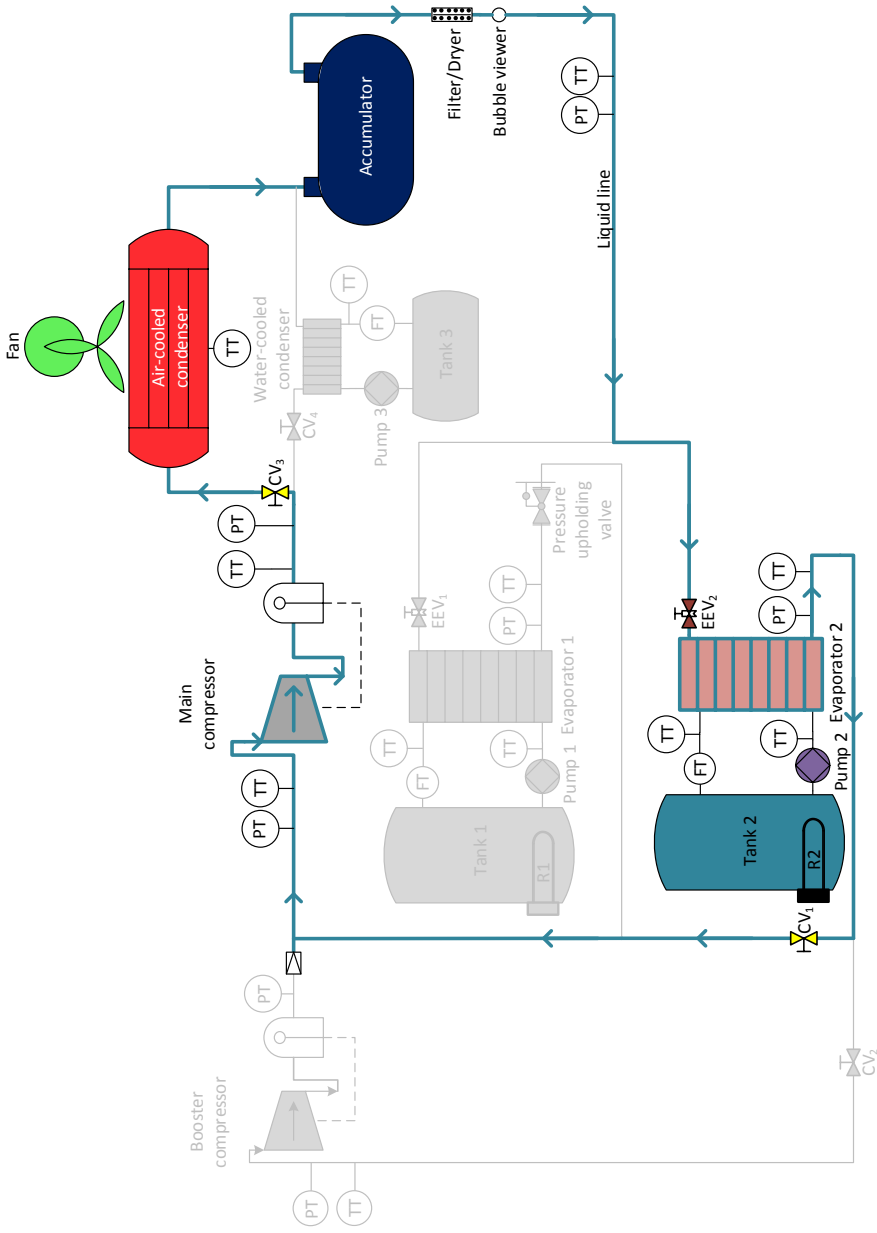

Figure 3.2 One-stage, one-load-demand configuration highlighted on the experimental plant layout.

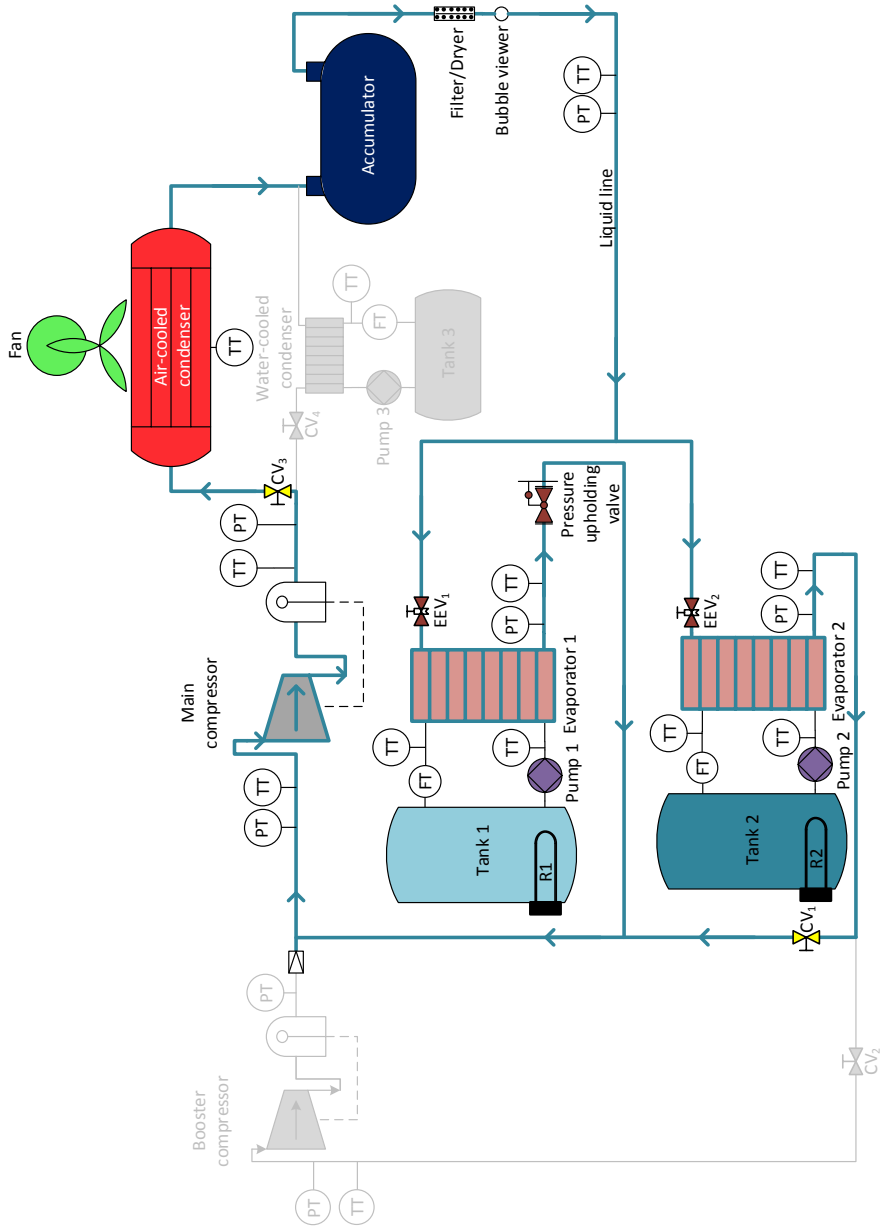

Figure 3.3 One-stage, two-load-demand configuration highlighted on the experimental plant layout.

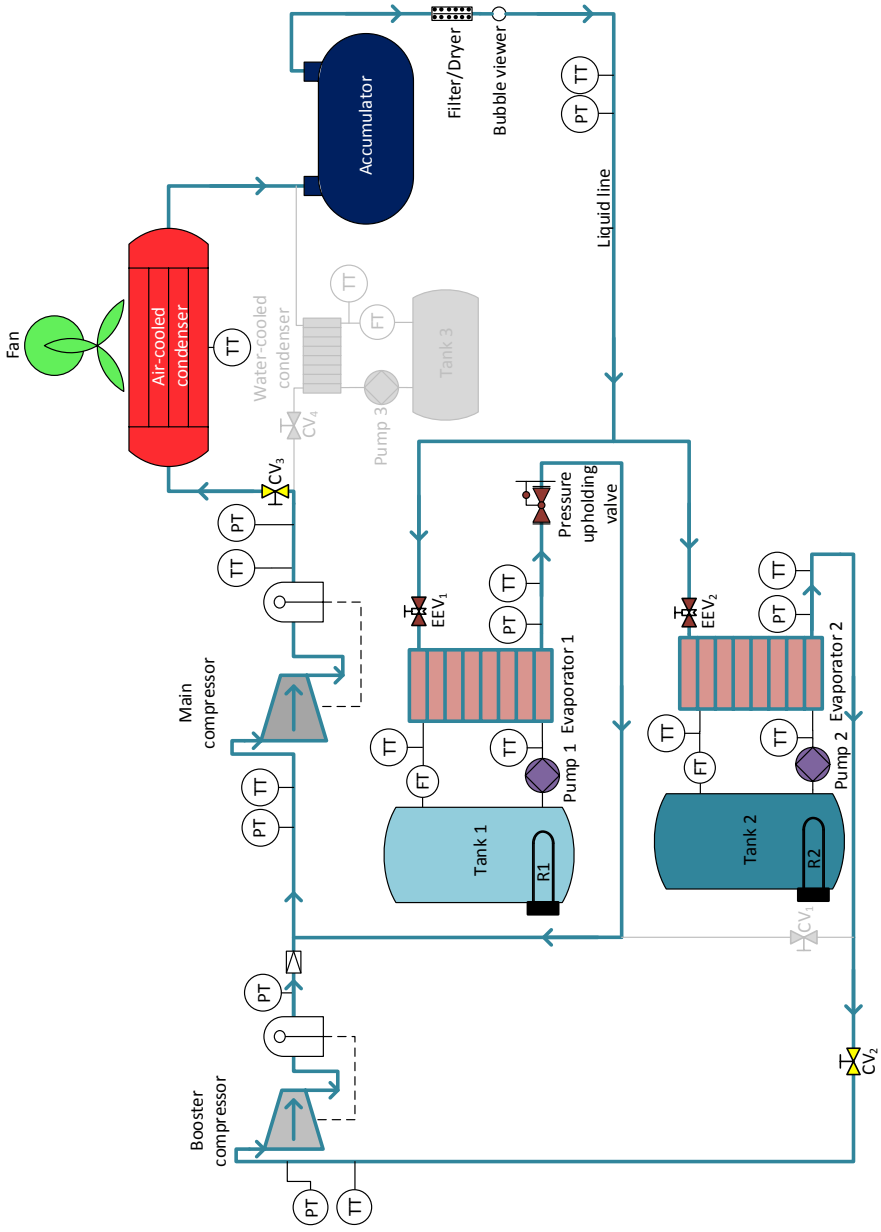

Figure 3.4 Two-stage, two-load-demand configuration highlighted on the experimental plant layout.

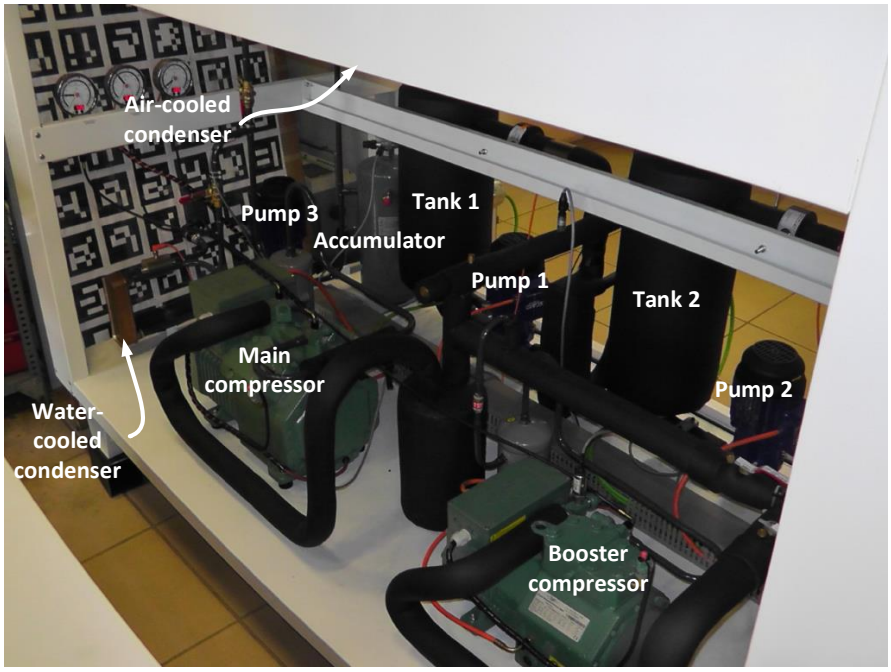

Figure 3.5 Compressors placed at the experimental facility.

opening to hold a specified set point on the degree of superheating. In order to perform the calculation of the degree of superheating, each SVC has a pressure transducer and a thermocouple analogue input. Evaporators, expansion valves, and secondary flux circuits are represented in Figure 3.6. Finally, the accumulator depicted in Figure 3.1 is only used to store the refrigerant when the plant is not working; in no case it is used in operation as a device which ensures that the refrigerant is saturated liquid at the expansion valve inlet, as other experimental plants do, for instance that described by Rasmussen *et al.* [1].

3.1.2 Sensors

The experimental plant has full instrumentation for research purposes. Thermocouples and pressure transducers have been placed at selected points to calculate all the refrigerant enthalpies and the degree of superheating at both evaporator outlets, whereas the brine volumetric flow rates are measured by magnetic-inductive flow sensors. All sensors are indicated in Figure 3.1, following standard nomenclature, and some of them are also visible in Figures 3.5 and 3.6. Nevertheless, there is no refrigerant mass flow sensor at the facility. This is a common issue at commercial refrigeration systems, since such sensors are too expensive and the measurement accuracy usually shows not to be as high as required. A summary of the experimental setup of apparatus is presented in Table 3.1.

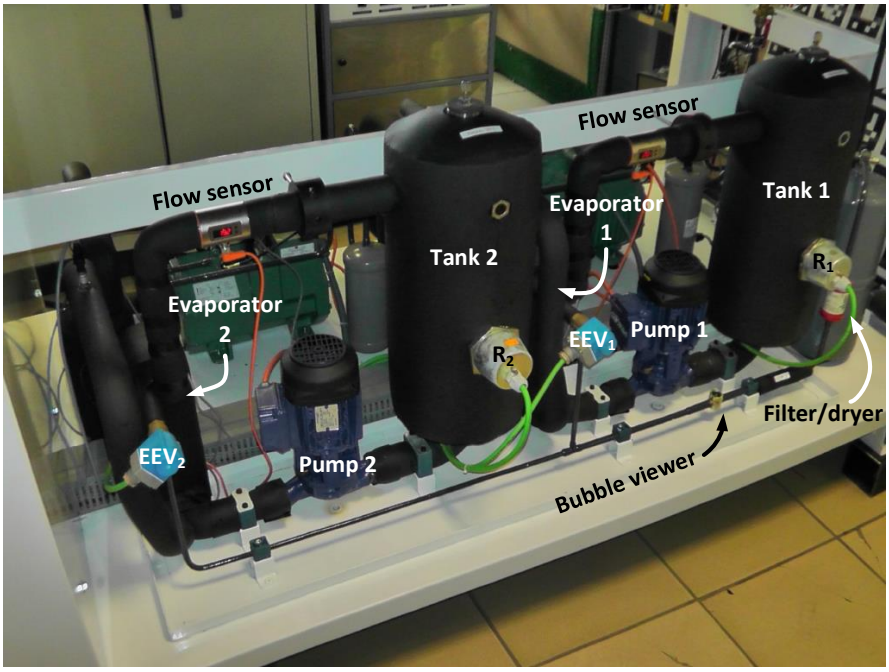

Figure 3.6 Evaporators, expansion valves, and secondary flux circuits.

3.1.3 Programmable Logic Controller (PLC)

A PLC is used for low-level control of the refrigeration plant. Along with the power module, a digital input module and a digital output module are used to manage digital signals. Furthermore, three analogue input/output mixed modules are set up, along with two specific thermocouple signal converters. In Appendix A the signals connected through the analogue mixed modules and the thermocouple signals wired through the converters are detailed.

Moreover, all digital and analogue signals from VFDs and SVCs are connected to the PLC through a communication bus over RS-485. The ModBus protocol [76] is selected due to its simplicity and reliability. The PLC is the master of the communication, whereas all VFDs and SVCs are slaves. The bus access method is time division, setting a maximum slot time of 100 ms. Table 3.2 summarises the total number of variables managed by the PLC.

The PLC also manages the control sample time, which basically depends on the communication bus cycle time. The data flow from and to the VFDs is always imperative, but the same is not suitable for the SVCs. If the EEVs are controlled through their SVCs, all information related to these controllers (which is read and written through the bus) is relevant. However, if the expansion valves are controlled straightly by the PLC through digital signals, most reading and writing operations concerning the SVCs are not required. This fact allows to reduce the bus cycle time, since the number of reading and writing

Table 3.1 Feature summary of the experimental plant.

Main Compressor		**Booster Compressor**	
Power [kW]	6.4	Power [kW]	1.8
Number of cylinders	4	Number of cylinders	2
Speed range [Hz]	[25 70]	Speed range [Hz]	[25 70]
Variable frequency drive (VFD)	Yes	Variable frequency drive (VFD)	Yes
Air-cooled condenser		**Water-cooled condenser**	
Type	Cross-flow tubes	Type	Brazed-plate
Secondary flux	Air	Secondary flux	Water
Current direction	Cross flow	Current direction	Counter-current
Fan power [kW]	1.05	Pump power [kW]	0.25
Evaporator 1		**Evaporator 2**	
Type	Brazed-plate	Type	Brazed-plate
Secondary flux	Brine of 28% mono-ethylene glycol aqueous solution	Secondary flux	Brine of 60% propylene glycol aqueous solution
Current direction	Counter-current	Current direction	Counter-current
Resistance power [kW]	2	Resistance power [kW]	2
Pump power [kW]	0.25	Pump power [kW]	0.25
Electronic expansion valve 1 (EEV_1)		**Electronic expansion valve 2 (EEV_2)**	
Method	Pulse-width modulation (PWM)	Method	Pulse-width modulation (PWM)
Thermocouples		**Pressure Transducers**	
Range [ºC]	[-40 180]	High pressure range [bar]	[0 30]
Precision [ºC]	0.1	Low pressure range [bar]	[0.5 7.5]
Volumetric flow sensor		Precision [bar]	0.01
Range [L min^{-1}]	[0.1 25]	**Refrigerant**	
Precision [L min^{-1}]	0.05	R404a	

operations is lower. Moreover, due to the unreliability of the SVCs regarding the bus data flow, it is possible to reduce the slot time up to 50 ms. Table 3.3 shows the total number of reading and writing operations per bus cycle and the timing for both valve control choices.

Even once selected a valve control mode, there are some data that the PLC must read imperatively once a bus cycle, whereas some others are not so relevant and they can be read at lower frequency. Taking this into account, the bus cycle is organised in such a way that all the mandatory required data are read once a cycle and the rest of them are read by using a shift scheme. A detailed description of the reading and writing operations carried out in both valve control modes as well as the shift scheme used in each case are provided in Appendix A.

Table 3.2 Variables managed by the PLC.

Type	Number
Digital inputs	15
Digital outputs	8
Analogue inputs	12
Analogue outputs	3
Thermocouple inputs	8
ModBus variables	60

Table 3.3 Bus timing for the two valve control modes.

Valve control mode	Reading and writing operations	Slot time [ms]	Bus cycle time [s]
Through SVCs	30	100	3
Straight PLC control	20	50	1

3.1.4 Supervision software and OPC communication

A Supervisory Control And Data Acquisition (SCADA) system is developed and works as human-machine interface. It allows to control the plant manually in open loop and monitor all cycle variables when a high-level controller is applied. Figure 3.7 shows the SCADA screen when a high-level controller, namely through OLE for Process Control (OPC) communication standard, is performed.

OPC is a communication standard used to connect devices from different manufacturers [77]. Here, OPC is used for communication between the PLC and MATLAB® software [78]. As explained previously, the PLC is used to data acquisition and low-level control, whereas the computing program is devoted to implementing high-level controllers.

As seen in Figure 3.8, the PLC is connected to the computer by an Ethernet link. The SCADA system and the PLC are directly communicated as long as they are from the same manufacturer. MATLAB®, however, needs to use an OPC server to access process variables. OPC is set up in MATLAB®/Simulink environment where the number of read and written data is gathered in Table 3.4.

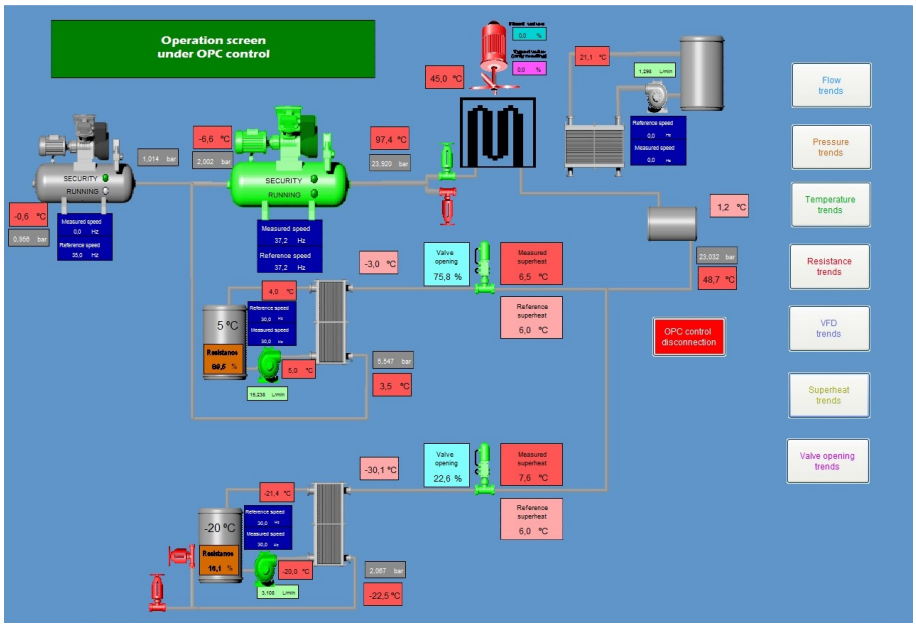

Figure 3.7 SCADA screen under OPC control.

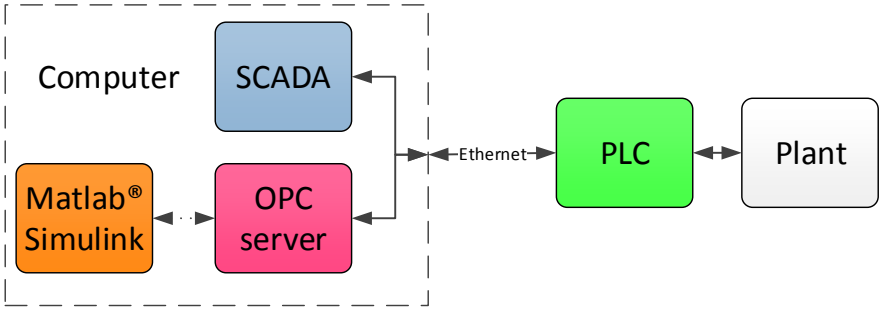

Figure 3.8 Communication diagram.

Table 3.4 Process variables managed through OPC.

	Analogue	**Digital**
Read data	50	5
Written data	13	-

3.2 Identification

As stated in Chapter 2, all elements of the cycle are separately modelled, creating dynamic submodels for the refrigerant flow along the heat exchangers and static models for the compressors, expansion valves, and secondary fluxes at the evaporators and condenser. The identification of all components according to experimental data is addressed below.

3.2.1 Expansion valves

The static model considered for both expansion valves has been previously presented in Chapter 2, Subsection 2.1.1. Notwithstanding, the mass flow characteristic of the valve is included in Equation (3.1) as a remainder, once the notation has been adapted for the multi-load-demand case.

$$\dot{m}_e = c_{eev}\, A_v\, \sqrt{2\rho_{c,out}\Delta P_{eev}} = c_{eev} A_v \sqrt{2\rho_{c,out}(P_{c,out} - P_e)} \tag{3.1}$$

The coefficient c_{eev} is a characteristic parameter of the valve, which allows to predict the refrigerant mass flow when varying the valve opening and the cycle variables, such as pressures and enthalpies. Test data and mass flow models of EEVs are very limited in open literature, as stated by Park *et al.* [79]. The simplest model consisting of a unique value of the valve coefficient c_{eev}, despite being in general valid for single-phase flows, produces non-negligible deviations when considering several operating points, because more complex phenomena occur when the refrigerant expands through the valve and becomes two-phase. The original works by Schurt *et al.* proposed a correlation for c_{eev} where its value depends only on the degree of subcooling [11, 33]. Considering the facility under study, the component selection and performance range of the manipulated variables allow only to achieve cycles with very low degree of subcooling, even zero in some cases. It causes this correlation to produce very similar values of c_{eev}, and it is not valid when T_{SC} reaches zero. A sensitivity analysis has been carried out and the conclusions have shown that inaccuracy when estimating the refrigerant mass flow through the valve model involves great differences between the experimental and simulated variables when validating the whole cycle. Therefore, a more complex model is better suited than that proposed by Schurt *et al.* Then, as proposed by Shanwei *et al.* [80], a polynomial correlation for c_{eev} is considered, where its dependence on all input parameters of the expansion valve model is highlighted in Equation Set (3.2). The degree of subcooling T_{SC} is also included as recommended by Shanwei *et al.* [80], since that dependence becomes relevant when analysing experimental data with very low degree of subcooling.

$$\begin{aligned} c_{eev} &= c_{eev}(A_v, \Delta P_{eev}, \rho_{c,out}, T_{SC}) \\ c_{eev} &= 10^{-9}\left(n_0 + n_1 \frac{A_v}{100} + n_2 \frac{\Delta P_{eev}}{P_{c,out}} + n_3 \frac{\rho_{c,out}}{\rho_{c,f,out}} + n_4 \frac{T_{SC}}{T_{c,sat,out}}\right) \end{aligned} \tag{3.2}$$

In Equation Set (3.2) the temperature $T_{c,sat,out}$ refers to the saturation temperature at the outlet condenser pressure $P_{c,out}$, whereas the density $\rho_{c,f,out}$ matches the density of saturated liquid at the outlet condenser pressure. An identification method to calculate

the coefficient c_{eev} and the parameters $n_i \quad \forall i = 0,1,...,4$ which define its polynomial correlation from experimental data is intended. However, since there is no refrigerant mass flow sensor at the facility under study, it is not possible to directly apply Equation (3.1). Nevertheless, an estimation of the refrigerant mass flow can be obtained in steady state by applying energy balance at the corresponding evaporator, as expressed in Equation (3.3).

$$\dot{Q}_e = \dot{m}_{e,sec}\, c_{p,e,sec}\, (T_{e,sec,in} - T_{e,sec,out}) = \dot{m}_e\, (h_{e,out} - h_{e,in}) \tag{3.3}$$

In steady state $\dot{m}_{e,in} = \dot{m}_{e,out} \equiv \dot{m}_e$, thus $\dot{m}_e$ is calculated using Equation (3.3). As an example, Table 3.5 gathers some experimental data set used to estimate the refrigerant mass flow $\dot{m}_{e5}$ which expands in EEV_1 and later circulates through Evaporator 1, while Table 3.6 does the same regarding the refrigerant mass flow $\dot{m}_{e20}$ which expands in EEV_2 and circulates through Evaporator 2. The specific enthalpies required in the energy balance shown in Equation (3.3) are obtained using the *CoolProp* tool from the pressure-temperature pairs $\{P_e - T_{e,out}\}$ and $\{P_{c,out} - T_{c,out}\}$ gathered in Tables 3.5 and 3.6, since the refrigerant is single-phase at the evaporator and condenser outlet.

Table 3.5 Experimental data for the refrigerant mass flow estimation concerning the expansion valve EEV_1 (Evaporator 1, at 5 °C).

Variable	Unit	Experimental data					
P_{e5}	bar	5.42	5.63	5.58	5.57	5.60	5.56
$T_{e5,out}$	°C	5.0	3.6	3.2	3.1	3.3	3.3
$P_{c,out}$	bar	20.97	20.97	22.01	21.08	24.06	21.07
$T_{c,out}$	°C	45.5	45.7	47.2	45.6	51.0	45.5
$\dot{m}_{e5,sec}$	kg s^{-1}	0.32	0.33	0.32	0.32	0.32	0.32
$T_{e5,sec,in}$	°C	4.9	6.3	4.9	4.9	4.9	4.9
$T_{e5,sec,out}$	°C	4.1	5.1	4.0	4.0	3.9	3.9
$\dot{m}_{e5}$	g s^{-1}	8.2	13.0	10.4	9.4	11.3	10.3

Once estimated $\dot{m}_e$ for a variety of steady-state experimental points, a least squares method is applied to minimize the errors between refrigerant mass flow calculated from Equations (3.1) – (3.2) and the values estimated by applying Equation (3.3) for all available steady-state experimental points. Identified values of all parameters included in Equation Set (3.2) for both expansion valves are shown in Table 3.7, while the mean value and Root Mean Square (RMS) of mass flow relative errors are gathered in Table 3.8. Relative error and RMS are calculated using Equations (3.4) and (3.5), respectively, where Z is the total number of experimental data.

$$RE_{\dot{m}_e} = \frac{|\, \dot{m}_{e,predict} - \dot{m}_{e,meas}\,|}{\dot{m}_{e,meas}} \tag{3.4}$$

Table 3.6 Experimental data for the refrigerant mass flow estimation concerning the expansion valve EEV_2 (Evaporator 2, at -20 °C).

Variable	Unit	Experimental data					
P_{e20}	bar	1.80	1.87	1.88	2.11	1.92	1.84
$T_{e20,out}$	°C	-29.0	-27.9	-23.9	-23.2	-26.8	-27.4
$P_{c,out}$	bar	20.97	20.97	22.01	21.08	24.06	21.07
$T_{c,out}$	°C	45.5	45.7	47.2	45.6	51.0	45.5
$\dot{m}_{e20,sec}$	g s^{-1}	74.1	74.4	66.2	71.5	72.0	70.8
$T_{e20,sec,in}$	°C	-19.6	-19.9	-20.8	-20.2	-19.9	-19.6
$T_{e20,sec,out}$	°C	-21.1	-21.0	-22.4	-21.3	-21.3	-21.4
$\dot{m}_{e20}$	g s^{-1}	4.8	3.5	4.5	3.0	4.7	5.2

$$\text{RMS} = \sqrt{\sum_{i=1}^{Z} \frac{RE^2}{Z}} \tag{3.5}$$

Table 3.7 Identified parameters of the c_{eev} correlation for valves EEV_1 and EEV_2.

Expansion valve	n_0	n_1	n_2	n_3	n_4
EEV_1	328.53	0.88	-4.38	-323.52	960.07
EEV_2	805.43	0.39	98.15	-892.56	2524.11

Table 3.8 Mean value and RMS of the relative error between predicted and estimated refrigerant mass flow concerning valves EEV_1 and EEV_2.

Expansion valve	$\overline{RE}$ [%]	RMS [%]
EEV_1	3.72	4.50
EEV_2	11.56	16.80

3.2.2 Compressors

The static model considered for the compressors has been previously presented in Chapter 2, Subsection 2.1.2. Notwithstanding, the equations defining the model are included in Equation Set (3.6) as a remainder. Note that the notation has been modified to adapt the

model to both compressors in all configurations.

$$\dot{m}_{comp} = \left[S_t - c \left(\left(\frac{P_{comp,dis}}{P_{comp,suc}} \right)^{\frac{c_{v,suc,g}}{c_{p,suc,g}}} - 1 \right) \right] \frac{N}{v_{comp,suc}} \tag{3.6a}$$

$$\begin{aligned} \dot{W}_{comp} &= b\, \dot{m}_{comp}\, (h_{comp,dis,is} - h_{comp,suc}) \\ T_{comp,dis,is} &= T_{dis} + \frac{h_{comp,dis,is} - h_{dis,g}}{c_{p,dis,g}} \\ h_{comp,dis} &= h_{comp,suc} + \frac{\dot{W}_{comp} - UA(T_{comp,dis,is} - T_{surr})}{\dot{m}_{comp}} \end{aligned} \tag{3.6b}$$

As shown in Equation Set (3.6), the compressor model can be split into two submodels for identification purposes: one defining the compressed refrigerant mass flow (Equation (3.6a)), and another defining the specific enthalpy increase through the compressor (Equation Set (3.6b)). b, c, S_t, and UA are the parameters to be estimated. To correctly identify the compressor parameters, a measurement or at least an estimation of the refrigerant mass flow is also required. Once again Equation (3.3) is used to estimate the corresponding refrigerant mass flow at steady-state points. Given that the compressor model is affine in the parameters to be estimated, linear regression techniques can be applied. Thus, a convenient formulation of the model is expressed in Equation (3.7), where $\boldsymbol{\theta} = [b \;\; UA \;\; c \;\; S_t]^T$ is the parameter vector to be estimated. However, each steady-state experimental point generates vector $\boldsymbol{\Gamma}_i$ and matrix $\boldsymbol{\varphi}_i$ as detailed in Equation Set (3.8), whereas $\boldsymbol{\xi}_i$ is the residue vector for experimental point $i \;\; \forall i = 1,2,...,Z$.

$$\boldsymbol{\Gamma} = \boldsymbol{\varphi} \cdot \boldsymbol{\theta} \tag{3.7}$$

$$\boldsymbol{\Gamma}_i = \boldsymbol{\varphi}_i \cdot \boldsymbol{\theta} + \boldsymbol{\xi}_i \quad \forall i = 1,2,...,Z$$

$$\boldsymbol{\Gamma}_i = \begin{bmatrix} \Gamma_{h_{comp,dis}} \\ \Gamma_{\dot{m}_{comp}} \end{bmatrix} \quad \boldsymbol{\theta} = \begin{bmatrix} \boldsymbol{\theta}_{h_{comp,dis}} \\ \boldsymbol{\theta}_{\dot{m}_{comp}} \end{bmatrix} \quad \boldsymbol{\varphi}_i = \begin{bmatrix} \boldsymbol{\varphi}_{h_{comp,dis}} & \mathbf{o} \\ \mathbf{o} & \boldsymbol{\varphi}_{\dot{m}_{comp}} \end{bmatrix} \tag{3.8a}$$

$$\begin{aligned} \Gamma_{h_{comp,dis}} &= h_{comp,dis} - h_{comp,suc} \\ \boldsymbol{\varphi}_{h_{comp,dis}} &= \begin{bmatrix} h_{comp,dis,is} - h_{comp,suc} & \dfrac{T_{surr} - T_{comp,dis,is}}{\dot{m}_{comp}} \end{bmatrix} \\ \boldsymbol{\theta}_{h_{comp,dis}} &= \begin{bmatrix} b \\ UA \end{bmatrix} \end{aligned} \tag{3.8b}$$

$$\begin{aligned}
\Gamma_{\dot{m}_{comp}} &= \dot{m}_{comp} \\
\varphi_{\dot{m}_{comp}} &= \left[\; -\frac{N}{v_{comp,suc}} \left(\left(\frac{P_{comp,dis}}{P_{comp,suc}} \right)^{\frac{cv,suc,g}{cp,suc,g}} - 1 \right) \qquad \frac{N}{v_{comp,suc}} \; \right] \\
\theta_{\dot{m}_{comp}} &= \left[\begin{array}{c} c \\ S_t \end{array} \right]
\end{aligned} \tag{3.8c}$$

As indicated in Equation (3.9), the specific values of the parameters $\hat{\theta}$ are calculated by minimizing the quadratic norm of the residue vector ξ, where $\Gamma \in \mathbb{R}^{2Z\times 1}$ and $\varphi \in \mathbb{R}^{2Z\times 4}$, being Z the total number of experimental data. Note that φ^{+} refers to the pseudoinverse of matrix φ.

$$\hat{\theta} = arg\min_{\theta} ||\xi||^2 \rightarrow \hat{\theta} = \varphi^{+} \cdot \Gamma \tag{3.9}$$

The parameters obtained are shown in Table 3.9 for both compressors, while the mean value and RMS of refrigerant mass flow and discharge enthalpy relative errors are gathered in Table 3.10. Both relative errors are calculated in this case using Equations (3.10) and (3.11), whereas the RMS is again calculated using Equation (3.5).

$$RE_{\dot{m}_{comp}} = \frac{|\, \dot{m}_{comp,predict} - \dot{m}_{comp,meas} \,|}{\dot{m}_{comp,meas}} \tag{3.10}$$

$$RE_{h_{comp,dis}} = \frac{|\, h_{comp,dis,predict} - h_{comp,dis,meas} \,|}{h_{comp,dis,meas}} \tag{3.11}$$

Table 3.9 Estimated values of the compressor parameters.

Compressor	$\widehat{b}$	$\widehat{c}/10^{-5}$ [m^3]	$\widehat{S_t}/10^{-5}$ [m^3]	$\widehat{UA}$ [W K^{-1}]
Main	1.398	-3.35	0	1.3906
Booster	1.887	54.16	38.54	2.1513

Table 3.10 Mean value and RMS of relative errors concerning the refrigerant mass flow and the discharge specific enthalpy of the compressors.

Compressor	Output variable	$\overline{RE}$ [%]	RMS [%]
Main	Refrigerant mass flow	3.01	3.71
	Discharge specific enthalpy	0.64	0.77
Booster	Refrigerant mass flow	12.78	14.50
	Discharge specific enthalpy	0.64	0.92

Note that the parameter S_t of the main compressor is zero; the reason is that the dependence of the refrigerant mass flow on N is very small, thus the identification method produces a negligible value for this parameter. This causes the identified parameter c to be negative for the model to generate a positive value of $\dot{m}_{comp}$. This issue does not appear when identifying the booster compressor, where all dependences of $\dot{m}_{comp}$ are significant.

3.2.3 Evaporators

Both evaporators are identified following a similar procedure, since they are both brazed-plate heat exchangers, namely their internal configurations are the same. As stated in Chapter 2, the MB approach is applied to model the refrigerant behaviour along the evaporator. Therefore, it is divided into two variable-length zones, where the refrigerant is two-phase fluid and superheated vapour, respectively.

It has been shown in Chapter 2 that system dynamics of a heat exchanger are mainly affected by refrigerant thermodynamic properties and geometric parameters, such as the internal volume, which is usually known. However, system statics depend strongly on thermal powers $\dot{Q}_{e,tp}$ and $\dot{Q}_{e,sh}$, whose calculation is determined by the specific configuration of the heat exchanger and heat transfer at both zones. Therefore, since the heat transfer coefficients have influence especially on system statics, the heat exchanger identification is performed in steady state.

As commented in Chapter 2, the steady-state model of the evaporator depends on its specific configuration. In this case, both evaporators are brazed-plate counter-current heat exchangers. The equations which detail heat transfer at the evaporator were in depth analysed in Chapter 2, Subsection 2.1.3, but they are included here in Equation Sets (3.12) – (3.14) to improve the comprehensibility of the identification procedure. Then, heat transfer at the superheated vapour zone is determined by Equation Set (3.12), while the equations which detail heat transfer at the two-phase zone are shown in Equation Set (3.13). Eventually, Equation Set (3.14) shows how to calculate the refrigerant properties at the evaporator outlet.

$$
\begin{aligned}
\dot{Q}_{e,sh} &= \varepsilon_{e,sh}(\dot{m}c_p)_{min}(T_{e,sec,in} - T_e) \\
C_{e,sh} &= \frac{(\dot{m}c_p)_{min}}{(\dot{m}c_p)_{max}} \\
NTU_{e,sh} &= \frac{UA_{e,sh}}{(\dot{m}c_p)_{min}} \\
UA_{e,sh} &= \alpha_{e,sh}\,(1-\zeta_{e,tp})\,A_{e,trnsf}\,L_e \\
\varepsilon_{e,sh} &= g_{he}(NTU_{e,sh}, C_{e,sh}) \\
\dot{Q}_{e,sh} &= \dot{m}_e(h_{e,out} - h_{e,g}) \\
T_{e,sec,mid} &= T_{e,sec,in} - \frac{\dot{Q}_{e,sh}}{\dot{m}_{e,sec}\,c_{p,e,sec}}
\end{aligned}
\tag{3.12}
$$

$$
\begin{aligned}
\dot{Q}_{e,tp} &= \varepsilon_{e,tp}(\dot{m}c_p)_{min}(T_{e,sec,mid} - T_e) \\
C_{e,tp} &= \frac{(\dot{m}c_p)_{min}}{(\dot{m}c_p)_{max}} = \{phase\ change\} = 0 \\
NTU_{e,tp} &= \frac{UA_{e,tp}}{(\dot{m}c_p)_{min}} \\
UA_{e,tp} &= \alpha_{e,tp}\ \zeta_{e,tp}\ A_{e,trnsf}\ L_e \\
\varepsilon_{e,tp} &= g_{he}(NTU_{e,tp}, C_{e,tp}) \\
\dot{Q}_{e,tp} &= \dot{m}_e(h_{e,g} - h_{e,in}) \\
T_{e,sec,out} &= T_{e,sec,mid} - \frac{\dot{Q}_{e,tp}}{\dot{m}_{e,sec}\ c_{p,e,sec}}
\end{aligned}
\tag{3.13}
$$

$$
T_{e,out} = T(P_e, h_{e,out}) \qquad T_{SH} = T_{e,out} - T_e \tag{3.14}
$$

The identification objective is to estimate the overall heat transfer coefficients $\alpha_{e,tp}$ and $\alpha_{e,sh}$. This poses some problems, since to calculate these coefficients from measured experimental data it is necessary to know how long the corresponding zones are, and this state variable $\zeta_{e,tp}$ is inaccessible, because only measurements of both refrigerant and secondary flux external variables can be obtained.

It is known that heat transfer at phase change is more effective than for single-phase fluid [70, 71], thus $\alpha_{e,tp}$ is expected to be higher than $\alpha_{e,sh}$. Nevertheless, since both coefficients are considered to be global, other thermal resistances which are condensed in such coefficients should be also considered. Firstly, there is a conduction thermal resistance through the heat exchanger itself at both zones. Secondly, there also exists a convective thermal resistance due to heat transfer between the heat exchanger and the secondary flux. An electric analogy of heat transfer at the evaporator is represented in Figure 3.9.

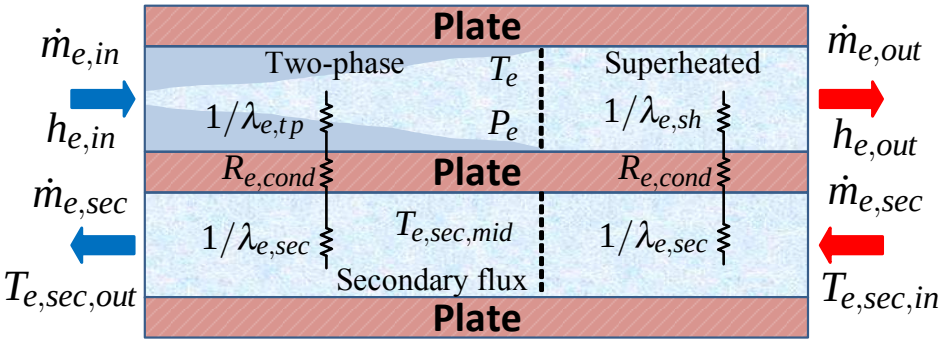

Figure 3.9 Electric analogy of heat transfer at the evaporator.

Superheated vapour zone

As stated in Equation Set (3.12), energy balance in steady state at the superheated vapour zone involves that $\dot{Q}_{e,sh} = \dot{m}_e\ (h_{e,out} - h_{e,g})$. The pressure P_e and the outlet temperature $T_{e,out}$ are measured, whereas $\dot{m}_e$ is estimated applying the global energy balance indicated in Equation (3.3).

Once calculated $\dot{Q}_{e,sh}$, Equation (3.15) shows how to estimate the efficiency at the superheated vapour zone $\varepsilon_{e,sh}$ from available data.

$$\varepsilon_{e,sh} = \frac{\dot{Q}_{e,sh}}{(\dot{m}c_p)_{min}(T_{e,sec,in} - T_e)} \tag{3.15}$$

If the heat-exchanger specific curve $\varepsilon = g_{he}(NTU,C)$ is inversely applied, the values of $NTU_{e,sh}$ and then $UA_{e,sh}$ can be calculated, which allows to achieve an experimental relationship between $\alpha_{e,sh}$ and $\zeta_{e,tp}$. The latter is indicated in Equation (3.16) and depicted in Figure 3.10. Although many steady-state points are considered for identification, only one representative curve corresponding to a single steady-state experimental point is shown in Figure 3.10, since its purpose is only to describe qualitatively the relationship between $\alpha_{e,sh}$ and $\zeta_{e,tp}$. For the sake of brevity, only figures related to Evaporator 1 are henceforth shown, since those corresponding to Evaporator 2 are qualitatively equivalent due to the same reason given above.

$$\alpha_{e,sh} = \frac{UA_{e,sh}}{A_{e,trnsf}L_e}\ \frac{1}{\zeta_{e,sh}} = \frac{UA_{e,sh}}{A_{e,trnsf}L_e}\ \frac{1}{1-\zeta_{e,tp}} \tag{3.16}$$

As seen in Figure 3.10, the greater $\zeta_{e,tp}$ is, the greater $\alpha_{e,sh}$ is, since the superheated vapour zone is smaller and the overall coefficient must be as high as necessary to effectively transfer the calculated thermal power $\dot{Q}_{e,sh}$.

Two-phase zone

Energy balance at the two-phase zone implies that $\dot{Q}_{e,tp} = \dot{m}_e\ (h_{e,g} - h_{e,in})$. Considering isenthalpic expansion at the corresponding valve, $h_{e,in} = h_{c,out}$ can be measured, thus the value of $\dot{Q}_{e,tp}$ is obtained.

The efficiency at the two-phase zone $\varepsilon_{e,tp}$ can be calculated as indicated in Equation (3.17), where $T_{e,sec,mid}$ is previously calculated applying secondary flux energy balance at the superheated vapour zone.

$$\begin{aligned} T_{e,sec,mid} &= T_{e,sec,in} - \frac{\dot{Q}_{e,sh}}{\dot{m}_{e,sec}\ c_{p,e,sec}} \\ \varepsilon_{e,tp} &= \frac{\dot{Q}_{e,tp}}{(\dot{m}c_p)_{min}(T_{e,sec,mid} - T_e)} \end{aligned} \tag{3.17}$$

Once again applying inversely the curve $\varepsilon = g_{he}(NTU,C)$, the values of $NTU_{e,tp}$ and $UA_{e,tp}$ can be computed. The experimental relationship between $\alpha_{e,tp}$ and $\zeta_{e,tp}$ shown

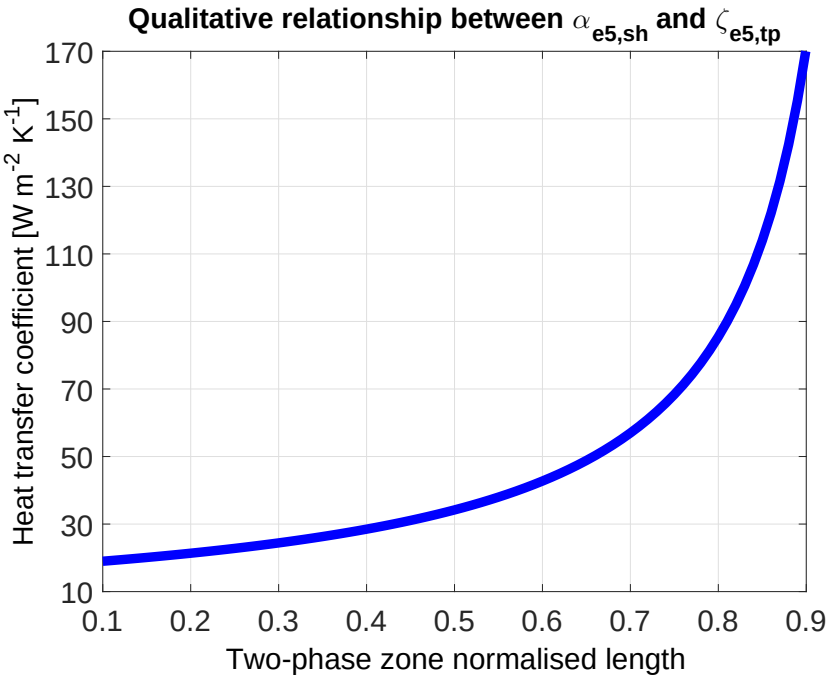

Figure 3.10 Qualitative relationship between $\alpha_{e,sh}$ and $\zeta_{e,tp}$ at Evaporator 1 (at 5 °C).

in Equation (3.18) is achieved, which is also represented in Figure 3.11. Once again the purpose of this figure is only to show qualitatively the relationship between $\alpha_{e,tp}$ and $\zeta_{e,tp}$.

$$\alpha_{e,tp} = \frac{UA_{e,tp}}{A_{e,trnsf}L_e}\frac{1}{\zeta_{e,tp}} \tag{3.18}$$

As expected, if the two-phase zone is greater, $\alpha_{e,tp}$ must be smaller to effectively transfer the measured thermal power $\dot{Q}_{e,tp}$, as indicated in Figure 3.11.

Hypothesis between $\alpha_{e,sh}$ and $\alpha_{e,tp}$

Combining Equations (3.16) and (3.18), the ratio between $\alpha_{e,tp}$ and $\alpha_{e,sh}$ is a function of $\zeta_{e,tp}$, for each experimental point. This ratio is represented in Figure 3.12 for a representative experimental point as depicted in Figures 3.10 and 3.11. The values close to limits ($\zeta_{e,tp} = 1$ and $\zeta_{e,tp} = 0$) are not represented because it would entail considering no superheated vapour zone and no two-phase zone, respectively.

As previously stated and represented by means of an electric analogy in Figure 3.9, the overall heat transfer coefficients $\alpha_{e,tp}$ and $\alpha_{e,sh}$ must be calculated considering a serial

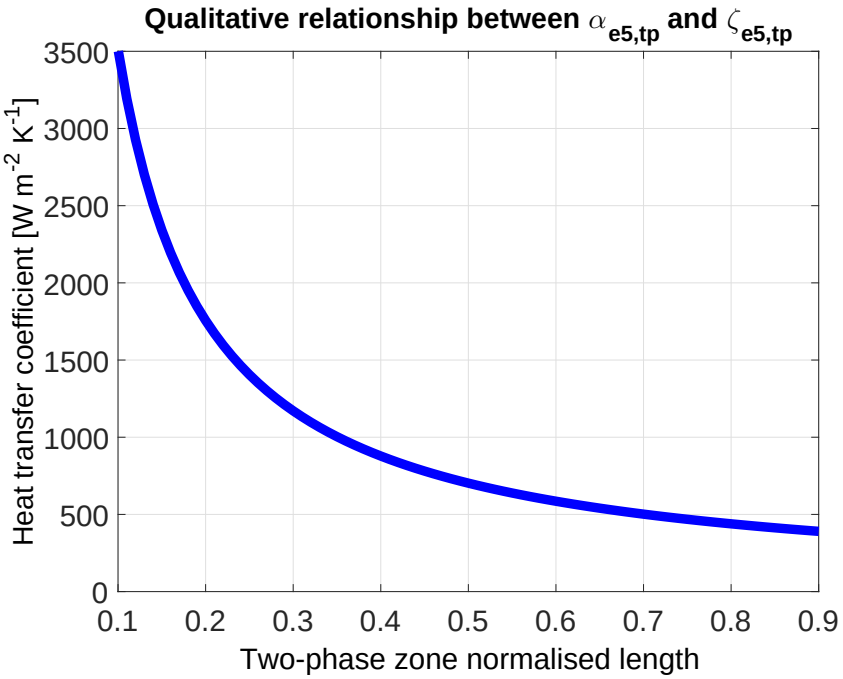

Figure 3.11 Qualitative relationship between $\alpha_{e,tp}$ and $\zeta_{e,tp}$ at Evaporator 1 (at 5 °C).

combination of all thermal resistances, as shown in Equation Set (3.19).

$$\begin{aligned} \frac{1}{\alpha_{e,tp}} &= \frac{1}{\lambda_{e,tp}} + R_{e,cond} + \frac{1}{\lambda_{e,sec}} \\ \frac{1}{\alpha_{e,sh}} &= \frac{1}{\lambda_{e,sh}} + R_{e,cond} + \frac{1}{\lambda_{e,sec}} \end{aligned} \tag{3.19}$$

Reference values or at least orders of magnitude of convective heat transfer coefficients in the literature [70] are collected in Table 3.11, as well as the conduction thermal resistance, which has been estimated considering the thickness and conductivity of the plate material.

From these reference data on, the estimated ratio between $\alpha_{e,tp}$ and $\alpha_{e,sh}$ is in the order of 10. Considering this value and using Figure 3.12, a probable range for the length of the two-phase zone $\zeta_{e,tp}$ can be obtained. Ranges of $\zeta_{e5,tp} \in [0.58, 0.7]$ and $\zeta_{e20,tp} \in [0.81, 0.93]$ are achieved.

Considering such plausible ranges, it is possible to calculate average values of the overall heat transfer coefficients $\alpha_{e,sh}$ and $\alpha_{e,tp}$ using experimental data such as those depicted in Figures 3.10 and 3.11. The average values and standard deviations of all coefficients are gathered in Table 3.12, considering both evaporators.

Note that the range for $\zeta_{e20,tp}$ causes the length of the superheated vapour zone $\zeta_{e20,sh}$ to be small. It causes the identification of $\alpha_{e20,sh}$ to be more difficult and numerically sensitive than those of $\alpha_{e5,tp}$ and $\alpha_{e5,sh}$: that is why the standard deviation of $\alpha_{e20,sh}$ is

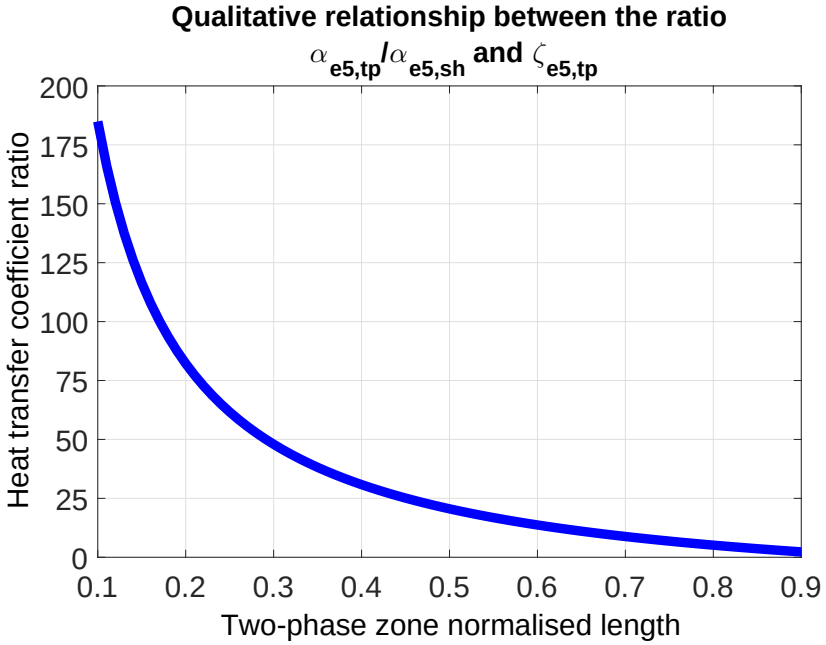

Figure 3.12 Qualitative relationship between the ratio $\alpha_{e,tp}/\alpha_{e,sh}$ and $\zeta_{e,tp}$ at Evaporator 1 (at 5 °C).

Table 3.11 Orders of magnitude of the thermal resistances involved in heat transfer at the evaporator.

Heat transfer coefficients and thermal resistances	**Two-phase (tp)**	**Superheated vapour (sh)**
λ_e [W m^{-2} K^{-1}]	$\sim 10^5$	$\sim 5 \cdot 10^1$
$R_{e,cond}$ [m^2 K W^{-1}]	$2.05 \cdot 10^{-6}$	
$\lambda_{e,sec}$ [W m^{-2} K^{-1}]	$\sim 5 \cdot 10^2$	
α_e [W m^{-2} K^{-1}]	~ 499	~ 45.4

much greater than the others shown in Table 3.12. The main reason is the asymptotic feature of the relationship between $\alpha_{e,sh}$ and $\zeta_{e,tp}$, when the latter tends to a value close to one, as shown in Figure 3.10.

Furthermore, the highly nonlinear features of the refrigeration system are known to cause the coefficients to vary for different operating points. Indeed, correlations usually produce different values for heat transfer coefficients when the flow conditions vary and specially when the temperature difference between the refrigerant and the secondary flux

Table 3.12 Identified overall heat transfer coefficients at both evaporators.

Evaporator	Heat transfer coefficient	Mean value [W m^{-2} K^{-1}]	Standard deviation [W m^{-2} K^{-1}]
Evaporator 1	$\widehat{\alpha}_{e5,tp}$	520.5	40.11
	$\widehat{\alpha}_{e5,sh}$	51.9	8.85
Evaporator 2	$\widehat{\alpha}_{e20,tp}$	144.8	13.8
	$\widehat{\alpha}_{e20,sh}$	14.87	7.26

is modified. However, the identification methodology has been applied for a wide (as wide as possible considering the features of the experimental facility concerning the component selection and the performance range of the manipulated variables) set of steady-state operating points. It causes the standard deviations of the heat transfer coefficients to be greater than wished. If a more accurate estimation of the heat transfer coefficients is desired, considering diverse values for a range of operating conditions, the identification method could be applied online using filtered measurable variables, such as the degree of superheating, pressures, and inlet and outlet temperatures of the heat exchangers, to estimate the working conditions and calculate the corresponding heat transfer coefficients, in addition to an estimation of the heat exchanging zone lengths.

3.2.4 Condenser

Similarly, the MB approach is also applied when modelling the condenser. In this case the condenser length is divided into three zones, since three refrigerant states may simultaneously exist along the condenser: superheated vapour, two-phase fluid, and subcooled liquid.

It has been studied in Chapter 2 that the system dynamics of a heat exchanger depend only on refrigerant thermodynamic properties and the heat exchanger internal volume, which can be easily calculated or measured. However, the partial thermal powers $\dot{Q}_{c,sh}$, $\dot{Q}_{c,tp}$, and $\dot{Q}_{c,sc}$, related to the three possible zones, define system statics, and their calculation does depend to a great extent on the specific configuration of the heat exchanger and its ability to transfer heat in all zones. Thus, a steady-state model of the condenser is also considered for identification purposes.

As commented in Chapter 2, the identification procedure is focused on the air-cooled condenser, which has a cross-flow tube configuration. The equations which detail heat transfer at the condenser were in depth analysed in Chapter 2, Subsection 2.1.4, but they are included here in Equation Sets (3.20) – (3.24) to improve the comprehensibility of the identification procedure. Note that only condenser *mode* 1 is considered and pressure drop along the heat exchanger is also modelled, unlike the ideal model described in Subsection 2.1.4.

Then, Equation Set (3.20) describes heat transfer at the superheated vapour zone, Equation Set (3.21) does the same for the two-phase zone, and finally Equation Set (3.22) refers

to the subcooled liquid zone.

$$\begin{aligned}
\dot{Q}_{c,sh} &= \varepsilon_{c,sh}(\dot{m}c_p)_{min}(T_{c,in} - T_{c,sec,in}) \\
C_{c,sh} &= \frac{(\dot{m}c_p)_{min}}{(\dot{m}c_p)_{max}} \\
NTU_{c,sh} &= \frac{UA_{c,sh}}{(\dot{m}c_p)_{min}} \\
UA_{c,sh} &= \alpha_{c,sh}\ \zeta_{c,sh}\ A_{c,trnsf}\ L_c \\
\varepsilon_{c,sh} &= g_{he}(NTU_{c,sh}, C_{c,sh}) \\
\dot{Q}_{c,sh} &= \dot{m}_c(h_{c,in} - h_{c,g}) \\
P_{c,g} &= P_{c,in} - \zeta_{c,sh}\ k_{drop}\ \dot{m}_c^2
\end{aligned} \tag{3.20}$$

$$\begin{aligned}
\dot{Q}_{c,tp} &= \varepsilon_{c,tp}(\dot{m}c_p)_{min}(T_{c,g} - T_{c,sec,in}) \\
C_{c,tp} &= \frac{(\dot{m}c_p)_{min}}{(\dot{m}c_p)_{max}} = \{phase\ change\} = 0 \\
NTU_{c,tp} &= \frac{UA_{c,tp}}{(\dot{m}c_p)_{min}} \\
UA_{c,tp} &= \alpha_{c,tp}\ \zeta_{c,tp}\ A_{c,trnsf}\ L_c \\
\varepsilon_{c,tp} &= g_{he}(NTU_{c,tp}, C_{c,tp}) \\
\dot{Q}_{c,tp} &= \dot{m}_c(h_{c,g} - h_{c,f}) \\
P_{c,f} &= P_{c,g} - \zeta_{c,tp}\ k_{drop}\ \dot{m}_c^2
\end{aligned} \tag{3.21}$$

$$\begin{aligned}
\dot{Q}_{c,sc} &= \varepsilon_{c,sc}(\dot{m}c_p)_{min}(T_{c,f} - T_{c,sec,in}) \\
C_{c,sc} &= \frac{(\dot{m}c_p)_{min}}{(\dot{m}c_p)_{max}} \\
NTU_{c,sc} &= \frac{UA_{c,sc}}{(\dot{m}c_p)_{min}} \\
UA_{c,sc} &= \alpha_{c,sc}\ \zeta_{c,sc}\ A_{c,trnsf}\ L_c \\
\varepsilon_{c,sc} &= g_{he}(NTU_{c,sc}, C_{c,sc}) \\
\dot{Q}_{c,sc} &= \dot{m}_c(h_{c,f} - h_{c,out})
\end{aligned} \tag{3.22}$$

Eventually, Equation Set (3.23) indicates how to calculate the refrigerant state at the condenser outlet, while in Equation Set (3.24) the secondary flux outlet temperature model

is detailed.

$$\begin{aligned} P_{c,out} &= P_{c,f} - \zeta_{c,sc}\, k_{drop}\, \dot{m}_c^2 \\ T_{c,out} &= T(P_{c,out}, h_{c,out}) \\ T_{c,sat,out} &= T(P_{c,out}, q=0) \\ T_{SC} &= T_{c,sat,out} - T_{c,out} \end{aligned} \tag{3.23}$$

$$\begin{aligned} T_{c,sec,sh,out} &= T_{c,sec,in} + \frac{\dot{Q}_{c,sh}}{\dot{m}_{c,sec}\ \zeta_{c,sh}\ c_{p,c,sec}} \\ T_{c,sec,tp,out} &= T_{c,sec,in} + \frac{\dot{Q}_{c,tp}}{\dot{m}_{c,sec}\ \zeta_{c,tp}\ c_{p,c,sec}} \\ T_{c,sec,sc,out} &= T_{c,sec,in} + \frac{\dot{Q}_{c,sc}}{\dot{m}_{c,sec}\ \zeta_{c,sc}\ c_{p,c,sec}} \\ T_{c,sec,out} &= \zeta_{c,sh}\, T_{c,sec,sh,out} + \zeta_{c,tp}\, T_{c,sec,tp,out} + \zeta_{c,sc}\, T_{c,sec,sc,out} \end{aligned} \tag{3.24}$$

Once again the identification objective is to obtain average estimations of all overall heat transfer coefficients $\alpha_{c,sh}$, $\alpha_{c,tp}$, and $\alpha_{c,sc}$. In this case, to calculate the heat transfer coefficients it is necessary to know the corresponding zone lengths, namely $\zeta_{c,sh}$ and $\zeta_{c,tp}$, but their measurements are not available from experimental data.

Similarly, according to the dominance of heat transfer when the fluid is two-phase, it is guessed that $\alpha_{c,tp}$ is higher than $\alpha_{c,sh}$ and $\alpha_{c,sc}$ [70, 71]. Nevertheless, there is no previous assumption of the relationship between single-phase heat transfer coefficients. Moreover, just like at the evaporators, other thermal resistances must be taken into account, since the coefficients to be estimated are global according to the proposed formulation. A diagram which illustrates this issue by applying an electric analogy is shown in Figure 3.13.

Superheated vapour zone

As indicated in Equation Set (3.20), energy balance in steady state at the superheated vapour zone involves that $\dot{Q}_{c,sh} = \dot{m}_c\ (h_{c,in} - h_{c,g})$. The inlet pressure $P_{c,in}$ and the inlet temperature $T_{c,in}$ are measured, whereas the refrigerant mass flow $\dot{m}_c$ is estimated applying the global energy balance indicated in Equation (3.3). Nevertheless, the refrigerant pressure distribution cannot be calculated without zone length estimations, as expressed in Equation Set (3.25), where k_{drop} concerns the pressure drop factor along the whole condenser.

$$\begin{aligned} P_{c,g} &= P_{c,in} - \zeta_{c,sh}\, k_{drop}\, \dot{m}_c^2 \\ P_{c,f} &= P_{c,g} - \zeta_{c,tp}\, k_{drop}\, \dot{m}_c^2 \\ P_{c,out} &= P_{c,f} - \zeta_{c,sc}\, k_{drop}\, \dot{m}_c^2 \end{aligned} \tag{3.25}$$

Linear modelling of pressure drop involves that partial pressure drops at each zone depend on zone lengths. Therefore, $P_{c,g}$ and, as a result, $h_{c,g}$ and $\dot{Q}_{c,sh}$, cannot be computed without supposing $\zeta_{c,sh}$.

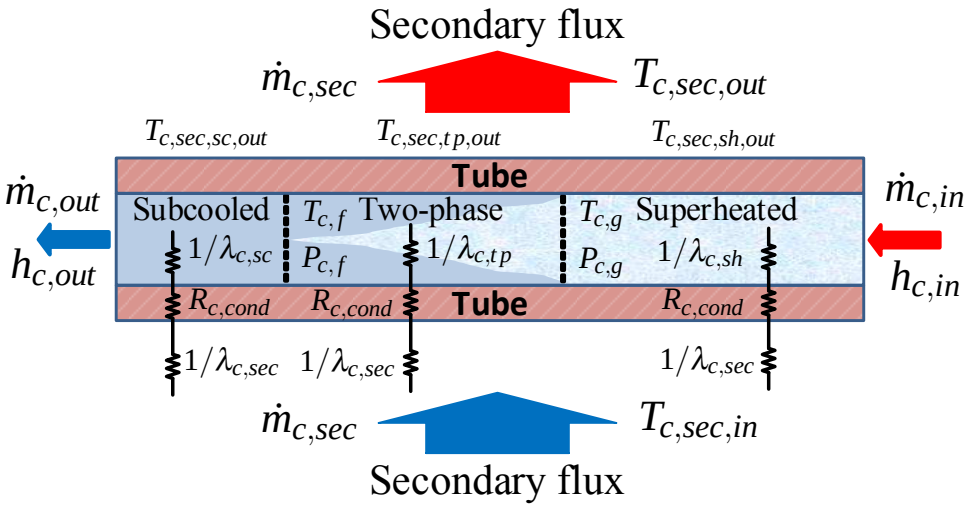

Figure 3.13 Electric analogy of heat transfer at the condenser.

For a certain value of $\zeta_{c,sh}$, according to Equation Set (3.20), the efficiency at the superheated vapour zone $\varepsilon_{c,sh}$ is computed from the calculated value of $\dot{Q}_{c,sh}$ as shown in Equation (3.26).

$$\varepsilon_{c,sh} = \frac{\dot{Q}_{c,sh}}{(\dot{m}c_p)_{min}(T_{c,in} - T_{c,sec,in})} \tag{3.26}$$

To calculate $(\dot{m}c_p)_{min}$ it is also necessary to suppose $\zeta_{c,sh}$, since the secondary flux mass flow $\dot{m}_{c,sec}$ is supposed to be distributed among the zones according to their lengths. Just like at the evaporator, assuming that the heat-exchanger specific curve $\varepsilon = g_{he}(NTU,C)$ is inversely applied, the values of $NTU_{c,sh}$ and then $UA_{c,sh}$ can be calculated. An experimental relationship between $\alpha_{c,sh}$ and $\zeta_{c,sh}$ is obtained, which is indicated in Equation (3.27) and depicted in Figure 3.14. Many steady-state points are considered for identification, but only one curve corresponding to a single representative steady-state experimental point is shown in Figure 3.14 in order to represent qualitatively the relationship between $\alpha_{c,sh}$ and $\zeta_{c,sh}$.

$$\alpha_{c,sh} = \frac{UA_{c,sh}(\zeta_{c,sh})}{A_{c,trnsf}L_c}\frac{1}{\zeta_{c,sh}} \tag{3.27}$$

The dependence of $UA_{c,sh}$ on $\zeta_{c,sh}$ is explicitly indicated in Equation (3.27). As expected, greater values of $\zeta_{c,sh}$ involve smaller values of $\alpha_{c,sh}$, since the superheated vapour zone is longer.

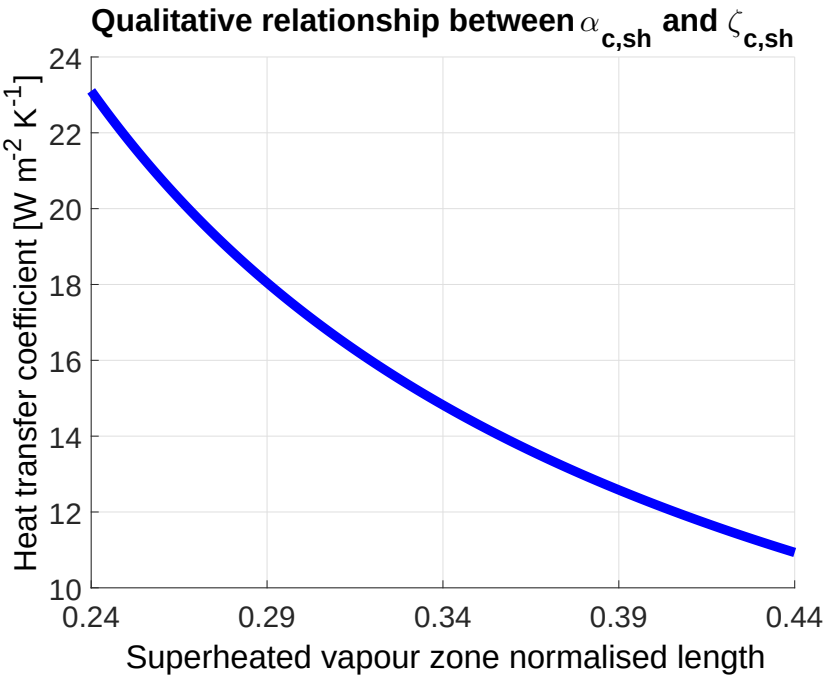

Figure 3.14 Qualitative relationship between $\alpha_{c,sh}$ and $\zeta_{c,sh}$.

Two-phase zone

Energy balance at the two-phase zone involves that $\dot{Q}_{c,tp} = \dot{m}_c\,(h_{c,g} - h_{c,f})$. Once estimated $\dot{m}_c$, pressures $P_{c,f}$ and $P_{c,g}$ allow to completely determine $\dot{Q}_{c,tp}$. As indicated in Equation Set (3.25), $P_{c,f}$ depends explicitly on $\zeta_{c,tp}$, whereas it is also influenced by $\zeta_{c,sh}$ through $P_{c,g}$. Therefore, estimations of both $\zeta_{c,sh}$ and $\zeta_{c,tp}$ are required to compute $\dot{Q}_{c,tp}$.

Given reasonable values of $\zeta_{c,sh}$ and $\zeta_{c,tp}$, the efficiency at the two-phase zone $\varepsilon_{c,tp}$ can be calculated as shown in Equation (3.28), according to Equation Set (3.21).

$$\varepsilon_{c,tp} = \frac{\dot{Q}_{c,tp}}{(\dot{m}c_p)_{min}\left(T_{c,g} - T_{c,sec,in}\right)} \tag{3.28}$$

By applying the specific curve $\varepsilon = g_{he}(NTU,C)$ at the two-phase zone, the values of $NTU_{c,tp}$ and $UA_{c,tp}$ can be calculated. The experimental relationship between $\alpha_{c,tp}$, $\zeta_{c,sh}$, and $\zeta_{c,tp}$ indicated in Equation (3.29) is obtained.

$$\alpha_{c,tp} = \frac{UA_{c,tp}(\zeta_{c,sh},\zeta_{c,tp})}{A_{c,trnsf}L_c}\,\frac{1}{\zeta_{c,tp}} \tag{3.29}$$

Figure 3.15 illustrates the double dependence of $\alpha_{c,tp}$. Once again, although many steady-state points are considered for identification, curves relative to a single experimental point are shown in Figure 3.15, since its purpose is only to represent qualitatively the relationship

between $\alpha_{c,tp}$, $\zeta_{c,tp}$, and $\zeta_{c,sh}$. On the one hand, in Figure 3.15(a) the experimental relationship between $\alpha_{c,tp}$ and $\zeta_{c,tp}$ is represented, for fixed $\zeta_{c,sh}$. The greater $\zeta_{c,tp}$ is, the smaller $\alpha_{c,tp}$ is, since the two-phase zone is longer. On the other hand, Figure 3.15(b) shows the experimental relationship between $\alpha_{c,tp}$ and $\zeta_{c,sh}$, for fixed $\zeta_{c,tp}$. This dependence is minor, since for fixed $\zeta_{c,tp}$ the calculation of $\alpha_{c,tp}$ is only affected by $\zeta_{c,sh}$ through pressure $P_{c,g}$. Supposing a certain $\zeta_{c,tp}$, if the superheated vapour zone is longer, it involves a greater pressure drop at this zone and thus $P_{c,g}$ is lower. As stated in Equation Set (3.21), the hottest point related to heat transfer at the two-phase zone is $T_{c,g}$, which is lower when $P_{c,g}$ decreases. It entails lower temperature difference between the refrigerant and the secondary flux, and that is the reason why $\alpha_{c,tp}$ is slightly greater in order to actually transfer $\dot{Q}_{c,tp}$.

Subcooled liquid zone

Energy balance at the subcooled liquid zone imposes that $\dot{Q}_{c,sc} = \dot{m}_c\,(h_{c,f} - h_{c,out})$. Despite measuring the outlet pressure $P_{c,out}$ and the outlet temperature $T_{c,out}$, and estimating $\dot{m}_c$, $\dot{Q}_{c,sc}$ cannot be calculated without estimations of $\zeta_{c,tp}$ and $\zeta_{c,sh}$, since $P_{c,f}$ depends on both zone lengths.

Supposing plausible values of $\zeta_{c,sh}$ and $\zeta_{c,tp}$, the efficiency at the subcooled liquid zone $\varepsilon_{c,sc}$ can be computed as shown in Equation (3.30), according to Equation Set (3.22).

$$\varepsilon_{c,sc} = \frac{\dot{Q}_{c,sc}}{(\dot{m}c_p)_{min}(T_{c,f} - T_{c,sec,in})} \tag{3.30}$$

By applying inversely the curve $\varepsilon = g_{he}(NTU,C)$, the values of $NTU_{c,sc}$ and then $UA_{c,sc}$ can be computed. The experimental relationship between $\alpha_{c,sc}$, $\zeta_{c,sh}$, and $\zeta_{c,tp}$ indicated in Equation (3.31) and represented in Figure 3.16 arises. Similarly, for the sake of clarity, only the curves related to a single experimental steady-state point are shown in Figure 3.16.

$$\alpha_{c,sc} = \frac{UA_{c,sc}(\zeta_{c,sh},\zeta_{c,tp})}{A_{c,trnsf}L_c}\,\frac{1}{\zeta_{c,sc}} = \frac{UA_{c,sc}(\zeta_{c,sh},\zeta_{c,tp})}{A_{c,trnsf}L_c}\,\frac{1}{1-\zeta_{c,sh}-\zeta_{c,tp}} \tag{3.31}$$

Firstly, in Figure 3.16(a) the experimental relationship between $\alpha_{c,sc}$ and $\zeta_{c,tp}$ is depicted, for fixed $\zeta_{c,sh}$. As expected, greater values of $\zeta_{c,tp}$ involves shorter subcooled liquid zone, which causes $\alpha_{c,sc}$ to be greater. Secondly, Figure 3.16(b) shows the experimental relationship between $\alpha_{c,sc}$ and $\zeta_{c,sh}$, for fixed $\zeta_{c,tp}$; the effect of $\zeta_{c,sh}$ on $\alpha_{c,sc}$ is shown to be similar. An asymptotic behaviour is observed, since when $\zeta_{c,sh}$ or $\zeta_{c,tp}$ increases, the subcooled liquid zone length $\zeta_{c,sc}$ tends ultimately to zero.

Hypothesis between $\alpha_{c,sh}$, $\alpha_{c,tp}$, and $\alpha_{c,sc}$

According to Equations (3.27) and (3.29), the ratio between $\alpha_{c,tp}$ and $\alpha_{c,sh}$ turns out to be a function of $\zeta_{c,tp}$ and $\zeta_{c,sh}$, as represented in Figure 3.17(a). Similarly, the ratio between $\alpha_{c,sh}$ and $\alpha_{c,sc}$ is a function of the same variables, as shown in Equations (3.27) and (3.31). This ratio is also shown in Figure 3.17(b). Note that the depicted surface refers to a single representative steady-state experimental point.

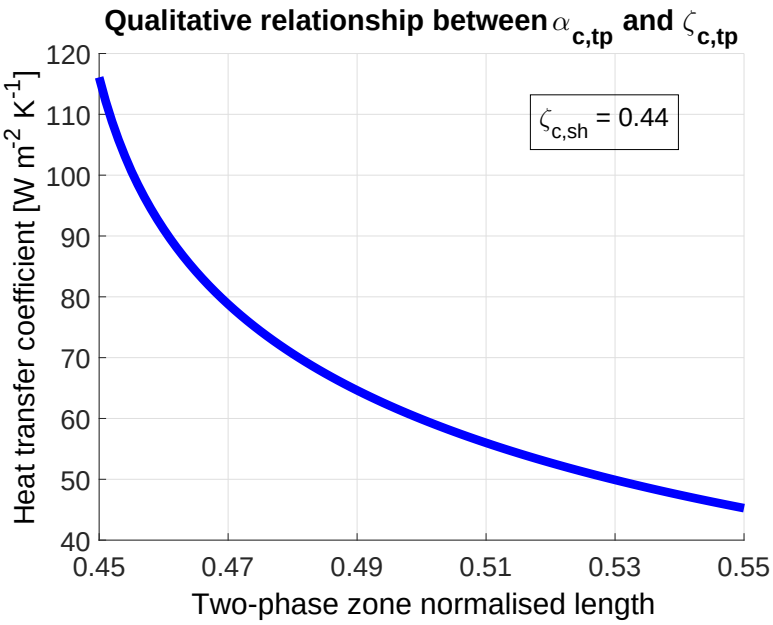

(a) Qualitative relationship between $\alpha_{c,tp}$ and $\zeta_{c,tp}$, for fixed $\zeta_{c,sh} = 0.44$

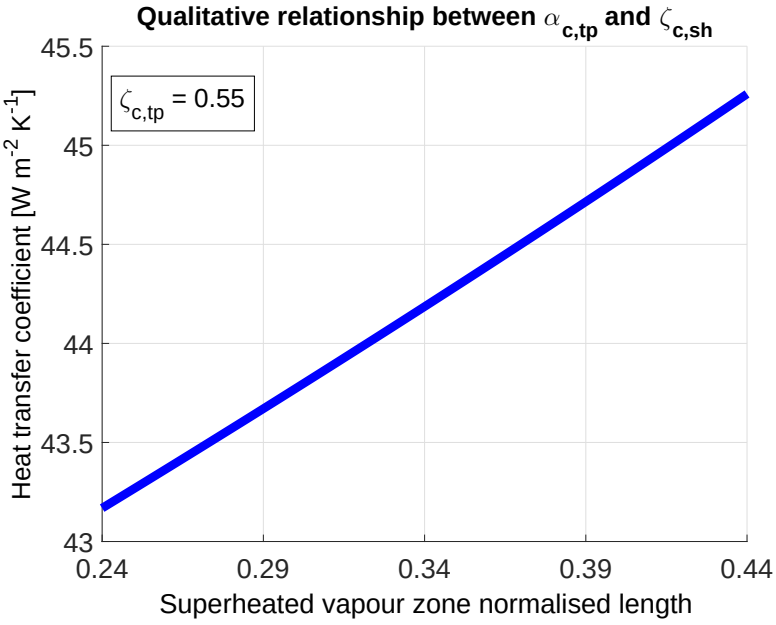

(b) Qualitative relationship between $\alpha_{c,tp}$ and $\zeta_{c,sh}$, for fixed $\zeta_{c,tp} = 0.55$

Figure 3.15 Qualitative relationship between $\alpha_{c,tp}$, $\zeta_{c,tp}$, and $\zeta_{c,sh}$.

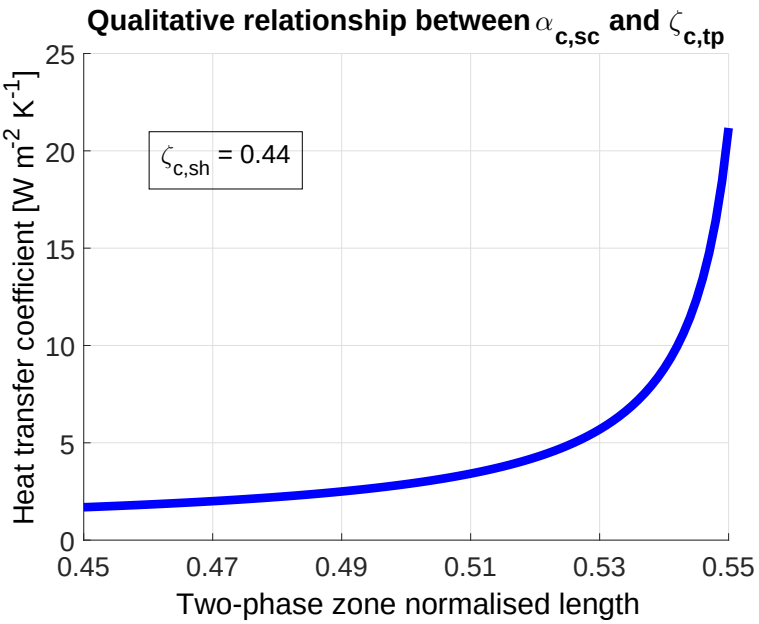

(a) Qualitative relationship between $\alpha_{c,sc}$ and $\zeta_{c,tp}$, for fixed $\zeta_{c,sh} = 0.44$

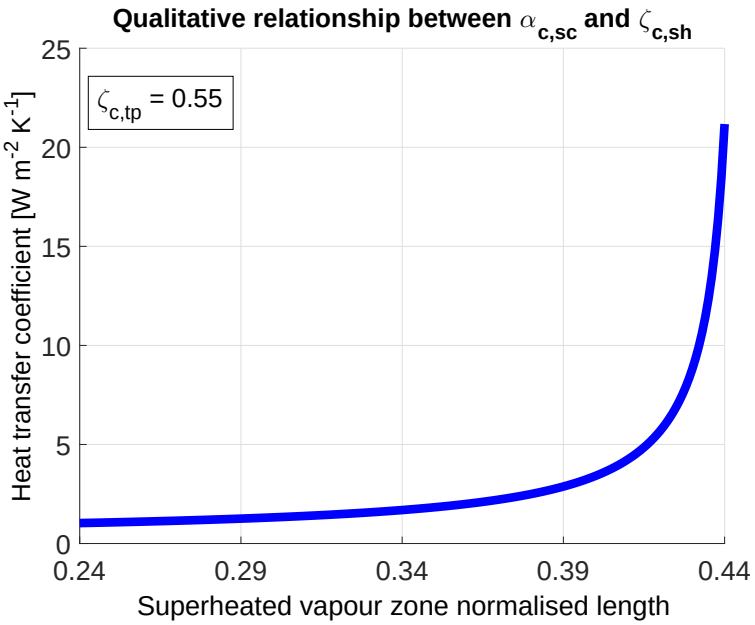

(b) Qualitative relationship between $\alpha_{c,sc}$ and $\zeta_{c,sh}$, for fixed $\zeta_{c,tp} = 0.55$

Figure 3.16 Qualitative relationship between $\alpha_{c,sc}$, $\zeta_{c,tp}$, and $\zeta_{c,sh}$.

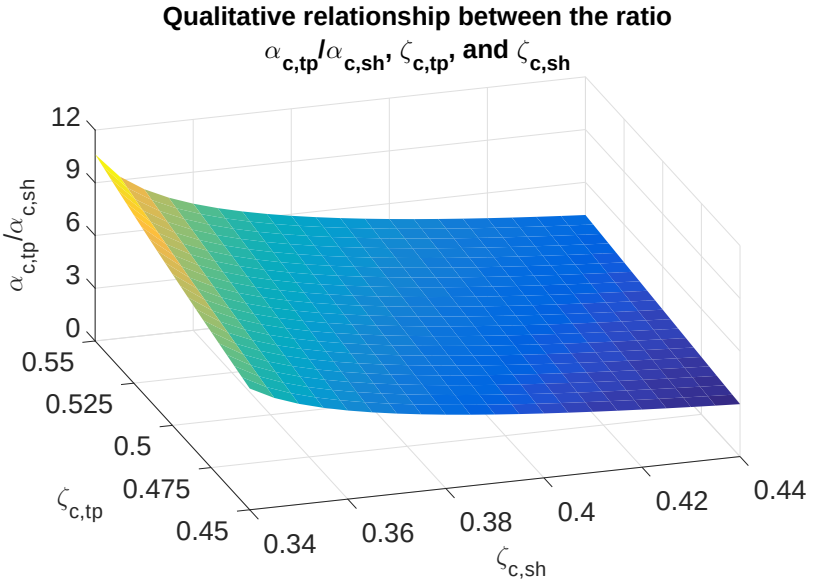

(a) Qualitative relationship between $\alpha_{c,tp}/\alpha_{c,sh}$, $\zeta_{c,tp}$, and $\zeta_{c,sh}$

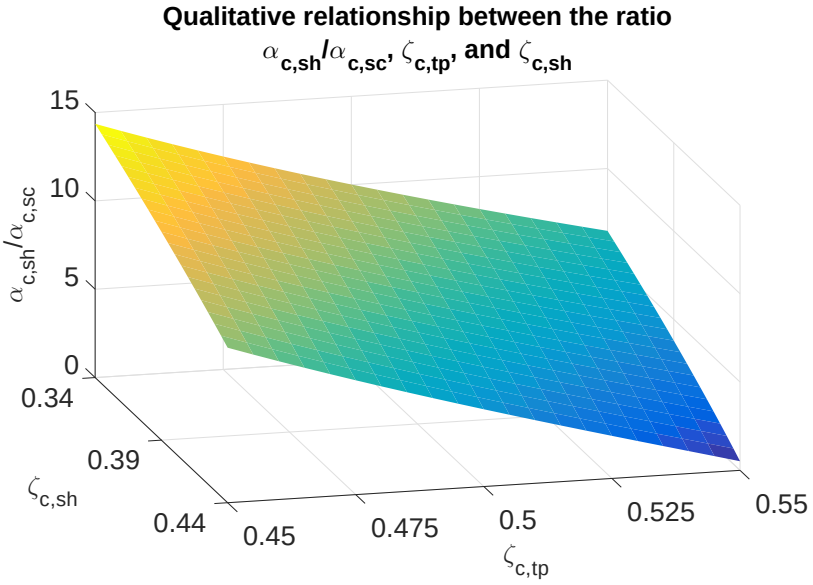

(b) Qualitative relationship between $\alpha_{c,sh}/\alpha_{c,sc}$, $\zeta_{c,tp}$, and $\zeta_{c,sh}$

Figure 3.17 Qualitative relationships between the ratios $\alpha_{c,tp}/\alpha_{c,sh}$ and $\alpha_{c,sh}/\alpha_{c,sc}$, and zone lengths $\zeta_{c,tp}$ and $\zeta_{c,sh}$.

According to Figure 3.17, the initial guess about dominance of $\alpha_{c,tp}$ over $\alpha_{c,sh}$ and $\alpha_{c,sc}$ is confirmed. Regarding single-phase heat transfer coefficients, the ratio between $\alpha_{c,sh}$ and $\alpha_{c,sc}$ shows to be dependent on the zone lengths. When $\zeta_{c,sc} = 1 - \zeta_{c,sh} - \zeta_{c,tp}$ gets close to zero, the ratio takes values less than one, while for greater $\zeta_{c,sc}$ the ratio reaches values up to 20. In Figure 3.18 a detailed view of Figure 3.17(b) for small values of $\zeta_{c,sc}$ is shown, where ratios $\alpha_{c,sh}/\alpha_{c,sc}$ below one can be observed.

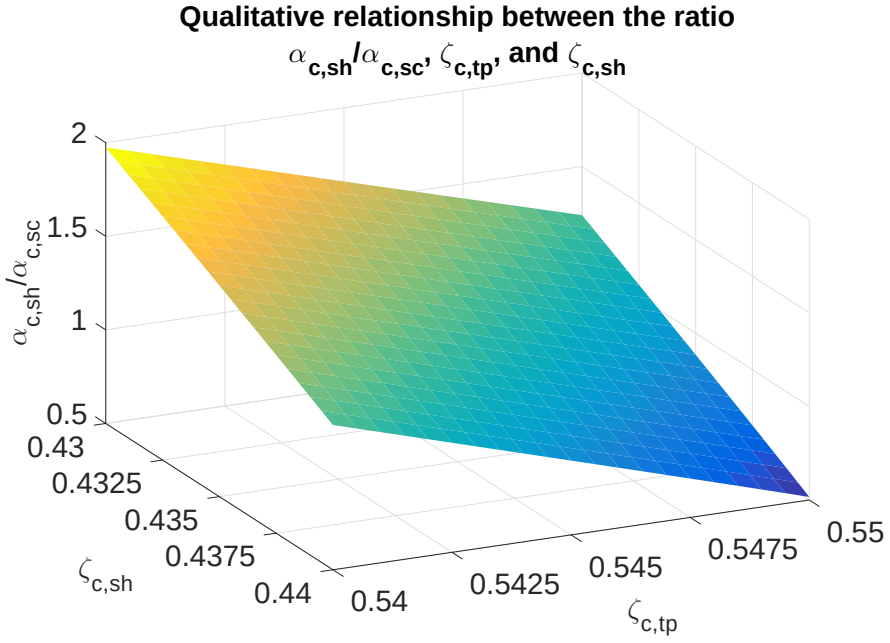

Figure 3.18 Detailed view of the qualitative relationship between the ratio $\alpha_{c,sh}/\alpha_{c,sc}$, $\zeta_{c,tp}$, and $\zeta_{c,sh}$, for small values of $\zeta_{c,sc}$.

Like at evaporators, the overall heat transfer coefficient at each condenser zone is the result of serial combination of all involved thermal resistances, as represented in Figure 3.13 and indicated in Equation Set (3.32), where the difference between internal and external heat transfer areas have been disregarded due to the small tube thickness.

$$\begin{aligned}
\frac{1}{\alpha_{c,sh}} &= \frac{1}{\lambda_{c,sh}} + R_{c,cond} + \frac{1}{\lambda_{c,sec}} \\
\frac{1}{\alpha_{c,tp}} &= \frac{1}{\lambda_{c,tp}} + R_{c,cond} + \frac{1}{\lambda_{c,sec}} \\
\frac{1}{\alpha_{c,sc}} &= \frac{1}{\lambda_{c,sc}} + R_{c,cond} + \frac{1}{\lambda_{c,sec}}
\end{aligned} \tag{3.32}$$

Reference values of convective heat transfer coefficients for the refrigerant (superheated

vapour, two-phase, and subcooled liquid zones) and secondary flux [70, 71] are stated in Table 3.13, along with the calculated conduction thermal resistance.

Table 3.13 Orders of magnitude of the thermal resistances involved in heat transfer at the condenser.

Heat transfer coefficients and thermal resistances	Superheated vapour (sh)	Two-phase fluid (tp)	Subcooled liquid (sc)
λ_c [W m^{-2} K^{-1}]	$\sim 5 \cdot 10^1$	$\sim 5 \cdot 10^5$	$\sim 1 \cdot 10^2$
$R_{c,cond}$ [m^2 K W^{-1}]		$5.26 \cdot 10^{-6}$	
$\lambda_{c,sec}$ [W m^{-2} K^{-1}]		$\sim 1.6 \cdot 10^2$	
α_c [W m^{-2} K^{-1}]	~ 38	~ 159	~ 61

From these reference data on, some practical ratios between $\alpha_{c,sh}$, $\alpha_{c,tp}$, and $\alpha_{c,sh}$ are calculated, giving rise to the values shown in Equation Set (3.33).

$$\frac{\alpha_{c,tp}}{\alpha_{c,sh}} = 4.2 \qquad \frac{\alpha_{c,sh}}{\alpha_{c,sc}} = 0.62 \tag{3.33}$$

Considering these reference ratios and turning to Figures 3.17 and 3.18 (given that the ratio between $\alpha_{c,sh}$ and $\alpha_{c,sc}$ is less than one), reasonable ranges for $\zeta_{c,sh}$ and $\zeta_{c,tp}$ are achievable: $\zeta_{c,sh} \in [0.43, 0.44]$ and $\zeta_{c,tp} \in [0.54, 0.55]$. Those ranges allow to obtain estimations of the overall heat transfer coefficients $\alpha_{c,sh}$, $\alpha_{c,tp}$, and $\alpha_{c,sc}$, using the curves corresponding to all steady-state experimental points similar to those represented in Figures 3.14 – 3.16. The average values and standard deviations of all identified coefficients are shown in Table 3.14.

Table 3.14 Identified overall heat transfer coefficients at the condenser.

Heat transfer coefficient	Mean value [W m^{-2} K^{-1}]	Standard deviation [W m^{-2} K^{-1}]
$\widehat{\alpha}_{c,sh}$	11.04	0.6
$\widehat{\alpha}_{c,tp}$	44.55	4.0
$\widehat{\alpha}_{c,sc}$	13.93	11.61

Note that the ranges for $\zeta_{c,sh}$ and $\zeta_{c,tp}$ cause the length of the subcooled liquid zone $\zeta_{c,sc}$ to be very small, less than 3%. It agrees with the experimental data, due to the low degree of subcooling achieved in all experiments, even zero in some cases. This is an intrinsic feature of the experimental facility, since the component selection and the performance range of the manipulated variables allow only to achieve cycles with very low degree

of subcooling. It causes the identification of $\alpha_{c,sc}$ to be more difficult and numerically sensitive than those of $\alpha_{c,sh}$ and $\alpha_{c,tp}$: that is why the standard deviation of $\alpha_{c,sc}$ is much greater than the others shown in Table 3.14. The main reason is the asymptotic feature of the relationship between $\alpha_{c,sc}$, $\zeta_{c,sh}$ and $\zeta_{c,tp}$, when those cause $\zeta_{c,sc}$ to achieve a value close to zero, as shown in Figure 3.16. However, since the expected length of the subcooled liquid zone is very low compared to the superheated vapour zone and the two-phase zone, some inaccuracy in the identified value of this heat transfer coefficient does not involve great divergence between the experimental and simulated values concerning the condenser outlet variables. In any case, the validity of the general methodology holds, since the deviation of the identified value of $\alpha_{c,sc}$ could be reduced if more experimental steady-state points with greater degree of subcooling were available, which would cause $\zeta_{c,sc}$ to achieve greater values and would avoid numerical sensitivity when calculating this heat transfer coefficient.

3.3 Validation

All elements of the experimental plant have been separately modelled, creating models for the refrigerant flow along the heat exchangers and for the compressors, expansion valves and secondary fluxes at the evaporators and condenser. However, global validation is performed, in order to get an overall assessment of accuracy achieved when identifying the model parameters. Therefore, combined validation of steady-state models of both evaporators, both electronic expansion valves, both compressors and the air-cooled condenser is intended.

It has been highlighted in Subsection 3.1.1 that the plant is designed to be fully configurable: it is possible in principle to control a two-compression-stage cycle with two refrigeration levels and a one-stage cycle with one or two refrigeration levels. Nevertheless, the component selection has been focused on the multi-load-demand configuration, therefore a cycle with only one compression stage and one evaporator could be studied, but the control range is very reduced due to the physical limits of the manipulated elements, specially the main compressor power. It makes very difficult to operate and achieve experimental results with this configuration. Therefore, global validation considering the one-stage, two-load-demand configuration and the two-stage, two-load-demand one is addressed.

3.3.1 One-compression-stage, two-load-demand configuration

This configuration was illustrated in Figure 1.4 and highlighted on the experimental plant layout in Figure 3.3. For the sake of clarity, the layout is replicated in Figure 3.19.

Note that the pressure upholding valve just holds the pressure differential between Evaporator 1 and Evaporator 2, since both chambers require diverse pressure levels, which involves different evaporation temperatures. The less restrictive it is, the less the pressure differential is between both evaporators, which implies that the temperature difference between the refrigerant and the secondary flux in Evaporator 1 is greater. On the experimental plant this is a manual valve, since the opening can be neither electronically operated nor adjusted online. The expansion through the pressure upholding valve is

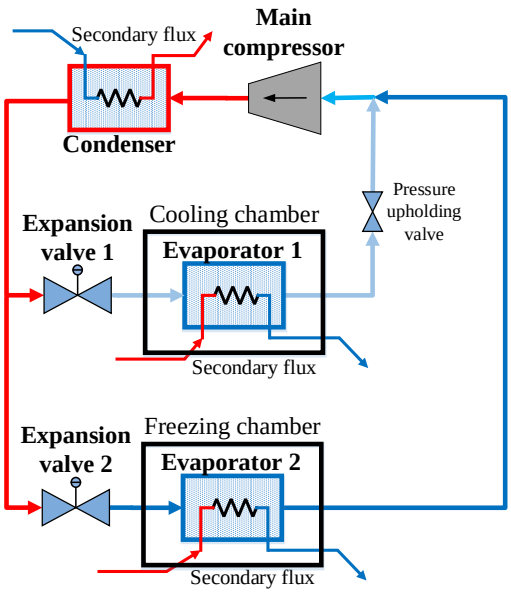

Figure 3.19 One-stage, two-load-demand refrigeration cycle.

assumed to be isenthalpic, whereas mass and energy balances are posed at the compressor intake, since at this point two refrigerant flows with different mass flows and specific enthalpies are mixed together: that circulating through the Evaporator 2 at -20 °C, and the other expanded through the pressure upholding valve. In Figure 3.20 an ideal P-h diagram of such a cycle is depicted (without considering the pressure drop at the condenser), along with the refrigerant-specific saturation curves, where the function of such valve is clarified.

In Figure 3.20 temperature levels of all secondary fluxes are also represented:

- *Freezing level*: represents the refrigerant saturation pressure at the inlet temperature of the secondary flux at Evaporator 2 (-20 °C).
- *Cooling level*: refers to the refrigerant saturation pressure at the inlet temperature of the secondary flux at Evaporator 1 (5 °C).
- *Ambient*: refers to the refrigerant saturation pressure at the inlet temperature of the condenser secondary flux, which matches ambient temperature when using the air-cooled condenser.

They have been included in the P-h diagram only to represent qualitatively the sign of the temperature difference between the refrigerant and the secondary flux at both heat exchangers.

Since all components have been identified in steady state, the global validation is carried out considering equilibrium points. The pressure upholding valve has been identified using

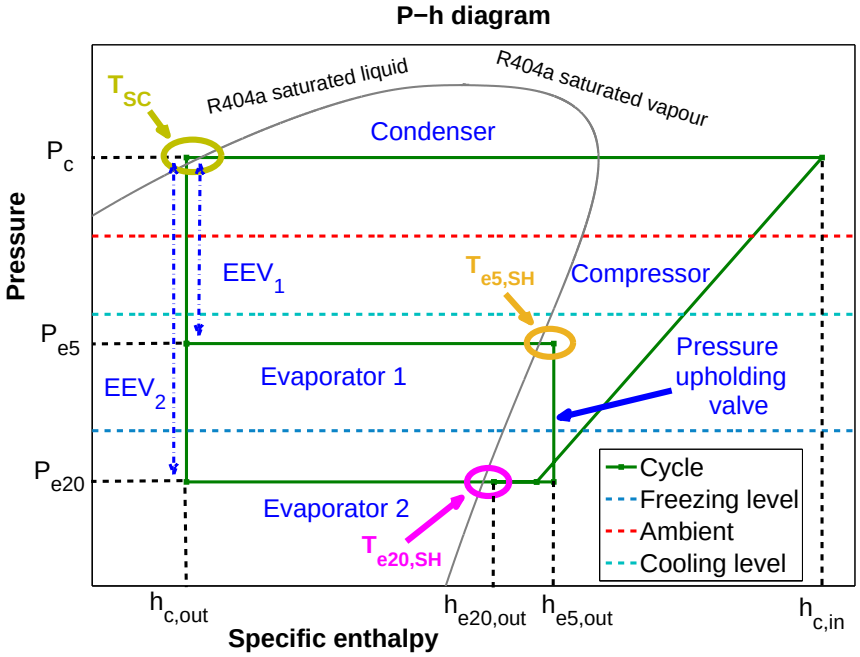

Figure 3.20 P-h diagram of a one-stage, two-load-demand cycle.

the same methodology explained in Subsection 3.2.1 for the electronic expansion valves, giving rise to the model shown in Equation (3.34).

$$\dot{m}_{e5,out} = c_{puv}\sqrt{2\rho_{e5,out}(P_{e5} - P_{e20})} \tag{3.34}$$

No valve opening factor is considered in Equation (3.34), since the manual open setting is not changed during the experiments and they are all carried out with the same open setting. This information is implicit in parameter c_{puv}, whose estimated value and standard deviation are stated in Equation (3.35). In this case a unique value of the coefficient c_{puv} is valid to describe the mass flow characteristic of this valve, since the refrigerant at the pressure upholding valve is not a two-phase fluid, but superheated vapour, as appreciated in the P-h diagram shown in Figure 3.20.

$$\widehat{c}_{puv} = 2.86 \cdot 10^{-6}\ \mathrm{m}^2 \qquad \sigma_{c_{puv}} = 5.5 \cdot 10^{-8}\ \mathrm{m}^2 \tag{3.35}$$

In Figure 3.21 some experimental and simulated P-h diagrams are overlaid at various operating points. Table 3.15 gathers some relative errors of the estimation on measurable variables for different operating points.

Note that in Figure 3.21 pressure drop at the condenser is indeed represented both in the experimental cycle and in the simulated one. Experimental data show that pressure drop at the evaporators is negligible, which is related to heat exchanger design, since plate heat exchangers usually cause lower pressure drop than tube ones. It can be observed in

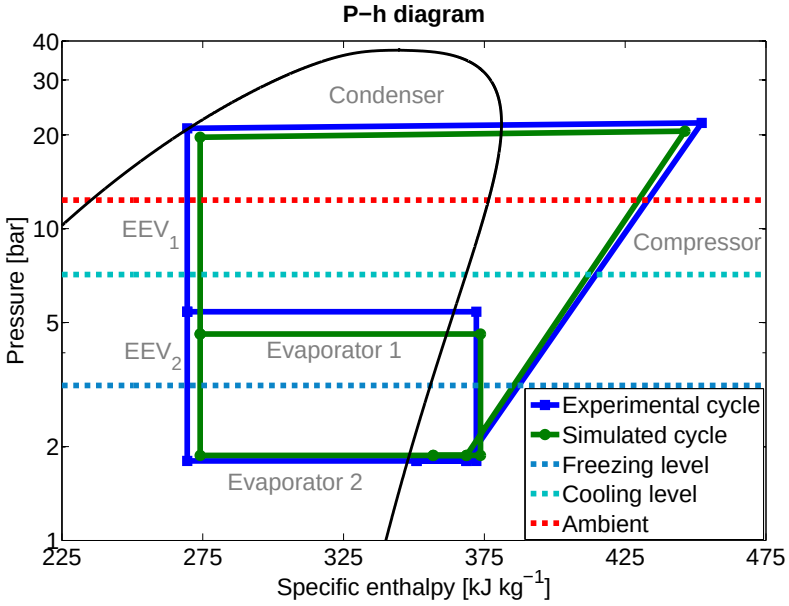

(a) Operating point 1 (OP_1)

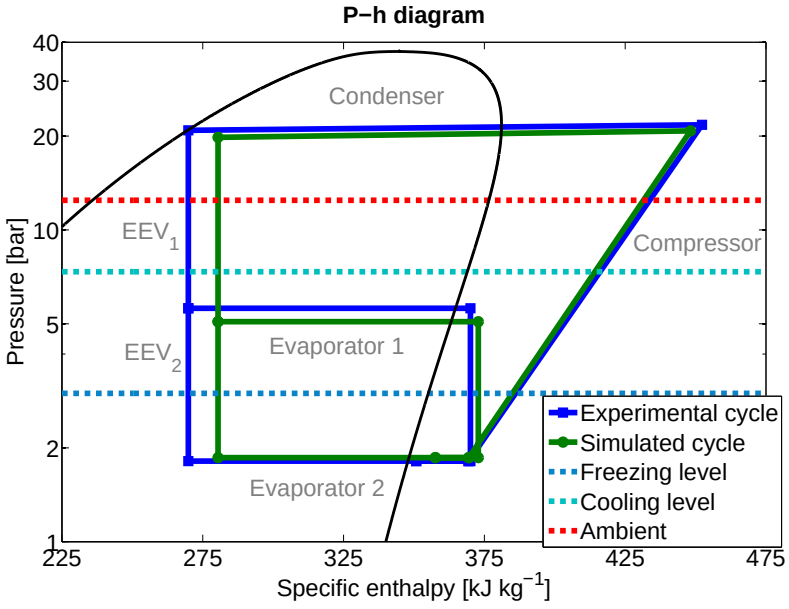

(b) Operating point 2 (OP_2)

Figure 3.21 Experimental and simulated P-h diagrams at different operating points considering the one-stage, two-load-demand configuration.

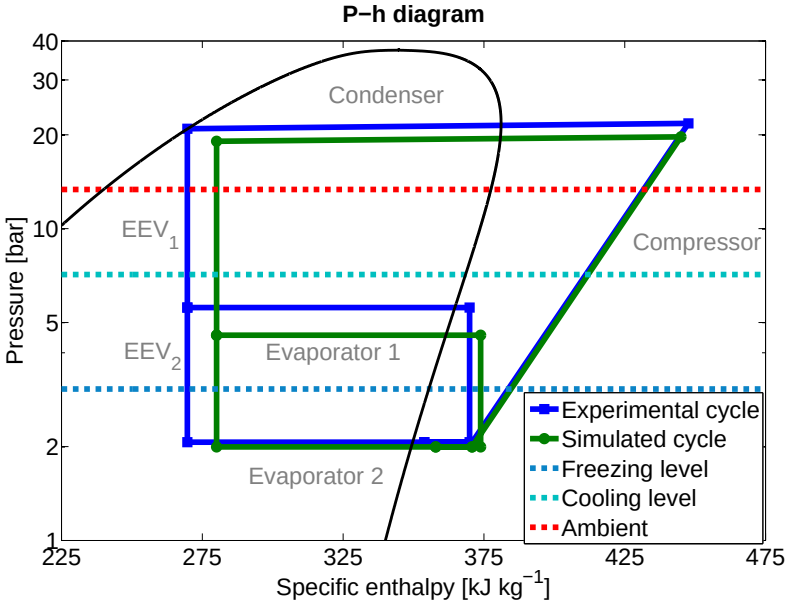

(c) Operating point 3 (OP_3)

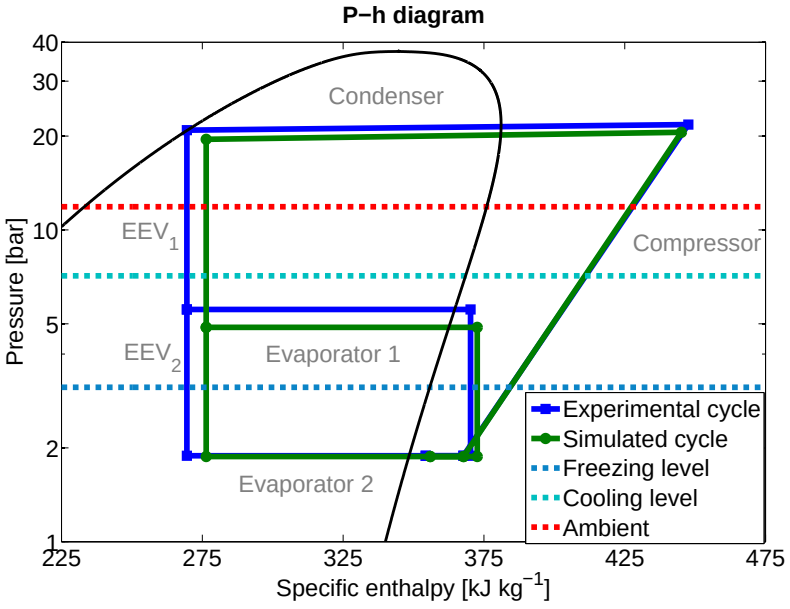

(d) Operating point 4 (OP_4)

Figure 3.21 Experimental and simulated P-h diagrams at different operating points considering the one-stage, two-load-demand configuration.

Table 3.15 Relative errors [%] on diverse measurable variables in the one-stage, two-load-demand cycle.

Variable	Operating point			
	$\mathbf{OP_1}$	$\mathbf{OP_2}$	$\mathbf{OP_3}$	$\mathbf{OP_4}$
P_{e20}	4.71	2.80	3.11	0.22
P_{e5}	15.13	9.31	18.39	12.21
$P_{c,in}$	10.06	8.77	12.35	10.30
$h_{e20,out}$	1.69	1.94	1.14	0.45
$h_{e5,out}$	0.40	0.76	1.06	0.64
$h_{c,out}$	1.70	3.91	3.85	2.55

Figure 3.21 and Table 3.15 that the identified overall heat transfer coefficients at all heat exchangers, along with the parameters of the other elements of the cycle, allow the whole steady state cycle to be correctly estimated. Although some errors could be seen as too high, the identified steady-state model is intended to be used within model-based control strategies, and it is expected that the robustness of the controllers will be able to deal with such modelling errors.

3.3.2 Two-compression-stage, two-load-demand configuration

This configuration was illustrated in Figure 1.5 and highlighted on the experimental plant layout in Figure 3.4. Once again for the sake of clarity the layout is replicated in Figure 3.22.

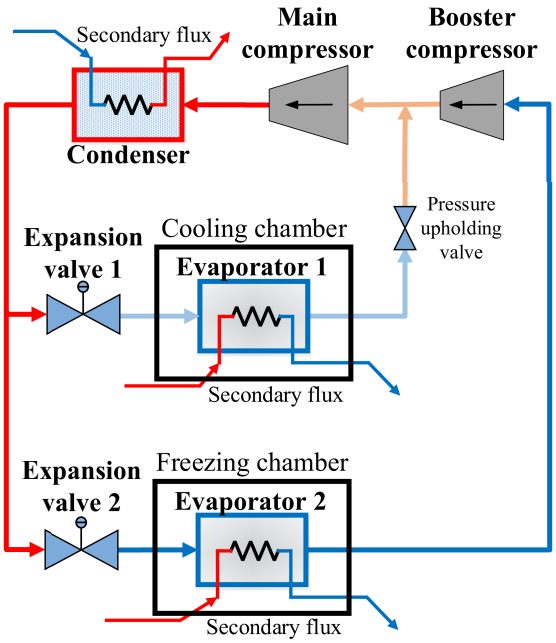

Figure 3.22 Two-compression-stage, two-load-demand refrigeration cycle.

In this configuration the booster compressor is responsible for increasing the refrigerant pressure from Evaporator 1 to Evaporator 2. Thus, the pressure upholding valve located at Evaporator 1 outlet is fully opened in this configuration, since the pressure difference between both evaporators is held by the booster compressor. A typical P-h diagram of the two-stage, two-load-demand cycle is represented in Figure 3.23, as well as the R404a saturation curves. Once again for the sake of simplicity, no pressure drop at the condenser is represented.

Some experimental and simulated P-h diagrams are plotted together in Figure 3.24, considering different steady-state operating points. Moreover, Table 3.16 gathers some estimation errors, both on intensive and extensive variables. It is important to remark that the P-h diagrams in Figure 3.24 do include pressure drop at the condenser, both in the experimental cycle and in the simulated one. Minor deviations are appreciated when comparing simulated and experimental P-h diagrams, therefore the separately identified models allow to correctly estimate the whole steady-state cycle. As previously stated, it must be taken into account that the proposed steady-state model is intended to be included

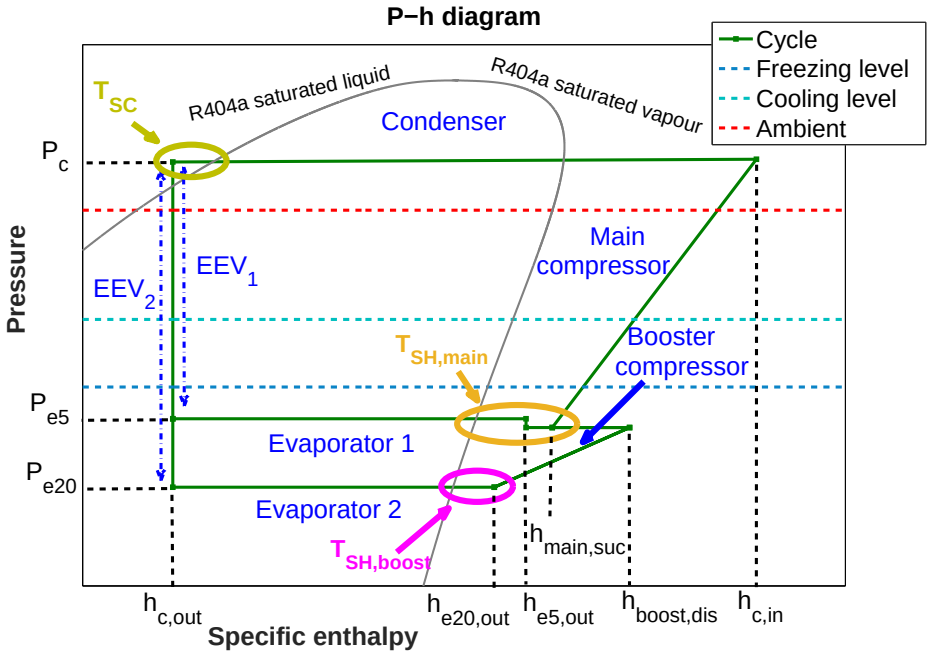

Figure 3.23 P-h diagram of a two-stage, two-load-demand cycle.

in model-based control strategies. This is a control-oriented model whose main features are simplicity and high calculation speed, while it is expected that the robustness of controllers can cope with the modelling errors.

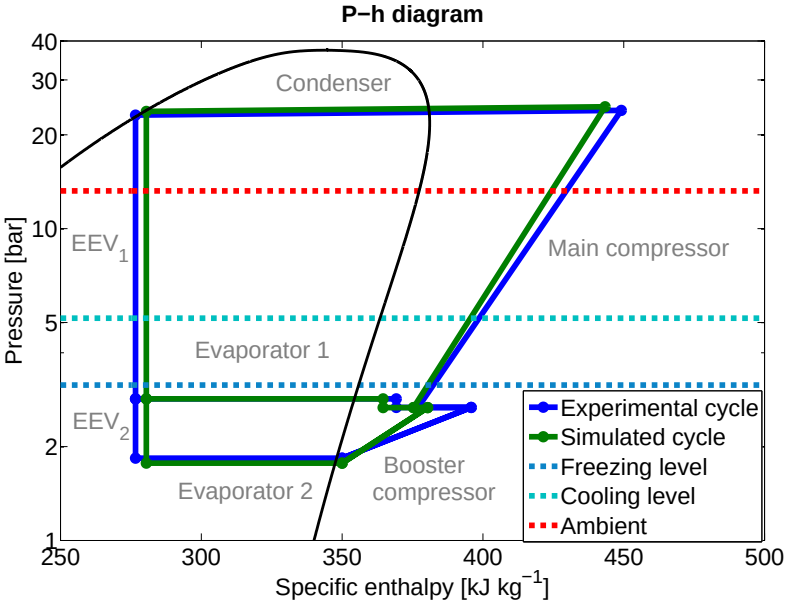

(a) Operating point 1 (OP_1)

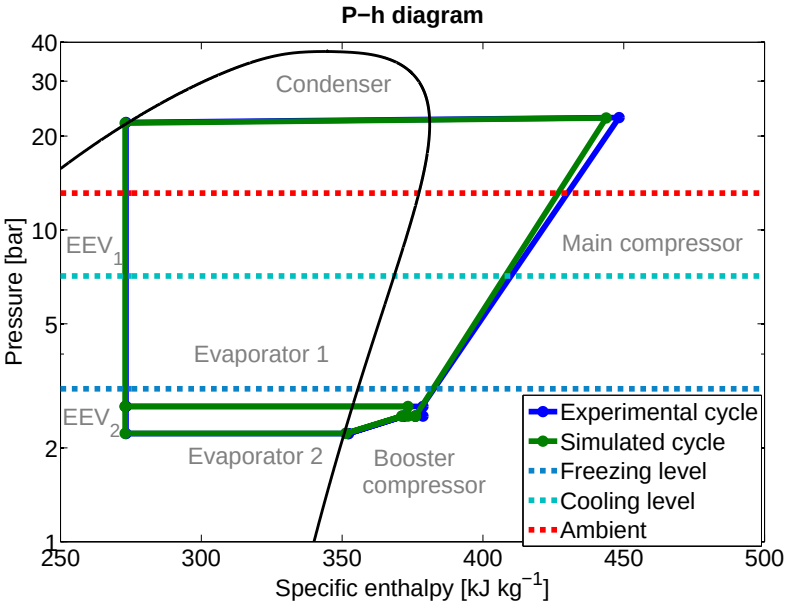

(b) Operating point 2 (OP_2)

Figure 3.24 Experimental and simulated P-h diagrams at different operating points considering the two-stage, two-load-demand configuration.

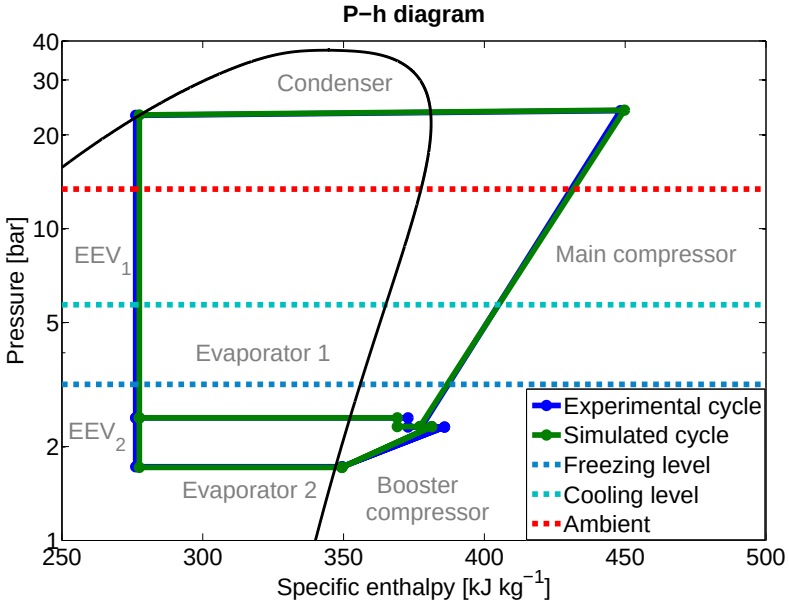

(c) Operating point 3 (OP_3)

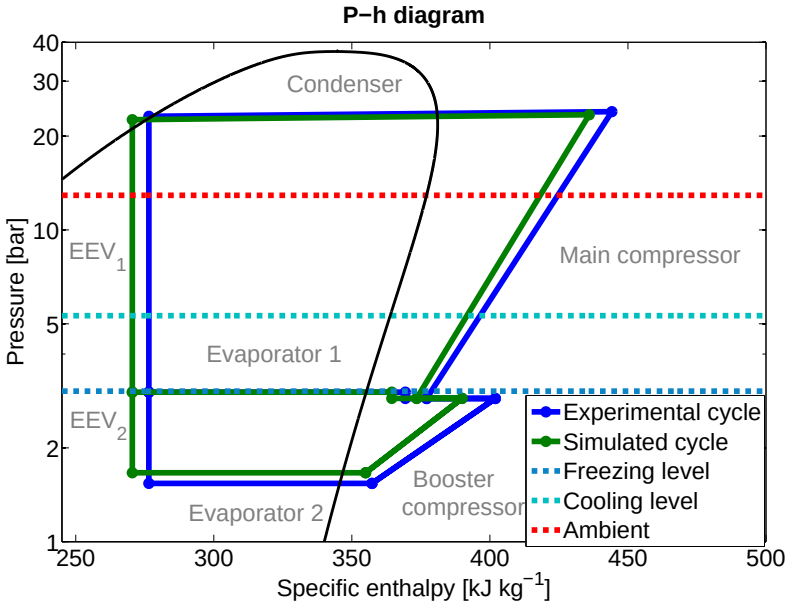

(d) Operating point 4 (OP_4)

Figure 3.24 Experimental and simulated P-h diagrams at different operating points considering the two-stage, two-load-demand configuration.

Table 3.16 Relative errors [%] on diverse measurable variables in the two-stage, two-load-demand cycle.

Variable	Operating point			
	OP_1	OP_2	OP_3	OP_4
P_{e20}	3.596	0.160	0.474	8.179
P_{e5}	0.007	0.003	0.011	0.005
$P_{c,in}$	2.745	0.294	0.400	2.263
$P_{c,out}$	2.716	0.440	0.298	2.431
$h_{e20,out}$	0.003	0.255	0.020	0.652
$h_{e5,out}$	1.269	1.411	1.025	1.329
$h_{boost,dis}$	3.910	0.199	1.182	2.995
$h_{main,suc}$	0.422	0.007	0.143	0.960
$h_{main,dis}$	1.285	1.022	0.316	1.843
$h_{c,out}$	1.386	0.111	0.469	2.168

3.4 Final remarks

This Chapter has been devoted to the two-stage, two-load-demand experimental refrigeration plant mentioned in Chapter 1. The design, implementation, and automation of the plant have been detailed, whereas parameter identification and validation have been also addressed. The modelling conclusions obtained in Chapter 2 have been applied to the identification procedure, namely the steady-state models presented in Chapter 2 for the compressors and expansion valves have been identified using experimental data. Regarding the heat exchangers, parameter dependence of heat exchanger dynamics and statics has been studied, concluding that the heat transfer coefficients influence essentially system statics but they do not affect much system dynamics. Therefore, steady-state identification of the heat exchangers has been also addressed. A novel identification procedure focused on the heat exchangers has been presented. Diverse refrigerant phases along each heat exchanger, according to the MB modelling approach, have been considered, thus diverse zones are differentiated, whose lengths are inaccessible state variables. It has been assumed that a unique overall heat transfer coefficient can be identified for each zone. Coherent values have been calculated taking into account some orders of magnitude of convective heat transfer coefficients in the literature and their influence on overall coefficients.

In spite of individually modelling all elements of the cycle, global validation considering the one-compression-stage, two-load-demand configuration and the two-compression-stage, two-load-demand one has been performed. Minor differences have been noticed when comparing simulated and experimental P-h diagrams, giving rise to estimation errors around 10% in the key variables. The identification procedure of the heat exchangers is

also a contribution of the Thesis, since it may be useful when no heat transfer correlation fits to the configuration or the flow conditions of the heat exchanger to be identified.

Once defined the modelling of the system and performed the identification of its parameters, the following objective is to develop a model-based optimization and control strategy which allows the refrigeration cycle to effectively provide the required cooling power while achieving the highest possible energy efficiency. The identified models of each element of the experimental plant are considered in Chapter 4 to analyse the optimization stage of the model-based control strategy.

4 Optimization and controllability analysis

If you optimize everything, you will always be unhappy.

Donald Knuth

Contents

Energy efficiency and optimal operation of vapour-compression refrigeration systems are addressed in this Chapter. Global optimization of a one-stage, one-load-demand cycle is carried out, where the calculation of the cycle which generates a certain cooling load while maximizing energy efficiency is intended. The *COP* has been considered as energy-efficiency metrics, but it can be easily adapted to other metrics. As justified in Chapter 1, the secondary flows are considered as disturbances, thus only two manipulated variables are available: the compressor speed N and the valve opening A_v. It is shown how the minimum variable set completely defining a cycle is made up of three variables, which agrees with the conclusions expressed in other works [12, 13, 14]. The cooling demand imposes a constraint between these three variables, therefore a two-degree-of-freedom

optimization is carried out. Some limitations of the components, in addition to some operating constraints, are also imposed, while a nonlinear steady-state model of the whole cycle is used to characterise the feasible variable sets. Given a specific facility, the different optimal cycles for a certain achievable cooling load range are compared. It is shown that not all optimal cycles are achieved with minimum degree of superheating at the evaporator outlet, which emphasises the need for a control strategy capable of driving the cycle to the optimum.

However, many control strategies in the literature show some trouble in reaching the optimal cycle satisfying a certain cooling demand, as detailed in Chapter 1. In this Chapter the control problem is in depth analysed. For the sake of simplicity only the compressor speed and the expansion valve opening are considered as manipulated inputs, since increasing the problem size does not change the *one-degree-of-underactuation* nature of the system, which has been justified in Chapter 1. The underactuated features of the system do not necessarily mean that optimal control cannot be achieved, since there are other works, especially regarding mechanical systems, where despite their underactuated characteristics, complex control laws which succeed in controlling the whole state have been developed [81, 82, 83, 84, 85]. The simplified dynamic model presented in Chapter 2 is reformulated in such a way that a controllability analysis based on linear control theory is carried out, whereas a pointwise nonlinear analysis based on the phase portrait method is also performed, considering the most frequent condenser *modes* in steady state.

The contents of this Chapter have been included in some of the publications presented in Chapter 1, Section 1.5 [50, 51, 53, 57, 60].

4.1 Global optimization

4.1.1 Problem statement

As mentioned in Chapter 1, there exist two approaches to energy-efficiency optimization concerning vapour-compression refrigeration cycles. An ideal P-h diagram of a one-compression-stage, one-load-demand cycle was shown in Figure 1.2. The traditional procedure to achieve high energy efficiency in industry is to keep a low degree of superheating at the evaporator outlet, which ensures safe operation of the compressor and supposedly high COP. Nevertheless, alternatively to the conventional set point selection, it is suitable to propose a global optimization to obtain the optimal cycle, given a certain cooling demand, a specific facility and some constraints regarding the secondary fluxes. The solution should also observe all physical and technological constraints of the components, in addition to some operating limitations, such as that of minimum degree of superheating.

First of all, regardless of the selected energy-efficiency metrics, it is essential to define the minimum number of independent variables completely and unequivocally defining a given cycle in steady state, given a facility and considering known all disturbances regarding the secondary flux inlets. As previously mentioned, the secondary flows at the evaporator and condenser are considered as disturbances, thus only two manipulated variables are available: the compressor speed N and the valve opening A_v. For a simple

one-stage, one load-demand cycle and given the considerations mentioned above, this minimum set is made up of three variables, which may be selected for instance as indicated in Equation (4.1).

$$\boldsymbol{\psi}_{cycle} = [h_{e,out} \;\; h_{c,out} \;\; \dot{m}]^T \tag{4.1}$$

By selecting this variable set, which includes two intensive variables (the refrigerant output enthalpies at the evaporator and condenser) and an extensive one (the refrigerant mass flow $\dot{m}$, also called *active charge* by some authors [13]), the definition of the cooling power generated at the evaporator $\dot{Q}_e$ is very simple, considering isenthalpic expansion at the valve, as indicated in Equation (4.2).

$$\dot{Q}_e = \dot{m}\,(h_{e,out} - h_{e,in}) = \dot{m}\,(h_{e,out} - h_{c,out}) \tag{4.2}$$

The objective of the optimization is to obtain the optimal cycle which can be achieved using a given facility while generating the desired cooling power, therefore Equation (4.2) imposes an equality constraint on the decision variables. Thus, a two-degree-of-freedom optimization is performed. In addition, some physical and technological limitations of the components, in addition to some operating constraints, are imposed. Thus, maximum and minimum values of both manipulated variables are considered, in addition to some operating constraints, such as upper and lower limits of the condenser and evaporator pressures and the compression ratio. Furthermore, two operating constraints are imposed concerning the following variables:

- Degree of superheating: a minimum value is imposed to avoid liquid droplets at the compressor intake and therefore ensure safe operation.
- Temperature difference between the refrigerant and the secondary flux at the evaporator and the condenser: a minimum value recommended by the manufacturer to achieve high heat transfer efficiency according to the heat exchanger design is considered.

4.1.2 Nonlinear steady-state model

A nonlinear steady-state model of the whole system is used to calculate all cycle variables from the variable set $\boldsymbol{\psi}_{cycle}$. It is based in separate steady-state models of all elements, which have been described in Chapter 2, Section 2.1.

An iterative procedure has been designed to solve the model of the whole system, which is detailed in Figure 4.1. A certain variable set $\boldsymbol{\psi}_{cycle}$ (including the variables $h_{e,out}$, $h_{c,out}$, and $\dot{m}$, as stated in Equation (4.1)) is proposed as solution, in such a way that the cooling demand is satisfied, that means, Equation (4.2) holds. From this proposed solution, it is necessary to calculate the remaining cycle variables to define if the solution satisfies all constraints. Due to the component model features, it is required to initially make a guess on both cycle pressures P_e and P_c, and iteratively calculate their actual values. Applying the steady-state models of the four components, all cycle variables are calculated and gathered in output vectors $\boldsymbol{y}_{valv}$, $\boldsymbol{y}_{comp}$, $\boldsymbol{y}_e$, and $\boldsymbol{y}_c$, as expressed in Equation Set (4.3). Moreover, two closing conditions are obtained: firstly, a value of $h_{e,in}$ is calculated, which

should match the proposed value of $h_{c,out}$ in ψ_{cycle}; secondly, two values of the specific enthalpy at the condenser inlet, $h_{c,in}$ and $h_{c,in}^{'}$ are produced, which should match. Errors $e_{it,h_{e,in}}$ and $e_{it,h_{c,in}}$ are used to correct the initial guess on the cycle pressures P_e and P_c, and the iterative procedure finalises when the errors $e_{it,h_{e,in}}$ and $e_{it,h_{c,in}}$ approach zero for a reasonable accuracy.

$$\begin{aligned} \boldsymbol{y}_{valve} &= \begin{bmatrix} A_v \end{bmatrix} & \boldsymbol{y}_{comp} &= \begin{bmatrix} h_{c,in} \\ N \\ \dot{W}_{comp} \end{bmatrix} \\ \boldsymbol{y}_e &= \begin{bmatrix} T_{SH} \\ T_{e,sec,out} \\ \zeta_{e,tp} \end{bmatrix} & \boldsymbol{y}_c &= \begin{bmatrix} T_{SC} \\ T_{c,sec,out} \\ \zeta_{c,sh} \\ \zeta_{c,tp} \end{bmatrix} \end{aligned} \tag{4.3}$$

If the iterative procedure finalises successfully, that means that the proposed solution describes an achievable cycle which satisfies the cooling demand, but to determine if it is feasible the remaining constraints must be now checked considering all cycle variables, including the calculated steady-state control actions N and A_v. Only if the cycle satisfies all constraints it can be considered as a *candidate* to be the global optimum. Instead, if the procedure does not finalise successfully, that means that there is no achievable cycle described by the proposed solution, therefore it is neglected as a *candidate*. The convergence of the iterative procedure is not guaranteed, since it depends on the initial guess on the cycle pressures, but considering proper values usually leads to successful results. Nevertheless, the uniqueness of the solution is guaranteed because it has been explained previously that the minimum number of variables completely defining a one-stage, one load-demand cycle in steady-state is three, in the case of considering only the compressor speed and the expansion valve opening as manipulated variables. Thus, if a given solution ψ_{cycle} produces a successful execution of the iterative procedure, that means that it describes unequivocally an achievable cycle which satisfies the cooling demand and the cycle pressures obtained by the iterative procedure are the unique pair corresponding to this cycle.

4.1.3 Optimization results

The objective of this Subsection is to represent the results of the global optimization for a given facility and an achievable cooling load range. The *COP* is selected as energy-efficiency metrics, but the optimization procedure can be easily adapted to other metrics, since the feasibility of the *candidate* cycles is similarly assessed. Thus, in Figure 4.2 the *COP* (subfigure 4.2(a)), the degree of superheating (subfigure 4.2(a)), the cycle pressures (subfigure 4.2(b)), the refrigerant mass flow (subfigure 4.2(c)), and finally the steady-state manipulated variables (subfigure 4.2(d)) of the optimal cycles are represented, for a given load range.

Minimum and maximum compressor speeds are set to 30 and 50 Hz, respectively, whereas a minimum value of 2 K is imposed for the degree of superheating. In the light of the results represented in Figure 4.2, some interesting conclusions may be derived.

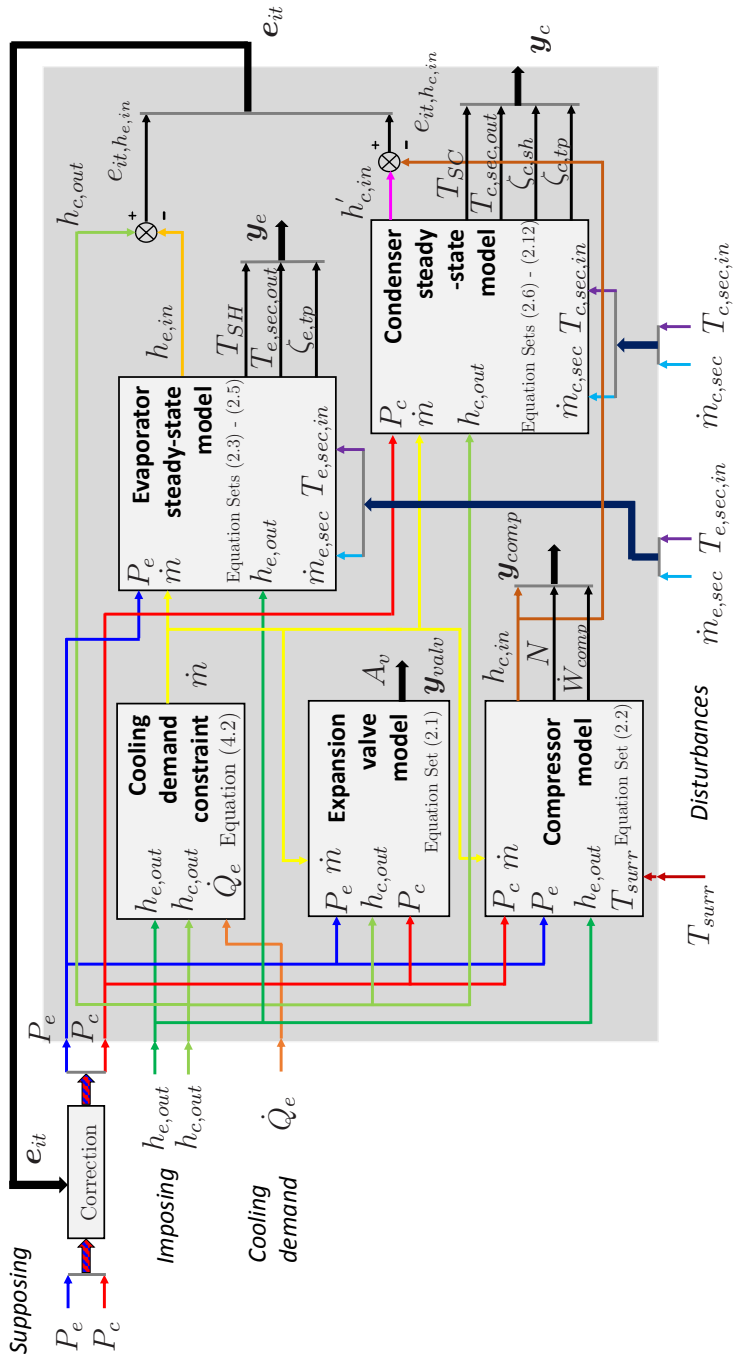

Figure 4.1 Iterative procedure to solve the steady-state model of the whole cycle.

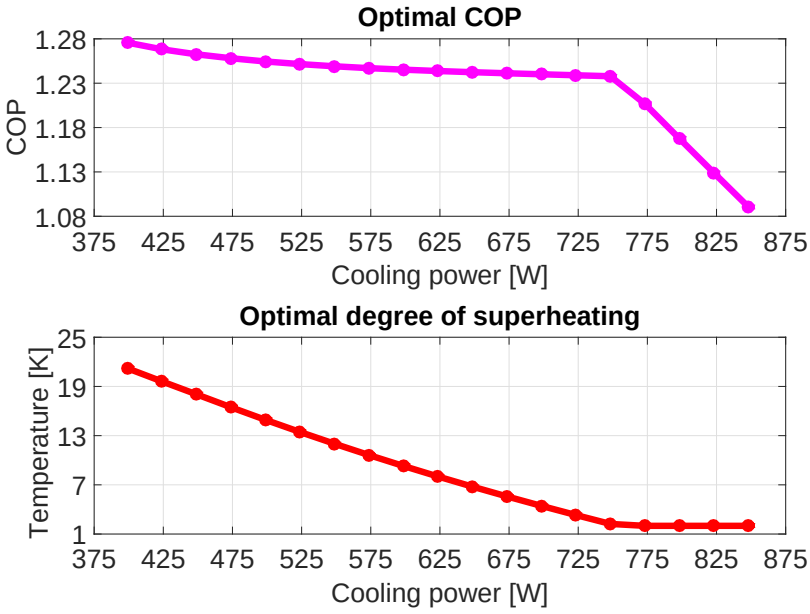

(a) Optimal *COP* and degree of superheating

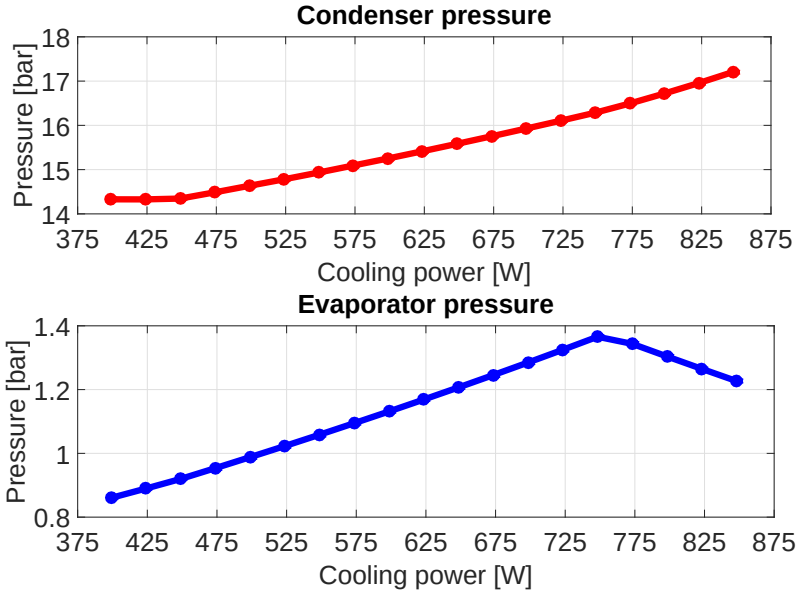

(b) Condenser and evaporator pressures

Figure 4.2 Optimal cycle variables for a given cooling load range.

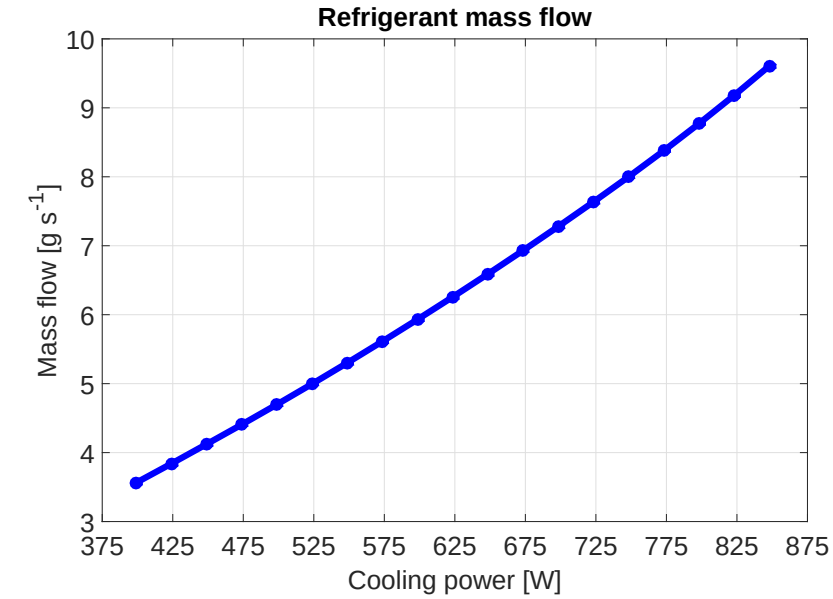

(c) Refrigerant mass flow or *active charge*

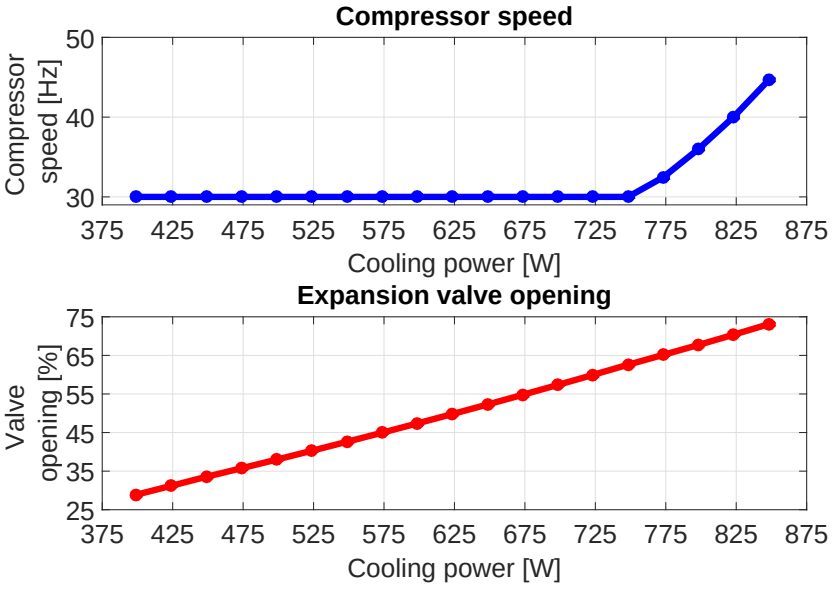

(d) Steady-state manipulated variables

Figure 4.2 Optimal cycle variables for a given cooling load range.

Firstly, and most importantly, it is highlighted that optimal cycles are not achieved with minimum degree of superheating for all the cooling load range, but for low and medium cooling load the optimal cycle requires a greater degree of superheating. It involves that the control strategy conventionally applied (setting a constant degree of superheating as reference) might drive the cycle far away from the optimum, specially when the cooling load is lower than the design value. Therefore, an improvement on energy efficiency could be achieved if the cycle was optimally operated, in particular for low cooling load.

Secondly, it is observed that the *COP* is greatly reduced when, to satisfy the cooling demand, the cycle needs to increase the compressor speed above its minimum. This occurs when it is no longer possible to satisfy the cooling demand by increasing the expansion valve opening, which implies that a greater refrigerant mass flow circulates.

Thirdly, concerning the pressures, for very low cooling demand the dominant constraint is that of minimum condenser pressure, which is determined by the inlet temperature of the condenser secondary flux and the minimum temperature difference between the refrigerant and the secondary flux imposed at the condenser for heat exchanger efficiency purposes.

Obviously the results cannot be extrapolated to all refrigeration systems nor all cooling demands, since the objective function is as nonlinear as the system model. However, it may be worth calculating the optimal cycle for the facility under study to satisfy a given cooling demand using the steady-state model, because it might provide some guidelines on set point selection, as analysed in Chapter 5.

4.2 Controllability analysis

As stated in Section 4.1, a one-compression-stage, one-load-demand cycle is completely defined by a set ψ_{cycle} made up of three variables, whether considering only the compressor speed N and the expansion valve opening A_v as manipulated variables. The variable set may be selected as indicated in Equation (4.1), but any set including three independent variables is valid to describe the cycle.

It has been also stated that the simplified control-oriented model presented in Chapter 2 for the whole cycle is considered as starting point for the controllability analysis. It concentrates the dominant dynamics at the condenser and proposes a three-variable state vector, both in *mode* 1 and 2, as indicated in Equations (4.4) and (4.5).

$$\boldsymbol{x}_{c,m1} = [P_c \;\; \zeta_{c,sc} \;\; h_{c,sc}]^T \tag{4.4}$$

$$\boldsymbol{x}_{c,m2} = [P_c \;\; \zeta_{c,sh} \;\; \bar{\gamma}_c]^T \tag{4.5}$$

Since the variables included in the state vector are independent, both in *mode* 1 and 2, the state vector can represent a valid variable set to completely describe the cycle. Therefore, it is suitable to study the controllability of the condenser dynamic model, since driving the state from a random initial point to the desired point corresponds to driving the whole cycle to the point defined by the desired state.

The reduced model of the condenser when working in *mode* 1 has been detailed in Chapter 2, Subsection 2.2.3, but it is also included in Equation Sets (4.6) and (4.7) to

improve the comprehension of the controllability analysis. Moreover, the expressions of the elements $f_{c,m1,i}\ \forall i = 1,2,3$ are also replicated in Equation Set (4.8) for comparison purposes.

$$\begin{aligned} \boldsymbol{Z}_{c,m1}(\boldsymbol{x}_{c,m1}, \boldsymbol{w}_c)\ \dot{\boldsymbol{x}}_{c,m1} &= \boldsymbol{f}_{c,m1}(\boldsymbol{x}_{c,m1}, \boldsymbol{w}_c) \\ \boldsymbol{x}_{c,m1} &= [P_c\ \ \zeta_{c,sc}\ \ h_{c,sc}]^T \\ \boldsymbol{w}_c &= [\dot{m}_{c,sec}\ \ T_{c,sec,in}\ \ \dot{m}\ \ h_{c,in}]^T \end{aligned} \tag{4.6}$$

$$\begin{aligned} \boldsymbol{Z}_{c,m1}(\boldsymbol{x}_{c,m1}, \boldsymbol{w}_c) &= \begin{bmatrix} z_{c,m1,11} & -1 & z_{c,m1,13} \\ z_{c,m1,21} & 0 & z_{c,m1,23} \\ z_{c,m1,31} & -1 & z_{c,m1,33} \end{bmatrix} \\ \boldsymbol{f}_{c,m1}(\boldsymbol{x}_{c,m1}, \boldsymbol{w}_c) &= [f_{c,m1,1}\ \ f_{c,m1,2}\ \ f_{c,m1,3}]^T \end{aligned} \tag{4.7}$$

$$\begin{aligned} f_{c,m1,1}(\boldsymbol{x}_{c,m1}, \boldsymbol{w}_c) &= \frac{1}{\rho_{c,tp}\, V_R}\ \frac{1}{h_{c,f} - h_{c,sc}}\left(\dot{Q}_{c,sc} + \dot{m}\,(h_{c,f} - h_{c,sc})\right) \\ f_{c,m1,2}(\boldsymbol{x}_{c,m1}, \boldsymbol{w}_c) &= \frac{1}{\rho_{c,tp}\ \zeta_{c,tp}\ V_R}\left(\dot{Q}_{c,tp} + \dot{m}\,(h_{c,g} - h_{c,tp}) + \frac{h_{c,f} - h_{c,tp}}{h_{c,f} - h_{c,sc}}\ \dot{Q}_{c,sc}\right) \\ f_{c,m1,3}(\boldsymbol{x}_{c,m1}, \boldsymbol{w}_c) &= \frac{1}{\rho_{c,sc}\, V_R}\frac{1}{h_{c,f} - h_{c,sc}}\left(\dot{Q}_{c,sc} + \dot{m}\,(h_{c,f} - h_{c,sc})\right) \end{aligned} \tag{4.8}$$

Similarly, the reduced model of the condenser when working in *mode* 2 is indicated in Equation Set (4.9), where the structure of coefficient matrix $\boldsymbol{Z}_{c,m2}$ and force function $\boldsymbol{f}_{c,m2}$ are presented in Equation Set (4.10). The expressions of the elements $f_{c,m2,i}\ \forall i = 1,2,3$ are detailed in Equation Set (4.11).

$$\begin{aligned} \boldsymbol{Z}_{c,m2}(\boldsymbol{x}_{c,m2}, \boldsymbol{w}_c)\ \dot{\boldsymbol{x}}_{c,m2} &= \boldsymbol{f}_{c,m2}(\boldsymbol{x}_{c,m2}, \boldsymbol{w}_c) \\ \boldsymbol{x}_{c,m2} &= [P_c\ \ \zeta_{c,sh}\ \ \bar{\gamma}_c]^T \end{aligned} \tag{4.9}$$

$$\begin{aligned} \boldsymbol{Z}_{c,m2}(\boldsymbol{x}_{c,m2}, \boldsymbol{w}_c) &= \begin{bmatrix} z_{c,m2,11} & 0 & z_{c,m2,13} \\ z_{c,m2,21} & 1 & 0 \\ z_{c,m2,31} & -1 & z_{c,m2,33} \end{bmatrix} \\ \boldsymbol{f}_{c,m2}(\boldsymbol{x}_{c,m2}, \boldsymbol{w}_c) &= [f_{c,m2,1}\ \ f_{c,m2,2}\ \ f_{c,m2,3}]^T \end{aligned} \tag{4.10}$$

$$
\begin{aligned}
f_{c,m2,1}(\boldsymbol{x}_{c,m2}, \boldsymbol{w}_c) &= \frac{1}{\rho_{c,tp}\ \zeta_{c,tp}\ V_R}\left[\dot{Q}_{c,tp} - \dot{m}\ (h_{c,out} - h_{c,tp}) + \right. \\
&\left. + \frac{h_{c,g} - h_{c,tp}}{h_{c,g} - h_{c,sh}}\left(\dot{Q}_{c,sh} + \dot{m}\ (h_{c,in} - h_{c,sh})\right)\right] \\
f_{c,m2,2}(\boldsymbol{x}_{c,m2}, \boldsymbol{w}_c) &= \frac{1}{\rho_{c,sh}\ V_R}\frac{1}{h_{c,g} - h_{c,sh}}\left(-\dot{Q}_{c,sh} + \dot{m}\ (h_{c,g} - h_{c,in})\right) \\
f_{c,m2,3}(\boldsymbol{x}_{c,m2}, \boldsymbol{w}_c) &= \frac{1}{\rho_{c,tp}\ V_R}\frac{1}{h_{c,g} - h_{c,sh}}\left(\dot{Q}_{c,sh} - \dot{m}\ (h_{c,g} - h_{c,in})\right)
\end{aligned}
\tag{4.11}
$$

4.2.1 Analysis based on linear theory

A convenient model representation in *mode* 1 can be obtained applying algebraic manipulation, as shown in Equation Set (4.12), where force function $\hat{\boldsymbol{f}}_{c,m1}$ has a null element. The same strategy can be applied to obtain the model representation in *mode* 2 indicated in Equation Set (4.13), where force function $\hat{\boldsymbol{f}}_{c,m2}$ has also a null element.

$$
\begin{aligned}
&\hat{\boldsymbol{Z}}_{c,m1}\ \dot{\boldsymbol{x}}_{c,m1} = \hat{\boldsymbol{f}}_{c,m1} \\
&\hat{\boldsymbol{Z}}_{c,m1} = \begin{bmatrix} z_{c,m1,11} & -1 & z_{c,m1,13} \\ z_{c,m1,21} & 0 & z_{c,m1,23} \\ z_{c,m1,31} - \dfrac{\rho_{c,tp}}{\rho_{c,sc}} z_{c,m1,11} & -1 + \dfrac{\rho_{c,tp}}{\rho_{c,sc}} & z_{c,m1,33} - \dfrac{\rho_{c,tp}}{\rho_{c,sc}} z_{c,m1,13} \end{bmatrix} \\
&\hat{\boldsymbol{f}}_{c,m1} = [f_{c,m1,1}\ \ f_{c,m1,2}\ \ 0]^T
\end{aligned}
\tag{4.12}
$$

$$
\begin{aligned}
&\hat{\boldsymbol{Z}}_{c,m2}\ \dot{\boldsymbol{x}}_{c,m2} = \hat{\boldsymbol{f}}_{c,m2} \\
&\hat{\boldsymbol{Z}}_{c,m2} = \begin{bmatrix} z_{c,m2,11} & 0 & z_{c,m2,13} \\ z_{c,m2,21} & 1 & 0 \\ z_{c,m2,31} + \dfrac{\rho_{c,sh}}{\rho_{c,tp}} z_{c,m2,21} & -1 + \dfrac{\rho_{c,sh}}{\rho_{c,tp}} & z_{c,m2,33} \end{bmatrix} \\
&\hat{\boldsymbol{f}}_{c,m2} = [f_{c,m2,1}\ \ f_{c,m2,2}\ \ 0]^T
\end{aligned}
\tag{4.13}
$$

Considering the representation shown in Equation Set (4.12), elements $f_{c,m1,1}$ and $f_{c,m1,2}$ can be considered as virtual manipulated inputs, since for a given state and disturbances their values depend on the actual manipulated inputs $\dot{m}$ and $h_{c,in}$, whose values depend in turn on the actual control actions N and A_v. In other words, given the state and disturbances, the actual manipulated inputs $\dot{m}$ and $h_{c,in}$ can be calculated from the virtual manipulated inputs $f_{c,m1,1}$ and $f_{c,m1,2}$ by solving the nonlinear system generated by the two first equations of Equation Set (4.8). The same can be applied to elements $f_{c,m2,1}$ and $f_{c,m2,2}$ in Equation Set (4.13), where the two first equations of Equation Set (4.11) generate the nonlinear system from which $\dot{m}$ and $h_{c,in}$ are calculated. Then, the underactuated features of the

whole cycle also emerge here, when studying only the condenser model, since the control objective is to regulate the three states by manipulating only two variables.

Coefficient matrices $\hat{\boldsymbol{Z}}_{c,m1}$ and $\hat{\boldsymbol{Z}}_{c,m2}$ depend on the state, manipulated variables, and disturbances, in addition to thermodynamic properties of the refrigerant when evaluated at the intensive variables gathered in the state, specially the condenser pressure P_c. None of them are singular for a wide enough pressure range, reasonable values of disturbances, and achievable control actions, thus each one can be inverted giving rise to the model representation indicated in Equation Set (4.14), which is valid for *modes* 1 and 2 if changing the corresponding subscript $mi \;\; \forall i = 1,2$.

$$\begin{aligned} \hat{\boldsymbol{Z}}_{c,mi}\, \dot{\boldsymbol{x}}_{c,mi} &= \hat{\boldsymbol{f}}_{c,mi} \\ \hat{\boldsymbol{Z}}_{c,mi}^{-1} &\equiv \hat{\boldsymbol{Z}}_{c,mi,inv} \\ \hat{\boldsymbol{Z}}_{c,mi,inv} &= \begin{bmatrix} \hat{z}_{c,mi,inv,11} & \hat{z}_{c,mi,inv,12} & \hat{z}_{c,mi,inv,13} \\ \hat{z}_{c,mi,inv,21} & \hat{z}_{c,mi,inv,22} & \hat{z}_{c,mi,inv,23} \\ \hat{z}_{c,mi,inv,31} & \hat{z}_{c,mi,inv,32} & \hat{z}_{c,mi,inv,33} \end{bmatrix} \end{aligned} \tag{4.14a}$$

$$\begin{aligned} \dot{\boldsymbol{x}}_{c,mi} = \hat{\boldsymbol{Z}}_{c,mi,inv}\, \hat{\boldsymbol{f}}_{c,mi} &= \begin{bmatrix} \hat{z}_{c,mi,inv,11} & \hat{z}_{c,mi,inv,12} & \hat{z}_{c,mi,inv,13} \\ \hat{z}_{c,mi,inv,21} & \hat{z}_{c,mi,inv,22} & \hat{z}_{c,mi,inv,23} \\ \hat{z}_{c,mi,inv,31} & \hat{z}_{c,mi,inv,32} & \hat{z}_{c,mi,inv,33} \end{bmatrix} \begin{bmatrix} f_{c,mi,1} \\ f_{c,mi,2} \\ 0 \end{bmatrix} = \\ &= \begin{bmatrix} \hat{z}_{c,mi,inv,11} & \hat{z}_{c,mi,inv,12} \\ \hat{z}_{c,mi,inv,21} & \hat{z}_{c,mi,inv,22} \\ \hat{z}_{c,mi,inv,31} & \hat{z}_{c,mi,inv,32} \end{bmatrix} \begin{bmatrix} f_{c,mi,1} \\ f_{c,mi,2} \end{bmatrix} \end{aligned} \tag{4.14b}$$

The model representation shown in Equation (4.14b) has a linear structure if $\hat{\boldsymbol{f}}_{c,mi}$ is considered as the manipulated input vector, in spite of all elements in $\hat{\boldsymbol{Z}}_{c,mi,\text{inv}}$ and $\hat{\boldsymbol{f}}_{c,mi}$ being nonlinear functions of the state $\boldsymbol{x}_{c,mi}$, the actual manipulated inputs $\dot{m}$ and $h_{c,in}$, and the disturbances $\dot{m}_{c,sec}$ and $T_{c,sec,in}$ included in $\boldsymbol{w}_c$. Given the linear structure of the model representation, and despite the system nonlinearities, the linear controllability matrix $\mathbb{C}$ gives a first overall assessment of the difficulties which emerge when controlling the system. As described in Equation Set (4.15), its rank is shown to match at most the number of columns in matrix $\boldsymbol{B}_{c,mi}$, namely the number of manipulated inputs. Then, the controllability analysis based on linear theory suggests that the system is not fully controllable.

$$\dot{\boldsymbol{x}}_{c,mi} = \boldsymbol{A}_{c,mi}\, \boldsymbol{x}_{c,mi} + \boldsymbol{B}_{c,mi}\, \boldsymbol{u}_{c,mi} \tag{4.15a}$$

$$\boldsymbol{A}_{c,mi} = \begin{bmatrix} 0 & 0 & 0 \\ 0 & 0 & 0 \\ 0 & 0 & 0 \end{bmatrix}$$

$$\boldsymbol{B}_{c,mi} = \hat{\boldsymbol{Z}}_{c,mi,inv} = \begin{bmatrix} \hat{z}_{c,mi,inv,11} & \hat{z}_{c,mi,inv,12} \\ \hat{z}_{c,mi,inv,21} & \hat{z}_{c,mi,inv,22} \\ \hat{z}_{c,mi,inv,31} & \hat{z}_{c,mi,inv,32} \end{bmatrix} \tag{4.15b}$$

$$\boldsymbol{u}_{c,mi} = \hat{\boldsymbol{f}}_{c,mi} = \begin{bmatrix} f_{c,mi,1} \\ f_{c,mi,2} \end{bmatrix}$$

$$\mathbb{C} = \begin{bmatrix} \boldsymbol{B}_{c,mi} & \boldsymbol{A}_{c,mi}\,\boldsymbol{B}_{c,mi} & \boldsymbol{A}_{c,mi}^2\,\boldsymbol{B}_{c,mi} \end{bmatrix} \tag{4.15c}$$

$$rank(\mathbb{C}) = rank(\boldsymbol{B}_{c,mi}) \leqslant 2$$

4.2.2 Nonlinear analysis based on the phase portrait method

However, all elements in matrix $\boldsymbol{B}_{c,mi}\ \forall i = 1,2$ depend on the disturbances and the state. Therefore, the conclusions provided by the controllability analysis on the simplified SMB model based on linear theory could be questionable, since it is a highly nonlinear system. That is the reason why the linear controllability study is extended to a nonlinear analysis based on the phase portrait method. The dynamic equations of the control-oriented SMB model are highly nonlinear and include indeed thermodynamic functions which are used to evaluate refrigerant properties. This causes an analytical study to be very difficult to carry out, therefore a graphic method is instead addressed to evaluate the controllability of the system.

If the model representation shown in Equation (4.14b) is considered, for both condenser *modes*, vectors $\boldsymbol{\chi}_{c,m1}$ and $\boldsymbol{\chi}_{c,m2}$ can be defined as the deviations of the states with respect to the desired values, as indicated in Equation Set (4.16). For the sake of simplicity, the desired state is not expected to vary with time, thus the error model shown in Equation (4.17) arises, valid for both *modes*.

$$\begin{aligned} \boldsymbol{\chi}_{c,m1} &\equiv \boldsymbol{x}_{c,m1} - \boldsymbol{x}_{c,m1}^{ref} = \begin{bmatrix} P_c - P_c^{ref} \\ \zeta_{c,sc} - \zeta_{c,sc}^{ref} \\ h_{c,sc} - h_{c,sc}^{ref} \end{bmatrix} \\ \boldsymbol{\chi}_{c,m2} &\equiv \boldsymbol{x}_{c,m2} - \boldsymbol{x}_{c,m2}^{ref} = \begin{bmatrix} P_c - P_c^{ref} \\ \zeta_{c,sh} - \zeta_{c,sh}^{ref} \\ \bar{\gamma}_c - \bar{\gamma}_c^{ref} \end{bmatrix} \end{aligned} \tag{4.16}$$

$$\dot{\boldsymbol{\chi}}_{c,mi} = \dot{\boldsymbol{x}}_{c,mi} - \dot{\boldsymbol{x}}_{c,mi}^{ref} = \dot{\boldsymbol{x}}_{c,mi} = \begin{bmatrix} \hat{z}_{c,mi,inv,11} & \hat{z}_{c,mi,inv,12} \\ \hat{z}_{c,mi,inv,21} & \hat{z}_{c,mi,inv,22} \\ \hat{z}_{c,mi,inv,31} & \hat{z}_{c,mi,inv,32} \end{bmatrix} \begin{bmatrix} f_{c,mi,1} \\ f_{c,mi,2} \end{bmatrix} \tag{4.17}$$

For the sake of notation simplicity, let rename the elements of the matrix defining the dynamic model of $\boldsymbol{\chi}_{c,mi}$ as shown in Equation (4.18).

$$\begin{aligned}\dot{\boldsymbol{\chi}}_{c,mi} = \begin{bmatrix} \dot{\chi}_{c,mi,1} \\ \dot{\chi}_{c,mi,2} \\ \dot{\chi}_{c,mi,3} \end{bmatrix} &= \begin{bmatrix} \hat{z}_{c,mi,inv,11} & \hat{z}_{c,mi,inv,12} \\ \hat{z}_{c,mi,inv,21} & \hat{z}_{c,mi,inv,22} \\ \hat{z}_{c,mi,inv,31} & \hat{z}_{c,mi,inv,32} \end{bmatrix} \begin{bmatrix} f_{c,mi,1} \\ f_{c,mi,2} \end{bmatrix} \equiv \\ &\equiv \begin{bmatrix} b_{c,mi,11} & b_{c,mi,12} \\ b_{c,mi,21} & b_{c,mi,22} \\ b_{c,mi,31} & b_{c,mi,32} \end{bmatrix} \begin{bmatrix} f_{c,mi,1} \\ f_{c,mi,2} \end{bmatrix}\end{aligned} \tag{4.18}$$

In order to make the graphic results of the nonlinear controllability analysis more intelligible, the three-dimensional problem is simplified into a two-dimensional one. It is considered that one of the virtual manipulated inputs is devoted to controlling one of the state variables, in such a way that this state holds its reference value. Therefore, the control problem is reduced to driving the two remaining states to their references by using only one manipulated input. It allows the phase portrait of this reduced problem to be represented in a two-dimensional chart.

Consider for instance *mode* 1. If a secondary controller is responsible for holding $h_{c,sc}$ at its reference value $h_{c,sc}^{ref}$ at any instant, it can be assumed that $\dot{\chi}_{c,m1,3} = 0$. The dynamic model of the remaining states is simplified as shown in Equation Set (4.19), where the secondary control law is explicitly calculated in Equation Set (4.19a).

$$\dot{\chi}_{c,m1,3} = 0 \Rightarrow b_{c,m1,31}\, f_{c,m1,1} + b_{c,m1,32}\, f_{c,m1,2} = 0 \Rightarrow f_{c,m1,1} = -\frac{b_{c,m1,32}}{b_{c,m1,31}} f_{c,m1,2} \tag{4.19a}$$

$$\begin{aligned}\begin{bmatrix} \dot{\chi}_{c,m1,1} \\ \dot{\chi}_{c,m1,2} \end{bmatrix} &= \begin{bmatrix} b_{c,m1,11} & b_{c,m1,12} \\ b_{c,m1,21} & b_{c,m1,22} \end{bmatrix} \begin{bmatrix} f_{c,m1,1} \\ f_{c,m1,2} \end{bmatrix} = \\ &= \begin{bmatrix} b_{c,m1,12} - \dfrac{b_{c,m1,32}}{b_{c,m1,31}} b_{c,m1,11} \\ b_{c,m1,22} - \dfrac{b_{c,m1,32}}{b_{c,m1,31}} b_{c,m1,21} \end{bmatrix} f_{c,m1,2} \equiv \\ &\equiv \begin{bmatrix} d_{c,m1,1} \\ d_{c,m1,2} \end{bmatrix} f_{c,m1,2} = \\ &= \boldsymbol{D}_{c,m1}\, f_{c,m1,2}\end{aligned} \tag{4.19b}$$

The reduced two-dimensional problem shows not to be fully controllable if the elements $d_{c,m1,1}$ and $d_{c,m1,2}$ are constant. In particular, the one-dimensional controllable subspace $\mathbb{S}_{c,m1}$ can be analytically calculated as shown in Equation Set (4.20) and it corresponds to the line represented in Figure 4.3 considering random values of $d_{c,m1,1}$ and $d_{c,m1,2}$. The arrows in Figure 4.3 represent that the movement due to the available control action is possible along the line in both directions, but in any case its magnitude is limited by the physically achievable control action. As Figure 4.3 illustrates, only initial points within the controllable subspace $\mathbb{S}_{c,m1}$ can be driven to the origin by any controller, and moreover it

will fail in achieving the origin from any initial point out of the controllable subspace $\mathbb{S}_{c,m1}$, since controllability is a system property, not a controller-dependent one. Furthermore, it is shown in Equation Set (4.21) that the distance $\delta_{c,m1}$ from any initial point to the controllable subspace $\mathbb{S}_{c,m1}$ does not vary for any control action $f_{c,m1,2}$.

$$\begin{aligned}
\mathbb{S}_{c,m1} &= \left\{ \begin{bmatrix} \chi_{c,m1,1} \\ \chi_{c,m1,2} \end{bmatrix} \in \mathbb{R}^2 \;\middle|\; \begin{vmatrix} \chi_{c,m1,1} & d_{c,m1,1} \\ \chi_{c,m1,2} & d_{c,m1,2} \end{vmatrix} = 0 \right\} = \\
&= \left\{ \begin{bmatrix} \chi_{c,m1,1} \\ \chi_{c,m1,2} \end{bmatrix} \in \mathbb{R}^2 \;\middle|\; \chi_{c,m1,1}\, d_{c,m1,2} - \chi_{c,m1,2}\, d_{c,m1,1} = 0 \right\} = \\
&= \left\{ \begin{bmatrix} \chi_{c,m1,1} \\ \chi_{c,m1,2} \end{bmatrix} \in \mathbb{R}^2 \;\middle|\; \chi_{c,m1,2} = \frac{d_{c,m1,2}}{d_{c,m1,1}}\, \chi_{c,m1,1} \right\}
\end{aligned} \tag{4.20}$$

$$\begin{aligned}
\delta_{c,m1} &\equiv \begin{vmatrix} \chi_{c,m1,1} & d_{c,m1,1} \\ \chi_{c,m1,2} & d_{c,m1,2} \end{vmatrix} \\
\dot{\delta}_{c,m1} &= \dot{\chi}_{c,m1,1}\, d_{c,m1,2} - \dot{\chi}_{c,m1,2}\, d_{c,m1,1} = \\
&= (d_{c,m1,1}\, d_{c,m1,2} - d_{c,m1,2}\, d_{c,m1,1})\, f_{c,m1,2} = 0 \qquad \forall f_{c,m1,2}
\end{aligned} \tag{4.21}$$

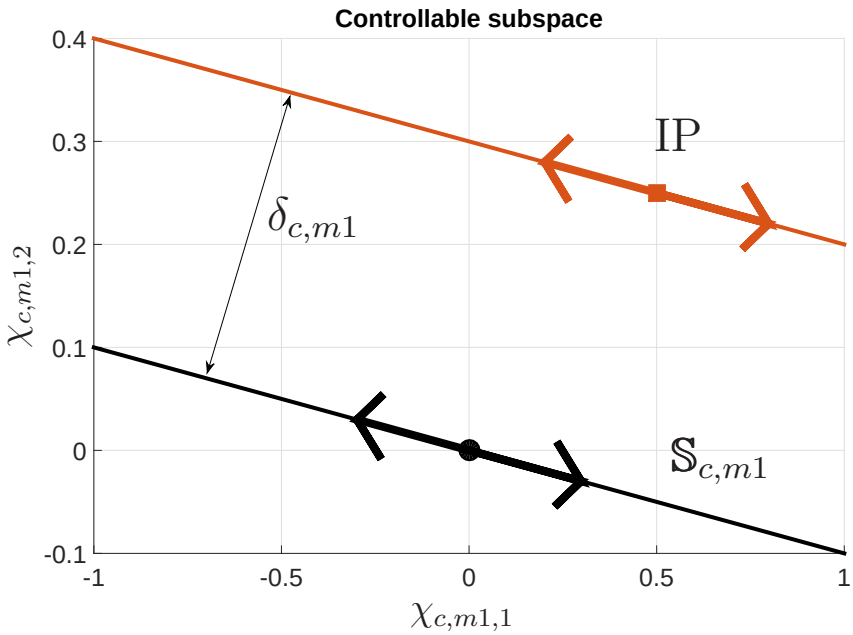

Figure 4.3 Controllable subspace of the system described in Equation (4.19b) for constant values of parameters $d_{c,m1,1}$ and $d_{c,m1,2}$.

Nevertheless, the parameters $d_{c,m1,1}$ and $d_{c,m1,2}$ of the system to be controlled indicated in Equation (4.19b) are not constant, but state-dependent, as well as the virtual manipulated input $f_{c,m1,2}$. Moreover, they depend on the actual manipulated variables $\dot{m}$ and $h_{c,in}$. Therefore a pointwise analysis is carried out, considering the nonlinear equations of the system.

First of all, some equilibrium points have been considered on the phase portrait shown in Figure 4.4. All of them observe the limitation of $h_{c,sc} = h_{c,sc}^{ref}$ imposed previously, thus the two-dimensional control problem of driving $\chi_{c,m1,1}$ and $\chi_{c,m1,2}$ to the origin by using only $f_{c,m1,2}$ as manipulated input is addressed.

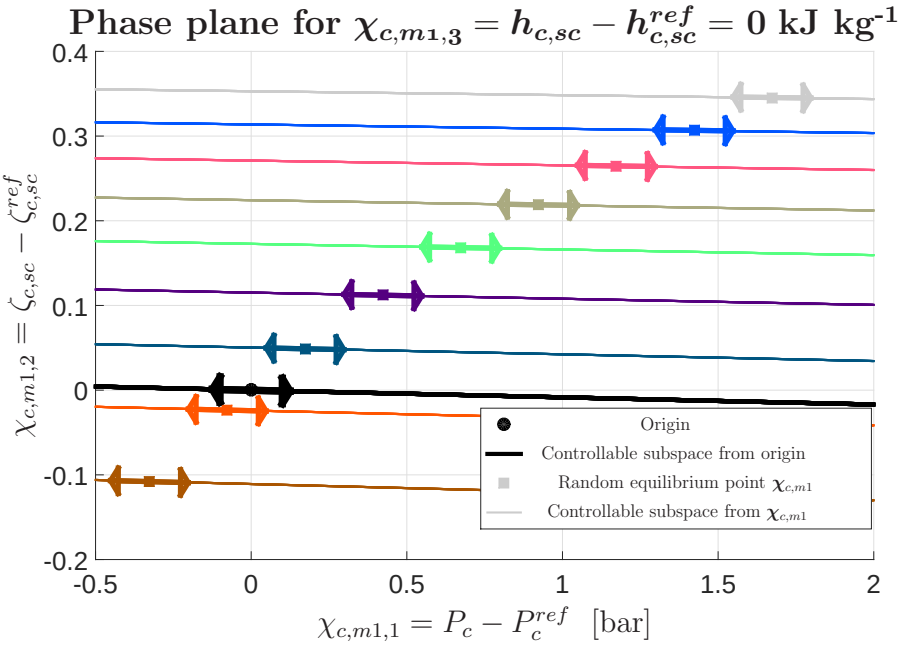

Figure 4.4 Phase plane of the system described in Equation (4.19b).

Then, the values of parameters $d_{c,m1,1}$ and $d_{c,m1,2}$ corresponding to each equilibrium point have been precisely calculated for a variety of actual manipulated inputs $\dot{m}$ and $h_{c,in}$ effectively achievable by the compressor and the expansion valve. All pairs $\{\dot{m}, h_{c,in}\}$ must satisfy the secondary control law shown in Equation Set (4.19a) to ensure that the assumption of $\chi_{c,m1,3} = 0$ holds at any instant. The values of $d_{c,m1,1}$ and $d_{c,m1,2}$ define the slope of the line which represents the controllable subspace for each equilibrium point, as shown in Figure 4.4 for reasonable ranges of $\chi_{c,m1,1}$ and $\chi_{c,m1,2}$ around the origin. Note that the origin and its controllable subspace $\mathbb{S}_{c,m1}$ have been graphically emphasized. Naturally, the values of $d_{c,m1,1}$ and $d_{c,m1,2}$ achieved for each pair $\{\dot{m}, h_{c,in}\}$ are different and thus generate different slopes, but the standard deviation of such slopes with respect

to the mean value has been estimated and it is lower than 1% of the mean value.

As observed on the phase portrait depicted in Figure 4.4, the lines representing the controllable subspaces for each equilibrium point turn out to be quasi-parallel, thus the control problem despite being highly nonlinear is in practice very similar to that analysed in Figure 4.3. Therefore, achieving the origin from an arbitrary equilibrium point is not possible unless the latter is within the controllable subspace from the origin. Intersection between the lines exist since they are not parallel, but in any case the intersection point is distant enough to prevent any controller to achieve appreciable movement out of the controllable subspace due to the physical limits on the control actions.

Similar qualitative results have been obtained when considering $\chi_{c,m1,1}$ and $\chi_{c,m1,2}$ as the state variable regulated by the secondary controller. Figure 4.5 represents the phase portrait when $\chi_{c,m1,1}$ is held at zero at any instant, i.e. the condenser pressure P_c is held at its reference value P_c^{ref}. Furthermore, Figure 4.6 shows the phase portrait when $\chi_{c,m1,2}$ is held at zero at any instant, i.e. the normalised length of the subcooled liquid zone $\zeta_{c,sc}$ is held at its reference value $\zeta_{c,sc}^{ref}$.

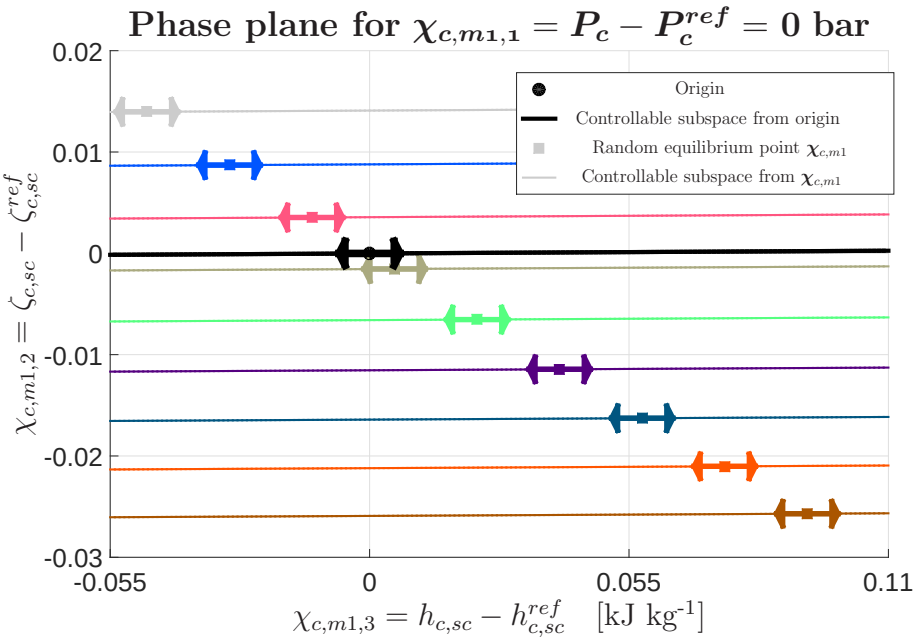

Figure 4.5 Phase plane of the system described in Equation (4.18), when considering $\chi_{c,m1,1}$ controlled.

If the three-dimensional problem is considered, without considering that one of the virtual manipulated inputs is devoted to controlling one of the state variables, the result of

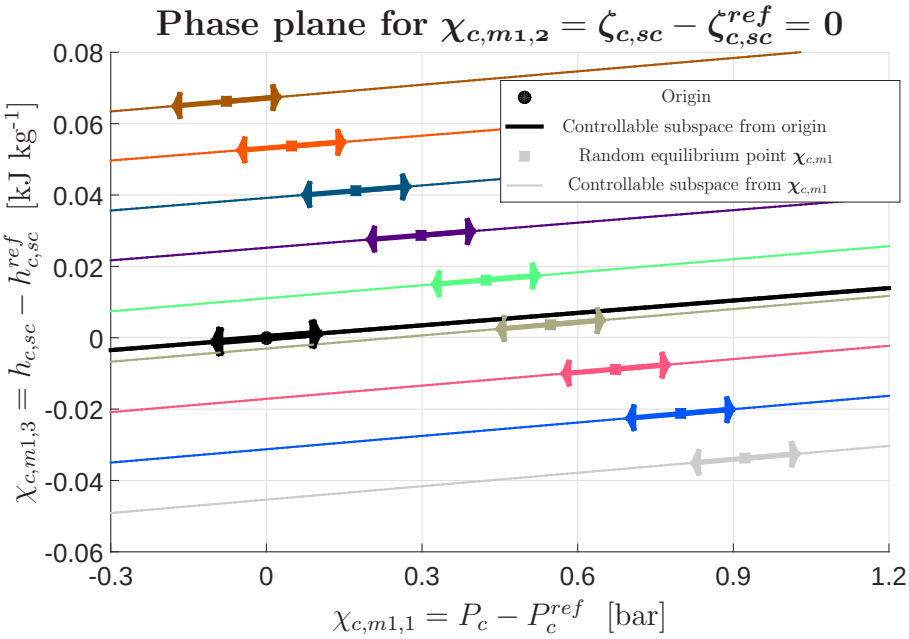

Figure 4.6 Phase plane of the system described in Equation (4.18), when considering $\chi_{c,m1,2}$ controlled.

the nonlinear analysis is a *phase volume*, where the controllable subspaces are quasi-parallel planes.

The condenser *mode* 1 has been previously considered, but the same procedure can be applied to cycles operating in *mode* 2. Then, the phase portraits corresponding to the reduced control problems where each state variable in *mode* 2 is held at its reference value by the secondary controller are included in Figures 4.7 – 4.9.

In conclusion, the degree of controllability of the system both in *modes* 1 and 2 has been graphically proved to be in practice two, as suggested by the analysis based on linear control theory. This explains that all control strategies fail in achieving the optimal cycle for a certain cooling load, as stated in Chapter 1. As shown by the controllability analysis, there exist difficulties in achieving not only the optimal cycle, but in general any given feasible steady-state cycle when starting at a random point, since controllability is a system property, not a controller-dependent issue. Moreover, the controllability analysis has shown that the set of achievable cycles by any control law from a certain starting point is a two-dimensional subspace, which imposes an extra constraint on the search for high energy efficiency.

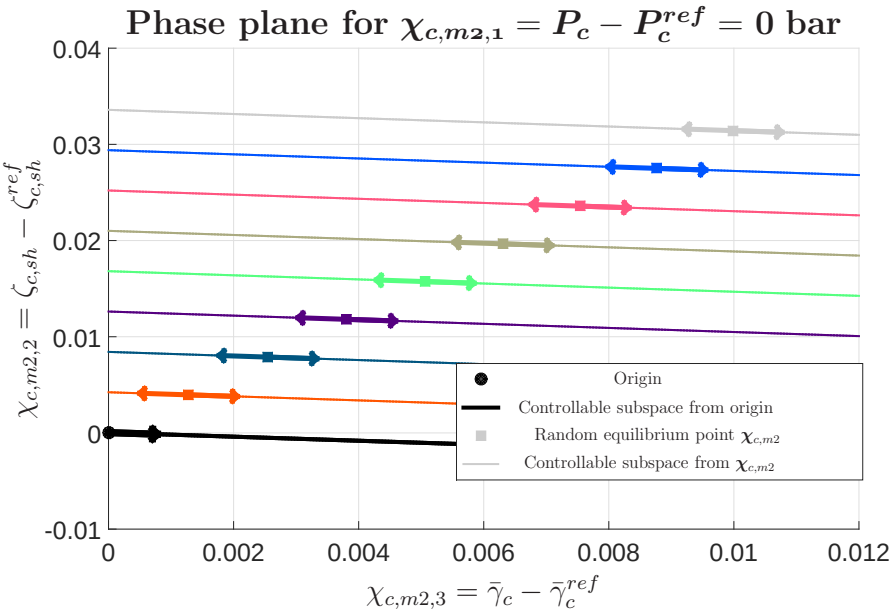

Figure 4.7 Phase plane of the system described in Equation (4.18), when considering $\chi_{c,m2,1}$ controlled.

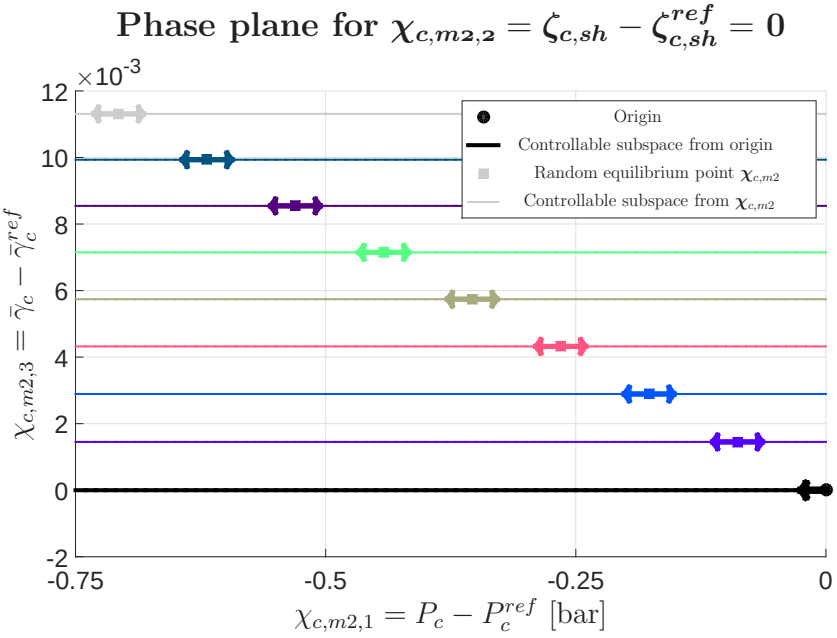

Figure 4.8 Phase plane of the system described in Equation (4.18), when considering $\chi_{c,m2,2}$ controlled.

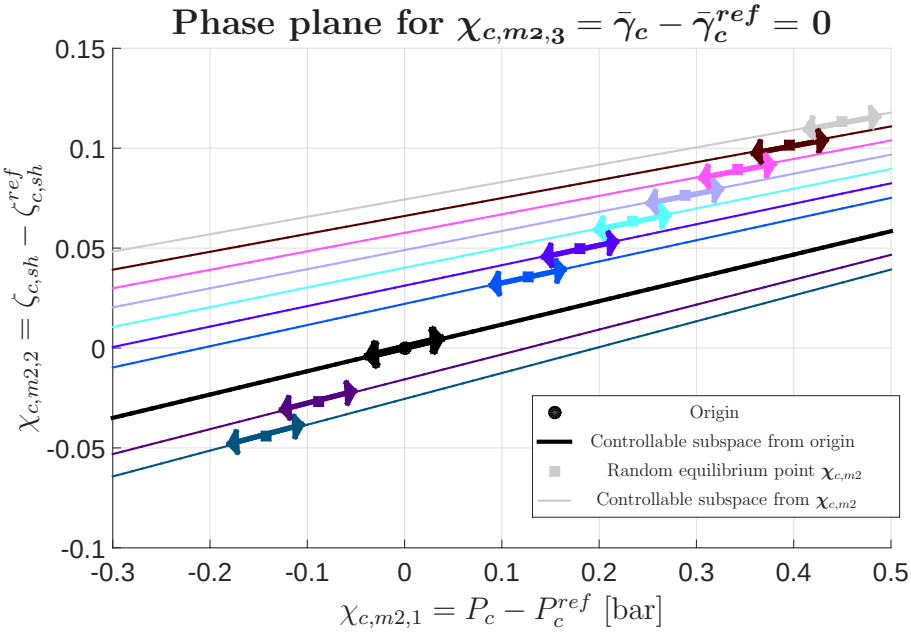

Figure 4.9 Phase plane of the system described in Equation (4.18), when considering $\chi_{c,m2,3}$ controlled.

4.3 Final remarks

In this Chapter the optimal control of vapour-compression refrigeration systems has been addressed. Global optimization of the cycle which satisfies a certain cooling demand has been studied, considering the *COP* as energy-efficiency metrics. The minimum number of variables completely defining a one-stage, one-load-demand cycle is three, provided that two manipulated variables (the compressor speed and the expansion valve opening) have been considered. A nonlinear steady-state model has been used to evaluate the feasibility of the *candidate* cycles, while some technological and operating constraints are also imposed. The model is based in separate steady-state models of all elements, which have already been described in Chapter 2. Optimization results state that optimal cycles are not achieved with minimum degree of superheating for all cooling demand range. It reaffirms the need for a control strategy capable of driving the cycle to the highest efficiency point calculated by the global optimizer.

Moreover, the controllability of the system has been analysed, given the difficulties shown by many control strategies in the literature when trying to achieve the optimal cycle. Considering the state dimension of the simplified control-oriented model presented in Chapter 2 and the length of the variable set which completely defines a cycle, and

assuming that the condenser concentrates the dominant system dynamics, the control problem has been focused on the latter and a controllability analysis on the simplified model has been carried out. Both linear theory and a nonlinear pointwise analysis based on the phase portrait method suggest that in practice there is no full controllability and only a two-dimensional subspace of the three-dimensional solution space can be explored by manipulating the available inputs. Moreover, this issue is expected to appear when applying any control law, since controllability is a system property, not a controller-dependent issue. The controllability analysis is one of the main contributions of the Thesis, since to the author's knowledge it has not been done yet and it highlights the reasons why many control strategies in the literature fail in achieving the optimal cycle.

In the following Chapter the control stage of the strategy is to be analysed. In particular, the results of the global optimization and the lack of full controllability suggested by the analysis performed in this Chapter are taken into account to develop a suboptimal hierarchical control strategy which leads the cycle to effectively achieve the highest possible efficiency while satisfying the cooling load.

5 Control

Action seems to follow feeling, but really action and feeling go together; and by regulating the action, which is under the more direct control of the will, we can indirectly regulate the feeling, which is not.

WILLIAM JAMES

Contents

Control of one-stage, one-load-demand vapour-compression refrigeration systems is addressed in this Chapter. It was stated in Chapter 1 that there are mainly two schemes in the literature about control. The conventional scheme in industry is very simple: in addition to the reference on $T_{e,sec,out}$ imposed by the cooling demand, a low but constant set point on T_{SH} is applied and the controller is designed to get these two variables to track their references as efficiently as possible in presence of disturbances by manipulating N and A_v. Optimal steady-state operation is not explored through the references in the conventional control scheme, but the low degree of superheating set as reference is believed to lead the cycle to high energy efficiency. However, there are other control strategies in the literature where energy efficiency is considered when calculating the references for the low-level controller, which may be updated according to the dynamic behaviour of the system. The objective of this Chapter is to make a contribution in both control schemes: tracking control applied to the conventional scheme, and *energy-efficiency-aware* control.

Regarding the tracking control, most developed techniques are linear controllers. However, as analysed in the literature, when modelling a refrigeration system linearly, some problems could arise and lead to closed-loop instability when applying a linear controller. This is due to the high thermal inertia, dead times, high coupling between system variables, and strong nonlinearities. If the controller was robust enough, it could cope with those issues even at operating points further from the design point, despite its linearity. Indeed, these uncertainties should be studied not only along frequency, as proposed by Larsen and Holm [38], but also at several operating points which could be reached. These operating points depend mainly on the cooling demand, which may vary according to the external conditions of the plant (for instance ambient temperature, inlet temperature of evaporator secondary flux, etc). Therefore, a controller which outperforms at the design point is not intended, but a controller which could work well at several and distant operating points, along with diverse frequency ranges.

According to this, the development of a multivariable centralised H_∞ controller, based on the *S/KS/T* Mixed Sensitivity Problem, is proposed in this Chapter. The objective of this controller is only to track the references on T_{SH} and $T_{e,sec,out}$, which are selected as indicated within the conventional control scheme: the cooling demand is expressed as a desired value for $T_{e,sec,out}$, while a low but constant degree of superheating is set as reference for the tracking controller. First of all, multivariable linear models are proposed and identified at a number of operating points, in order to characterise the main system dynamics. These operating points are selected according to the desired working area of the system, consisting of positive degree of superheating T_{SH}, and also bearing in mind that, for energy-efficiency purposes, some zones of the working area are more likely to be explored in steady state. The linear models have been identified using the step response method, and one of the operating points has been selected as the design one, seeking to minimise the uncertainty region. Secondly, a controllability analysis of the nominal model (that identified at the design point) is performed to find out possible dynamic constraints in its closed-loop performance, being imposed by the inherent features of the system. Finally, a methodology which easily allows to impose the desired performance of the closed-loop system on the calculation of the weighting matrices of the *S/KS/T* Problem is described. This methodology has already successfully applied to other thermodynamic systems, and it has evidenced to be effective in enhancing the closed-loop performance in spite of its

simplicity [86, 87].

Concerning the *energy-efficiency-aware* control, it is observed that all strategies in the literature show trouble in reaching the optimal cycle satisfying a certain cooling demand, as detailed in Chapter 1. Indeed, the mentioned control strategies described in Chapter 1 do not even aspire to achieve the global optimal cycle, but they propose suboptimal solutions manipulating the available control actions. Given the lack of full controllability suggested by the existing control strategies and shown by the controllability analysis performed in Chapter 4, a suboptimal model-based control architecture is proposed. It has been stated that a cycle is defined by three variables but only two can be effectively controlled, and one of them must be devoted to satisfying the cooling demand. Therefore, an online one-degree-of-freedom optimization is proposed to obtain the best reference for the remaining variable to be controlled according to the selected energy-efficiency metrics. The hierarchical control structure is similar to that used by Jain [12]; the difference lies that in this case the global optimal solution is not projected from the optimization space onto the control space, but a suboptimal solution is calculated online considering the dynamic behaviour of the uncontrolled variable. The optimizer considers the cooling demand constraint, as well as some limitations of the components and operating constraints, while a nonlinear steady-state model of the whole cycle is used to characterise the feasible variable sets. Furthermore, the low-level controller which realises the references provided by the optimizer is a novel technique in predictive control field, called Practical Nonlinear Model Predictive Control (PNMPC) [88, 89].

Regarding the online optimizer, the different suboptimal cycles for a given facility and a certain cooling demand are compared regarding the *COP* according to the value considered for the uncontrolled variable. These optimization results are compared to those of the global optimization presented in Chapter 4, Section 4.1. The performance of the SHC architecture is compared to the FB+FF strategy proposed by Jain [12] and the TV-ESC developed by Guay [48], regarding the *COP* achieved in steady state and the dynamic behaviour of the controlled variables.

The contents of this Chapter have been included in some of the publications presented in Chapter 1, Section 1.5 [50, 51, 53, 55, 56, 60, 62, 64].

5.1 Robust H_∞ tracking controller

5.1.1 Modelling

Only the heat exchangers are dynamically modelled, since their dynamics are dominant over the remaining components of the cycle, as stated in Chapter 1. The compressor and expansion valve are statically modelled as detailed in Chapter 2, Subsections 2.1.1 and 2.1.2 respectively. However, the original dynamic modelling of the heat exchangers developed by Li and Alleyne is considered for the design of the robust controller [23]. This model was mostly described in Chapter 2, Subsection 2.2.1, but the latter was in turn a simplification of the original modelling by Li and Alleyne. Only the significant differences are remarked here, since the complete model equations can be found in the work cited for the keen reader.

For all *modes*, the state vectors in Equation Set (5.1) gather all relevant information concerning the condenser and the evaporator at each instant. Note that in this case the wall temperatures at all zones are included as states, which increases the dimension of both state vectors.

$$\begin{aligned} \boldsymbol{x}_c &= [h_{c,sh} \;\; P_c \;\; h_{c,sc} \;\; \zeta_{c,sh} \;\; \zeta_{c,tp} \;\; T_{c,tp,w} \;\; T_{c,sc,w} \;\; \bar{\gamma}_c]^T \\ \boldsymbol{x}_e &= [\zeta_{e,tp} \;\; P_e \;\; h_{e,sh} \;\; T_{e,tp,w} \;\; T_{e,sh,w} \;\; \bar{\gamma}_e]^T \end{aligned} \tag{5.1}$$

The constant dynamic structure formulated in the nonlinear descriptor form shown in Equation Set (2.14) holds for all *modes*. In case of losing any zone, the related state variables hold their values, being only transformed the appropriate equations of the models into auxiliary ones which simply get the corresponding variable to track a reference value.

Some technological requirements are taken into account for the design of the robust controller. As commented in Chapter 1, the refrigerant flow at the compressor intake should never be two-phase, leading the evaporator to work only in *mode* 1. Furthermore, due to energy-efficiency purposes, some combinations of the manipulated variables are more likely to be explored in steady state. Then, the *COP* is represented in the space of the manipulated variables for a given facility in Figure 5.1. Note that zero *COP* values correspond to infeasible combinations of N and A_v.

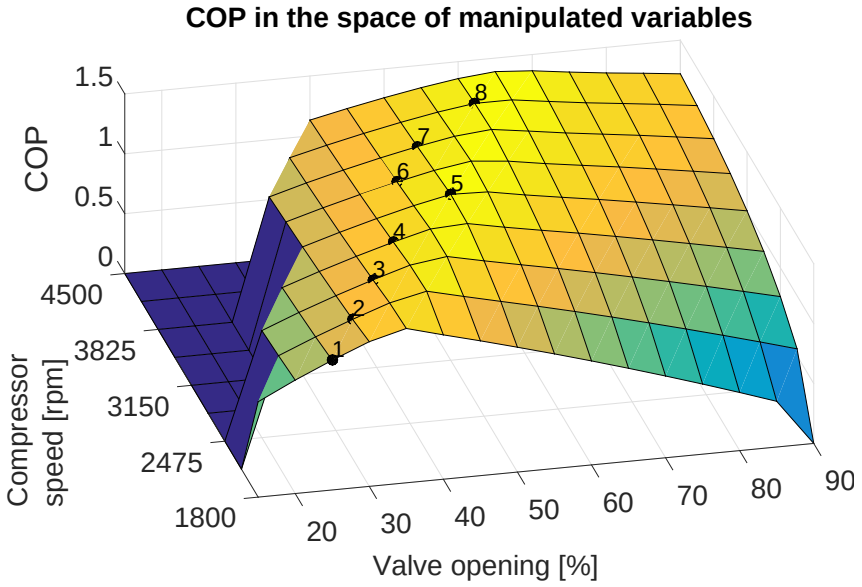

Figure 5.1 Achieved *COP* values in the space of manipulated variables.

A maximum *COP* line from $N = 1800$ rpm to $N = 4500$ rpm and from $A_v = 35\%$ to $A_v = 65\%$ can be noticed in Figure 5.1. The working area, defined as the combinations of manipulated variables which lead to the desired operation of the evaporator (*mode* 1) while ensuring high *COP*, is highlighted in Figure 5.2.

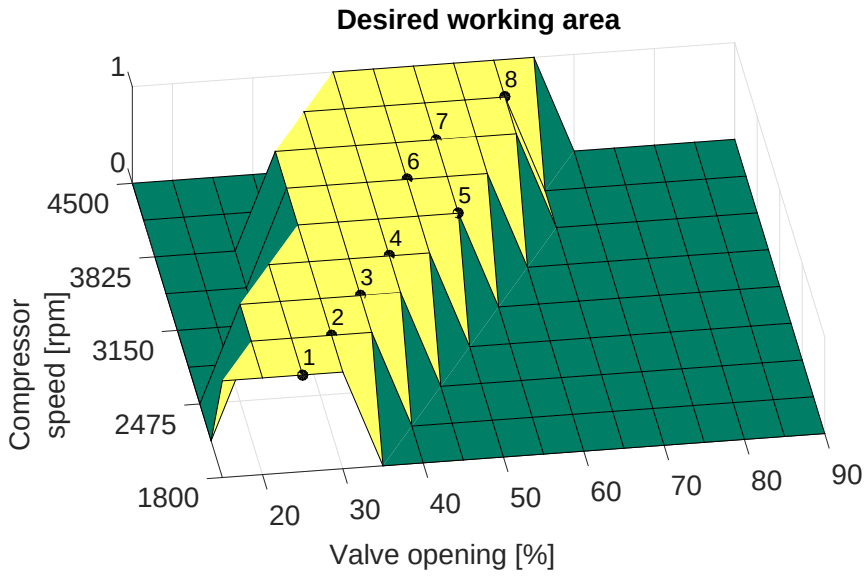

Figure 5.2 Working area represented in the space of manipulated variables.

A series of eight operating points have been selected based on the working area defined in Figure 5.2, and taking into account the maximum *COP* line depicted in Figure 5.1, which approximately matches the right border in Figure 5.2. These points are not uniformly arranged over the working area, but focused around the line which ensures higher *COP* values. Table 5.1 gathers the selected operating points.

Table 5.1 Selected operating points.

Operating point	N **[rpm]**	A_v **[%]**
OP_1	1800	25
OP_2	2138	30
OP_3	2475	35
OP_4	2813	40
OP_5	3150	50
OP_6	3488	45
OP_7	3825	50
OP_8	4163	60

The main dynamics of the system at the selected operating points are characterised by

means of low-order MIMO linear models. These models have been identified using the well-known step response method. Figure 5.3 shows a typical step response (specifically at the operating point OP_4), being those corresponding to the other operating points qualitatively similar. Since the $T_{e,sec,out}$ step response when applying a change on N shows overshooting but not oscillations, and the rest of step responses exhibit non-minimum phase behaviour (although this effect is very fast in the case of the T_{SH} step response when applying a change on N and it is not appreciable in Figure 5.3(a)), every model is expressed in the continuous transfer matrix form shown in Equation (5.2), whose transfer functions have been modelled as a static gain (K_{ij}) and the time constants corresponding to a zero ($\tau_{z_{ij}}$) and two poles, one fast ($\tau_{fast_{ij}}$) and another one slower ($\tau_{slow_{ij}}$).

$$\begin{bmatrix} \Delta T_{SH}(s) \\ \Delta T_{e,sec,out}(s) \end{bmatrix} = \boldsymbol{G}(s) \begin{bmatrix} \Delta N(s) \\ \Delta A_v(s) \end{bmatrix}$$

$$\boldsymbol{G}(s) = \begin{bmatrix} \dfrac{K_{11}(\tau_{z_{11}}s+1)}{(\tau_{fast_{11}}s+1)(\tau_{slow_{11}}s+1)} & \dfrac{K_{12}(\tau_{z_{12}}s+1)}{(\tau_{fast_{12}}s+1)(\tau_{slow_{12}}s+1)} \\ \dfrac{K_{21}(\tau_{z_{21}}s+1)}{(\tau_{fast_{21}}s+1)(\tau_{slow_{21}}s+1)} & \dfrac{K_{22}(\tau_{z_{22}}s+1)}{(\tau_{fast_{22}}s+1)(\tau_{slow_{22}}s+1)} \end{bmatrix} \tag{5.2}$$

The selected nominal operating point is OP_4, since it minimises the uncertainty region. The numerical values of K_{ij}, $\tau_{z_{ij}}$, $\tau_{fast_{ij}}$, and $\tau_{slow_{ij}}$ are collected in Table 5.2.

5.1.2 Controllability analysis

After identifying a linear model which describes the main dynamics of the system at the nominal operating point, a controllability analysis is carried out with the aim of finding out possible limitations on its closed-loop performance [90]. A study of the *zeros* and *poles* and their directions, *singular values*, and *condition number* of the system is performed.

Prior to the controllability analysis, the system has to be *adjusted in scale*, according to the maximum deviation of each input and output, which are indicated in Equation Set (5.3).

$$\begin{aligned} \boldsymbol{u} \quad & \begin{cases} \Delta N^{max} = 337 \text{ rpm} \\ \Delta A_v^{max} = 10\% \end{cases} \\ \boldsymbol{y} \quad & \begin{cases} \Delta T_{SH}^{max} = 4^{\circ}\text{C} \\ \Delta T_{e,sec,out}^{max} = 0.05^{\circ}\text{C} \end{cases} \end{aligned} \tag{5.3}$$

Using these values, the system can be now scaled according to Equation (5.4), where $\boldsymbol{G}_{nom}(s)$ is the transfer matrix identified at the nominal operating point and $\hat{\boldsymbol{G}}_{nom}(s)$ is the

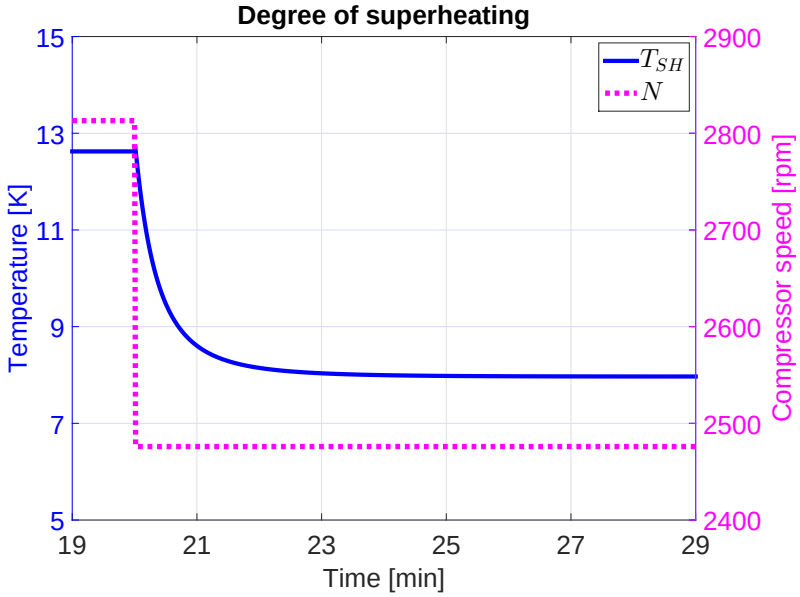

(a) Dynamic response of T_{SH} when applying a step change on N

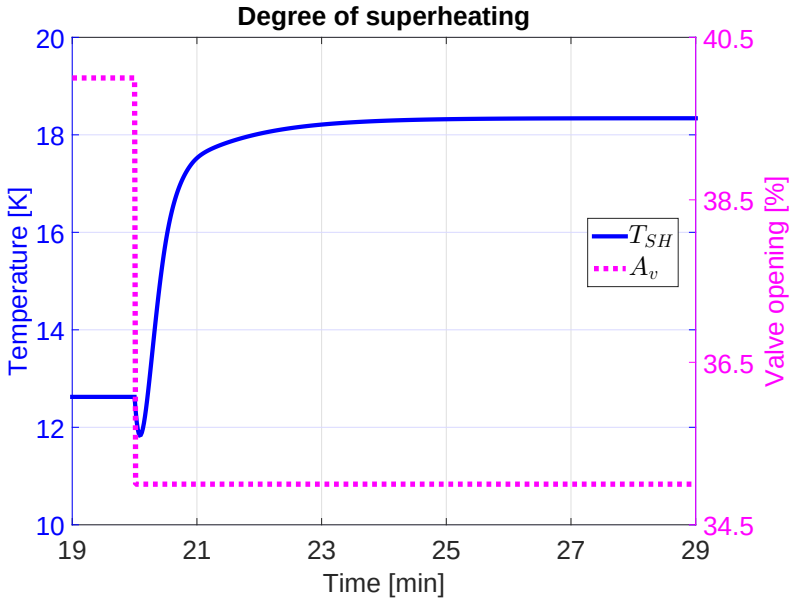

(b) Dynamic response of T_{SH} when applying a step change on A_v

Figure 5.3 Step response at the nominal operating point (OP_4).

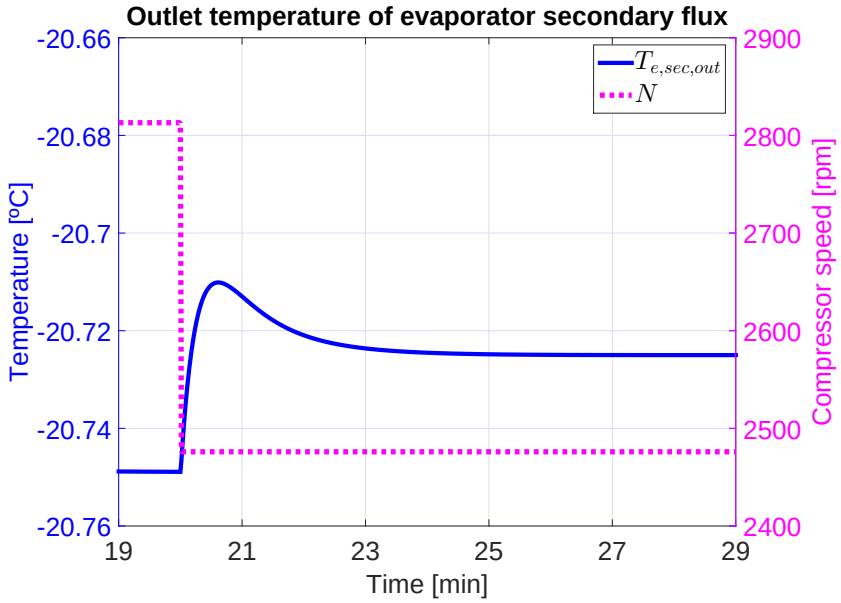

(c) Dynamic response of $T_{e,sec,out}$ when applying a step change on N

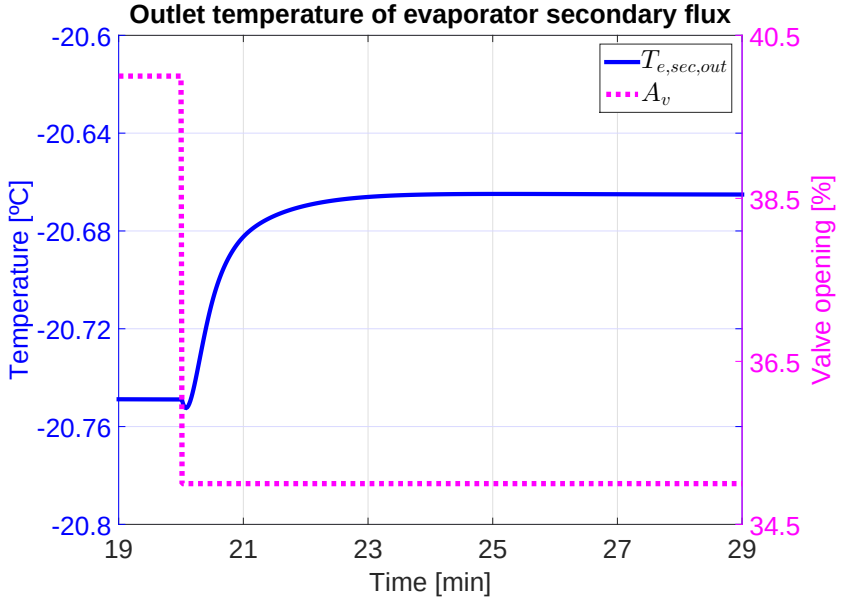

(d) Dynamic response of $T_{e,sec,out}$ when applying a step change on A_v

Figure 5.3 Step response at the nominal operating point (OP_4).

Table 5.2 Numerical values of the identified transfer functions.

Operating point	K $\begin{bmatrix} \text{K rpm} & \text{K \%} \\ \text{K rpm} & \text{K \%} \end{bmatrix}$	τ_z [s]	τ_{fast} [s]	τ_{slow} [s]
OP_1	$\begin{bmatrix} 1.4\cdot10^{-2} & -1.1 \\ -6.3\cdot10^{-5} & -1.6\cdot10^{-2} \end{bmatrix}$	$\begin{bmatrix} -1 & -9.1 \\ 200 & -3.6 \end{bmatrix}$	$\begin{bmatrix} 0.3 & 6.7 \\ 18.2 & 3.6 \end{bmatrix}$	$\begin{bmatrix} 28.6 & 20 \\ 105.3 & 28.6 \end{bmatrix}$
OP_2	$\begin{bmatrix} 1.8\cdot10^{-2} & -1.5 \\ -6.5\cdot10^{-5} & -1.6\cdot10^{-2} \end{bmatrix}$	$\begin{bmatrix} -1 & -5.5 \\ 133 & -3.6 \end{bmatrix}$	$\begin{bmatrix} 0.25 & 4 \\ 15.4 & 3.6 \end{bmatrix}$	$\begin{bmatrix} 25 & 26.3 \\ 66.7 & 33 \end{bmatrix}$
OP_3	$\begin{bmatrix} 1.6\cdot10^{-2} & -1.3 \\ -6.7\cdot10^{-5} & -1.6\cdot10^{-2} \end{bmatrix}$	$\begin{bmatrix} -1 & -5.5 \\ 133 & -5 \end{bmatrix}$	$\begin{bmatrix} 0.3 & 4 \\ 15.4 & 6.7 \end{bmatrix}$	$\begin{bmatrix} 25 & 25 \\ 66.7 & 30.3 \end{bmatrix}$
OP_4	$\begin{bmatrix} 1.4\cdot10^{-2} & -1.1 \\ -7.1\cdot10^{-5} & -1.7\cdot10^{-2} \end{bmatrix}$	$\begin{bmatrix} -1 & -9.1 \\ 142.9 & -6.7 \end{bmatrix}$	$\begin{bmatrix} 0.3 & 6.7 \\ 14.3 & 10 \end{bmatrix}$	$\begin{bmatrix} 28.6 & 20 \\ 66.7 & 25 \end{bmatrix}$
OP_5	$\begin{bmatrix} 1.3\cdot10^{-2} & -1.14 \\ -9.1\cdot10^{-5} & -1.5\cdot10^{-2} \end{bmatrix}$	$\begin{bmatrix} -13 & -13.9 \\ 55 & -12.5 \end{bmatrix}$	$\begin{bmatrix} 11.1 & 9.1 \\ 10.8 & 20 \end{bmatrix}$	$\begin{bmatrix} 12.5 & 22 \\ 20 & 20 \end{bmatrix}$
OP_6	$\begin{bmatrix} 1.1\cdot10^{-2} & -1 \\ -6.2\cdot10^{-5} & -1.7\cdot10^{-2} \end{bmatrix}$	$\begin{bmatrix} -1 & -10 \\ 105.3 & -5 \end{bmatrix}$	$\begin{bmatrix} 0.3 & 4 \\ 12.5 & 7.1 \end{bmatrix}$	$\begin{bmatrix} 13.2 & 20 \\ 58.8 & 25 \end{bmatrix}$
OP_7	$\begin{bmatrix} 9.9\cdot10^{-3} & -1 \\ -6.8\cdot10^{-5} & -1.8\cdot10^{-2} \end{bmatrix}$	$\begin{bmatrix} -1 & -11.8 \\ 105.3 & -5.5 \end{bmatrix}$	$\begin{bmatrix} 0.3 & 5 \\ 12.5 & 10.5 \end{bmatrix}$	$\begin{bmatrix} 13.2 & 18.2 \\ 58.8 & 25 \end{bmatrix}$
OP_8	$\begin{bmatrix} 1.7\cdot10^{-2} & -1.1 \\ -1.6\cdot10^{-4} & -1.5\cdot10^{-2} \end{bmatrix}$	$\begin{bmatrix} -1.25 & -11.8 \\ 41.7 & -10 \end{bmatrix}$	$\begin{bmatrix} 0.5 & 6.7 \\ 13.6 & 11.8 \end{bmatrix}$	$\begin{bmatrix} 22.2 & 20 \\ 33.3 & 20 \end{bmatrix}$

scaled transfer matrix at the same point.

$$\hat{\boldsymbol{G}}_{nom}(s) = \boldsymbol{SM}_{err}^{-1}\, \boldsymbol{G}_{nom}(s)\, \boldsymbol{SM}_u \tag{5.4}$$

Scaling matrices $\boldsymbol{SM}_{err}$ and $\boldsymbol{SM}_u$ have been calculated as indicated in Equation Set (5.5).

$$\begin{aligned} \boldsymbol{SM}_{err} &= \begin{bmatrix} \Delta T_{SH}^{max} & 0 \\ 0 & \Delta T_{e,sec,out}^{max} \end{bmatrix} = \begin{bmatrix} 4 & 0 \\ 0 & 0.05 \end{bmatrix} \\ \boldsymbol{SM}_u &= \begin{bmatrix} \Delta N^{max} & 0 \\ 0 & \Delta A_v^{max} \end{bmatrix} = \begin{bmatrix} 337 & 0 \\ 0 & 10 \end{bmatrix} \end{aligned} \tag{5.5}$$

The first step of the analysis consists in studying the *poles* and *zeros* of the system, as explained by Skogestad and Postlethwaite [90]. Table 5.3 shows these values in the continuous time domain.

Table 5.3 *Poles* and *zeros* of the nominal model.

Roots	Value
Poles	$-7 \cdot 10^{-2}$
	$-5 \cdot 10^{-2}$
	$-4 \cdot 10^{-2}$
	$-3.5 \cdot 10^{-2}$
	$-1.5 \cdot 10^{-2}$
	$-1.5 \cdot 10^{-1}$
	$-1 \cdot 10^{-1}$
	-3.7
Zeros	$-4.51 \cdot 10^{-2} \pm 9.45 \cdot 10^{-3} j$
	$-1.224 \cdot 10^{-2}$
	$-1.224 \cdot 10^{-2}$
	$-1.1 \cdot 10^{-1}$
	$1.21 \cdot 10^{-1}$

The system is stable, as observed in Table 5.3, since there are no unstable *poles*. However, there is a transmission *zero* placed in the right-half plane (RHP), which imposes some constraints considering the closed-loop performance [91]. The RHP-*zero* is located at $z_{RHP} = 1.21 \cdot 10^{-1}$. As stated by Skogestad and Postlethwaite [90], this yields the upper bound to the attainable control bandwidth ω_{cr} stated in Equation (5.6), which leads to the approximate lower bound for the rise time of at least one output t_r indicated in Equation (5.7).

$$\omega_{cr} < \frac{|z_{RHP}|}{2.8} = 4.32 \cdot 10^{-2} \text{ rad/s} \tag{5.6}$$

$$t_r \approx \frac{\pi}{2\omega_{cr}} > 36.4 \text{ s} \tag{5.7}$$

Considering the output direction of the system for the RHP-*zero* is also relevant given the multivariable nature of the system. So, z_{RHP} has the output direction shown in Equation (5.8).

$$\begin{bmatrix} T_{SH} \\ T_{e,sec,out} \end{bmatrix} = \begin{bmatrix} 0.97 \\ 0.245 \end{bmatrix} \tag{5.8}$$

It can be seen in Equation (5.8) that the first component is quite bigger than the second one. Therefore, although the degrading effect of a RHP-*zero* can be moved to a given output [92], its natural effect is focused on the first variable. This way, the control of the degree of superheating at the evaporator outlet is more limited than that of the outlet temperature of the evaporator secondary flux. Therefore, if a tight control on T_{SH} is imposed, the behaviour of $T_{e,sec,out}$ would be strongly degraded.

The *singular values* of the system along frequency are the next topic to be analysed, focusing on the minimum *singular value* because of its relevance as a controllability index. The *singular values* of the nominal model are shown in Figure 5.4, whereas Table 5.4 presents their directions at low frequency [90]. It can be observed that from $\omega_{min,SV} = 10^{-1}$ rad/s onwards the minimum *singular value* becomes less than 0 dB, what means that until that frequency independent output changes can be applied. From $\omega_{min,SV}$ onwards, the dependence between both outputs becomes remarkable. Nevertheless, taking into account the limitations obtained from Equations (5.6) and (5.7), both outputs are independent for all allowed frequencies.

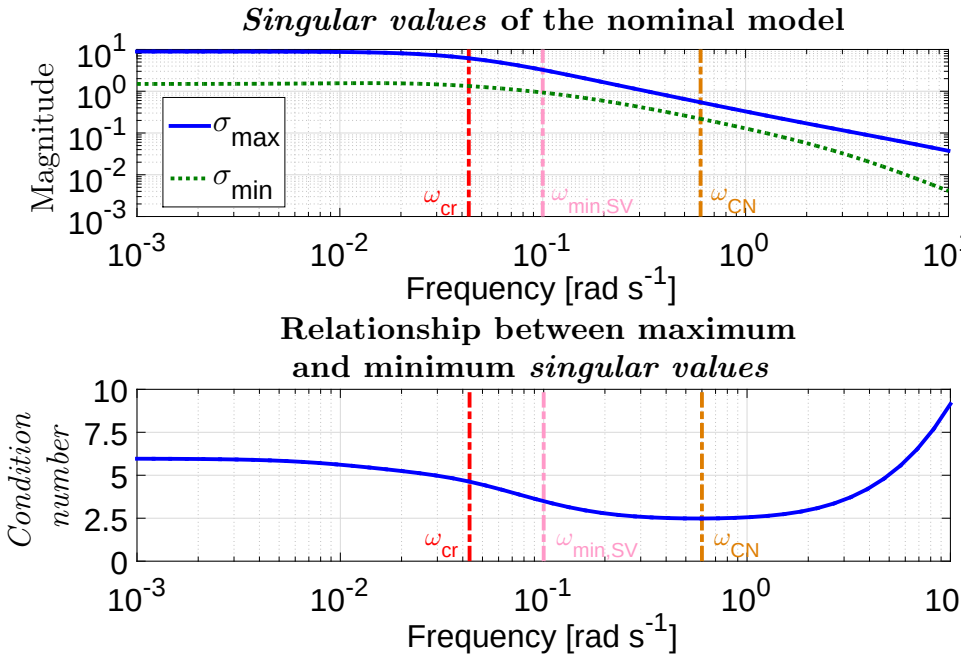

Figure 5.4 *Singular values* and *condition number* of the nominal model along frequency.

Table 5.4 Directions of the *singular values* at low frequency.

Singular value	**Input direction** $[\boldsymbol{N} \quad \boldsymbol{A_v}]^{\boldsymbol{T}}$	**Output direction** $[\boldsymbol{T_{SH}} \quad \boldsymbol{T_{e,sec,out}}]^{\boldsymbol{T}}$
Maximum	$[0.0871 \quad 0.996]^T$	$[0.31 \quad 0.95]^T$
Minimum	$[0.9962 \quad -0.0871]^T$	$[0.95 \quad -0.31]^T$

Eventually, the *condition number* for all considered frequencies is also depicted in Figure 5.4, where the decrease in the minimum *singular value* is faster than that in the maximum value from frequencies roughly $\omega_{CN} = 6 \cdot 10^{-1}$ rad/s. This implies a significant

increase of the *condition number*, which implies that the system can be considered ill-conditioned from ω_{CN} on, therefore making it strongly sensitive to uncertainties. Hence, an additional approximate lower bound for the rise time is obtained, as stated in Equation (5.9). Comparing this bound to that presented in Equation (5.7), the latter seems to impose a harder constraint.

$$t_r \approx \frac{\pi}{2 \cdot \omega_{CN}} = \frac{\pi}{2 \cdot 6 \cdot 10^{-1}} > 2.634 \text{ s} \tag{5.9}$$

5.1.3 H_∞ control synthesis

S/KS/T Mixed Sensitivity Problem

A centralised multivariable robust controller is designed as tracking controller, since the closed-loop system should work fine all over the working area depicted in Figure 5.2. It is difficult to find out the way variations in each model parameter affect the system outputs. Therefore, it is not reasonable to synthesise a controller based on parametric uncertainty, as usual in very complex systems. Thus, a centralised H_∞ controller, based on unstructured uncertainty, is designed, using the Mixed Sensitivity Problem approach.

Following this approach, the controller design can be seen as an optimization. In Figure 5.5 the general formulation of the control problem is represented, where $\boldsymbol{GP}(s)$ is the generalised plant, $\boldsymbol{K}(s)$ the multivariable controller, $\boldsymbol{u}$ the control vector, $\boldsymbol{v}$ the measured variables, $\boldsymbol{\omega}$ the exogenous signals, and $\boldsymbol{z}$ figures the error variables.

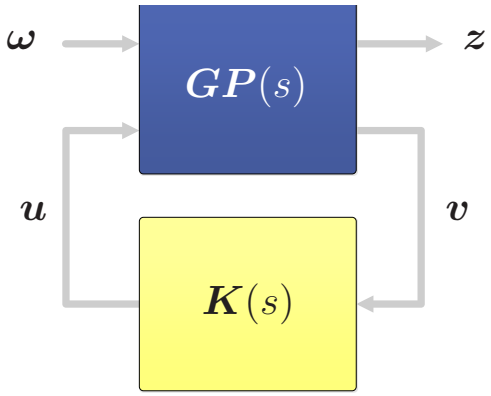

Figure 5.5 General formulation of the control problem.

The objective of the optimal H_∞ control problem is to calculate a controller so that the ratio γ between the energy of $\boldsymbol{z}$ and $\boldsymbol{\omega}$ is as much as possible reduced. This optimal problem is still open, but a solution exists for the suboptimal case [93, 94]. Therefore, the value of γ is decreased as much as possible through an iterative procedure.

The *S/KS/T* Mixed Sensitivity Problem provides the configuration which allows the generation of the generalised plant [95], as shown in Figure 5.6. The closed-loop transfer matrix $\boldsymbol{T}_{\boldsymbol{z\omega}}(s)$ is stated in Equation (5.10), where $\boldsymbol{S}_0(s)$ is the output sensitivity transfer

matrix, $\boldsymbol{T}_0(s)$ is the output complementary sensitivity transfer matrix, and $\boldsymbol{K}(s)\boldsymbol{S}_0(s)$ is the control sensitivity transfer matrix; all of them are indicated in Equation (5.11). $\boldsymbol{W_S}(s)$, $\boldsymbol{W_T}(s)$ and $\boldsymbol{W_{KS}}(s)$ stand for their respective weighting matrices, which are to be designed in order to impose frequency ranges for $\boldsymbol{T_{z\omega}}(s)$.

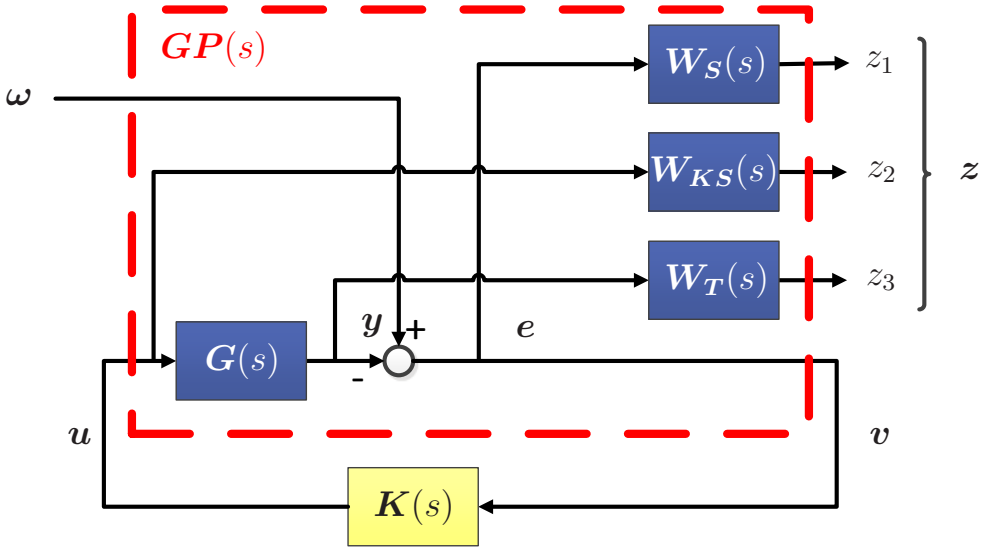

Figure 5.6 *S/KS/T* Mixed Sensitivity configuration.

$$\boldsymbol{T_{zw}}(s) = \begin{bmatrix} \boldsymbol{W_S}(s)\boldsymbol{S}_0(s) \\ \boldsymbol{W_{KS}}(s)\boldsymbol{K}(s)\boldsymbol{S}_0(s) \\ \boldsymbol{W_T}(s)\boldsymbol{T}_0(s) \end{bmatrix} \tag{5.10}$$

$$\begin{aligned} \boldsymbol{S}_0(s) &= [\boldsymbol{I} + \boldsymbol{G}(s)\boldsymbol{K}(s)]^{-1} \\ \boldsymbol{K}(s)\boldsymbol{S}_0(s) &= \boldsymbol{K}(s)\,[\boldsymbol{I} + \boldsymbol{G}(s)\boldsymbol{K}(s)]^{-1} \\ \boldsymbol{T}_0(s) &= \boldsymbol{G}(s)\boldsymbol{K}(s)\,[\boldsymbol{I} + \boldsymbol{G}(s)\boldsymbol{K}(s)]^{-1} \end{aligned} \tag{5.11}$$

Proper shaping of $\boldsymbol{T}_0(s)$ is desirable for tracking problems, noise attenuation, and robust stability regarding multiplicative output uncertainties. Moreover, convenient shaping of $\boldsymbol{S}_0(s)$ improves the dynamic performance of the closed-loop system. Matrix $\boldsymbol{K}(s)\boldsymbol{S}_0(s)$ only helps to prevent numerical issues in the controller synthesis.

Therefore, since the controller is obtained from the generalised plant, the synthesis problem with this configuration is reduced to the design of some appropriate weighting matrices which will impose the control specifications. Once this is done, the generalised plant can be built up as shown in Figure 5.6, and consequently the controller can be computed through a synthesis algorithm.

Design of weighting matrices

The selection of the weighting matrices $\boldsymbol{W_S}(s)$ and $\boldsymbol{W_T}(s)$ has been accomplished following the design rules proposed by Ortega *et al.* [86, 96]. Thus, once the scaled nominal model is available (see Equation (5.4)), the maximum *singular values* of the multiplicative output uncertainty can be estimated as shown in Equation (5.12), where $\hat{\boldsymbol{G}}(j\omega)$ is the frequency response of the scaled nominal model and $\hat{\boldsymbol{G}}_{OP_i}(j\omega)$ stands for the system frequency response at the operating point $\mathrm{OP_i}$ (i = 1,2,...,8). These maximum *singular values* are shown in Figure 5.7.

$$\sigma_{max}(\hat{\boldsymbol{E}}_{OP_i}(j\omega)) = \sigma_{max}\Big((\hat{\boldsymbol{G}}_{OP_i}(j\omega) - \hat{\boldsymbol{G}}(j\omega))\,\hat{\boldsymbol{G}}^{-1}(j\omega)\Big) \tag{5.12}$$

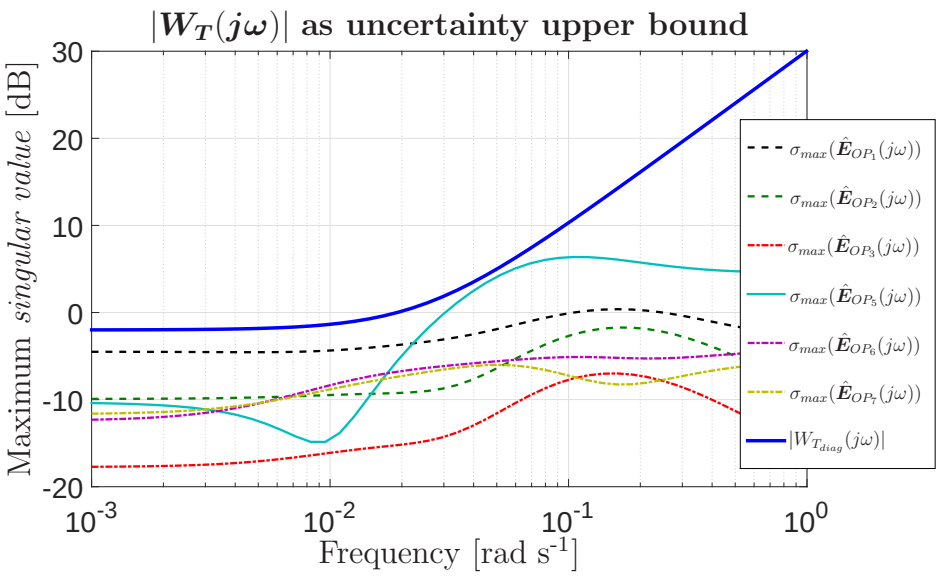

Figure 5.7 $|\boldsymbol{W_T}(j\omega)|$ as an upper bound of the maximum *singular values* of the multiplicative output uncertainties.

Then, $\boldsymbol{W_T}(s)$ is designed as a square diagonal matrix, as indicated in Equation (5.13), where its diagonal elements are the same: a transfer function $W_{T_{diag}}(s)$ which must be stable, minimum phase, and with a high gain at high frequency, but the most important requirement is that its magnitude must be greater than the maximum *singular value* of the calculated uncertainty, for all non-nominal models and frequency, as shown in Equation (5.14). $W_{T_{diag}}(s)$ has been designed as indicated in Equation (5.15), and its magnitude is depicted over Figure 5.7, proving the fulfilment of the specifications.

$$\boldsymbol{W_T}(s) = W_{T_{diag}}(s)\boldsymbol{I}_{2x2} \tag{5.13}$$

$$|W_{T_{diag}}(j\omega)| \geqslant \sigma_{max}(\hat{\boldsymbol{E}}_{OP_i}(j\omega)) \quad \forall\omega,\ \forall \mathrm{OP_i} \tag{5.14}$$

$$W_{T_{diag}}(s) = \frac{31.773s + 0.79433}{0.00565s + 1} \tag{5.15}$$

$\boldsymbol{W_S}(s)$ is taken as a square diagonal matrix of transfer functions, as stated in Equation (5.16), where each diagonal element $W_{S_j}(s)$ is designed following the general formulation stated in Equation (5.17).

$$\boldsymbol{W_S}(s) = \begin{bmatrix} W_{S_{T_{SH}}}(s) & 0 \\ 0 & W_{S_{T_{e,sec,out}}}(s) \end{bmatrix} \tag{5.16}$$

$$W_{S_j}(s) = \frac{\mu_j s + 10^{(\kappa_j - 1)}\omega_T}{s + \beta_j 10^{(\kappa_j - 1)}\omega_T} \qquad j = T_{SH}, T_{e,sec,out} \tag{5.17}$$

ω_T is the crossover frequency of $W_{T_{diag}}(s)$ and its value is about $1.92 \cdot 10^{-2}$ rad/s, as observed in Figure 5.7. The design parameters μ_j and β_j $(j = T_{SH}, T_{e,sec,out})$ are the transfer function gains at high and low frequencies, respectively. According to the methodology proposed by Ortega and Rubio [96], the values shown in Equation Set (5.18) have been chosen.

$$\begin{aligned} \mu_{T_{SH}} &= \mu_{T_{e,sec,out}} = 0.5 \\ \beta_{T_{SH}} &= \beta_{T_{e,sec,out}} = 10^{-4} \end{aligned} \tag{5.18}$$

Eventually, dimensionless parameters $\kappa_{T_{SH}}$ and $\kappa_{T_{e,sec,out}}$ determine the corresponding transfer function bandwidth. The higher this parameter is, the faster the corresponding output tracks its reference. In this design values of $\kappa_{T_{SH}} = 0.95$ and $\kappa_{T_{e,sec,out}} = 1.05$ are used. Then, the weighting design is completed after making weight $\boldsymbol{W_{KS}}(s)$ equal to the identity matrix in order to avoid numerical problems in the synthesis algorithm.

Once the weighting matrices have been designed, the generalised plant shown in Figure 5.6 can be built up, and therefore, the controller can be computed.

Design results

The H_∞ controller synthesis yields $\gamma = 1.3392$. In agreement with Equation (5.19) and bearing in mind that it is a multivariable problem, it is considered that the design is suitable, since γ is close enough to one to ensure that all the sensitivity functions keep below their weighting functions. However, they are depicted below in order to check if the design is robust enough.

$$||\boldsymbol{T_{zw}}(s)||_\infty = \left|\left| \begin{pmatrix} \boldsymbol{W_S}(s)\boldsymbol{S_0}(s) \\ \boldsymbol{W_{KS}}(s)\boldsymbol{K}(s)\boldsymbol{S_0}(s) \\ \boldsymbol{W_T}(s)\boldsymbol{T_0}(s) \end{pmatrix} \right|\right|_\infty < \gamma \tag{5.19}$$

The diagonal output sensitivity transfer functions and their weighting transfer functions are shown in Figure 5.8. Moreover, in Figure 5.9 the diagonal output complementary sensitivity transfer functions and $W_{T_{diag}}(s)$ are represented. Indeed it is proven that all the

sensitivity functions hold below their weights within the considered frequency range and hence the designed controller is robust.

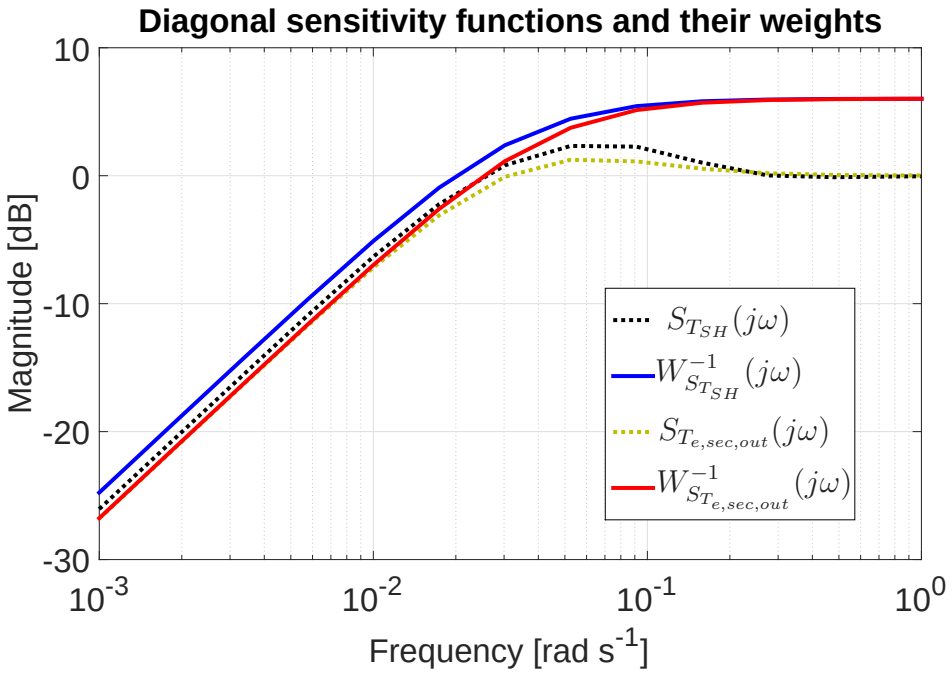

Figure 5.8 Diagonal output sensitivity functions and their weights.

Table 5.5 shows the crossover frequencies with -3 dB (ω_B) of the diagonal sensitivity functions shown in Figure 5.9, which provide an insight of closed-loop response for each output variable, together with the corresponding rise time (t_r). It is shown how the closed-loop response of $T_{e,sec,out}$ is expected to be faster than that of T_{SH}.

Table 5.5 Crossover frequencies of the diagonal output sensitivity functions.

Output variable	ω_B [rad s^{-1}]	t_r [s]
T_{SH}	$1.5 \cdot 10^{-2}$	102.3
$T_{e,sec,out}$	$1.8 \cdot 10^{-2}$	89.1

At this point, it is important to remember that the controller has been synthesised from a scaled model. To figure out the controller to be implemented in the real application it is necessary to carry out a reverse scaling procedure, according to Equation (5.20), where

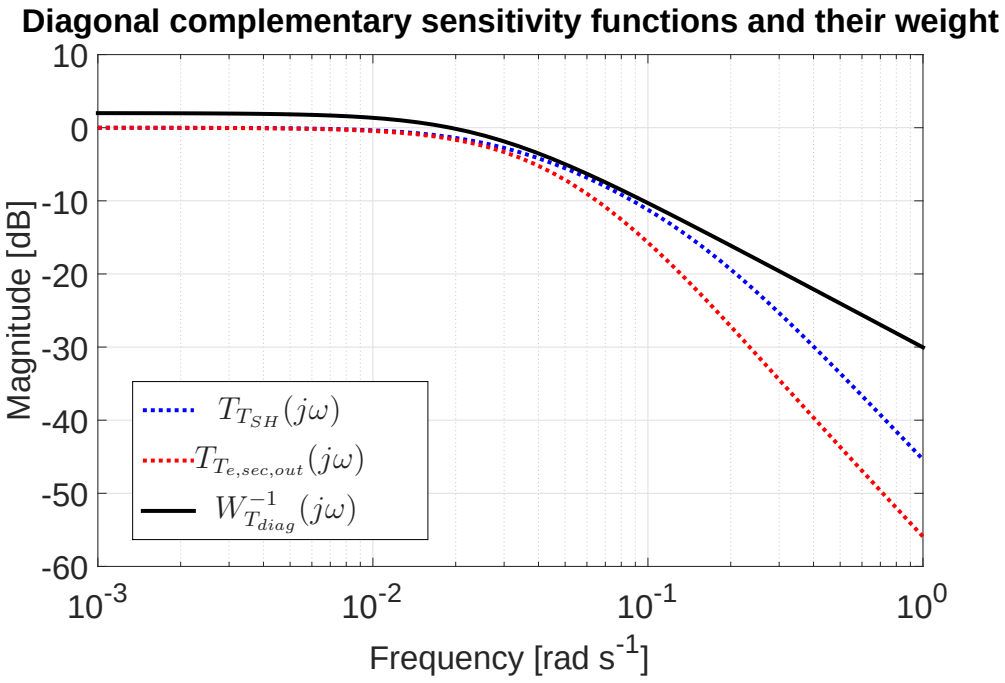

Figure 5.9 Diagonal output complementary sensitivity functions and their weight.

$\boldsymbol{SM}_u$ and $\boldsymbol{SM}_{err}$ were defined in Equation (5.5).

$$\boldsymbol{K}(s) = \boldsymbol{SM}_u \, \hat{\boldsymbol{K}}(s) \, \boldsymbol{SM}_{err}^{-1} \tag{5.20}$$

Numerical issues must be addressed in order to avoid controller fragility. Firstly, since $\boldsymbol{K}(s)$ is usually a high order controller (in this case as far as 12), its order should be reduced. To do this, the *Hankel singular values* are computed and lower energy states are thus not considered [90]. Secondly, the controller has some *poles* near zero, but not integral effect, therefore it is convenient to turn these *poles* into integrators in order to ensure zero steady-state error.

5.1.4 Tracking controller comparison

Reference tracking

Simulation results provided by the designed H_∞ controller are presented in this Subsection, in comparison with those given by a decentralised PID controller (similar to that described by Marcinichen *et al.* [27]), and those provided by a MPC. The decentralised PID controller has been designed at the nominal operating point OP_4 and it manipulates N and A_v to control $T_{e,sec,out}$ and T_{SH}, respectively. Regarding the MPC, it has been designed considering the multivariable model at the nominal operating point OP_4 and following the standard generalised predictive controller procedure with constraints involving control

and output variables [97, 98]. Prediction and control horizons of 15 and 10 sample times are respectively applied, taking into account that the prediction horizon starts when the non-minimum phase behaviour is over. Error and control variable weights are gathered in Equation Set (5.21). The sampling time is set to 6 seconds, due to the duty cycle of the selected expansion valve. The refrigerant used to simulate the compression cycle is R404a and all simulations have been carried out using MATLAB® computing software and the *CoolProp* tool [69].

$$\boldsymbol{R} = \begin{bmatrix} 8.7 & 0 \\ 0 & 2.8 \cdot 10^4 \end{bmatrix} \qquad \boldsymbol{Q} = \begin{bmatrix} 10^2 & 0 \\ 0 & 2.8 \cdot 10^6 \end{bmatrix} \tag{5.21}$$

Firstly, the H_∞ controller performance is studied at the nominal operating point (OP_4). Two downward steps on the set points are applied in Figure 5.10, being the first one at $t = 65$ min on the reference on T_{SH}, holding the set point on $T_{e,sec,out}$. The second one is applied at $t = 110$ min, swapping variable references. The manipulated variables are shown in Figure 5.11. Note that the variations of the steps applied on the reference on $T_{e,sec,out}$ are small in order to avoid the saturation of the valve opening, whose capacity is reduced due to the model choice [11].

As observed in Figure 5.10, showing a similar rise time, the H_∞ controller presents better performance and lower settling time than the PID controller. Regarding the MPC, it shows no overshooting, but its settling time is greater than that of the H_∞ controller. Higher speed of the predictive control has been intended by tuning the weights $\boldsymbol{Q}$ and $\boldsymbol{R}$, but the control system shows instability. Both centralised controllers (H_∞ and MPC) show lower coupling than the PID when alternating reference changes are simulated, but the H_∞ controller achieves better performance.

Similar simulations have been also carried out at a non-nominal operating point (namely OP_6) to prove the robustness of the H_∞ controller, using alternating references changes. Figures 5.12 and 5.13 show the simulation results for all controllers. It is important to remark that, while the H_∞ controller is robust and works fine at different operating points, the MPC which has been designed at the nominal point becomes unstable at the non-nominal one OP_6, showing its limited robustness. The simulation results included in Figures 5.12 and 5.13 concerning the MPC are achieved using a purpose-designed MPC at OP_6, considering the corresponding matrix transfer function and tuning again the weights and prediction and control horizons.

Moreover, the H_∞ controller performance in the troublesome output directions shown in Subsection 5.1.2 is studied in Figures 5.14 and 5.15. Simultaneous reference changes in the output direction of the system for the RHP-*zero* are applied at $t = 65$ min starting at the nominal operating point. Similarly, simultaneous reference changes in the output direction of the maximum and minimum *singular values* at low frequency (detailed in Table 5.4) are applied at $t = 155$ min and $t = 245$ min, respectively. Reference steps at $t = 110$ min and $t = 200$ min just drive the system to the nominal operating point after the reference changes in the troublesome output directions.

Some interesting indicators of the represented dynamic responses are gathered in Tables 5.6 and 5.7, comparing all controllers. Note that ISE and ITAE indices regarding coupling

measurement are not calculated in the cases of RHP-*zero*, and maximum and minimum *singular value* output directions, since simultaneous reference changes are applied, as previously commented.

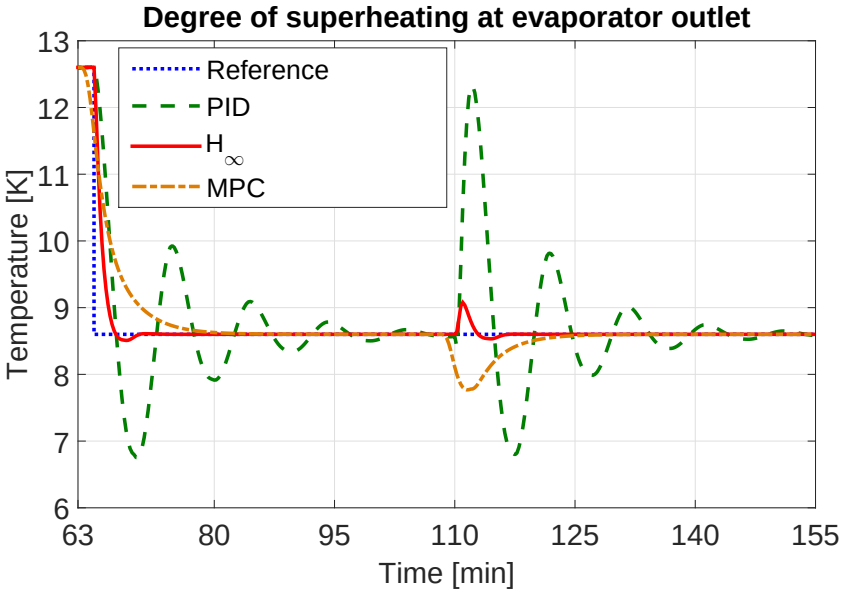

(a) Degree of superheating at evaporator outlet

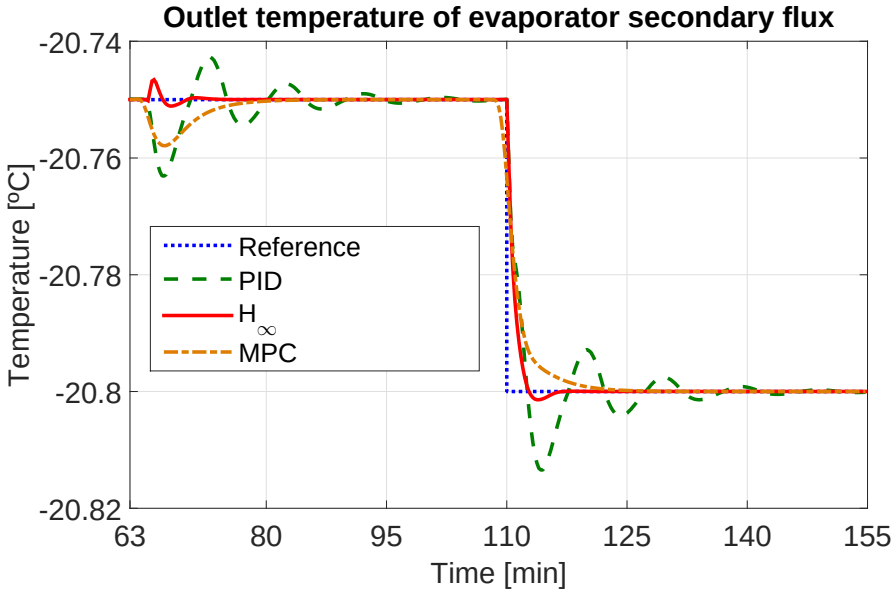

(b) Outlet temperature of evaporator secondary flux

Figure 5.10 Control of output variables at the nominal operating point.

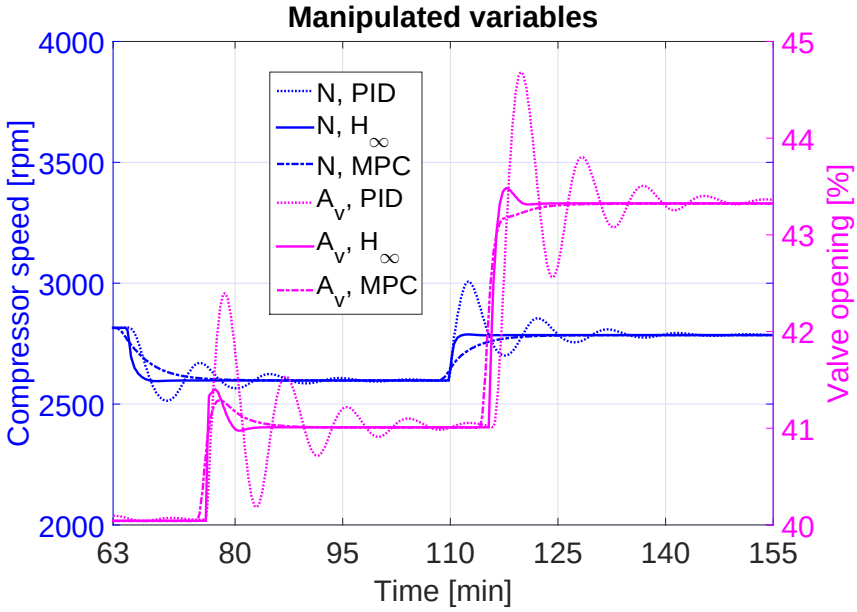

Figure 5.11 Manipulated variables at the nominal operating point.

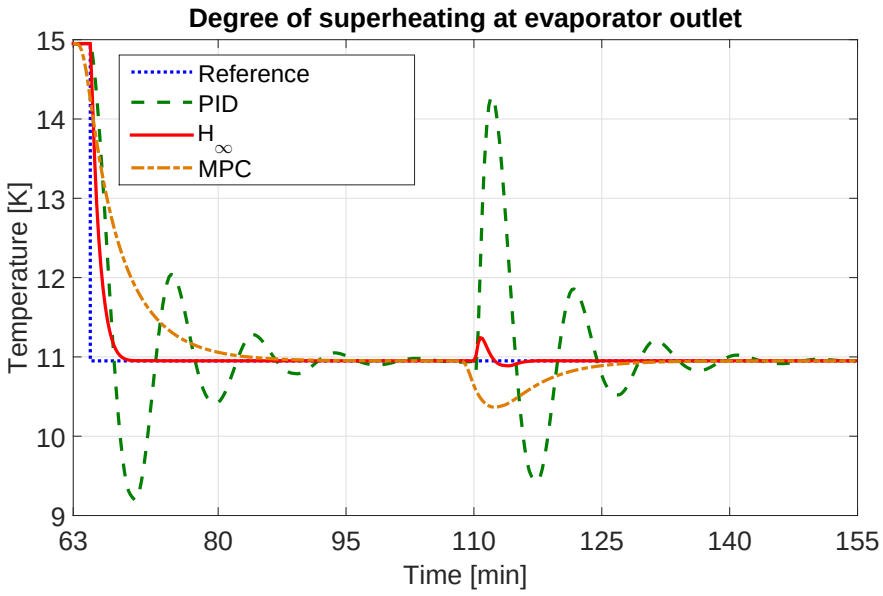

(a) Degree of superheating at evaporator outlet

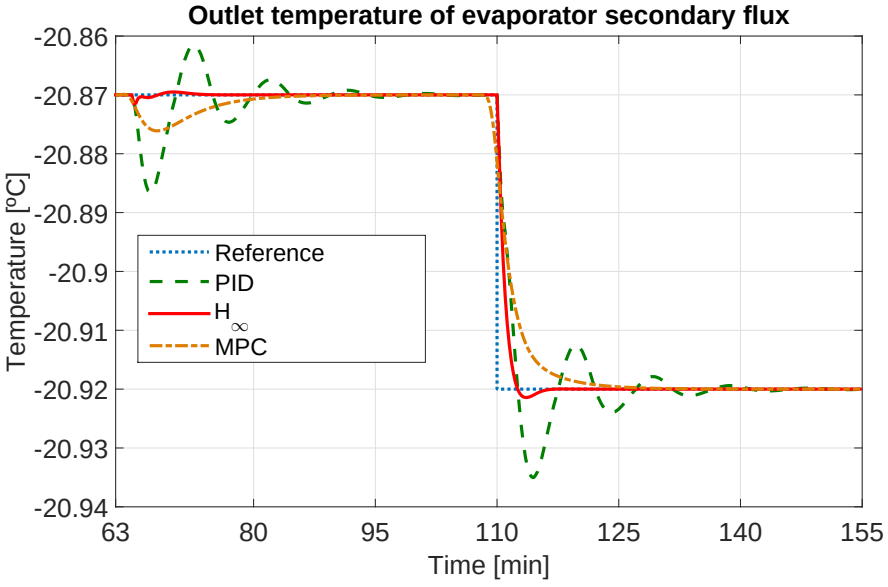

(b) Outlet temperature of evaporator secondary flux

Figure 5.12 Control of output variables at a non-nominal operating point (OP_6).

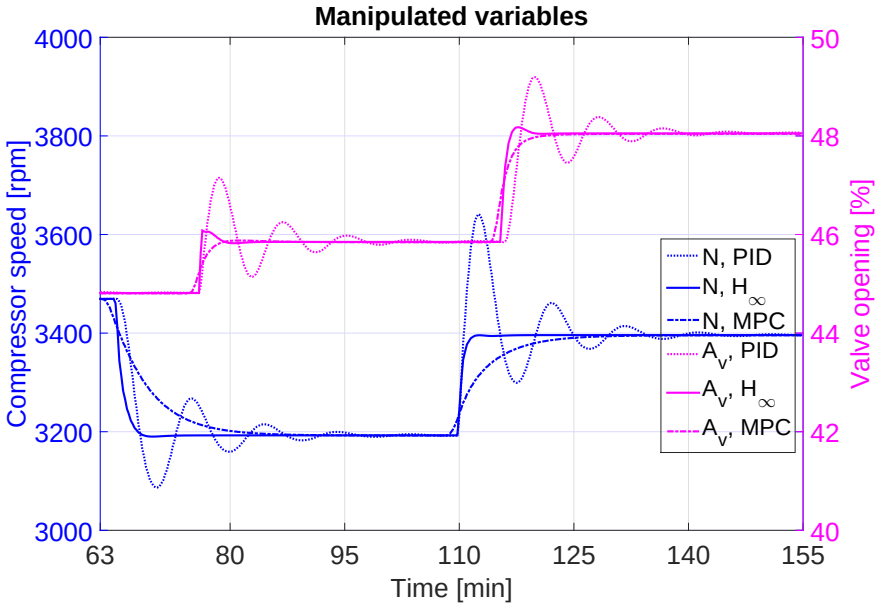

Figure 5.13 Manipulated variables at a non-nominal operating point (OP_6).

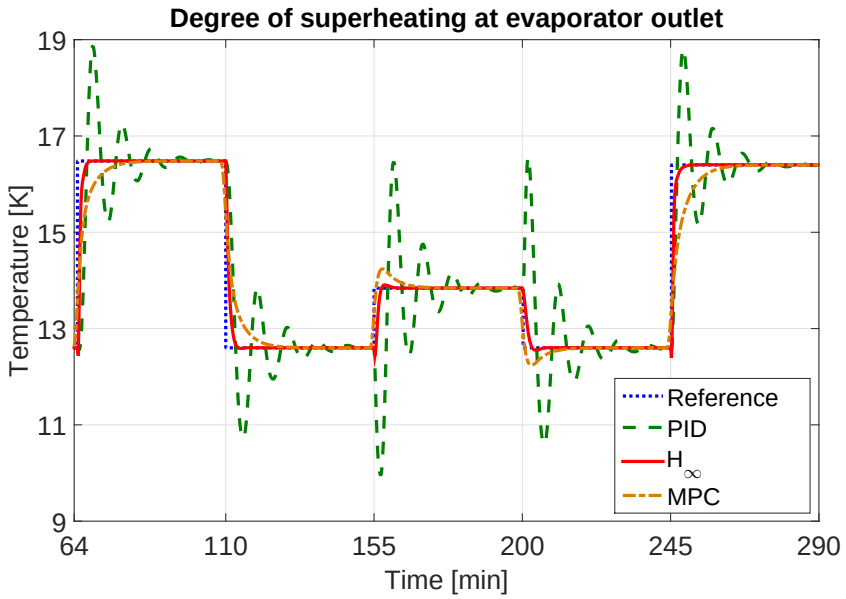

(a) Degree of superheating at evaporator outlet

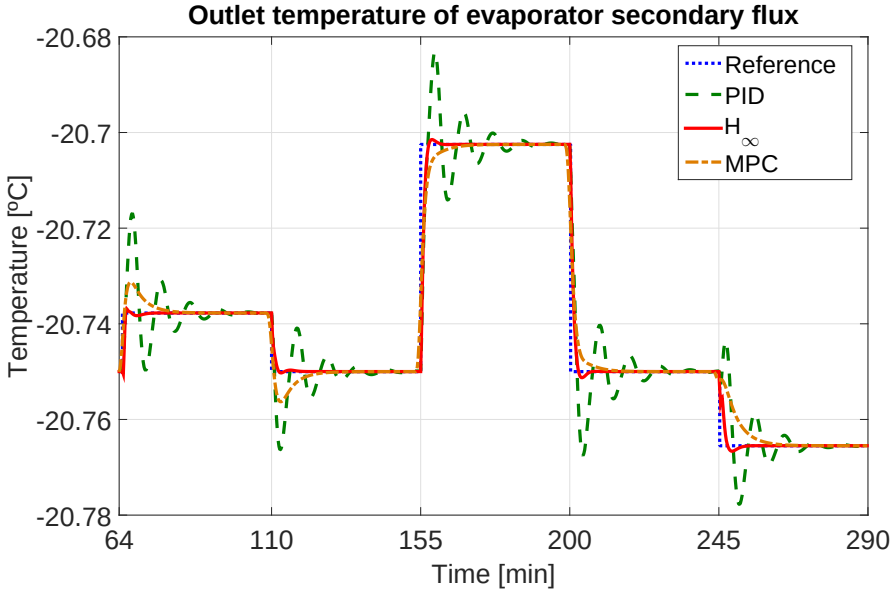

(b) Outlet temperature of evaporator secondary flux

Figure 5.14 Control of output variables in the troublesome output directions.

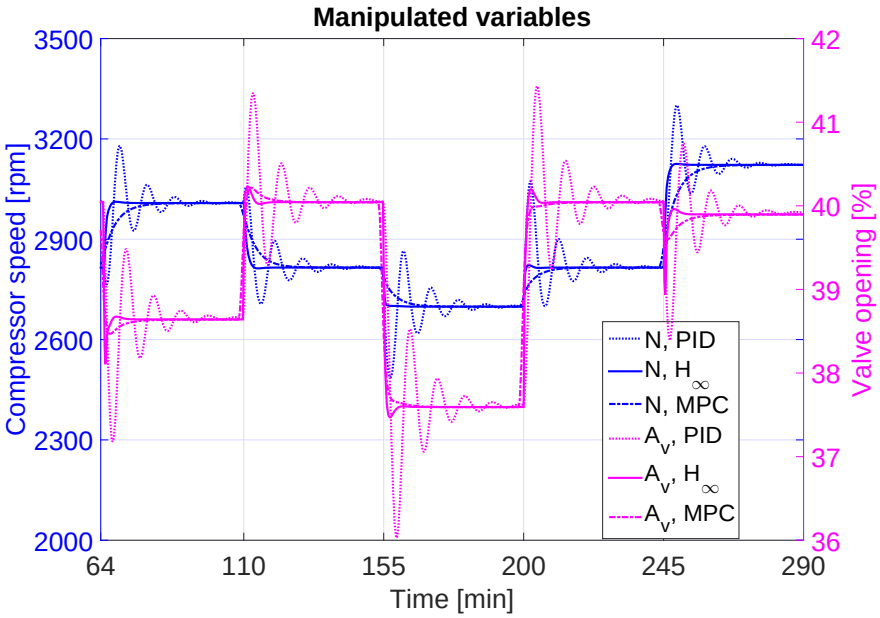

Figure 5.15 Manipulated variables when applying reference changes in the troublesome output directions.

Table 5.6 Closed-loop performance indicators of T_{SH} in different simulations.

Simulation	Controller	Reference tracking				Coupling measurement	
		t_s [s]	t_r [s]	PO [%]	ITAE [K s^2]	ISE [K s]	ITAE [K s^2]
Reference tracking at the nominal point OP_4	PID	1548	167	46.23	$7.13 \cdot 10^5$	$2.59 \cdot 10^3$	$7.90 \cdot 10^5$
	MPC	492	–	0	$2.62 \cdot 10^5$	$1.64 \cdot 10^2$	$1.57 \cdot 10^5$
	H_∞	129	164	2.25	$1.3 \cdot 10^4$	$1.41 \cdot 10^1$	$7.24 \cdot 10^3$
Reference tracking at the non-nominal point OP_6	PID	451	168	43.95	$5.06 \cdot 10^5$	$1.96 \cdot 10^3$	$5.48 \cdot 10^5$
	MPC	735	–	0	$4.82 \cdot 10^5$	$1.20 \cdot 10^2$	$1.99 \cdot 10^5$
	H_∞	77	-	0	$1.51 \cdot 10^4$	$5.26 \cdot 10^0$	$5.97 \cdot 10^3$
RHP-*zero* output direction	PID	1422	172	61.47	$5.96 \cdot 10^5$	–	–
	MPC	522	–	0	$2.57 \cdot 10^5$	–	–
	H_∞	131	-	0	$1.32 \cdot 10^4$	–	–
Maximum *singular value* output direction at low frequency	PID	2032	250	313.7	$8.3 \cdot 10^5$	–	–
	MPC	642	36	2.89	$9.81 \cdot 10^4$	–	–
	H_∞	123	139	5.43	$1.01 \cdot 10^4$	–	–
Minimum *singular value* output direction at low frequency	PID	1341	121	63.4	$5.32 \cdot 10^5$	–	–
	MPC	631	–	0	$3.78 \cdot 10^5$	–	–
	H_∞	129	-	0	$1.51 \cdot 10^4$	–	–

Table 5.7 Closed-loop performance indicators of $T_{e,sec,out}$ in different simulations.

Simulation	Controller	Reference tracking				Coupling measurement	
		t_s [s]	t_r [s]	PO [%]	ITAE [K s^2]	ISE [K s]	ITAE [K s^2]
Reference tracking at the nominal point OP_4	PID	967	154	26.8	$3.81 \cdot 10^3$	$3.53 \cdot 10^{-2}$	$3.25 \cdot 10^3$
	MPC	330	–	0	$2.08 \cdot 10^3$	$1.50 \cdot 10^{-2}$	$1.67 \cdot 10^3$
	H_∞	288	167	2.8	$1.94 \cdot 10^2$	$6.88 \cdot 10^{-4}$	$1.12 \cdot 10^2$
Reference tracking at the non-nominal point OP_6	PID	1176	154	30.2	$3.49 \cdot 10^3$	$5.25 \cdot 10^{-2}$	$3.09 \cdot 10^3$
	MPC	468	–	0	$2.83 \cdot 10^3$	$1.25 \cdot 10^{-2}$	$2.14 \cdot 10^3$
	H_∞	129	153	2.8	$1.45 \cdot 10^2$	$1.23 \cdot 10^{-4}$	$6.23 \cdot 10^1$
RHP-*zero* output direction	PID	1610	54	170	$4.12 \cdot 10^3$	–	–
	MPC	1368	34.2	0.03	$4.12 \cdot 10^3$	–	–
	H_∞	90	58	7.32	$1.01 \cdot 10^2$	–	–
Maximum *singular value* output direction at low frequency	PID	1104	129	33.6	$4.93 \cdot 10^3$	–	–
	MPC	255	–	0	$1.61 \cdot 10^3$	–	–
	H_∞	114	147	2.9	$1.84 \cdot 10^2$	–	–
Minimum *singular value* output direction at low frequency	PID	1770	243	79	$3.81 \cdot 10^3$	–	–
	MPC	942	–	0	$2.81 \cdot 10^3$	–	–
	H_∞	345	145	7.1	$1.59 \cdot 10^2$	–	–

Disturbance rejection

Simulation concerning disturbance rejection are presented below. Typical disturbances in refrigeration processes are focused on the inlet temperature of evaporator ($T_{e,sec,in}$) and condenser ($T_{c,sec,in}$) secondary fluxes. On the one hand, the first one is related to thermal load, since if it is modified while requiring the same outlet temperature of the evaporator secondary flux, it represents a step change on the cooling demand to be satisfied. On the other hand, the inlet temperature of condenser secondary flux stands for the hot source of the system and it may be either ambient or another fluid which plays its role. From the point of view of the controller, particularly hard to reject are changes on the inlet temperature of evaporator secondary flux, since these affect directly the outlet temperature, which is the main variable to be controlled.

The simulated disturbance profile is depicted in Figure 5.16, considering alternating changes on $T_{e,sec,in}$ and $T_{c,sec,in}$. Figures 5.17 and 5.18 show the PID, MPC, and H_∞ controller performance, where it is important to remark that the set points on $T_{e,sec,out}$ and T_{SH} are constant.

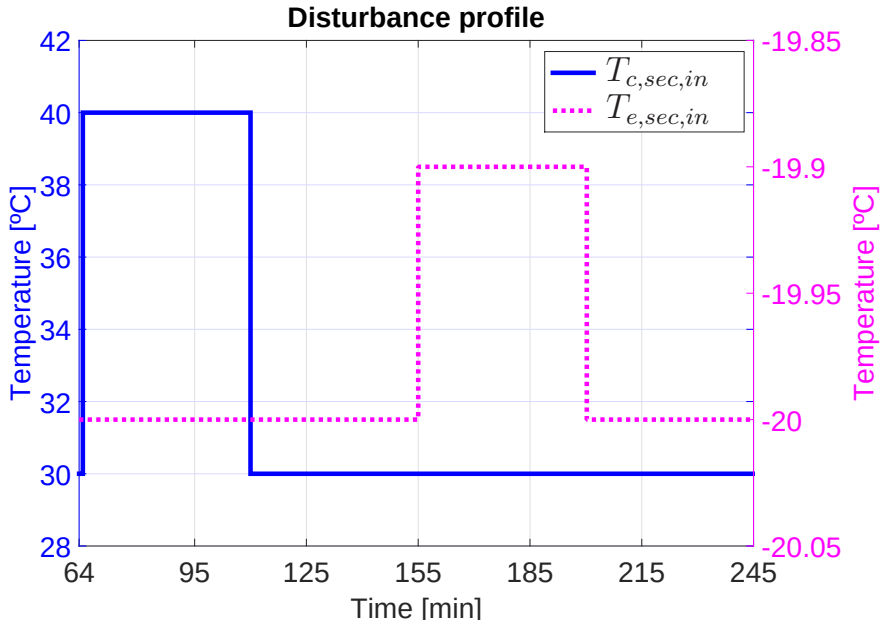

Figure 5.16 Simulated disturbance profile.

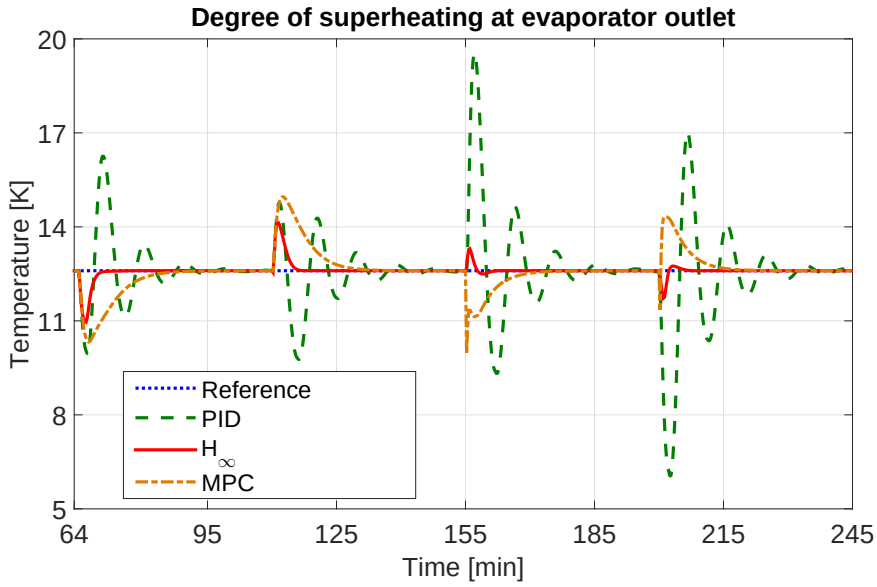

(a) Degree of superheating at evaporator outlet

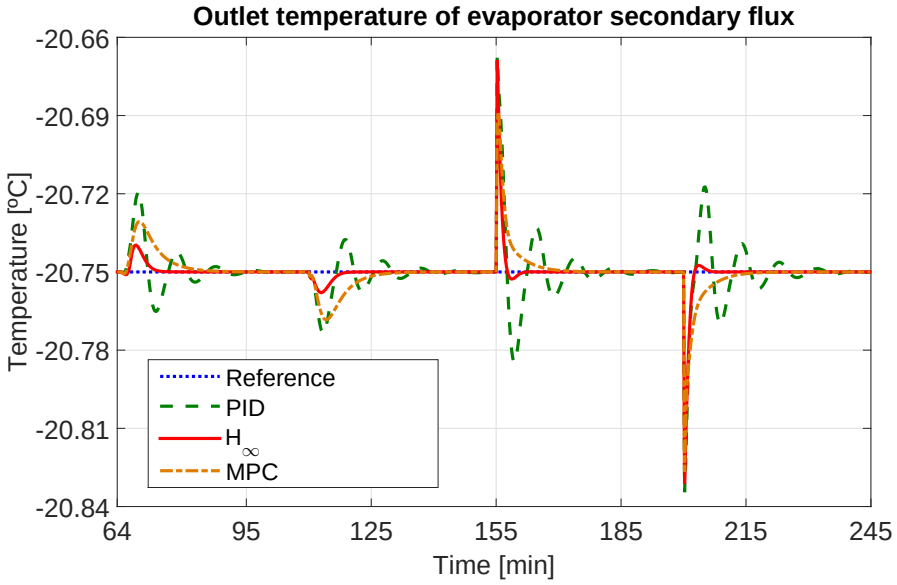

(b) Outlet temperature of evaporator secondary flux

Figure 5.17 Control of output variables when applying the disturbance profile shown in Figure 5.16.

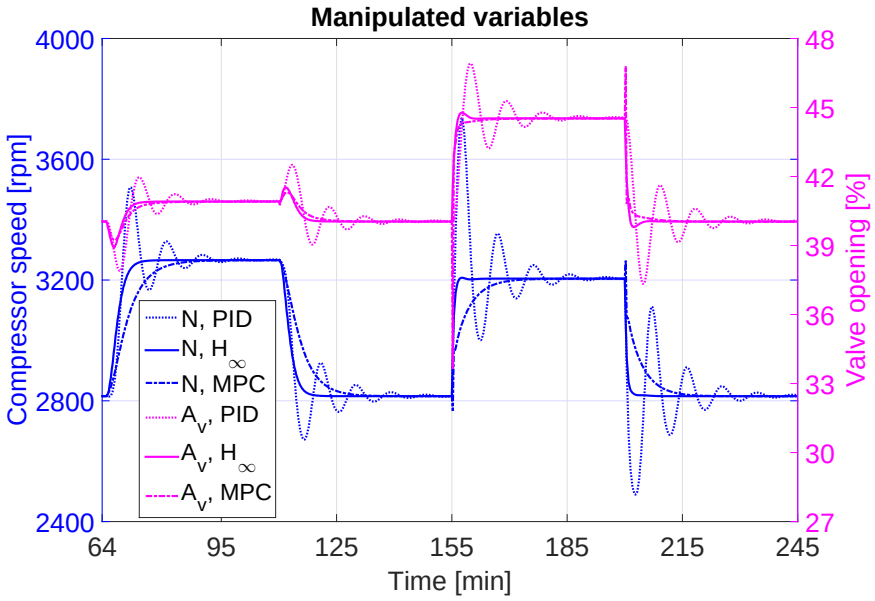

Figure 5.18 Manipulated variables when applying the disturbance profile shown in Figure 5.16.

As shown in Figure 5.17, the H_∞ controller rejects the disturbances successfully and faster than the PID and MPC. As expected, a step change on $T_{e,sec,in}$ involves an immediate response on $T_{e,sec,out}$, which is similar for all controllers. The robust controller corrects the deviation faster and almost without overshoot, while the PID controller rejects the disturbance only after several oscillations and the MPC avoids overshoot but its settling time is larger.

5.2 Suboptimal hierarchical control strategy

5.2.1 Overview

As mentioned in the introduction of this Chapter, given the reduced degree of controllability suggested by the existing control strategies in the literature and shown by the controllability analysis performed in Chapter 4, a suboptimal model-based control architecture is proposed. The optimization and control scheme is represented in Figure 5.19 and described below.

It has been stated in Chapter 4 that a one-compression-stage, one-load-demand cycle is completely defined by a set ψ_{cycle} made up of three variables, whether considering only the compressor speed N and the expansion valve opening A_v as manipulated variables. Then, the optimal cycle which satisfies a certain cooling demand is also defined by a three-variable set, as detailed in Section 4.1. The variable set may be selected as indicated in Equation (4.1), but any set including three independent variables is valid to describe

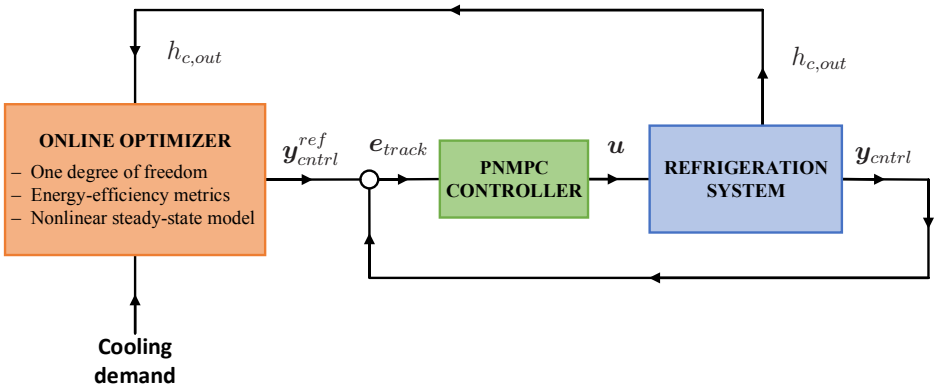

Figure 5.19 Suboptimal hierarchical control (SHC) architecture.

the cycle in steady state. In particular, the set ϕ_{cycle} shown in Equation (5.22) is more suitable for control purposes, since they are all measurable variables. Moreover, the cooling demand is explicitly expressed through $T_{e,sec,out}$, whereas the degree of superheating T_{SH} conventionally controlled in industry is also included. The third variable $h_{c,out}$ is selected in such a way that ϕ_{cycle} is made up by independent variables.

$$\phi_{cycle} = [T_{SH} \;\; h_{c,out} \;\; T_{e,sec,out}]^T \tag{5.22}$$

The controllability analysis performed in Chapter 4, Section 4.2 has shown that, starting at an arbitrary point, only a two-dimensional subspace can be explored by any controller, therefore the SHC strategy, by definition, gives up on controlling all variables in ϕ_{cycle}. Instead, among the achievable cycles defined by the controllable subspace, it aims to achieve the best cycle according to the selected energy-efficiency metrics. Then, the controlled output vector $\boldsymbol{y}_{cntrl}$ which includes the two regulated variables is defined as indicated in Equation (5.23).

$$\boldsymbol{y}_{cntrl} = [T_{SH} \;\; T_{e,sec,out}]^T \tag{5.23}$$

Note that the reference on $T_{e,sec,out}$ is imposed by the cooling demand and it must be satisfied at any instant. However, the reference on T_{SH} is intended to be calculated by the optimizer in order to achieve the best steady-state cycle given the measured value of the uncontrolled variable $h_{c,out}$. Since it is a state variable, the optimization must be performed online to increase energy efficiency while this variable evolves.

Therefore, the optimizer implements a one-degree-of-freedom optimization, since, among the three initial decision variables included in ϕ_{cycle}, one of them is devoted to satisfying the cooling demand ($T_{e,sec,out}$), and another one is uncontrolled and it is just measured ($h_{c,out}$). Although the latter evolves dynamically, the optimization is intended to be performed at a slower time scale than the dominant system dynamics, thus a nonlinear steady-state model is used to evaluate the feasible cycles according to the selected energy-efficiency metrics (in this case, the COP). Moreover, the optimizer must deal with physical,

technological, and operating constraints to generate a reference on T_{SH} which involves a feasible cycle in steady state while generating the required cooling power and given the uncontrolled state described by $h_{c,out}$.

Furthermore, the low-level controller which drives the manipulated variables N and A_v to get the controlled outputs to track their references is a novel technique in predictive control field, called Practical Nonlinear Model Predictive Control (PNMPC). This technique was proposed by Plucenio to provide a simpler implementation of MPC algorithms to nonlinear systems [88, 89]. The objective is to use quadratic programming (QP) solvers usually available in linear MPC codes in order to solve the nonlinear control problem.

Some details regarding the optimizer and the low-level controller are commented in the following Subsections.

5.2.2 Optimizer

As previously stated, the objective of the optimization stage is to calculate the steady-state cycle which satisfies the cooling demand as efficiently as possible. The solution must observe all physical, technological, and operating constraints given the uncontrollable state of the system described by the measured variable $h_{c,out}$. Once calculated the cycle, the output of the optimizer is the reference on T_{SH}, because the set point on $T_{e,sec,out}$ is always imposed by the cooling demand.

Since the desired solution is indeed a cycle, it may be described by the variable set ψ_{cycle} indicated in Equation (4.1). Among the three variables included in ψ_{cycle}, $h_{c,out}$ represents the uncontrolled state, thus there are only two decision variables. If the cooling demand constraint shown in Equation (4.2) is also imposed, the two-degree-of-freedom problem becomes a one-degree-of-freedom one, as explained previously.

Moreover, the solution cycle should observe other constraints, such as limits on the manipulated variables, upper and lower cycle pressures, and operating constraints. Among the latter, a minimum value of T_{SH} is imposed to ensure safe operation of the compressor, since it avoids liquid droplets at the intake. This constraint was also imposed on the global optimization performed in Chapter 4, Section 4.1. Moreover, a minimum value of the temperature difference between the refrigerant and the secondary flux is imposed at both heat exchangers to achieve high heat transfer efficiency according to the manufacturer recommendations.

A nonlinear steady-state model of the whole system is used to characterise the feasible variable sets. In particular, it allows the calculation of all cycle variables from the variable set ψ_{cycle}, which are required to impose the constraints previously mentioned. It is based in separate steady-state models of all elements, which have been already described in Chapter 2, Section 2.1. The iterative procedure designed to solve the model of the whole system which was described in Figure 4.1 is also used in this optimization. The only difference from the global optimization performed in Chapter 4, Section 4.1 lies in the number of decision variables in the optimization, which is reduced to two in this case, while it was three when calculating the global optimum.

Some optimization results are included in this Subsection to illustrate the influence of the uncontrolled state on the maximum achievable COP for a certain cooling demand. Consider the facility studied in Chapter 4, Section 4.1 regarding the global optimization.

Suppose also that the reference on the outlet temperature of the evaporator secondary flux is set to -22.4 °C, given a certain secondary mass flow and an inlet temperature of -20 °C. It involves a cooling demand $\dot{Q}_e$ around 600 W. Table 5.8 includes the main variables defining the global optimal cycle which satisfies the cooling demand.

Table 5.8 Variables defining the optimal cycle for a given cooling demand ($\dot{Q}_e$ = 600 W).

Variable	Value	Unit
Decision variables		
$h_{e,out}$	349.01	kJ kg^{-1}
$h_{c,out}$	248.10	kJ kg^{-1}
$\dot{m}$	5.93	g s^{-1}
Relevant internal variables		
P_e	1.132	bar
P_c	15.25	bar
T_{SH}	9.3	K
Manipulated variables		
N	30	Hz
A_v	47.36	%
Optimal COP		
COP	1.2453	—

The optimal cycle represents an upper bound on the achievable efficiency while providing the required cooling load. However, it has been previously stated that this cycle is not in general achievable by any controller if starting at a random initial point, unless the latter is within the two-dimensional controllable subspace calculated from the optimal point.

Figure 5.20 shows some relevant variables defining the suboptimal cycles generated by the optimizer, when imposing the required cooling load and given the measured value of the uncontrolled state. A feasible range of $h_{c,out}$ is studied and represented in the X-axis of all plots in Figure 5.20. The degree of superheating and refrigerant mass flow are depicted in Figure 5.20(a), the condenser and evaporator pressures in Figure 5.20(b), the steady-state manipulated variables in Figure 5.20(c), and the achieved *COP* in Figure 5.20(d).

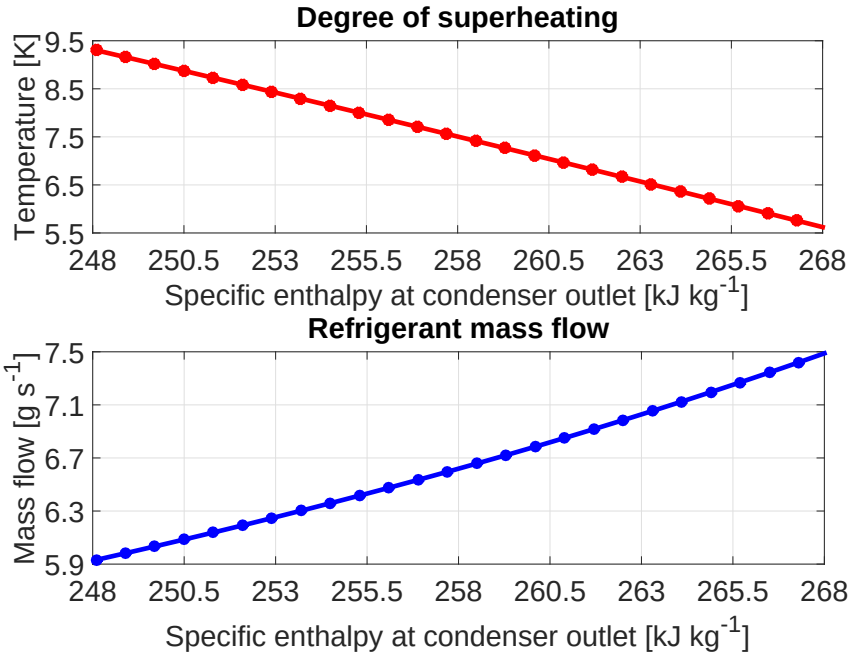

(a) Degree of superheating and refrigerant mass flow

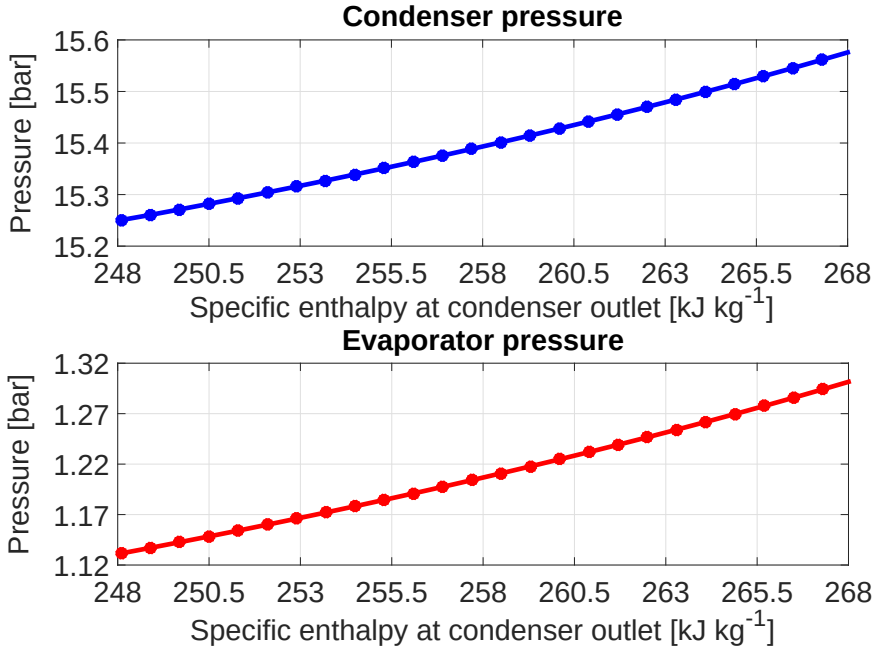

(b) Condenser and evaporator pressures

Figure 5.20 Suboptimal cycle variables for $\dot{Q}_e$ = 600 W and a feasible range of $h_{c,out}$.

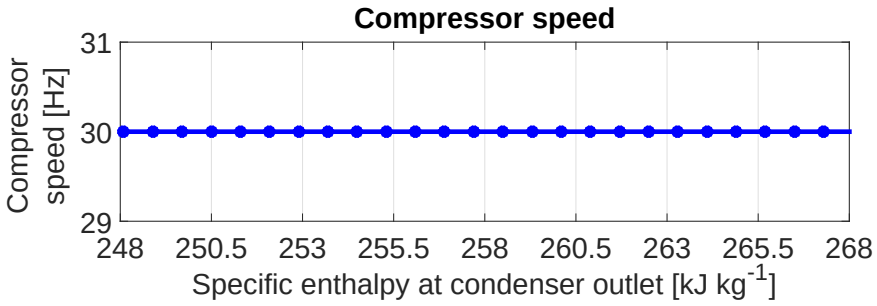

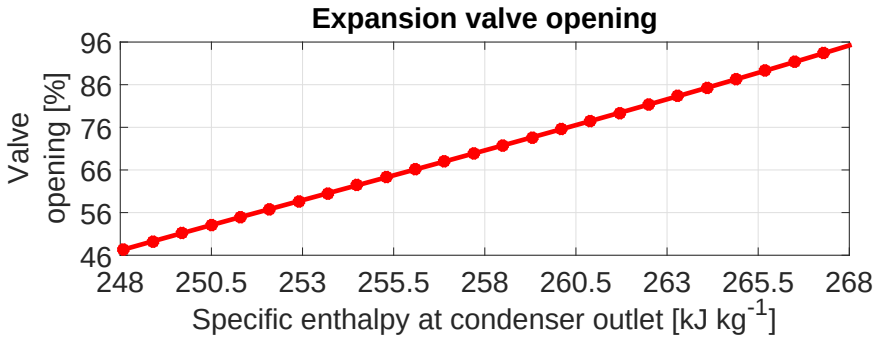

(c) Steady-state manipulated variables

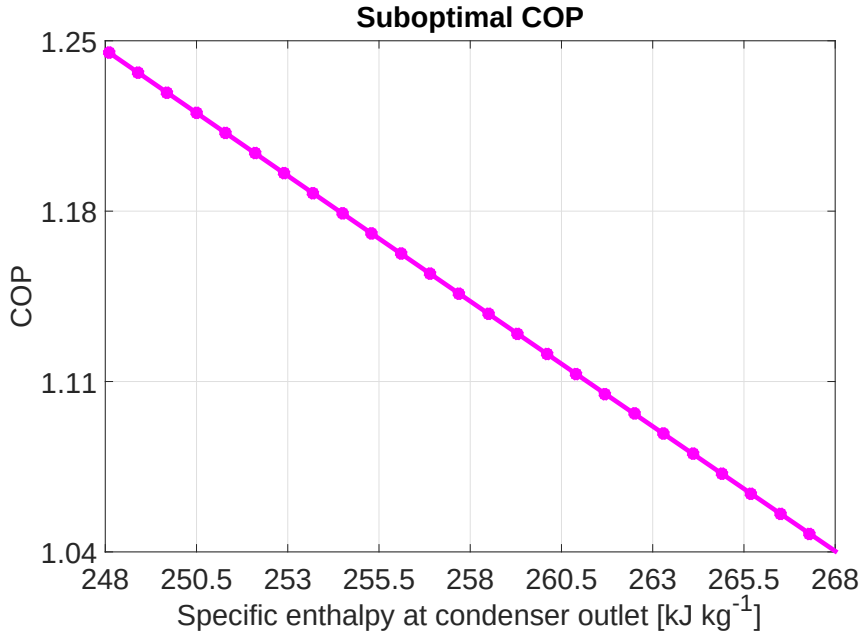

(d) Suboptimal *COP*

Figure 5.20 Suboptimal cycle variables for $\dot{Q}_e$ = 600 W and a feasible range of $h_{c,out}$.

The cycles detailed in Figure 5.20 through their relevant variables represent the best ones achievable by any controller given the uncontrolled state $h_{c,out}$. As expected, they achieve all lower *COP* than the optimum cycle detailed in Table 5.8, as shown in Figure 5.20(d), despite holding the compressor speed N at its lower bound, as observed in Figure 5.20(c). However, as represented in Figure 5.20(a), the refrigerant mass flow is greater than that included in Table 5.8 for all suboptimal cycles, which involves that the difference between $h_{e,out}$ and $h_{c,out}$ is smaller to provide the same cooling power $\dot{Q}_e$. Moreover, if the compressor must provide a greater pressure increase (as shown in Figure 5.20(b)) to a greater amount of refrigerant, the compressor outlet enthalpy $h_{c,in}$ is also increased, which involves that the difference between $h_{c,in}$ and $h_{e,out}$ is greater. Both effects penalize the *COP*, according to the definition expressed in Equation (1.1).

As stated in Subsection 5.2.1, the output of the optimizer is only the reference on T_{SH}, but the cycle achieved in steady state is completely defined by this reference along with the set point on $T_{e,sec,out}$ imposed by the cooling demand and the measured state $h_{c,out}$.

5.2.3 Practical Nonlinear Model Predictive Control (PNMPC)

The low-level controller responsible for getting the controlled outputs included in Equation (5.23) to track their references is a model predictive control technique which allows the application of QP solvers to nonlinear problems. This technique seeks a linear representation of the predicted output vector $\boldsymbol{y}_{predict}$ with regard to the future increments on the control actions $\boldsymbol{\Delta u}$, but linearisation at a given equilibrium point is not considered.

In conventional linear MPC techniques, such as Dynamical Matrix Control (DMC) and Generalised Predictive Control (GPC), the vector of predicted outputs $\boldsymbol{y}_{predict}$ along the prediction horizon PH is represented as a linear function of the vector of future increments on the control inputs $\boldsymbol{\Delta u}$ along the control horizon CH, as expressed in Equation (5.24), considering the free response $\boldsymbol{y}_{free}$ and the forced response $\boldsymbol{y}_{forced}$, where $\boldsymbol{G}$ is a constant matrix denominated dynamic matrix of the model.

$$\boldsymbol{y}_{predict} = \boldsymbol{y}_{free} + \boldsymbol{y}_{forced} = \boldsymbol{y}_{free} + \boldsymbol{G}\,\boldsymbol{\Delta u} \tag{5.24}$$

Albeit using different methods, in all conventional linear MPC algorithms the superposition principle provides an easy calculation of $\boldsymbol{y}_{predict}$. However, in the case of nonlinear systems this principle cannot be applied. Regardless of the system linearity, only the future increments on the control inputs can modify the predicted outputs. Then, a linear representation of the outputs in relation to these increments is intended without using the equilibrium point concept. Considering an arbitrary nonlinear system, the predicted output vector $\boldsymbol{y}_{predict}$ for a given prediction horizon is a nonlinear function of the current and past outputs $\boldsymbol{y}_{past}$, the past control inputs $\boldsymbol{u}_{past}$, and the future increments on the control actions $\boldsymbol{\Delta u}$, as stated in Equation (5.25), where $\boldsymbol{NLF}$ refers to the arbitrary nonlinear function which defines the system.

$$\boldsymbol{y}_{predict} = \boldsymbol{NLF}(\boldsymbol{y}_{past}, \boldsymbol{u}_{past}, \boldsymbol{\Delta u}) \tag{5.25}$$

The predicted output vector can be split into two parts: the free response $\boldsymbol{y}_{free}$ and the forced one $\boldsymbol{y}_{forced}$. The first one is only due to $\boldsymbol{y}_{past}$ and $\boldsymbol{u}_{past}$, and the future increments on

the control inputs $\boldsymbol{\Delta u}$ only affect the forced response. Plucenio proposes an approximation to the calculation of $\boldsymbol{y}_{forced}$ [88, 89], which is detailed in Equation Set (5.26).

$$\begin{aligned} \boldsymbol{y}_{predict} &= \boldsymbol{y}_{free} + \boldsymbol{y}_{forced} \\ \boldsymbol{y}_{free} &= \boldsymbol{NLF}(\boldsymbol{y}_{past}, \boldsymbol{u}_{past}, \boldsymbol{\Delta u} = \boldsymbol{0}) \\ \boldsymbol{y}_{forced} &= \boldsymbol{G}_{PNMPC}\, \boldsymbol{\Delta u} \quad \text{where} \quad \boldsymbol{G}_{PNMPC} = \left.\frac{\partial \boldsymbol{y}_{predict}}{\partial \boldsymbol{\Delta u}}\right|_{\boldsymbol{\Delta u}=\boldsymbol{0}} \end{aligned} \tag{5.26}$$

$\boldsymbol{G}_{PNMPC}$ is the Jacobian matrix of $\boldsymbol{y}_{predict}$, that means, the gradient of the predicted outputs in relation to future increments on the control inputs, calculated for $\boldsymbol{\Delta u} = \boldsymbol{0}$. Therefore, the approximation of the forced response is just a first-order linearisation of the MacLaurin series, since it is calculated considering $\boldsymbol{\Delta u} = \boldsymbol{0}$. Moreover, a correction factor given by the real process outputs is applied to the free response $\boldsymbol{y}_{free}$ to avoid offset and close the loop.

A numerical algorithm is used to calculate the predictions, since there exist multiple nonlinear modelling methods and the result is not always an explicit mathematical model, but a numerical solution, for example neural networks. In any case, the nonlinear model must provide the future outputs given the past outputs and inputs and a vector of future increments on the control inputs. The numerical algorithm to repeat at each iteration in order to calculate $\boldsymbol{y}_{free}$ and $\boldsymbol{G}_{PNMPC}$ for MIMO systems is the following:

1) Calculate the output vector $\boldsymbol{y}^0_{predict}$ by applying the model for $\boldsymbol{\Delta u} = \boldsymbol{0}$ (for all the control horizon CH) and considering the current and past outputs and inputs.
2) Do $\boldsymbol{y}_{free} = \boldsymbol{y}^0_{predict}$ (free response).
3) Calculate the output vector $\boldsymbol{y}^{1,i}_{predict}$ considering the current and past outputs and inputs, and applying a small but non zero value υ as first future increment on the ith control input, being the remaining future increments zero.
4) Do $\boldsymbol{G}_{PNMPC}(:, i) = \frac{\boldsymbol{y}^{1,i}_{predict} - \boldsymbol{y}^0_{predict}}{\upsilon}$, that means, the approximated partial derivative of all outputs in relation to a change in the ith input at the first instant of the control horizon.
5) Repeat steps 3) and 4) for all control inputs ($\forall i = 1,...,MI$), generating the corresponding MI first columns of the matrix $\boldsymbol{G}_{PNMPC}$. The control horizon CH is the same for all control inputs.
6) Calculate the output vector $\boldsymbol{y}^{2,i}_{predict}$ considering the current and past outputs and inputs, and applying a small but non zero value υ as second future increment on the ith control input, being the remaining future increments zero.
7) Do $\boldsymbol{G}_{PNMPC}(:, MI + i) = \frac{\boldsymbol{y}^{2,i}_{predict} - \boldsymbol{y}^0_{predict}}{\upsilon}$, that means, the approximated partial derivative of all outputs in relation to a change in the ith input at the second instant of the control horizon.
8) Repeat steps 6) and 7) for all control inputs ($\forall i = 1,...,MI$), generating the corresponding MI second columns of the matrix $\boldsymbol{G}_{PNMPC}$.

9) Proceed with the same calculations for all control horizon CH.

Once estimated the matrix $\boldsymbol{G}_{PNMPC}$, QP optimization algorithms applied in standard linear MPC formulations can be used to determine $\boldsymbol{\Delta u}$.

Conventional MPC strategies usually add a disturbance model to the prediction algorithm, which helps the control strategy to reject disturbances and mitigate noise effects. The PNMPC technique uses the same correction mechanism as the GPC algorithm: the integral of the filtered prediction error is added to the prediction itself. Figure 5.21 shows the block diagram of the observer used in the PNMPC, in this case for a single output, where $y_{predict,wc}$ is the predicted output without correction, η is the correction to be added to the output without correction, y is the measured output and $\nu = y - y_{predict}$ refers to the prediction error. $F(z)$ is a low-pass filter, whose frequency parameters, together with the integral gain k_{int}, are designed to guarantee a desired behaviour on disturbance rejection and noise reduction.

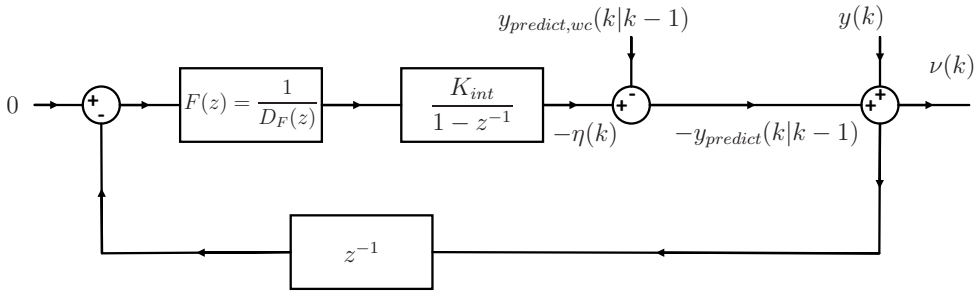

Figure 5.21 Disturbance model used in the PNMPC.

The PNMPC strategy is used as low-level control to drive the controlled outputs to the references provided by the optimizer. In this case the cost function J_{PNMPC} is detailed in Equation (5.27), where the weighting matrices $\boldsymbol{Q}$ and $\boldsymbol{R}$ are design parameters, as well as the prediction and control horizons PH and CH.

$$\begin{aligned} J_{PNMPC} = & \sum_{i=1}^{PH} [\boldsymbol{y}_{cntrl}^{ref}(k+i) - \boldsymbol{y}_{cntrl}(k+i|k)]^T \; \boldsymbol{Q} \; [\boldsymbol{y}_{cntrl}^{ref}(k+i) - \boldsymbol{y}_{cntrl}(k+i|k)] + \\ & + \sum_{i=1}^{CH} \boldsymbol{\Delta u}(k+i-1|k)^T \; \boldsymbol{R} \; \boldsymbol{\Delta u}(k+i-1|k) \end{aligned} \tag{5.27}$$

The constraint awareness inherent to predictive control is used to impose some limitations on the manipulated inputs and controlled outputs, as shown in Equation Set (5.28).

$$\begin{array}{ccccc} \boldsymbol{\Delta u}_{min} & \leqslant & \boldsymbol{\Delta u} & \leqslant & \boldsymbol{\Delta u}_{max} \\ \boldsymbol{u}_{min} & \leqslant & \boldsymbol{u} & \leqslant & \boldsymbol{u}_{max} \\ \boldsymbol{y}_{cntrl,min} & \leqslant & \boldsymbol{y}_{cntrl} & \leqslant & \boldsymbol{y}_{cntrl,max} \end{array} \tag{5.28}$$

5.2.4 *Energy-efficiency-aware* controller comparison

Some simulation results achieved by the control architecture previously presented are included in this Subsection. They are compared to those provided by two different control strategies already studied in the literature about refrigeration systems and mentioned in Chapter 1: the FB+FF strategy proposed by Jain [12] and the TV-ESC developed by Guay [48], regarding the *COP* achieved in steady state and the dynamic behaviour of the controlled variables.

Feedback-plus-feedforward control strategy (FB+FF)

This control strategy, proposed by Jain [12], is described in Figure 5.22. The layout is very similar to that represented in Figure 5.19 for the SHC architecture, but there are some conceptual differences which are described below.

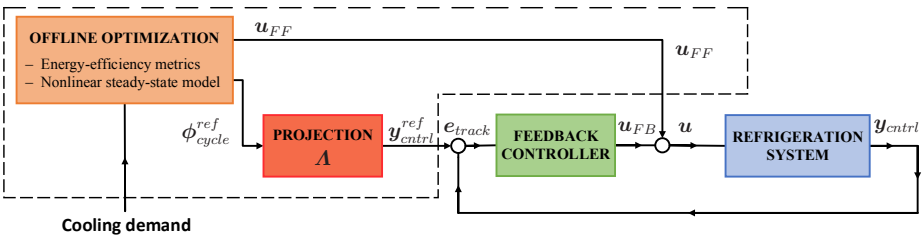

Figure 5.22 Feedback-plus-feedforward optimization and control architecture by Jain [12].

The FB+FF control strategy also imposes a hierarchical architecture, but the optimization stage is carried out offline, that means, for each cooling demand the global optimal cycle is calculated according to the selected energy-efficiency metrics and using the nonlinear steady-state model of the system. Since the calculation of the global optimum is intended, a two-degree-of-freedom problem must be solved. The output of the optimizer is the three-variable set ϕ_{cycle}^{ref} which defines completely the optimal cycle, where only $T_{e,sec,out}$ is imposed by the cooling demand and the other two variables are calculated by the optimizer. Moreover, it also generates the control actions corresponding to the optimal cycle in steady state, as previously shown in Table 5.8, which are used as the feedforward contribution to the controller output. They are supposed to drive the system to the vicinity of the desired point, where a linear feedback controller is applied to get the controlled outputs to track their references.

Nevertheless, there are three optimization degrees of freedom whereas there are only two control ones. Then, the optimal cycle defined by ϕ_{cycle}^{ref} is projected from the three-degree-of-freedom optimization space onto the two-degree-of-freedom control subspace, in such a way that the controlled output vector $\boldsymbol{y}_{cntrl}^{ref} \in \mathbb{R}^2$ turns out to be some linear combination of the variables included in $\phi_{cycle}^{ref} \in \mathbb{R}^3$, as stated in Equation (5.29).

$$\boldsymbol{y}_{cntrl}^{ref} = \boldsymbol{\Lambda}\, \boldsymbol{\phi}_{cycle}^{ref} \tag{5.29}$$

The projection matrix $\boldsymbol{\Lambda} \in \mathbb{R}^{2x3}$ is a design parameter which may be selected according to different criteria, including sensor cost and accuracy, among others. In this case, to ensure that the FB+FF strategy provides the desired cooling power and $\boldsymbol{y}_{cntrl}$ matches the controlled output vector defined by the SHC architecture, $\boldsymbol{\Lambda}$ is selected as indicated in Equation (5.30).

$$\boldsymbol{y}_{cntrl}^{ref} = \boldsymbol{\Lambda}\, \boldsymbol{\phi}_{cycle}^{ref} = \begin{bmatrix} 1 & 0 & 0 \\ 0 & 0 & 1 \end{bmatrix} \begin{bmatrix} T_{SH} \\ h_{c,out} \\ T_{e,sec,out} \end{bmatrix} = \begin{bmatrix} T_{SH} \\ T_{e,sec,out} \end{bmatrix} \tag{5.30}$$

According to Jain, the feedback controller is a LQR [12]. The only modification to the original formulation of the controller is the addition of a back-calculation-based anti-windup scheme, since the model has been augmented with two integrators to ensure zero steady-state error when tracking references, and optimal cycles are achieved with minimum compressor speed for a wide range of cooling demands, as detailed in Chapter 4, Section 4.1. For instance, the optimal cycle calculated for the cooling demand studied in Subsection 5.2.2 ($\dot{Q}_e$ = 600 W) shows to be achieved with the minimum compressor speed (N = 30 Hz), as indicated in Table 5.8.

Time-varying extremum-seeking control (TV-ESC)

This control strategy, proposed by Guay [48] and applied to refrigeration systems by Burns *et al.* [49], is described in Figure 5.23.

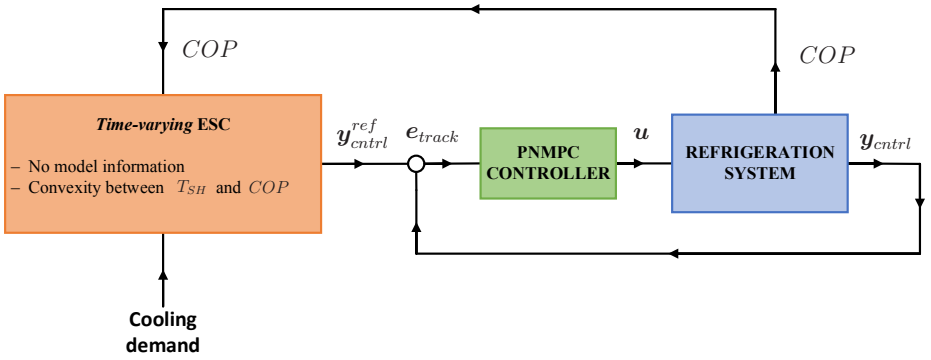

Figure 5.23 Extremum-seeking control architecture.

This control technique does not rely on any model and simply requires convexity between the input (additional reference to $T_{e,sec,out}$) and the objective function to be optimized. Although some discussion is included in the work by Burns *et al.* about the most suitable internal variable to be controlled according to technological reasons [49], the degree of superheating T_{SH} has been selected for comparison purposes. Then, the controlled output

vector is the same as that considered within the SHC architecture and the FB+FF strategy and indicated in Equations (5.23) and (5.30).

Therefore, the reference on $T_{e,sec,out}$ is imposed, as usually, by the cooling demand, and the TV-ESC defines the set point on T_{SH}. The objective function to be maximized is the *COP* in order to compare the results with the other techniques, but in this case a penalization term must be added to the objective function to ensure zero steady-state error when providing the required cooling load, since the maximum achievable *COP* varies for each cooling load, as studied in Chapter 4, Section 4.1.

The *time-varying* ESC approach is applied since it has shown to converge substantially faster than traditional *perturbation-based* ESC [49]. It uses adaptive filtering techniques to estimate the parameters of the gradient function from measured data, thus eliminating averaging in the controller.

Furthermore, the low-level controller which drives N and A_v to get the controlled outputs to track their references is the already explained PNMPC, although any technique which succeeds in controlling the selected variables may be valid, since the extremum-seeking control is intended to be assessed on its ability to achieve optimal steady-state operation and not on the controller performance when tracking the references provided by the TV-ESC.

Controller comparison

Some simulation results comparing the three described control strategies are included below. The study is focused on the arbitrary cooling demand already studied in Subsection 5.2.2. Suppose two random feasible cycles IP_1 and IP_2, defined by the variables gathered in Table 5.9. All control techniques are intended to be applied starting at these cycles to meet the cooling demand $\dot{Q}_e$ = 600 W.

Table 5.9 Variables defining the two initial points from which the control strategies are applied.

Variable	Unit	Initial point 1 (IP_1)	Initial point 2 (IP_2)
$h_{e,out}$	kJ kg^{-1}	350.01	348.51
$h_{c,out}$	kJ kg^{-1}	247.59	249.30
$\dot{m}$	g s^{-1}	5.45	6.22
P_e	bar	0.951	1.025
P_c	bar	15.02	15.41
T_{SH}	K	13.5	10.3
N	Hz	38	38
A_v	%	44.36	50.36

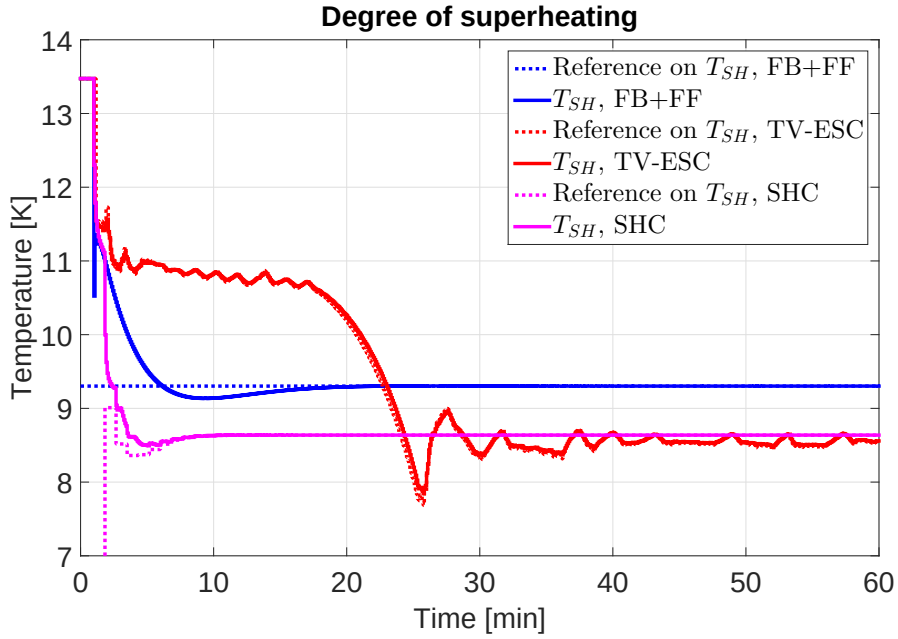

(a) Degree of superheating

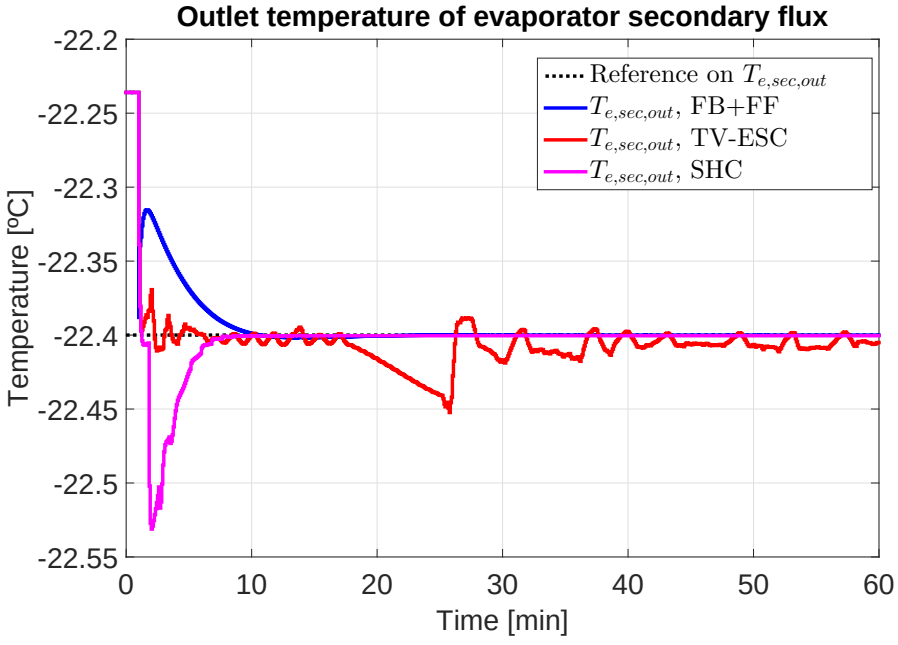

(b) Outlet temperature of evaporator secondary flux

Figure 5.24 Control performance comparison for $\dot{Q}_e$ = 600 W from starting point IP_1.

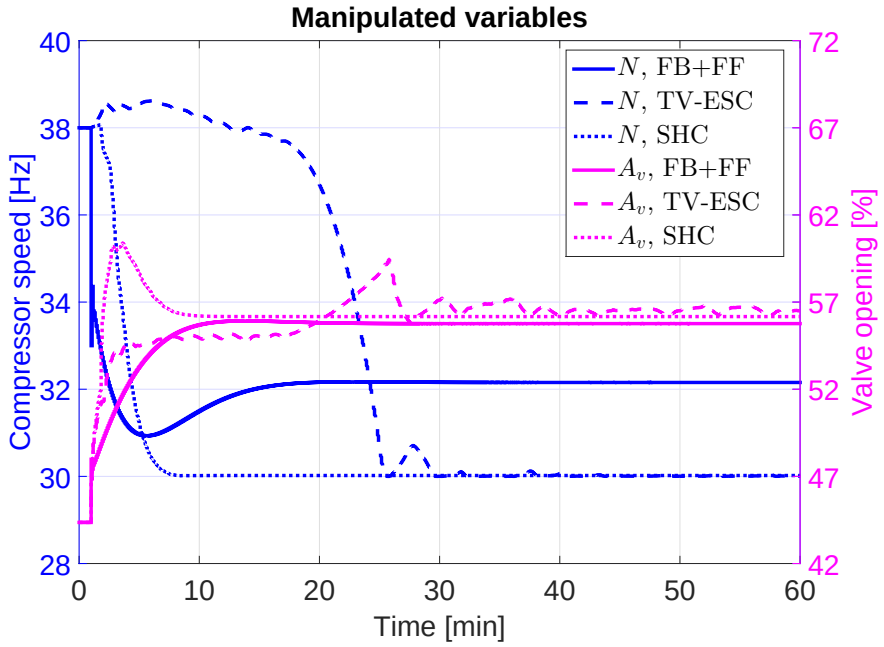

(c) Manipulated variables

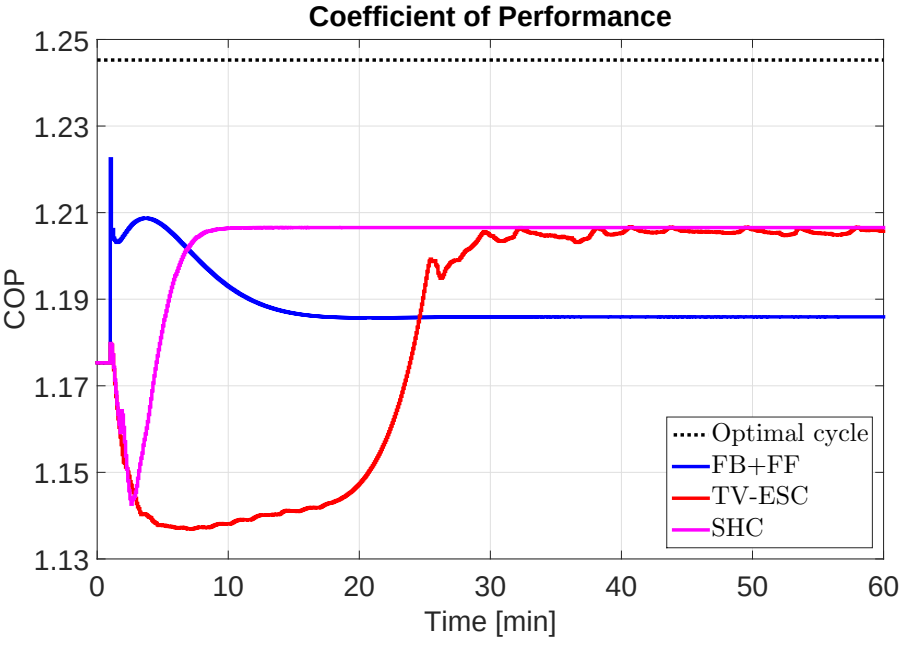

(d) Coefficient of Performance

Figure 5.24 Control performance comparison for $\dot{Q}_e$ = 600 W from starting point IP_1.

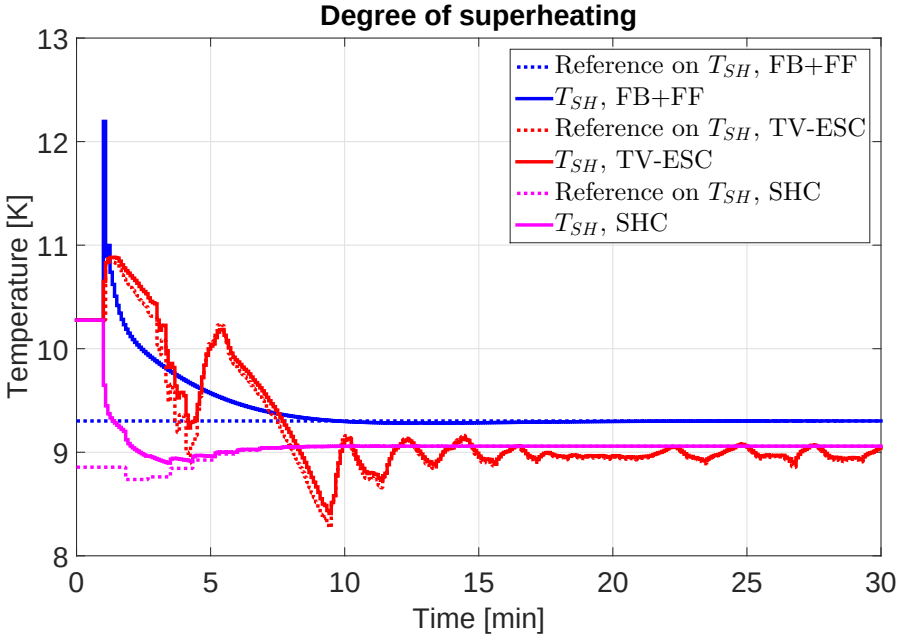

(a) Degree of superheating

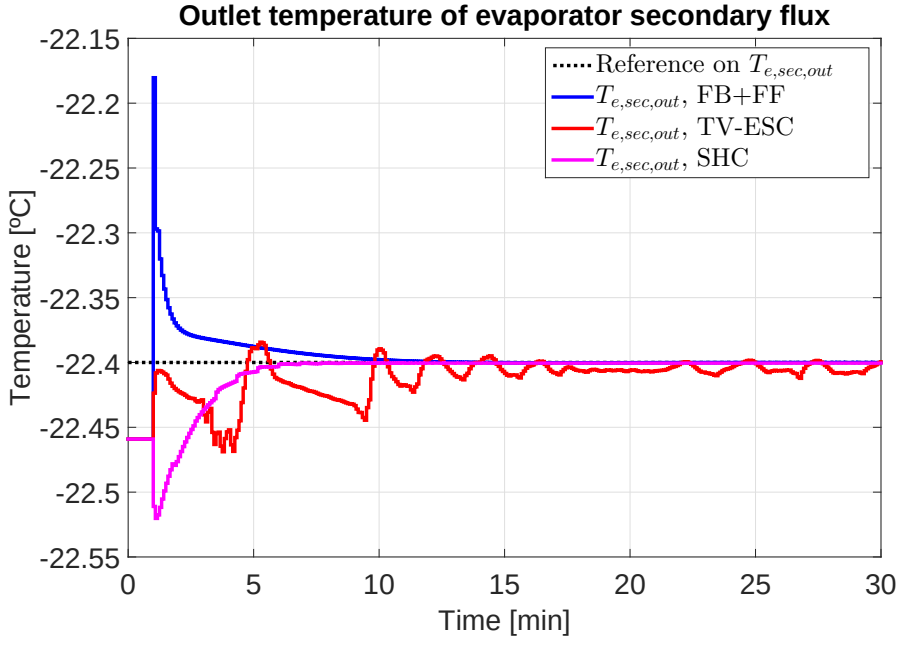

(b) Outlet temperature of evaporator secondary flux

Figure 5.25 Control performance comparison for $\dot{Q}_e$ = 600 W from starting point IP_2.

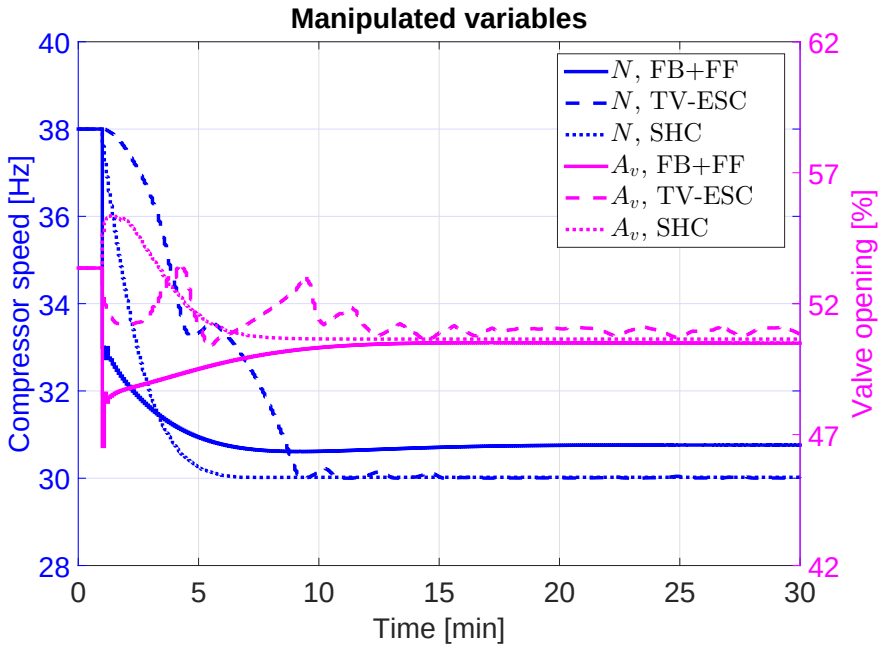

(c) Manipulated variables

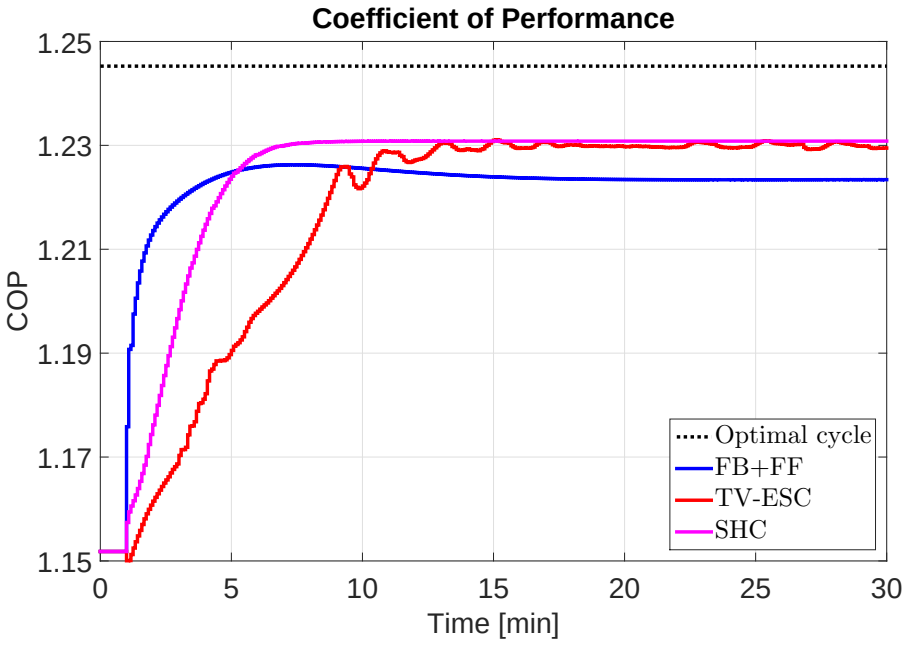

(d) Coefficient of Performance

Figure 5.25 Control performance comparison for $\dot{Q}_e$ = 600 W from starting point IP_2.

The performance of the three control strategies is compared in Figures 5.24 and 5.25 for both starting points. Several cycle variables are represented, including the controlled outputs, T_{SH} (Figures 5.24(a) and 5.25(a)) and $T_{e,sec,out}$ (Figures 5.24(b) and 5.25(b)). The manipulated variables N and A_v are shown in Figures 5.24(c) and 5.25(c), whereas the achieved COP is depicted in Figures 5.24(d) and 5.25(d). The control is active from $t = 1$ min, being the previous evolution due to open-loop response. The control sampling time is 5 seconds for all strategies, whereas the reference on T_{SH} is updated every 50 seconds in the SHC strategy. Moreover, the actual values considered for the constraint management by the PNMPC are shown in Equation Set (5.31), while the controller design parameters are indicated in Equation Set (5.32). Note also that the constraints on limits and rate limits concerning the manipulated variables described in Equation Set (5.31) and considered by the PNMPC for the SHC and the TV-ESC are also imposed on the control actions calculated by the FB+FF controller.

$$\begin{aligned} \boldsymbol{\Delta u}_{min} &= \begin{bmatrix} -5\ \text{Hz} \\ -20\% \end{bmatrix} & \boldsymbol{\Delta u}_{max} &= \begin{bmatrix} 5\ \text{Hz} \\ 20\% \end{bmatrix} \\ \boldsymbol{u}_{min} &= \begin{bmatrix} 30\ \text{Hz} \\ 10\% \end{bmatrix} & \boldsymbol{u}_{max} &= \begin{bmatrix} 50\ \text{Hz} \\ 100\% \end{bmatrix} \\ \boldsymbol{y}_{cntrl,min} &= \begin{bmatrix} 2°\text{C} \\ -25°\text{C} \end{bmatrix} & \boldsymbol{y}_{cntrl,max} &= \begin{bmatrix} 40°\text{C} \\ -20°\text{C} \end{bmatrix} \end{aligned} \tag{5.31}$$

$$\begin{aligned} PH &= 10 & CH &= 3 \\ \boldsymbol{Q} &= \begin{bmatrix} 1 & 0 \\ 0 & 1 \end{bmatrix} & \boldsymbol{R} &= \begin{bmatrix} 1 & 0 \\ 0 & 1 \end{bmatrix} \end{aligned} \tag{5.32}$$

It is observed in Figures 5.24 and 5.25 that all controllers succeed in providing the required cooling power starting at both initial points. However, the SHC strategy achieves higher COP in steady state than the FB+FF controller for comparable settling time, as shown in Figures 5.24(d) and 5.25(d) and indicated in Table 5.10. The main reason is the selected reference on T_{SH}, which is not modified along time by the FB+FF strategy, being that corresponding to the optimal cycle for the desired cooling load included in Table 5.8. However, it is updated online according to the evolution of $h_{c,out}$ within the SHC strategy. The COP is enhanced because the optimal value of T_{SH} imposed by the FB+FF controller might be not optimal if the whole cycle is not controlled, as in the present case, due to the uncontrolled evolution of the third variable defining the cycle. Regarding the TV-ESC, it succeeds in achieving approximately the same suboptimal COP as the SHC strategy without requiring a model-based optimization, as indicated in Table 5.10, but the settling time and controller performance are degraded by the continuous search for higher COP and the deviations around the desired value of $T_{e,sec,out}$. It affects not only the instantaneous compression power $\dot{W}_{comp}$ required to drive the system from the initial point to the suboptimal cycle, but also the mechanical energy applied by the compressor E_{comp}, which can be estimated within the transient period applying Equation (5.33). Whilst the COP is an index of the system performance in steady state regarding energy efficiency, the mechanical energy applied by the compressor E_{comp} is an index of the controller

performance in transient, which is shown for the TV-ESC and SHC strategies in Table 5.11. The FB+FF strategy has not been included in the transient analysis because its steady-state performance is shown to be worse than the other two strategies, therefore the transient performance is irrelevant compared to the steady-state performance. However, the TV-ESC and SHC strategies achieve the same *COP* in steady state, thus the difference between them regarding the transient performance is to be analysed. The considered transient period is from $t_{start} = 1$ min to $t_{settle} = 30$ min in the case of IP_1, and from $t_{start} = 1$ min to $t_{settle} = 15$ min in the case of IP_2.

Table 5.10 Achieved *COP* in steady state.

Control strategy	Initial point 1 (IP_1)	Initial point 2 (IP_2)
FB+FF	1.1859	1.2234
TV-ESC	1.2057	1.2299
SHC	1.2065	1.2308

$$E_{comp} = \int_{t_{start}}^{t_{settle}} \dot{W}_{comp}\, dt \tag{5.33}$$

Table 5.11 Mechanical energy E_{comp} required by the control strategy to drive the system from the initial point to the suboptimal one [W h].

Control strategy	Initial point 1 (IP_1)	Initial point 2 (IP_2)
TV-ESC	266.36	124.23
SHC	256.43	122.51

The improvement of the *COP* in steady state of the SHC strategy with respect to the FB+FF controller achieves 1.73% for IP_1 and 0.6% for IP_2, whereas the energy supplied to the compressor within the transient period E_{comp} is reduced in 3.72% in the case of IP_1 and 1.38% in the case of IP_2 when applying the SHC strategy.

Note that the qualitative performance of the three strategies is the same for both initial points, but the achieved *COP* is different despite the cooling demand being identical. This is due to the controllability issues analysed by means of the phase portrait method in Chapter 4, Section 4.2. Each initial point defines a certain controllable subspace, where the SHC and TV-ESC strategies look for the maximum achievable *COP* using very different techniques, while the FB+FF controller achieves a cycle with lower *COP*. Nevertheless, the optimal *COP* cannot be achieved through control unless the initial point lies within the controllable subspace calculated from the optimal cycle. Then, the initial point constrains the maximum achievable efficiency; in this case, IP_1 turns out to impose a more restrictive

limit than IP_2 on the achievable *COP*, as shown in Table 5.10.

5.3 Final remarks

This Chapter has been devoted to control, where the two main schemes in the literature have been considered: the conventional scheme and the *energy-efficiency-aware* one.

On the one hand, in addition to the reference on the outlet temperature of the evaporator secondary flux imposed by the cooling demand, a low but constant set point on the degree of superheating is applied in the conventional scheme, and the controller is designed to get these two variables to track their references. A centralised multivariable H_∞ controller, based on the *S/KS/T* Mixed Sensitivity Problem, has been proposed. Linear models have been identified at a number of operating points to capture the main dynamics of the system, and one of them has been selected as nominal while handling the others as unstructured uncertainties. The controllability analysis carried out on the nominal model has exposed some dynamic constraints on the closed-loop performance. Simulation results provided by the H_∞ controller, a decentralised PID, and a conventional MPC have been presented, including reference tracking, coupling measurement, and disturbance rejection. The troublesome output directions which arise in the controllability analysis have been also studied. The H_∞ controller shows to be faster, more effective, and with lower coupling between the controlled variables. Moreover, the H_∞ controller is robust when controlling the system at a non-nominal point, while the MPC designed at the nominal operating point turns out to be unstable.

On the other hand, energy efficiency is considered when calculating the references for the low-level controller in the *energy-efficiency-aware* scheme. Given the lack of full controllability suggested by the analysis performed in Chapter 4, a suboptimal hierarchical control strategy is proposed. Among the achievable cycles defined by the controllable subspace, an optimizer calculates that reaching maximal *COP*. A one-degree-of-freedom optimization is carried out, since among the three variables defining the cycle, one is devoted to satisfying the cooling demand, whereas another one represents the uncontrolled state and it is just measured. The output of the optimizer is the reference on the degree of superheating, which is updated online. The Practical Nonlinear Model Predictive Control technique is used as low-level controller. The performance of the proposed controller is compared in simulation to that of two different strategies, namely a feedback-plus-feedforward controller and a *time-varying* extremum-seeking controller. All strategies succeed in satisfying the cooling demand, but only the suboptimal hierarchical control strategy and the extremum-seeking technique achieve the highest achievable *COP*, although the settling time and controller performance show to be much better when applying the model-based technique. Regardless of the control law, the controllability issues are highlighted, since the initial point defines the controllable subspace and thus it constrains the maximum achievable efficiency in steady state. The suboptimal hierarchical control strategy is also a contribution of the Thesis, since it improves the steady-state performance of existing model-based strategies, such as the feedback-plus-feedforward one, while improving the transient performance of other suboptimal control laws such as the extremum-seeking one.

6 Conclusions

I think and think for months and years. Ninety-nine times, the conclusion is false. The hundredth time I am right.

ALBERT EINSTEIN

Contents

This final Chapter of the Thesis summarises the main contributions of the work. The achievements are highlighted and some possible future lines of research and novel ideas are presented.

6.1 Thesis contributions and conclusions

The Thesis has dealt with modelling, optimization, and control of vapour-compression refrigeration systems. Moreover, the steady-state identification of an experimental plant has been addressed. Most work has been devoted to the one-compression-stage, one-load-demand configuration, although multi-stage and multi-load-demand configurations have been also studied when analysing and identifying the experimental plant. The main objective of the control system is to satisfy the cooling demand with as much as possible energy efficiency, which is described in this field using the Coefficient of Performance (*COP*). In this Thesis a particular application of refrigeration systems has been considered, where the cycle is intended to provide the required cooling power to a continuous flow entering the evaporator as secondary flux. Neither the mass flow nor the inlet temperature of such secondary flux are to be controlled in this stage, since they may be managed

by another high-level controller. Therefore, the cooling demand can be expressed as a reference on the outlet temperature of the evaporator secondary flux, where the mass flow and inlet temperature behave as measurable disturbances to the refrigeration system. The same is considered for the condenser secondary flux, thus only the compressor speed and the valve opening are considered as manipulated variables, whereas both secondary flux mass flows and inlet temperatures act as measurable disturbances.

First of all, an accurate dynamic model is required to design advanced control strategies, but the necessary trade-off between accuracy and computation time must be also taken into account. Moreover, a steady-state model is also useful to address set-point optimization. In Chapter 2 some features of the modelling of vapour-compression refrigeration systems have been addressed, focusing on the one-compression-stage, one-load-demand cycle, since more complex configurations only include the elements of which the simplest cycle is made up: expansion valve, compressor, evaporator, and condenser. On the one hand, steady-state models have been developed and detailed for all elements, paying special attention to the heat exchangers. On the other hand, regarding dynamic modelling, some approaches have been assessed and the *moving boundary* (MB) approach to heat exchanger modelling has been selected and the *switched moving boundary* (SMB) model developed by Li has been taken as starting point [22]. Some considerations have been taken into account in order to reduce the model order and therefore the complexity of the original SMB model. Firstly, the frequency ratio between the dynamics of both the evaporator and the condenser regarding their internal volumes and refrigerant thermodynamic properties has been studied and evaluated. Secondly, the dynamics related to mass flow imbalance in the cycle have been assessed. A simplified control-oriented nonlinear model of the whole cycle has been proposed, whose state vector is made up of only three variables, all related to the condenser, which turns out to generate the slowest and thus dominant dynamics. Differences between the control-oriented model and the original SMB model have been evaluated in simulation, showing to be negligible regarding dominant dynamics, whereas the computation time is dramatically reduced almost without loss of accuracy, at least in steady state. Considering that all control strategies of these systems are focused on their performance in terms of energy efficiency in steady state, the lack of accuracy in transient affects barely the achieved *COP* and thus the control objective. The control-oriented dynamic model, which reduces the complexity of the original SMB model while retaining the dominant dynamics, is one of the main contributions of the Thesis.

Secondly, the modelling conclusions have been applied when identifying the two-stage, two-load-demand configurable experimental refrigeration plant. In Chapter 3 the plant has been described, concerning its physical elements, actuators and sensors, as well as the PLC features and the ModBus protocol issues. The high-level control environment through MATLAB®/Simulink and its communication with the low-level controller over OPC standard have been also addressed. Regarding identification, the steady-state models presented in Chapter 2 for the compressors and expansion valves have been identified using experimental data, whereas parameter dependence of heat exchanger dynamics and statics has been studied, concluding that the heat transfer coefficients influence essentially system statics but they do not affect much system dynamics. Therefore, steady-state identification of the heat exchangers has been also addressed. A novel identification procedure focused on the heat exchangers has been presented. Diverse refrigerant phases along each heat

exchanger, according to the MB modelling approach, have been considered, thus diverse zones are differentiated, whose lengths are inaccessible state variables. It has been assumed that a unique overall heat transfer coefficient can be identified for each zone. Coherent values have been calculated taking into account some orders of magnitude of convective heat transfer coefficients in the literature and their influence on overall coefficients. In spite of individually modelling all elements of the cycle, global validation considering the one-stage, two-load-demand configuration and the two-stage, two-load-demand one has been performed, in order to check how precise the parameters obtained are to describe the steady-state behaviour of the whole cycle. Minor differences have been noticed when simulated and experimental P-h diagrams are compared, and estimation errors on different measurable cycle variables have been calculated, giving rise to values around 10% in the key variables, such as pressures and specific enthalpies. The identification procedure of the heat exchangers is also a contribution of the Thesis, since it may be useful when no heat transfer correlation fits to the configuration or the flow conditions of the heat exchanger to be identified. Moreover, experimental data are considered within the identification procedure, resulting in a grey-box approach, whereas using only correlations implies a white-box approach.

Thirdly, the optimal control of vapour-compression refrigeration systems has been addressed in Chapter 4. Global optimization of the cycle which satisfies a certain cooling load has been carried out, considering the COP as energy-efficiency metrics. The minimum number of variables completely defining a one-stage, one-load-demand cycle is three, provided that two manipulated variables (the compressor speed and the expansion valve opening) have been considered. A nonlinear steady-state model has been used to evaluate the feasibility of the *candidate* cycles, imposing some technological and operating constraints. It is based in separate steady-state models of all elements, which have been described in Chapter 2. Optimization results state that optimal cycles are not achieved with minimum degree of superheating for all cooling demand range. This leads to the proposal of a control strategy capable of driving the cycle to the optimum, since the simulations reveal that the overall energy efficiency could be improved if the cycle was optimally operated.

However, the controllability of the system has been analysed, given the difficulties shown by many control strategies in the literature when trying to achieve the optimal cycle. Considering the state dimension of the simplified control-oriented model presented in Chapter 2 and the length of the variable set which completely defines a cycle, and assuming that dominant system dynamics are concentrated at the condenser, the control problem has been focused on the latter and a controllability analysis on the simplified model has been carried out. Both linear theory and a nonlinear pointwise analysis based on the phase portrait method suggest that in practice there is no full controllability and only a two-dimensional subspace of the three-dimensional solution space can be explored by manipulating the available inputs. Therefore, there exist difficulties in achieving not only the optimal cycle, but in general any given feasible steady-state cycle when starting at an arbitrary cycle. Moreover, this issue is expected to appear when applying any control law, since controllability is a system property, not a controller-dependent issue. The controllability analysis is one of the main contributions of the Thesis, since to the author's knowledge it has not been done yet and it highlights the reasons why many control strategies

in the literature fail in achieving the optimal cycle.

Finally, the two main control schemes on refrigeration systems have been studied in Chapter 5: the conventional scheme and the *energy-efficiency-aware* one. In the first one, in addition to the reference on the outlet temperature of the evaporator secondary flux imposed by the cooling demand, a low but constant set point on the degree of superheating is applied, and the controller is designed to get these two variables to track their references. However, energy efficiency is considered when calculating the references for the low-level controller in the second scheme.

Regarding the tracking problem, the robust control of a one-stage, one-load-demand refrigeration system is intended, and a centralised multivariable H_∞ controller, based on the *S/KS/T* Mixed Sensitivity Problem, has been proposed. Linear models have been identified at a number of operating points to capture the main dynamics of the system, and one of them has been selected as nominal while handling the others as unstructured uncertainties. The controllability analysis carried out on the nominal model has exposed some dynamic constraints on the closed-loop performance, namely the *zero* analysis has shown a degrading effect in the RHP-*zero* direction and therefore an upper bound to the achievable control bandwidth. Moreover, the frequency constraints due to the uncertainties and the *condition number* appear to be less restrictive than that due to the RHP-*zero*. Simulation results provided by the H_∞ controller, a decentralised PID, and a conventional MPC have been presented, including reference tracking, coupling measurement, and disturbance rejection. Alternating step changes on references have been applied for all controllers, and not only at the nominal operating point, but also at a non-nominal point. Troublesome output directions which arise in the controllability analysis have been also studied by means of simultaneous reference changes starting at the nominal operating point. The simulation results are in agreement with the conclusions provided by the controllability analysis: the H_∞ controller shows to be faster, more effective, and with lower coupling between the controlled variables. Moreover, the H_∞ controller is robust when controlling the system at a non-nominal point, while the MPC designed at the nominal operating point turns out to be unstable.

Concerning the *energy-efficiency-aware* control, and given the lack of full controllability suggested by the analysis performed in Chapter 4, a suboptimal hierarchical control strategy is proposed to achieve the highest possible efficiency while satisfying the cooling load. Among the achievable cycles defined by the controllable subspace, an optimizer calculates that reaching maximal *COP*. A one-degree-of-freedom optimization is carried out, since among the three variables defining the cycle, one is devoted to satisfying the cooling demand, whereas another one represents the uncontrolled state and it is just measured. The output of the optimizer is the reference on the degree of superheating, which is updated online to adapt to the evolution of the uncontrolled state. The Practical Nonlinear Model Predictive Control technique is used as low-level controller to get the controlled outputs to track their references. Some simulation results achieved by the suboptimal hierarchical control strategy have been compared to those of two different strategies already studied in the literature about refrigeration systems, namely a feedback-plus-feedforward controller and a *time-varying* extremum-seeking controller. Starting at two different random initial points, a certain cooling demand is intended. All control strategies succeed in satisfying the cooling demand, but only the suboptimal hierarchical control strategy and

the extremum-seeking technique achieve the highest achievable *COP*, although the settling time and controller performance show to be much better when applying the model-based technique. Regardless of the control law, the controllability issues are highlighted, since the initial point defines the controllable subspace and thus it constrains the maximum achievable efficiency in steady state, as previous analysed when studying the results of the optimizer. The suboptimal hierarchical control strategy is also a contribution of the Thesis, since it improves the steady-state performance of existing model-based strategies, such as the feedback-plus-feedforward one, while improving the transient performance of other suboptimal control laws such as the extremum-seeking one.

6.2 Future work

In this Section a number of stimulating challenging lines of research are suggested, including some already started. In the following, some of these ideas are briefly outlined.

- The extension of the control-oriented modelling proposed in Chapter 2 to multi-stage, multi-load-demand cycles is intended, since only the number of elements is increased, as well as their interconnection. However, multi-load and/or multi-stage configurations include the elements of which the simplest cycle is made up: expansion valve, compressor, evaporator, and condenser, and they have been separately modelled. The assumptions made for the one-stage, one-load-demand cycle are expected to hold when analysing more complex cycles, which would allow to extend the control-oriented dynamic modelling to such configurations.
- Regarding the heat exchanger identification, the methodology presented in Chapter 3 could be extended to achieve a more accurate estimation of the heat transfer coefficients based on an online identification procedure, where filtered measurable variables, such as the degree of superheating, pressures, and inlet and outlet temperatures of the heat exchangers, are used to estimate the working conditions and calculate the corresponding heat transfer coefficients, in addition to an estimation of the heat exchanging zone lengths.
- The optimization stage of the proposed control strategy in Chapter 5 is expected to be improved to reduce the computation time. Moreover, the extension of the SHC strategy to multi-load-demand and multi-compression-stage cycles is intended, where even though the number of manipulated inputs is greater, the variable set defining a cycle in steady state also grows in size and the *degree of underactuation* remains the same. Therefore, the controllability issues analysed in Chapter 4 are also expected to appear and the SHC strategy might produce better results regarding efficiency than the *energy-efficiency-aware* control strategies studied so far in the literature.
- Experimental test of the designed optimization and control strategies at the configurable facility is intended. However, despite being in principle possible to configure the plant to work with one compression stage and one load demand, the component selection has been focused on the multi-load-demand configuration. Therefore, a cycle with only one compression stage and one evaporator could be studied, but

the control range is very reduced due to the physical limits of the manipulated elements, specially the main compressor power. It makes very difficult to operate and achieve experimental results with this configuration. Therefore, the extension of the optimization and control strategies developed in this Thesis to multi-stage, multi-load-demand cycles will allow to test them at the experimental facility.

- Energy efficiency of refrigeration systems is intended to be improved by introducing Thermal Energy Storage (TES) units, based on Phase-Change Materials (PCM). Algorithms are intended to be developed for the automatic governance of the TES charge/discharge actions, in such a way that cooling generation costs are minimized. Three main factors are involved: the first two are daily forecast in cooling demand and the fact that the performance of the refrigeration cycle may vary along the day (according to environmental conditions, for instance). These two factors, when taken into consideration, might induce a significant reduction in the energy consumption. The third factor to take in mind is the hourly electric energy cost, which might lead to a more cost-effective cooling generation/storage in some particular periods along the day. Optimization of cooling generation and storage management is to be addressed, bearing in mind the three main factors previously stated. The theoretical results and simulation studies are to be experimentally tested at the two-stage, two-load-demand plant, which is intended to be upgraded by adding PCM-based TES units for cold storage, as shown in Figure 6.1.

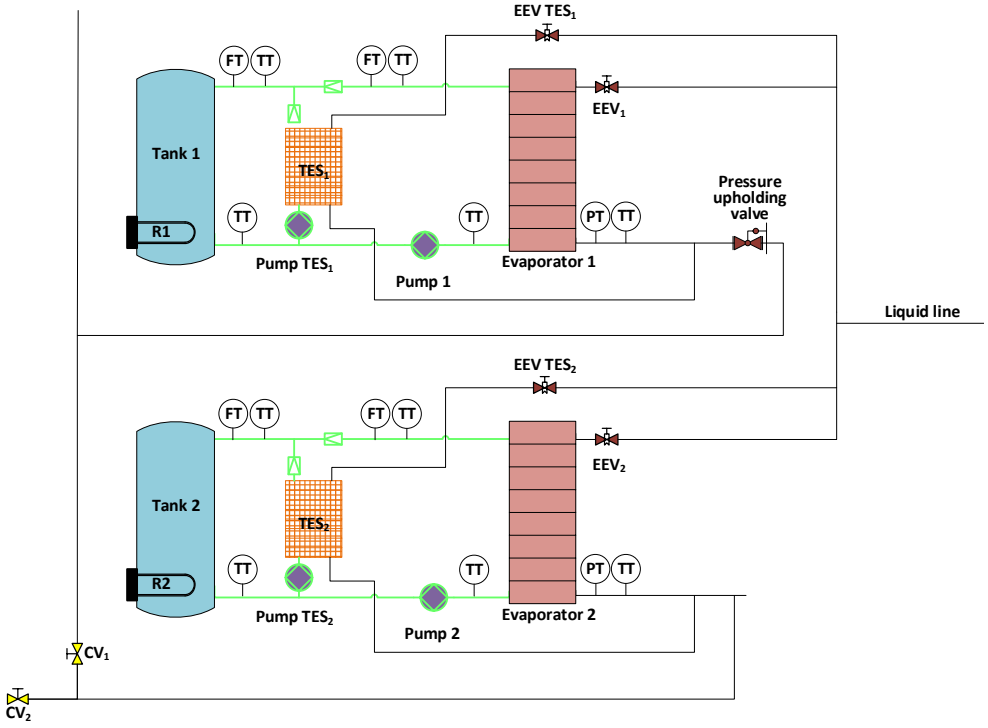

Figure 6.1 Upgrade of the experimental plant including the PCM-based TES units.

Appendix A
Signal distribution and PLC bus cycle

This Appendix gathers some specific information regarding the PLC used at the experimental plant. Signal wiring through the thermocouple converters and analogue mixed modules is described, as well as the reading and writing operations carried out by the communication bus at both valve control modes and the shift scheme used in each case.

A.1 Signal wiring

Table A.1 gathers the thermocouple signals wired through the converters, while in Table A.2 the specific signals connected through the analogue mixed modules are shown.

Table A.1 Thermocouple signal converters.

Converter	Thermocouple signals
I	Booster compressor suction temperature Evaporator 1 inlet brine temperature Water-cooled condenser outlet water temperature Liquid line temperature
II	Evaporator 2 inlet brine temperature Ambient temperature Main compressor discharge temperature Main compressor intake temperature

Table A.2 Analogue input/output mixed modules.

Module	Input signals	Output signals
I	Main compressor discharge pressure	Condenser fan speed
	Main compressor intake pressure	-
	Booster compressor discharge pressure	-
	Liquid line pressure	-
II	Pump 1 brine volumetric flow	Tank 1 resistance
	Pump 2 brine volumetric flow	Tank 2 resistance
	Pump 3 water volumetric flow	-
	Booster compressor intake pressure	-
III	Evaporator 1 outlet brine temperature	-
	Evaporator 2 outlet brine temperature	-
	Evaporator 1 outlet refrigerant pressure	-
	Evaporator 2 outlet refrigerant temperature	-

A.2 PLC bus cycle

Tables A.3 and A.4 show all reading and writing operations carried out at the communication bus using both valve control modes. Furthermore, the shift scheme used for the low priority register is summarised in Tables A.5 and A.6, for both valve control modes.

Table A.3 Bus cycle when the valves are controlled by the PLC.

Slot	Reading operations	Writing operations
1	Main compressor VFD speed	-
2	Booster compressor VFD speed	-
3	Pump 3 VFD speed	-
4	Pump 1 VFD speed	-
5	Pump 2 VFD speed	-
6	EEV_1 SVC temperature	-
7	EEV_1 SVC alarm register 1	-
8	EEV_2 SVC temperature	-
9	EEV_2 SVC alarm register 1	-
10	Low priority register 1	-
11	Low priority register 2	-
13	-	Reference on the main compressor VFD speed
14	-	Reference on the booster compressor VFD speed
15	-	Reference on the pump 3 VFD speed
16	-	Reference on the pump 1 VFD speed
17	-	Reference on the pump 2 VFD speed
18	-	Pump 3 control register
19	-	Pump 1 control register
20	-	Pump 2 control register

Table A.4 Bus cycle when the valves are controlled by the SVCs.

Slot	Reading operations	Writing operations
1	Main compressor VFD speed	-
2	Booster compressor VFD speed	-
3	Pump 3 VFD speed	-
4	Pump 1 VFD speed	-
5	Pump 2 VFD speed	-
6	EEV_1 SVC temperature sensor	-
7	EEV_1 SVC pressure sensor	-
8	EEV_1 SVC degree of superheating	-
9	EEV_1 SVC valve opening	-
10	EEV_1 SVC alarm register 1	-
11	EEV_2 SVC temperature sensor	-
12	EEV_2 SVC pressure sensor	-
13	EEV_2 SVC degree of superheating	-
14	EEV_2 SVC valve opening	-
15	EEV_2 SVC alarm register 1	-
16	Low priority register 1	-
17	Low priority register 2	-
18	Low priority register 3	-
19	Low priority register 4	-
20	-	-
21	-	Reference on the main compressor VFD speed
22	-	Reference on the booster compressor VFD speed
23	-	Reference on the pump 3 VFD speed
24	-	Reference on the pump 1 VFD speed
25	-	Reference on the pump 2 VFD speed
26	-	Reference on the EEV_1 SVC degree of superheating
27	-	Reference on the EEV_2 SVC degree of superheating
28	-	Pump 3 control register
29	-	Pump 1 control register
30	-	Pump 2 control register

Table A.5 Shift scheme when the valves are controlled through the SVCs.

Turn 1	EEV_1 SVC cooling call	EEV_1 SVC alarm register 1	EEV_2 SVC state register 1	Main compressor VFD state register
Turn 2	EEV_1 SVC digital output register 1	EEV_1 SVC alarm register 2	EEV_2 SVC state register 2	Booster compressor VFD state register
Turn 3	EEV_1 SVC digital output register 2	EEV_1 SVC alarm register 3	EEV_2 SVC state register 3	Pump 3 VFD state register
Turn 4	EEV_1 SVC state register 1	EEV_2 SVC cooling call	EEV_2 SVC alarm register 1	Pump 1 VFD state register
Turn 5	EEV_1 SVC state register 2	EEV_2 SVC digital output register 1	EEV_2 SVC alarm register 2	Pump 2 VFD state register
Turn 6	EEV_1 SVC state register 3	EEV_2 SVC digital output register 2	EEV_2 SVC alarm register 3	-

Table A.6 Shift scheme when the valves are controlled straightly from the PLC.

Low priority register	**Turn 1**	**Turn 2**	**Turn 3**
1	Main compressor VFD state register	Booster compressor VFD state register	Pump 3 VFD state register
2	Pump 1 VFD state register	Pump 2 VFD state register	-

List of Figures

List of Tables

Bibliography

[1] B. P. Rasmussen, A. Musser, and A. G. Alleyne, "Model-driven system identification of transcritical vapor compression systems," *IEEE Trans. Control Syst. Technol.*, vol. 13, pp. 444–451, 2005.

[2] L. O. S. Buzelin, S. C. Amico, J. V. C. Vargas, and J. A. R. Parise, "Experimental development of an intelligent refrigeration system," *Int. J. Refrig.*, vol. 28, no. 2, pp. 165–175, 2005.

[3] K. A. Jahangeer, A. A. O. Tay, and M. R. Islam, "Numerical investigation of transfer coefficients of an evaporatively-cooled condenser," *Appl. Therm. Eng.*, vol. 31, no. 10, pp. 1655–1663, 2011.

[4] US Energy Information Administration, "Residential energy consumption survey (RECS)," Energy Information Administration, Washington D.C, USA, Tech. Rep., 2009.

[5] US Environmental Protection Agency, "National action plan for energy efficiency: Sector collaborative on energy efficiency accomplishments and next steps." [Online]. Available: http://www.epa.gov/cleanenergy/documents/suca/sector_collaborative.pdf

[6] V. D. Baxter, "Advances in supermarket refrigeration systems," *Oak Ridge Natl. Lab., Oak Ridge, Tennessee 37831-6070*, 2002.

[7] Y. Suzuki, Y. Yamaguchi, K. Shiraishi, D. Narumi, and Y. Shimoda, "Analysis and modeling of energy demand of retail stores," in *12th Conf. of Int. Build. Perform. Simul. Assoc.*, 2011.

[8] L. Pérez-Lombard, J. Ortiz, and C. Pout, "A review on buildings energy consumption information," *Energy and Build.*, vol. 40, no. 3, pp. 394–398, 2008.

[9] N. Kalkan, E. A. Young, and A. Celiktas, "Solar thermal air conditioning technology reducing the footprint of solar thermal air conditioning," *Renew. and Sustain. Energy Rev.*, vol. 16, no. 8, pp. 6352–6383, 2012.

[10] L. Larsen, "Model based control of refrigeration systems," Ph.D. dissertation, Central R. & D. Danfoss, DK-6430 Nordborg, Denmark, 2005.

[11] L. C. Schurt, C. J. L. Hermes, and A. Trofino-Neto, "A model-driven multivariable controller for vapor compression refrigeration systems," *Int. J. of Refrig.*, vol. 32, no. 7, pp. 1672–1682, 2009.

[12] N. Jain, "Thermodynamics-based optimization and control of integrated energy systems," Ph.D. dissertation, University of Illinois at Urbana-Champaign, 2013.

[13] J. B. Jensen and S. Skogestad, "Optimal operation of simple refrigeration cycles: Part *I*: Degrees of freedom and optimality of sub-cooling," *Comput. and Chem. Eng.*, vol. 31, no. 5, pp. 712–721, 2007.

[14] N. Jain and A. G. Alleyne, "Thermodynamics-based optimization and control of vapor-compression cycle operation: optimization criteria," in *Am. Control Conf., 2011*. IEEE, 2011, pp. 1352–1357.

[15] J. W. MacArthur, "Transient heat pump behaviour: a theoretical investigation," *Int. J. of Refr.*, vol. 7, no. 2, pp. 123–132, 1984.

[16] D. Limperich, M. Braun, K. Prölß, and G. Schmitz, "System simulation of automotive refrigeration cycles," in *Proc. of the 4th Int. Modelica Conf.*, 2005.

[17] H. Tummescheit, J. Eborn, and K. Prölss, "Airconditioning–a Modelica library for dynamic simulation of AC systems," in *Proc. of the 4th Int. Modelica Conf.*, 2005.

[18] J. W. MacArthur, G. D. Meixel, and L. S. Shen, "Application of numerical methods for predicting energy transport in earth contact systems," *Appl. Energy*, vol. 13, no. 2, pp. 121–156, 1983.

[19] X. Jia, C. Tso, P. Jolly, and Y. Wong, "Distributed steady and dynamic modelling of dry-expansion evaporators: Modèlisation du régime stable et du régime transitoire des évaporateurs à détente sèche," *Int. J. of Refr.*, vol. 22, no. 2, pp. 126–136, 1999.

[20] Y. Liang, S. Shao, C. Tain, and Y. Yang, "Dynamic simulation of variable capacity refrigeration systems under abnormal conditions," *Appl. Therm. Eng.*, vol. 30, no. 10, pp. 1205–1214, 2010.

[21] T. L. McKinley and A. G. Alleyne, "An advanced nonlinear switched heat exchanger model for vapor compression cycles using the moving-boundary method," *Int. J. of Refrig.*, vol. 31, no. 7, pp. 1253–1264, 2008.

[22] B. Li, "Dynamic modeling and control of vapor compression cycle systems with shut-down and start-up operations," Ph.D. dissertation, University of Illinois, Urbana-Champaign, USA, 2009.

[23] B. Li and A. G. Alleyne, "A dynamic model of a vapor compression cycle with shut-down and start-up operations," *Int. J. of Refrig.*, vol. 33, no. 3, pp. 538–552, 2010.

[24] H. Pangborn, A. G. Alleyne, and N. Wu, "A comparison between finite volume and switched moving boundary approaches for dynamic vapor compression system modeling," *Int. J. of Refrig.*, vol. 53, pp. 101–114, 2015.

[25] S. Bittanti and L. Piroddi, "Nonlinear identification and control of a heat exchanger: a neural network approach," *J. of the Frankl. Inst.*, vol. 334, no. 1, pp. 135–153, 1997.

[26] J. A. Romero, J. Navarro-Esbrí, and J. M. Belman-Flores, "A simplified black-box model oriented to chilled water temperature control in a variable speed vapour compression system," *Appl. Therm. Eng.*, vol. 31, no. 2, pp. 329–335, 2011.

[27] J. Marcinichen, T. del Holanda, and C. Melo, "A dual SISO controller for a vapor compression refrigeration system," in *Int. Refrig. and Air Cond. Conf.*, 2008, pp. 2444, 1–8.

[28] J. Wang, C. Zhang, Y. Jing, and D. An, "Study of neural network PID control in variable-frequency air-conditioning system," in *IEEE Int. Conf. on Control and Autom.*, 2007, pp. 317–322.

[29] C. P. Underwood, "Analysing multivariable control of refrigeration plant using MATLAB/Simulink," in *VII Int. IBPSA Conf.*, vol. 1, 2001, pp. 287–94.

[30] M. Salazar and F. Méndez, "PID control for a single-stage transcritical CO_2 refrigeration cycle," *Appl. Therm. Eng.*, vol. 67, no. 1, pp. 429–438, 2014.

[31] Y. Shen, W.-J. Cai, and S. Li, "Normalized decoupling control for high-dimensional MIMO processes for application in room temperature control HVAC systems," *Control Eng. Pract.*, vol. 18, no. 6, pp. 652–664, 2010.

[32] X.-D. He, "Dynamic modeling and multivariable control of vapor compression cycles in air conditioning systems," Ph.D. dissertation, Massachusetts Institute of Technology, Massachusetts, USA, 1996.

[33] L. C. Schurt, C. J. L. Hermes, and A. Trofino-Neto, "Assessment of the controlling envelope of a model-based multivariable controller for vapor compression refrigeration systems," *Appl. Therm. Eng.*, vol. 30, no. 13, pp. 1538–1546, 2010.

[34] M. Razi, M. Farrokhi, M. Saeidi, and A. F. Khorasani, "Neuro-predictive control for automotive air conditioning system," in *Eng. of Intell. Syst., 2006 IEEE Int. Conf. on*. IEEE, 2006, pp. 1–6.

[35] D. Sarabia, F. Capraro, L. F. Larsen, and C. de Prada, "Hybrid NMPC of supermarket display cases," *Control Eng. Pract.*, vol. 17, no. 4, pp. 428–441, 2009.

[36] N. L. Ricker, "Predictive hybrid control of the supermarket refrigeration benchmark process," *Control Eng. Pract.*, vol. 18, no. 6, pp. 608–617, 2010.

[37] H. Fallahsohi, C. Changenet, S. Placé, C. Ligeret, and X. Lin-Shi, "Predictive functional control of an expansion valve for minimizing the superheat of an evaporator," *Int. J. of Refrig.*, vol. 33, no. 2, pp. 409–418, 2010.

[38] L. S. Larsen and J. R. Holm, "Modelling and multi-variable control of refrigeration systems," *ECOS 2003*, 2003.

[39] A. Jakobsen, B. D. Rasmussen, M. Skovrup, and J. Fredsted, "Development of energy optimal capacity control in refrigeration systems," in *Proc. of 2000 Int. Refr. Conf.*, 2000, pp. 329–336.

[40] L. S. Larsen and C. Thybo, "Potential energy savings in refrigeration systems using optimal set-points," in *Control Appl., 2004. Proc. of the 2004 IEEE Int. Conf. on*, vol. 1. IEEE, 2004, pp. 701–704.

[41] N. Jain and A. G. Alleyne, "A framework for the optimization of integrated energy systems," *Appl. Therm. Eng.*, vol. 48, pp. 495–505, 2012.

[42] L. Zhao, W. Cai, X. Ding, and W. Chang, "Model-based optimization for vapor compression refrigeration cycle," *Energy*, vol. 55, pp. 392–402, 2013.

[43] L. Zhao, W.-J. Cai, X.-d. Ding, and W.-c. Chang, "Decentralized optimization for vapor compression refrigeration cycle," *Appl. Therm. Eng.*, vol. 51, no. 1, pp. 753–763, 2013.

[44] N. Jain and A. G. Alleyne, "Exergy-based optimal control of a vapor compression system," *Energy Convers. and Manag.*, vol. 92, pp. 353–365, 2015.

[45] J. B. Jensen and S. Skogestad, "Optimal operation of simple refrigeration cycles: Part *II*: Selection of controlled variables," *Comput. and Chem. Eng.*, vol. 31, no. 12, pp. 1590–1601, 2007.

[46] L. F. S. Larsen, C. Thybo, J. Stoustrup, and H. Rasmussen, "A method for online steady state energy minimization, with application to refrigeration systems," in *Decis. and Control, 43rd IEEE Conf. on*, vol. 5. IEEE, 2004, pp. 4708–4713.

[47] D. Burns and C. Laughman, "Extremum seeking control for energy optimization of vapor compression systems," in *Int. Refr. and Air Cond. Conf., 2012*, 2012.

[48] M. Guay, "A time-varying extremum-seeking control approach for discrete-time systems," *J. of Process Control*, vol. 24, no. 3, pp. 98–112, 2014.

[49] D. J. Burns, W. K. Weiss, and M. Guay, "Realtime setpoint optimization with time-varying extremum seeking for vapor compression systems," in *Am. Control Conf., 2015*. IEEE, 2015, pp. 974–979.

[50] G. Bejarano, C. Vivas, M. G. Ortega, and M. Vargas, "Suboptimal hierarchical control strategy to improve energy efficiency of vapour-compression refrigeration systems," *Appl. Therm. Eng.*, 2017, submitted for publication with preliminary review status: potentially publishable.

[51] G. Bejarano, M. G. Ortega, J. E. Normey-Rico, and F. R. Rubio, "Optimal control analysis of vapour-compression refrigeration systems. Application of Practical Nonlinear Model Predictive Control," *J. of Process Control*, 2017, submitted for publication with preliminary review status: potentially publishable.

[52] D. Rodríguez, G. Bejarano, J. A. Alfaya, M. G. Ortega, and F. Castaño, "Parameter identification of a multi-stage, multi-load-demand experimental refrigeration plant," *Control Eng. Pract.*, vol. 60, pp. 133–147, 2017.

[53] G. Bejarano, J. A. Alfaya, M. G. Ortega, and M. Vargas, "On the difficulty of globally optimally controlling refrigeration systems," *Appl. Therm. Eng.*, vol. 111, pp. 1143–1157, 2017.

[54] G. Bejarano, D. Rodríguez, J. A. Alfaya, M. G. Ortega, and F. Castaño, "On identifying steady-state parameters of an experimental mechanical-compression refrigeration plant," *Appl. Therm. Eng.*, vol. 109, pp. 318–333, 2016.

[55] G. Bejarano, J. A. Alfaya, M. G. Ortega, and F. R. Rubio, "Multivariable analysis and H_∞ control of a one-stage refrigeration cycle," *Appl. Therm. Eng.*, vol. 91, pp. 1156–1167, 2015.

[56] J. A. Alfaya, G. Bejarano, M. G. Ortega, and F. R. Rubio, "Controllability analysis and robust control of a one-stage refrigeration system," *Eur. J. of Control*, vol. 26, pp. 53–62, 2015.

[57] G. Bejarano, M. G. Ortega, and F. R. Rubio, "Optimización global estática de sistemas de refrigeración," in *XXXVII Jorn. de Autom., Madrid (Spain)*, 2016, pp. 19–26.

[58] D. Rodríguez, J. A. Alfaya, G. Bejarano, M. G. Ortega, and F. Castaño, "Identificación paramétrica del condensador de una planta experimental de refrigeración," in *XXXVII Jorn. de Autom., Madrid (Spain)*, 2016, pp. 27–34.

[59] D. Rodríguez, J. A. Alfaya, G. Bejarano, M. G. Ortega, and F. Castaño, "Steady-state parameter estimation of an experimental vapour compression refrigeration plant," in *Eur. Control Conf. (ECC), Aalborg (Denmark)*. IEEE, 2016, pp. 43–48.

[60] G. Bejarano, M. G. Ortega, and F. R. Rubio, "Optimization and multivariable robust control of refrigeration systems," in *XIV Simp. CEA de Ing. de Control, Logroño (Spain)*, 2016.

[61] D. Rodríguez, J. A. Alfaya, G. Bejarano, M. G. Ortega, and F. Castaño, "Estimación de parámetros de una planta experimental de refrigeración," in *XXXVI Jorn. de Autom., Bilbao (Spain)*, 2015, pp. 951–958.

[62] J. A. Alfaya, G. Bejarano, M. G. Ortega, and F. R. Rubio, "Multi-operating-point robust control of a one-stage refrigeration cycle," in *Eur. Control Conf. (ECC), Linz (Austria)*. IEEE, 2015, pp. 3490–3495.

[63] G. Bejarano, J. A. Alfaya, M. G. Ortega, and F. R. Rubio, "Design, automation and control of a two-stage, two-load-demand experimental refrigeration plant," in *23rd Mediterranean Conf. on Control and Autom., Torremolinos (Spain)*, 2015, pp. 537–544.

[64] J. A. Alfaya, G. Bejarano, M. G. Ortega, and F. R. Rubio, "Control robusto multivariable de un ciclo de refrigeración," in *XXXV Jorn. de Autom., Valencia (Spain)*, 2014.

[65] G. Bejarano, M. G. Ortega, F. R. Rubio, and F. Morilla, "Modelado simplificado y orientado al control de sistemas de refrigeración," in *XXXIV Jorn. de Autom., Terrassa (Spain)*, 2013, pp. 506–513.

[66] P. Millán, L. Orihuela, G. Bejarano, C. Vivas, T. Alamo, and F. R. Rubio, "Design and application of suboptimal mixed H_2/H_∞ controllers for networked control systems," *IEEE Trans. on Control Syst. Technol.*, vol. 20, no. 4, pp. 1057–1065, 2012.

[67] L. Orihuela, P. Millán, G. Bejarano, C. Vivas, and F. R. Rubio, "Optimal networked control of a 2 degree-of-freedom direct drive robot manipulator," in *Emerg. Technol. and Fact. Autom. (ETFA), 2010 IEEE Conf. on*. IEEE, 2010.

[68] G. Bejarano, C. Vivas, and F. R. Rubio, "Experiencias de identificación de un robot de accionamiento directo," in *XXX Jorn. de Autom., Valladolid (Spain)*, 2009.

[69] I. H. Bell, J. Wronski, S. Quoilin, and V. Lemort, "Pure and pseudo-pure fluid thermophysical property evaluation and the open-source thermophysical property library CoolProp," *Ind. and Eng. Chem. Res.*, vol. 53, no. 6, pp. 2498–2508, 2014. [Online]. Available: www.coolprop.org

[70] J. P. Holman, *Heat transfer*, 8th ed. MacGraw-Hill Inc, 2001.

[71] T. L. Bergman, F. P. Incropera, A. S. Lavine, and D. P. Dewitt, *Fundamentals of heat and mass transfer*, 7th ed. John Wiley & Sons, 2011.

[72] Engineering Science Data Unit, "ESDU 98005. Design and Performance Evaluation of Heat Exchangers: The Effectiveness - NTU Method," Engineering Science Data Unit (ESDU), International Publishing, London, England, Tech. Rep., 1998.

[73] ASHRAE, "ASHRAE Handbook: Fundamentals, SI Ed." *Am. Soc. of Heat., Refr. and Air Cond. Eng., Atlanta*, 2005.

[74] H. Rasmussen and L. F. S. Larsen, "Non-linear and adaptive control of a refrigeration system," *IET Control Theory Appl.*, vol. 5, no. 2, pp. 365–378, 2011.

[75] A. Mota-Babiloni, J. Navarro-Esbrí, Á. Barragán-Cervera, F. Molés, and B. Peris, "Analysis based on EU Regulation No 517/2014 of new HFC/HFO mixtures as alternatives of high GWP refrigerants in refrigeration and HVAC systems," *Int. J. of Refr.*, vol. 52, pp. 21–31, 2015.

[76] Modbus application protocol specification v1.1b3. [Online]. Available: http://www.modbus.org/tech.php

[77] OPC Foundation, *OPC Data Access Custom Interface*, 1998.

[78] The Mathworks Inc., *OPC Toolbox User's Guide*, 2008.

[79] C. Park, H. Cho, Y. Lee, and Y. Kim, "Mass flow characteristics and empirical modeling of r22 and r410a flowing through electronic expansion valves," *Int. J. of Refrig.*, vol. 30, no. 8, pp. 1401–1407, 2007.

[80] M. Shanwei, Z. Chuan, C. Jiangping, and C. Zhiujiu, "Experimental research on refrigerant mass flow coefficient of electronic expansion valve," *Appl. Therm. Eng.*, vol. 25, no. 14, pp. 2351–2366, 2005.

[81] I. Fantoni and R. Lozano, *Non-linear control for underactuated mechanical systems*. Springer Science & Business Media, 2002.

[82] G. V. Raffo, M. G. Ortega, and F. R. Rubio, "An underactuated H_∞ control strategy for a quadrotor helicopter," in *Eur. Control Conf. (ECC), 2009*. IEEE, 2009, pp. 3845–3850.

[83] G. V. Raffo, V. Madero, and M. G. Ortega, "An application of the underactuated nonlinear H_∞ controller to two-wheeled self-balanced vehicles," in *Emerg. Technol. and Fact. Autom. (ETFA), 2010 IEEE Conf. on*. IEEE, 2010, pp. 1–6.

[84] G. V. Raffo, M. G. Ortega, and F. R. Rubio, "An integral predictive/nonlinear H_∞ control structure for a quadrotor helicopter," *Automatica*, vol. 46, no. 1, pp. 29–39, 2010.

[85] G. V. Raffo, M. G. Ortega, and F. R. Rubio, "Nonlinear H_∞ controller for the quadrotor helicopter with input coupling," in *Proc. of the 18th IFAC World Congr., Milano, Italia*, vol. 18, 2011, pp. 13 834–13 839.

[86] M. G. Ortega, M. Vargas, F. Castaño, and F. R. Rubio, "Improved Design of the Weighting Matrices for the *S/KS/T* Mixed Sensitivity Problem - Application to a Multivariable Thermodynamic System," *IEEE Trans. on Control Syst. Technol.*, vol. 14, no. 1, pp. 82–90, 2006.

[87] M. G. Ortega, F. Castaño, M. Vargas, and F. Rubio, "Multivariable robust control of a rotary dryer: Analysis and design," *Control Eng. Pract.*, vol. 15, no. 4, pp. 487–500, 2007.

[88] A. Plucenio, D. J. Pagano, A. H. Bruciapaglia, and J. E. Normey-Rico, "A practical approach to predictive control for nonlinear processes," in *7th IFAC Symp. on Nonlinear Control Syst., Pretoria, South Africa*, vol. 7, 2007, pp. 210–215.

[89] A. Plucenio, "Desenvolvimento de técnicas de controle não linear para elevação de fluidos multifásicos," Ph.D. dissertation, Federal University of Florianópolis, Santa Catarina, Brazil, 2010.

[90] S. Skogestad and I. Postlethwaite, *Multivariable Feedback Control*, 2nd ed. New York: Wiley, 2005.

[91] K. J. Astrom, "Limitations on control system performance," *Eur. J. of Control*, vol. 6, no. 1, pp. 2–20, 2000.

[92] B. R. Holt and M. Morari, "Design of resilient processing plants-VI. The effect of right-half-plane zeros on dynamic resilience," *Chemic. Eng. Sci.*, vol. 40, no. 1, pp. 59–74, 1985.

[93] J. C. Doyle, K. Glover, P. Khargonekar, and B. Francis, "State-space solutions to standard H_2 and H_∞ control problems," *IEEE Trans. on Autom. Control*, vol. 34, no. 8, pp. 831–847, 1989.

[94] P. Iglesias and K. Glover, "State-space approach to discrete-time H_∞ control," *Int. J. of Control*, vol. 54, no. 5, pp. 1031–1073, 1991.

[95] K. Zhou, J. C. Doyle, and K. Glover, *Robust and optimal control*. Prentice Hall New Jersey, 1996, vol. 40.

[96] M. G. Ortega and F. R. Rubio, "Systematic design of weighting matrices for H_∞ mixed sensitivity problem," *J. of Process Control*, vol. 14, no. 1, pp. 89–98, 2004.

[97] E. F. Camacho and C. A. Bordons, *Model predictive control in the process industry*. Springer-Verlag New York, Inc., 1997.

[98] D. Limón, I. Alvarado, T. Alamo, and E. F. Camacho, "MPC for tracking piecewise constant references for constrained linear systems," *Automatica*, vol. 44, no. 9, pp. 2382–2387, 2008.